Non-adiabatic Effects in the Oxidation of Alkali Metals

Von der Fakultät für Physik der Universität Duisburg-Essen
zur Erlangung des akademischen Grades
Dr. rer. nat.
genehmigte Dissertation

von
David Krix
aus Bottrop

16. September 2010

1. Gutachter: Prof. Dr. Hermann Nienhaus
2. Gutachter: Prof. Dr. Marika Schleberger
3. Gutachter: Prof. Dr. Rainer Beck

Vorsitz der Prüfungsausschusses: Prof. Dr. Peter Kratzer

Weiteres Mitglied des Prüfungsausschusses: Prof. Dr. Axel Lorke

Tag der mündlichen Prüfung: 3. Februar 2011

Meinen Eltern

Abstract

Non-adiabatic effects during the oxidation of alkali metal surfaces were studied. For this purpose thin film Schottky diodes based on silicon substrates were developed. The diodes were used to detect low lying electron-hole pair excitations leading to chemicurrents through the devices. The chemicurrent concept has been combined with a setup to detect highly energetic exoelectrons emitted in the cause of the reactions. In contrast to previous studies, it has been found that the chemicurrent is not simply proportional to the reaction rate. Exposure dependent chemicurrent and exoemission efficiencies have to be assumed to correctly describe the time evolution of chemicurrent and exoemission traces.

Most experiments were carried for liquid nitrogen cooled samples at a temperature of 120 K. From independent photo emission experiments the reaction kinetics of the oxidation of alkali metal films in a low pressure oxygen atmosphere could be determined. The structure of the O 1s photoemission line was used to determine the chemical composition of the oxide films. For lithium and sodium substantial amounts of dissociatively adsorbed oxygen could be observed. Molecular adsorption as peroxides and superoxides is dominant for the other alkali metals. Unactivated adsorption of oxygen on fresh potassium films occurs predominantly as peroxide. The high exposure regime is dominated by diffusion of potassium atoms to the surface and the absorption of superoxide ions. Valence band photoemission (UPS) reveal the molecular adsorption which confirm the previous interpretation of the chemical shift in the O 1s XPS data.

Chemicurrent and exoemission data for oxygen adsorption show that non-adiabatic effects are not restricted to the dissociation of oxygen molecules. The second charge transfer $O_2^- \rightarrow O_2^{2-}$ efficiently generates low lying electronic excitations which can be measured as a chemicurrent. At the same time high energy exoelectrons are emitted via Auger processes. A shift between the chemicurrent and exoemission traces are observed which is explained by the low bandwidth of the alkali metals. If the injected hole state lives sufficiently long, there is the possibility for it to be injected below the band bottom. This suppresses the resonant ionization of the adsorbate, and hence reduces the chemicurrent. The exoemission, however, is not affected. The oxidation of the surface effectively decouples the adsorbate states from the metal leading to a longer lifetime of the injected hole states. An increase of the non-adiabaticity of the adsorption is the consequence.

Model calculations using a Newns-Anderson Hamiltonian were carried out to calculate non-adiabatic excitation spectra for the adsorption of an oxygen molecule on a clean K(100) surface. Parameters for the time-dependent Newns-Anderson calculation were obtained from independent DFT results. A large imbalance between excited holes and electrons is found. These results show that the effective temperature description of the spectra is not suitable for the system.

Kurzfassung

In dieser Arbeit werden nicht-adiabatische Effekte bei der Oxidation von Alkalimetalloberflächen untersucht. Hierzu wurden Dünnschicht-Schottkydioden auf der Basis von Siliziumsubstrat hergestellt. Die so hergestellten Dioden dienten als Detektoren zur Messung von durch niederenergetische Elektron-Loch-Paar-Anregungen induzierte Chemoströme. Das Chemostromkonzept wurde mit einem Aufbau zur Detektion von hochangeregten Exoelektronen, die im Verlauf der Reaktion freigesetzt werden, erweitert. Im Gegensatz zu vorhergehenden Studien wurde festgestellt, dass die Chemoströme keiner einfachen Proportionalität zur Reaktionsrate folgen. Bedeckungsabhängige Chemostrom- und Exoemissionseffizienzen müssen angenommen werden um die zeitliche Entwicklung des Chemostroms und der Exoemission korrekt wiederzugeben.

Die Experimente wurden größtenteils an mit flüssigem Stickstoff gekühlten Proben bei einer Temperatur von 120 K vorgenommen. Durch unabhängige Photoemissionsexperimente wurde die Reaktionskinetik der Oxidation von Alkalimetallfilmen bei tiefen Temperaturen in einer Sauerstoffatmosphäre bei niedrigem Druck bestimmt. Die Struktur der O 1s Photoemissionsline diente dazu die chemische Zusammensetzung der Oxidfilme zu bestimmen. Auf Lithium- und Natriumfilmen adsorbieren beträchtliche Anteile des angebotenen Sauerstoff dissoziativ. Bei den anderen Akalkimetallen wurde vorwiegend molekulare Adsorption als Peroxid und Superoxid gefunden. Auf unbedeckten Kaliumoberflächen wurde eine direkte Adsorption von Peroxidionen beobachtet. Bei höheren Bedeckungen wird die Reaktion durch die Diffusion von Kaliumatomen durch den Oxidfilm dominiert und durch Superoxidadsorption bestimmt. Valenzbandspektroskopie (UPS) untermauert die Interpretation der vorgestellten chemischen Verschiebung der O 1s Linie, die durch XPS-Messungen bestimmt wurde. Die Chemostrom und Exoemissionsdaten zeigen, dass die nicht-adiabatischen Effekte nicht auf die Dissoziation von Sauerstoffmolekülen beschränkt sind. Der zweite Ladungstransfer $O_2^- \rightarrow O_2^{2-}$ generiert tief liegende elektronische Anregungen, die als Chemostrom detektiert werden können. Gleichzeitig führen allerdings Augerprozesse zur Emission von Exoelektronen. Ein Versatz zwischen Chemostrom und Exoemission wurde beobachtet, welcher durch die niedrige Bandbreite der Alkalimetalle erklärt wird. Bei einer ausreichenden Lebensdauer des injizierten Lochzustands kann dieser unter die Bandkante des Metalls gedrückt werden, was die resonante Ionization des Adsorbats (und damit den Chemostrom) unterdrückt. Die Exoemission dagegen ist hiervon nicht betroffen. Die Oxidation der Oberfläche entkoppelt die Adsorbatzustände effektiv von denen des Metalls. Dies führt zu einer verlängerten Lebensdauer der injizierten Lochzustände, was eine erhöhte Nichtadiabatizität der Adsorption zur Folge hat.

Modelrechnung wurden unter Benutzung eines Newns-Anderson Hamiltonian durchgeführt um nicht-adiabatische Anregungensspektren hervorgerufen durch die Adsorption eines Sauerstoffmoleküls auf einer K(100) Oberfläche zu beschreiben. Parameter für das zeitabhängige Newns-Anderson Model wurden aus unabhängigen Dichtefunktionalrechnungen entnommen. Ein großes Ungleichgewicht zwischen angeregten Löcher und Elektronen wurde gefunden. Diese Ergebnisse zeigen, dass eine Beschreibung durch eine effektive Temperatur für die betrachteten Systeme nicht angemessen ist.

Es ist egal, ob eine Sache wahr ist oder nicht. Sie wird es mit der Zeit schon werden.

(Gabriel García Márquez)

Contents

1. Introduction

1.1. Energy Dissipation at Surfaces

The interaction between particles from the gas phase and solid surfaces plays a vital role in numerous applications. In particular, many technically relevant processes used by the chemical industry are based on the heterogeneous catalysis of reactions at metal surfaces. In spite of their wide use the details of these reactions have remained to the least elusive for a long time. Indeed, only with the advent of the ultra high vacuum technology in the early 1960s experiments became feasible that led to a sharp rise in knowledge and understanding of many aspects of surface chemistry.

One of the problems that remains without a satisfying answer up to today is in which way the energy released during a chemical reaction is dissipated into heat. It is a clear fact that most of the energy released during the formation of a chemical bond in an exothermal reaction eventually leads to a temperature rise of the lattice. Apart from the direct conversion of chemical into kinetic energy of the lattice, different paths of energy flow are thinkable. One is the intermediate excitation of the electronic system in the solid which subsequently relaxes through electron-phonon coupling. If the energy is dissipated directly into the lattice one often uses the term *adiabatic* as opposed to *non-adiabatic* energy dissipation which includes electronic excitations. These non-adiabatic pathways of energy release are the subject of this study.

Non-adiabatic excitations during a gas-surface reaction include a variety of elementary processes which may be observed experimentally. Figure 1.1 gives an overview over the most widely exploited processes for the study of non-adiabaticity, including the emission of light, the emission of charged particles from the surface and the excitation of electron-hole pairs in the solid. Chemiluminescence, i.e., the emission of a non-thermal spectrum of light, and exoelectron emission, i.e., the emission of electrons excited through an exothermic reaction, have been observed and studied for a wide range of reactions by a large number of people [Kra51, GAC70, KW75, Gre97, Nie02]. In spite of its popularity the investigation of electron exoemission is especially limited by the fact that

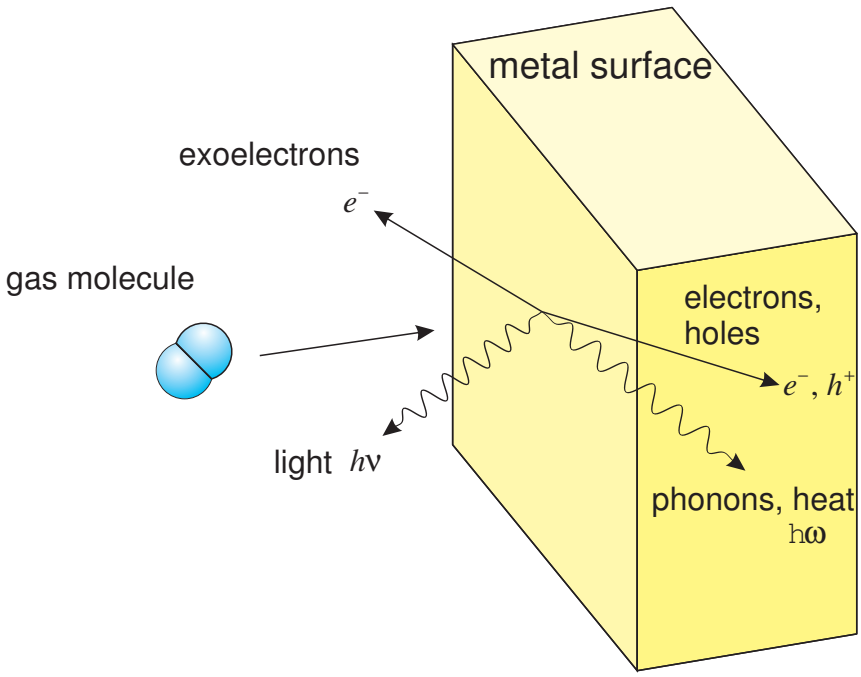

Figure 1.1.: Elementary excitation processes during the reaction of a gas molecule with a metal surface. They include the direct excitation of phonons, chemiluminescence, the emission of exoelectrons and the excitation of electron-hole pairs in the solid.

only electrons with energies sufficient to surmount the surface barrier can be observed. This reduces its practical use to highly exothermic reactions or to metal surfaces with low work functions, e.g., alkali metal surfaces [KTNL79, PLF81, BGG+93, GFG+94, GGBE94].

More recent attempts to circumvent this problem have used semiconductor devices with a built in barrier. In this way, electronic excitations in the solid become accessible to experimental studies which measure *chemicurrents*. Historically, chemicurrents were detected using thin film metal-semiconductor devices also known as Schottky diodes [NBG+99, GNWM01, GN04, KNN07, UKN10a]. Among the virtues of these devices are their simplicity of fabrication and electrical characterization, their well known transport properties and their low barrier height. In spite of these virtues, their fixed barrier height limits their use for spectroscopic applications and hence fail to deliver much needed input for a thorough comparison between experiment and theory.

It therefore seems that a different approach is needed to at least gain some insight into the spectrum of chemically excited electrons and holes. Several attempts have been

made to directly access the spectrum by altering the barrier height of Schottky diodes while keeping its reactive surface unchanged [NKG07]. A different approach is to use thin oxide layers in metal-insulator-metal (MIM) or metal-insulator-semiconductor (MIS) as tunneling devices which give, if limited, access to spectroscopic data [MHD06, KGK$^+$10]. These however also require a substantial amount of model assumptions in order to extract these data.

Given the results of these efforts so far, it is the objective of this thesis to compare the exoemission and chemicurrents in a single experiment. The oxidation of alkali metals is used as a prototype system as it is known that the violent adsorption of oxygen produces strong excitations of the electron system. The resulting exoemission has long been investigated and shall now be combined with chemicurrent experiment.

1.2. Thesis Outline

In the following chapters the background of non-adiabatic energy dissipation will be presented. Chapter 2 contains an overview over the experimental concepts of chemicurrent detection and the related properties of semiconductor devices. In particular, the basic theory of Schottky contacts and their application for chemicurrent detection will be presented. Chapter 3 discusses the theoretical concepts behind the non-adiabatic excitations and their relation to the breakdown of the Born-Oppenheimer approximation. A model by Norskov, Newns and Lundquist is introduced which captures the basic picture of non-adiabatic adsorption dynamics. The harpooning and chemical hole diving mechanism by Greber and Böttcher is presented. Finally, a computational model employing the time-dependent Newns-Anderson approach for the description of electron dynamics during an adsorbate-metal surface interaction will be presented.

The following chapters 4 and 5 present the experimental techniques and the setup. Chapter 6 deals with the thermochemical description of the alkali oxides and the gas phase electronic structure of the molecular oxygen ions. In chapter 7 the experimental results obtained through photoelectron spectroscopy, and chemicurrent and exoemission experiments are presented. Chapter 8 contains model calculations using density functional theory and results for the time-dependent Newns-Anderson model applied to the oxidation of a potassium surface.

The final chapter 9 summarizes the results from the previous chapters and gives an outlook on further experimental investigations.

2. Detection of Hot Charge Carriers using Semiconductor Devices

2.1. Phenomenological Theory of Chemicurrents

As discussed above, thin-film metal-semiconductor devices may be used to capture electronic excitation caused by chemical reactions. The principle of detecting hot electronic excitations relies on the ballistic transport of hot charge carriers through a metal film. In Figure 2.1 a schematic picture of the electronic band edges in a Schottky diode with a thin metallic electrode is presented. The bending of the conduction band minimum (CBM) and the valence band maximum (VBM) relative to the Fermi level (E_{F}) are shown. The Schottky barrier $\Phi_{\mathrm{Bn,Bp}}$ acts as a barrier for the majority charge carriers in the n- or p-doped semiconductor. Only electrons/holes with sufficient energy may cross the barrier from the metal film into the semiconductor.

Chemical reactions at the very surface of the metallic film may create hot electrons/holes which may penetrate the metal ballistically and traverse the Schottky barrier if they are sufficiently energetic. To be efficient, the width of the metal film must be well below the mean-free path of the electrons/holes in the metal. Depending on the kinetic energy the later is of the order of few nanometers [SD79].

If the flux onto the sample is sufficiently low and if the chemical reactions are independent events, the chemicurrent density $j_{cc}(t)$ will be proportional to the reaction rate $R(t)$. If multiple reaction steps are involved a general expression for the chemicurrent reads

$$j_{cc}(t) = \sum_i \alpha_i(t) e_0 R_i(t), \tag{2.1}$$

where the α_i determine the chemicurrent efficiency and the sum includes every reaction step.

A three step model for the chemicurrent has been proposed by Nienhaus [Nie02] which is similar to the four step model of ballistic electron injection (BEEM) [KB88].

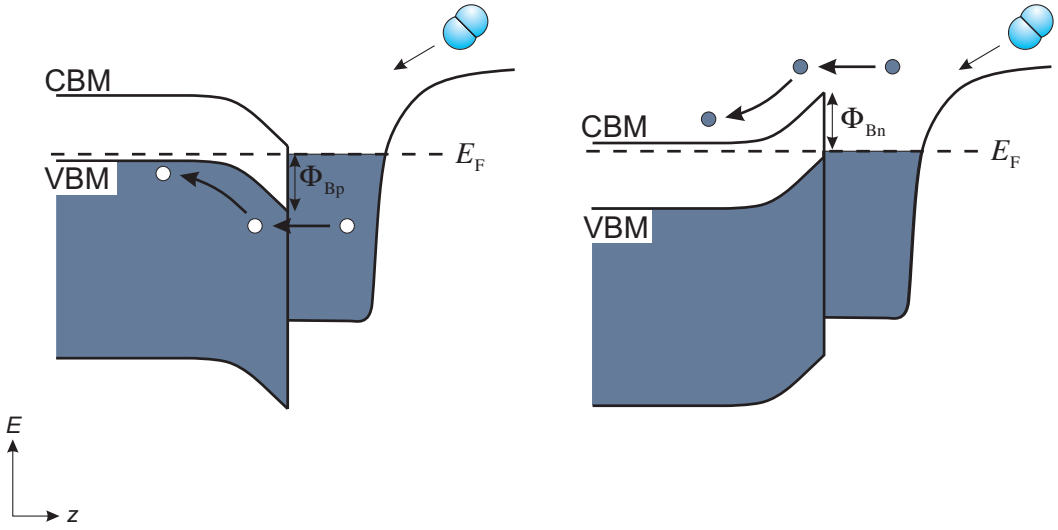

Figure 2.1.: Principle of chemicurrent detection for (Left panel) holes on p-doped semiconductor and (Right panel) electrons on n-type Schottky diodes. Majority carriers travel ballistically through the metal film and are injected into the semiconductor by crossing the Schottky barrier [Nie02].

The efficiency is determined by (i) the efficiency to generate a hot charge carrier of a given energy, (ii) the transport of this carrier through the metal film, (iii) its traversal of the Schottky barrier and (iv) electron loss and gain processes in the semiconductor. The chemicurrent efficiency may therefore be written as an integral over all k-space (or impulse space)

$$\alpha_i(t) = \int_0^\infty \int_{4\pi} d\Omega dk P_i(\mathbf{k},t) D_i(\mathbf{k},t) A_i(\mathbf{k},t) T_i(\mathbf{k},t). \tag{2.2}$$

The factor $D_i(\mathbf{k},t)$ describes the efficiency of the reaction to create a hot electron of an energy $E(\mathbf{k},t)$, the factor $A_i(\mathbf{k},t)$ determines the attenuation of the electrons in the film and $T_i(\mathbf{k},t)$ reflects the transport probability over the Schottky barrier. Additional contributions due to recombination currents and impact ionization in the semiconductor are modeled into the factor $P_i(\mathbf{k},t)$.

Experimentally the attenuation of electrons due to scattering in the film is easiest to access. According to Beer's law $A(\mathbf{k})$ depends exponentially on the thickness of the

metal d

$$A(\mathbf{k}) \approx \exp\left(-\frac{d}{\lambda_B(\mathbf{k})\cos(\theta)}\right), \tag{2.3}$$

where the attenuation length depends on the k-vector of the electron and θ is the angle between $\mathbf{k}$ and the normal of the surface.

2.2. Schottky Diodes

The properties of metal-semiconductor interfaces or Schottky diodes have been studied extensively in the past [Sze81, Mön01]. Their usefulness as detectors for hot charge carriers that are excited during chemical reactions has been shown in a number of publications [NBG+99, Nie02, GN04, Kri05]. Therefore only those facts necessary for the understanding of their use in chemicurrent detection shall be recapitulated.

2.2.1. Potential Step at the Interface

Figure 2.2 shows a simplified version of the potential energy landscape at the interface of a Schottky contact. The potential is characterized by a steep increase right at the junction between metal and semiconductor $z = 0$ and a slow tailing into the semiconductor. The electric potential ϕ is governed by Poisson's equation

$$\nabla^2\phi(\mathbf{r}) = -\frac{1}{\varepsilon(\mathbf{r})\varepsilon_0}\rho(\mathbf{r}), \tag{2.4}$$

where ρ is the charge density, ε is the relative electric permittivity and ε_0 is the permittivity of free space. For further discussion of the implications for the charge accumulated at the interface the problem shall be treated as one dimensional. The potential $\phi(z)$ can be approximated by

$$\phi(z) = \begin{cases} \frac{\phi_{\mathrm{bi}}}{W^2}(z-W)^2 & \text{, if } 0 \le z \le W, \\ 0 & \text{, everywhere else,} \end{cases} \tag{2.5}$$

which is compatible with the boundary conditions for ϕ to vanish in the bulk and to reach a constant value ϕ_{bi} at the interface. Equation 2.5 is valid under the assumption of total depletion of the space charge layer within a width W in the semiconductor, i.e., the charge is given by the dopant density $\rho = eN_D$. Formally, Eqns. (2.4) and (2.5) can

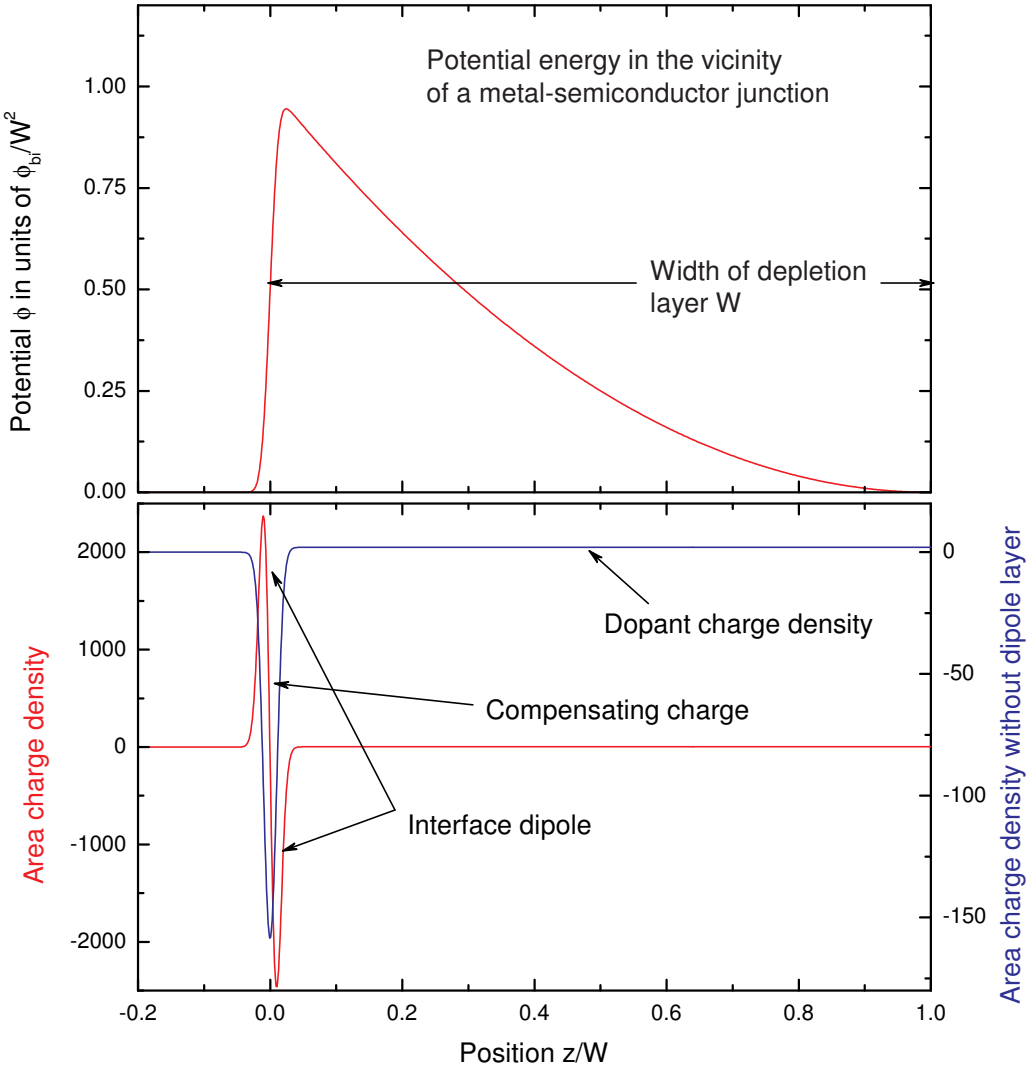

Figure 2.2.: (Upper panel) Electrical potential in the vicinity of a metal semiconductor junction (Lower panel) Corresponding charge density consisting of contributions from freely moving majority charge carriers and dopant atoms fixed in space.

be combined to give

$$\frac{\partial^2}{\partial z^2}\phi(z) = 2\Theta(z) + 4(z-W)\delta(z) + (z-W)^2\frac{\partial}{\partial z}\delta(z), \tag{2.6}$$

using Dirac's delta function $\delta(z)$. For further discussion we observe the definitions

$$\Theta(z) = \lim_{d\to 0} \frac{1}{2}\left[1 + \operatorname{erf}\left(\frac{z}{\sqrt{2}d}\right)\right], \tag{2.7}$$

$$\delta(z) = \lim_{d\to 0} \frac{1}{\sqrt{2\pi}d} \exp\left(-\frac{z^2}{2d^2}\right), \text{ and} \tag{2.8}$$

$$\frac{\partial}{\partial z}\delta(z) = \lim_{d\to 0} \frac{1}{\sqrt{2\pi}d^3} z \exp\left(-\frac{z^2}{2d^2}\right), \tag{2.9}$$

which allow us to plot the charge density as shown in the lower panel of Fig. 2.2. The spatial width d of the potential step at $z = 0$ therefore has to be chosen such that $d \ll W$. In reality d is of the order of atomic distances, while W is of the order of the Debye length, i.e., several hundred nanometers depending on the dopand density. For clarity the examples were computed using $d = 0.01$. As is apparent from the plot, the charge density can be seen as consisting of two contributions [Bar47]:

1. A dipole layer of atomic dimensions right at the interface, which can be seen to consist of a double layer at the metal surface, a double layer at the semiconductor interface and a dipole layer formed from surface charges on the metal and on the semiconductor.

2. A double layer consisting of a surface charge of atomic dimensions on the semiconductor surface and a space charge in the bulk of the semiconductor.

It is the purpose of every theory of the Schottky junction to derive a formula for the band bending and thus for the Schottky barrier. Figure 2.3 depicts a more detailed picture of the band bending at a metal-semiconductor junction. It can be studied in more detail when observing that bringing a metal surface close to a semiconductor gives rise to an electric field

$$E = \frac{W_\mathrm{m} - W_\mathrm{s}}{ea} \tag{2.10}$$

in the gap between the two, where a is the width of the gap, W_m is the metal's work function and W_s is the work function of the semiconductor. The charges in the semiconductor comprise the charge in the Schottky depletion layer σ_s and an interface charge σ_i. They both counteract the charge σ_m held on the metal such that

$$\sigma_m = -(\sigma_s + \sigma_i). \tag{2.11}$$

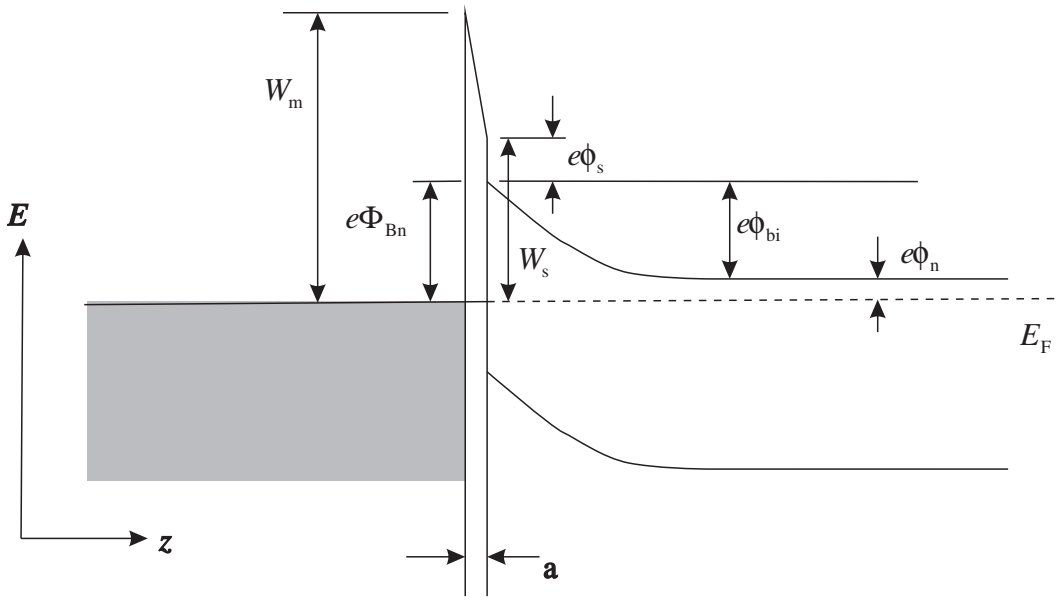

Figure 2.3.: Detailed energy-band diagram of a metal-n-semiconductor contact with an interfacial layer (vacuum) of the order of an atomic distance (after [Sze81]).

The magnitude of the surface charges is determined by the electric field

$$\varepsilon_m \varepsilon_0 \frac{W_m - W_s}{ea} = -(\sigma_s + \sigma_i) \tag{2.12}$$

where $\varepsilon_m \varepsilon_0$ is the permeability in the gap. While the work function of the metal is not changed very much by the additional charge, the work function of the semiconductor may be shifted appreciably. Likewise, the separation of the charge on the semiconductor the modified work function can be separated into two contributions from a surface potential ϕ_s and from the band bending ϕ_{bi}. It is apparent from the definitions and from Fig. 2.3 that

$$W_s = e_0(\phi_s + \phi_{bi} + \phi_n) \text{ and} \tag{2.13}$$

$$\Phi_{Bn0} = \phi_{bi} + \phi_n. \tag{2.14}$$

In the full depletion approximation the contribution of the depletion layer is given by the square root relation

$$\sigma_{\mathrm{i}} = \sqrt{2e\varepsilon_{\mathrm{s}}\varepsilon_0 N_{\mathrm{D}}\left(\Phi_{\mathrm{Bn0}} - \phi_{\mathrm{n}}\right)}. \tag{2.15}$$

Equation 2.12 can therefore be written in terms of the band bending ϕ_{bi} or alternatively in terms of the Schottky barrier Φ_{Bn0}

$$\varepsilon_{\mathrm{m}}\varepsilon_0 \frac{W_{\mathrm{m}} - e_0(\phi_{\mathrm{s}} - \Phi_{\mathrm{Bn0}})}{ea} = -\left(\sigma_{\mathrm{s}}(\Phi_{\mathrm{Bn0}}) + \sigma_{\mathrm{i}}(\Phi_{\mathrm{Bn0}})\right), \tag{2.16}$$

provided a relation for $\sigma_{\mathrm{s}}(\Phi_{\mathrm{Bn0}})$ can be found.

In the original papers by Bardeen it was assumed that surface states at the semiconductor surface were holding additional charges [Bar47]. As has been pointed out by Heine, localized surface states cannot exist at a metal semiconductor junction [Hei65]. Instead so called metal induced gap states (MIGS) were introduced in order to explain the relative insensitivity of the Schottky barrier to the metal work function [Ter84, Ter86]. On the metal side the MIGS are the usual oscillating Bloch functions of the bulk, whereas in the semiconductor the wave function $\Psi_{\mathrm{MIGS}}(z)$ falls of exponentially on a typical lengths scale q_{MIGS}.

In general the MIGS are assumed to have a density of states $D_{\mathrm{MIGS}}(E)$ and are filled up to their charge neutrality level (CNL), W_{CNL}, when no external field is applied. When assuming a constant density of states around the CNL the charge accumulated in the MIGS is simply given by

$$Q_{\mathrm{MIGS}} = eD_{\mathrm{MIGS}}(W_{\mathrm{CNL}})(W_{\mathrm{CNL}} - E_{\mathrm{F}}). \tag{2.17}$$

The penetration depth of the probability density $\left|\Psi_{\mathrm{MIGS,CNL}}(z)\right|^2$ at the charge neutrality level can then be used as a measure of the dipole length $a = \frac{1}{2}q_{\mathrm{MIGS,CNL}}$. Observing that the charge in the depletion layer is small compared to the one in the MIGS finally leads to the formula

$$\varepsilon_{\mathrm{m}}\varepsilon_0\left(W_{\mathrm{m}} - e_0(\phi_{\mathrm{s}} - \phi_{\mathrm{Bn0}})\right) = \frac{1}{2q_{\mathrm{MIGS,CNL}}} eD_{\mathrm{MIGS}}(W_{\mathrm{CNL}})(\phi_{\mathrm{Bn0}} - \phi_{\mathrm{CNL}}), \tag{2.18}$$

which is usually expressed in terms of the electronegativity $W_{\mathrm{x}} = A_{\mathrm{x}}X_{\mathrm{x}}$:

$$\varepsilon_{\mathrm{m}}\varepsilon_0\left(A_{\mathrm{x}}(X_{\mathrm{m}} - X_{\mathrm{s}}) - \phi_{\mathrm{Bn0}}\right) = \frac{1}{2q_{\mathrm{MIGS,CNL}}} eD_{\mathrm{MIGS,CNL}}(\phi_{\mathrm{Bn0}} - \phi_{\mathrm{CNL}}), \tag{2.19}$$

which is the formula derived by Mönch in the MIGS-and-electronegativity model [Mön96, Mön01].

2.2.2. Current-Voltage Characteristics

Various methods of determining the Schottky barrier are available. Capacitance-voltage measurements, internal photoemission and the determination of the Schottky barrier of very thin metal electrodes using photoemission (XPS) are regularly used. Current-voltage characteristics (I/V-curves) open an easy access to the barrier between metal and semiconductor. Thermionic emission of majority charge carriers is by far the dominating process in the temperature and doping range used for this study and therefore the current-voltage relation

$$I(V,T) = I_0(T)\left(\exp\left(\frac{e_0 V}{k_\mathrm{B} T}\right) - 1\right) \tag{2.20}$$

$$\text{with} \quad I_0(T) = AA^{**}T^2 \exp\left(-\frac{\Phi_\mathrm{B}}{k_\mathrm{B} T}\right) \tag{2.21}$$

holds [Sze81]. Equation (2.20) reflects the case of an ideal Schottky diode giving a relation between the current I through the diode and the applied voltage V, where A is the area of the diode, A^{**} is an effective Richardson constant and T is the temperature. Taking it as a fitting parameter the barrier height Φ_B can be determined from experimental I/V-curves. Equation (2.20) often poorly compares to experimental results and is thus often used in a modified form

$$I(V,T) = I_0(T)\left(\exp\left(\frac{e_0 V - RI(V,T)}{n(T) k_\mathrm{B} T}\right) - 1\right) \tag{2.22}$$

$$\text{with} \quad I_0(T) = AA^{**}T^2 \exp\left(-\frac{\Phi_{\mathrm{B,eff}}(T)}{k_\mathrm{B} T}\right), \tag{2.23}$$

introducing the effective barrier $\Phi_{\mathrm{B,eff}}$ and the ideality factor n. Due to the series and spread resistance of the film, I is given only implicitly and Eqn. (2.22) has to be solved numerically. In general both parameters are temperature dependent. A lowering of the effective barrier and ideality factors $n \gg 1$ are regularly observed when decreasing the diode temperature. Image-force lowering, recombination-generation currents, tunneling, and weak pinning by interface states have been proposed as an explanation for the temperature behavior [Sze81]. Tung gives an alternative explanation in terms of interface inhomogeneities leading to so called low barrier patches [Tun91]. Schmitsdorf *et al.*

have applied Tung's theory in order to explain the linear correlation between barrier heights and the respective ideality factor when the effective barrier height is plotted as a function of the ideality factor for a number of different diodes [Sch97, SKM97]. With their extrapolation scheme it is possible to determine the barrier height of an ideal diode, i.e., the barrier height of the homogeneous interface, from I/V-curves of non-ideal diodes. The same procedure has been successfully used to determine the homogeneous barrier height from I/V-curves recorded from one diode at different temperatures, although the scheme lacks a thorough theoretical background [Sch97, SKM97].

2.2.3. Capacitance of the Depletion Layer

A second method of determining the Schotty barrier is based on the measurement of the voltage dependent capacitance $C(V) = \left|\frac{\partial Q}{\partial V}\right|_V$. The voltage dependence is due to the varying of the width of the depletion layer W as a function of the stored charge

$$Q(V) = A\sqrt{2e_0\varepsilon_0\varepsilon_\mathrm{r}N_D(V_\mathrm{bi} - V)}. \tag{2.24}$$

The respective capacitance

$$C(V) = A\sqrt{\frac{e_0\varepsilon_0\varepsilon_\mathrm{r}N_D}{2(V_\mathrm{bi} - V)}} \tag{2.25}$$

of the ideal Schottky diode is therefore a function of the dopand density N_D and the applied voltage V [Sze81]. Equation 2.25 is usually written in a form more suitable for analysis

$$\frac{1}{C(V)^2} = \frac{2(V_\mathrm{bi} - V)}{A^2 e_0\varepsilon_0\varepsilon_\mathrm{r}N_D}, \tag{2.26}$$

which is a straight line. By extrapolating Eqn. (2.26) it can be seen that the intercept of the resulting straight line is at the Schottky barrier. The slope on the other hand gives access to the dopant concentration in the semiconductor.

2.3. Current Measurements

2.3.1. Photocurrent

Schottky diodes are known to be excellent photodetectors in the infrared [MS85]. Since chemicurrent measurements are performed in the dark only infrared light emitted from

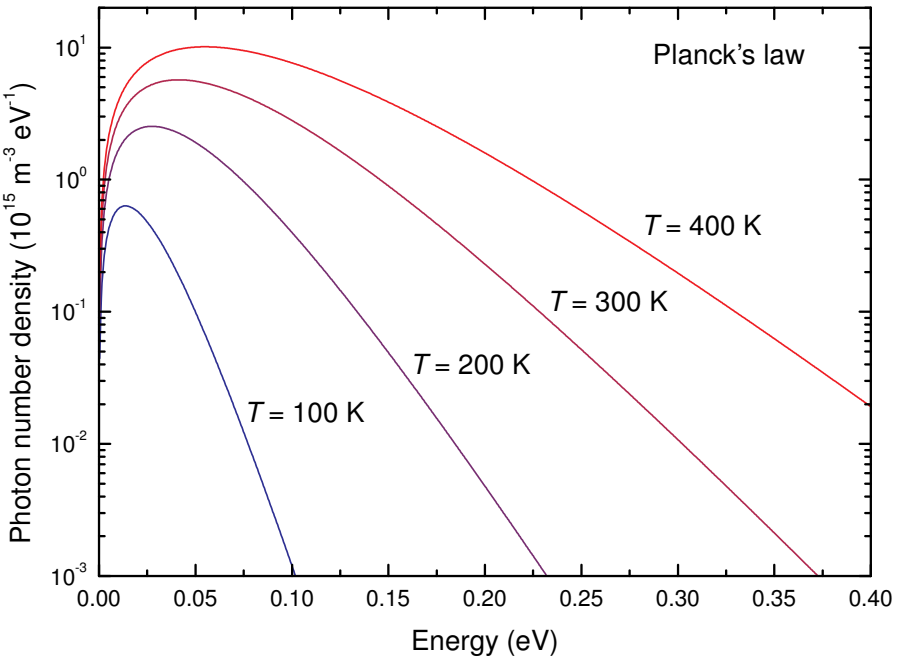

Figure 2.4.: Spectral photon number density as a function of photon energy. For black body radiation at $T = 300\,\mathrm{K}$ the intensity is still significant in the detection range of Schottky diodes, e.g., $\Phi_{\mathrm{Bp}} \approx 0.3\,\mathrm{eV}$ for Pt and Pd diodes on silicon.

the surrounding environment poses a problem if low barrier Schottky diodes are used, e.g., palladium based diodes. For a surrounding environment at $T = 300\,\mathrm{K}$ the high energy tail of the Planck distribution

$$u(E)dE = \frac{8\pi E^2}{h^3c^3}\frac{1}{\exp\left(\frac{E}{kT}\right) - 1}dE \tag{2.27}$$

is appreciable in the energy range around $E = 0.3\,\mathrm{eV}$. As is also apparent from Fig. 2.4, excitations across the bulk band gap can be neglected for thermal radiation from a room temperature source in the case of silicon Schottky diodes, $E_{\mathrm{gap,Si}} \approx 1.12\,\mathrm{eV}$.

2.3.2. Change of Device Parameters

It is a regular concern that changes in the device parameters, i.e., the Schottky barrier, may lead to an apparent current through the device. Such currents may occur if the

capacitance of the device is altered. Changes in the capacitance are accompanied by a displacement current

$$
\begin{aligned}
I_{\mathrm{D}}(t) &= \frac{dQ}{dt} && (2.28)\\
&= \left.\frac{\partial Q}{\partial V_{\mathrm{bi}}}\right|_{V} \frac{dV_{\mathrm{bi}}}{dt} + \left.\frac{\partial Q}{\partial V}\right|_{V_{\mathrm{bi}}} \frac{dV}{dt} && (2.29)\\
&= \frac{1}{2}Q \cdot \frac{1}{V_{\mathrm{bi}} - V}\frac{dV_{\mathrm{bi}}}{dt} - \frac{1}{2}Q \cdot \frac{1}{V_{\mathrm{bi}} - V}\frac{dV}{dt} && (2.30)\\
&= C(V_{\mathrm{bi}}, V)\left(\frac{dV_{\mathrm{bi}}}{dt} - \frac{dV}{dt}\right),
\end{aligned}
$$

which is indiscernible from a chemicurrent. As the interface is virtually impenetrable to majority charge carriers they have to flow through the shortcut imposed by a current amplifier connected to the diode. A term taking into account the changing area $\frac{\partial A}{\partial t}$ when loosing contact to parts of the film is not included in (2.31) because it does not lead to a current.

Typical dopant concentrations of the silicon substrates used in this study are $N_{\mathrm{D}} \approx 10^{16}\,\mathrm{cm}^{-3}$. According to (2.25) the Schottky diodes show capacitances on the order of a few nanofarads:

$$
\begin{aligned}
C(0\,\mathrm{V}) &= 1\,\mathrm{cm}^{-2}\sqrt{\frac{12 \cdot 10^{16}\,\mathrm{cm}^{-3} e_0 \varepsilon_0}{2 \cdot 0.5\,\mathrm{V}}} && (2.31)\\
&= 41\,\mathrm{nF},
\end{aligned}
$$

while using the static dielectric constant of silicon $\varepsilon_{\mathrm{r,Si}} \approx 12$, a barrier height $\Phi_{\mathrm{Bp}} \approx 0.5\,\mathrm{V}$ and a typical diode area $A = 1\,\mathrm{cm}^2$. Device changes as the source of chemicurrents can therefore be safely excluded in most cases when Schottky diodes are used.

3. Theoretical Concepts

3.1. Born-Oppenheimer-Approximation

In principle, a system consisting of an adsorbate and a metal surface may be described by the (non-relativistic) Hamiltonian

$$H(\mathrm{r},\mathrm{R}) = -\frac{\hbar^2}{2}\sum_{\alpha} M_{\alpha}^{-1}\nabla^2_{\mathbf{R}_\alpha} - \frac{\hbar^2}{2}\sum_{i} m_e^{-1}\nabla^2_{\mathbf{r}_i} + V(\mathbf{r},\mathbf{R}), \tag{3.1}$$

which describes the motion of the atomic nuclei at their positions $\mathbf{R}_\alpha$ and of the electrons with positions $\mathbf{r}_i$. The motion of nuclei and electrons is coupled by an interaction potential $V(\mathbf{r},\mathbf{R})$. In principle, all aspects of the system may be derived from the solutions $\Psi_j(\mathbf{r},\mathbf{R},t)$ of the time-dependent Schrödinger equation

$$H(\mathrm{r},\mathrm{R})\Psi_j(\mathbf{r},\mathbf{R},t) = i\hbar\frac{\partial}{\partial t}\Psi_j(\mathbf{r},\mathbf{R},t). \tag{3.2}$$

Although possible in theory, finding these solutions is a major theoretical and computational challenge due to the large number of particles involved in the problem.

The Born-Oppenheimer approximation (BOA) paves the way to greatly simplify this problem by decoupling the electronic from the nuclear degrees of freedom. Although the BOA was developed in order to describe the dynamics of molecules it has been shown to be applicable in adsorbate-surfaces problems [BO27, DH95, WTA04]. In a first step the full Hamiltonian (3.1) is rewritten as

$$H = -\frac{\hbar^2}{2}\sum_{\alpha} M_{\alpha}^{-1}\nabla^2_{\mathbf{R}_\alpha} + H_{el}(\mathbf{r};\mathbf{R}), \tag{3.3}$$

where the second term $H_{el}(\mathbf{r};\mathbf{R})$ contains the position of the nuclei only as parameters and can therefore be interpreted as a Hamiltonian of the electrons for fixed $\mathbf{R}$. The normalized eigenfunctions $\Phi_j(\mathbf{r};\mathbf{R})$ of the electronic Hamiltonian form a complete and

orthonormal basis set which are solutions to the timeindependent Schrödinger equation

$$H_{el}(\mathbf{r};\mathbf{R})\Phi_j(\mathbf{r};\mathbf{R}) = E_j(\mathbf{R})\Phi_j(\mathbf{r};\mathbf{R}). \tag{3.4}$$

The exact wave function

$$\Psi(\mathbf{r},\mathbf{R},t) = \sum_i \Phi_i(\mathbf{r};\mathbf{R})\Omega_i(\mathbf{R},t) \tag{3.5}$$

may be expressed as a linear combination of the $\Phi_j(\mathbf{r};\mathbf{R})$. Inserting equation (3.5) into the time dependent Schrödinger equation (3.2) using the Hamiltonian (3.1), multiplying with $\Phi_j^*(\mathbf{r};\mathbf{R})$ from the left and integrating over all $\mathbf{r}$ yields a set of coupled differential equations for every solution $E_j(\mathbf{R})$ of (3.4).

$$\begin{aligned}
i\hbar\frac{\partial}{\partial t}\Omega_j(\mathbf{R},t) &= i\hbar\frac{\partial}{\partial t}\int \Phi_j^*(\mathbf{r};\mathbf{R})\left(\sum_i \Phi_i(\mathbf{r};\mathbf{R})\Omega_i(\mathbf{R},t)\right)d\mathbf{r} \\
&= \int \Phi_j^*(\mathbf{r};\mathbf{R})\left(-\frac{\hbar^2}{2}\sum_\alpha M_\alpha^{-1}\nabla^2_{\mathbf{R}_\alpha} + H_{el}(\mathbf{r};\mathbf{R})\right)\left(\sum_i \Phi_i(\mathbf{r};\mathbf{R})\Omega_i(\mathbf{R},t)\right)d\mathbf{r} \\
&= -\hbar^2\sum_i\sum_\alpha M_\alpha^{-1}\left(\int \Phi_j^*(\mathbf{r};\mathbf{R})\left(\nabla_{\mathbf{R}_\alpha}\Phi_i(\mathbf{r};\mathbf{R})\right)d\mathbf{r}\right)\nabla_{\mathbf{R}_\alpha}\Omega_i(\mathbf{R},t) \\
&- \frac{\hbar^2}{2}\sum_i\sum_\alpha M_\alpha^{-1}\left(\int \Phi_j^*(\mathbf{r};\mathbf{R})\left(\nabla^2_{\mathbf{R}_\alpha}\Phi_i(\mathbf{r};\mathbf{R})\right)d\mathbf{r}\right)\Omega_i(\mathbf{R},t) \\
&- \frac{\hbar^2}{2}\sum_\alpha M_\alpha^{-1}\nabla^2_{\mathbf{R}_\alpha}\Omega_j(\mathbf{R},t) \\
&+ E_j(\mathbf{R})\Omega_j(\mathbf{R},t)
\end{aligned} \tag{3.6}$$

In the BOA transitions from one electronic state Φ_j to a different state Φ_i are neglected. Mathematically this means that the coupling vectors

$$\mathbf{d}_{ij}(\mathbf{R}) = -\sum_\alpha M_\alpha^{-1}\int \Phi_j^*(\mathbf{r};\mathbf{R})\nabla_{\mathbf{R}_\alpha}\Phi_i(\mathbf{r};\mathbf{R})d\mathbf{r} \tag{3.7}$$

$$D_{ij}(\mathbf{R}) = -\sum_\alpha M_\alpha^{-1}\int \Phi_j^*(\mathbf{r};\mathbf{R})\nabla^2_{\mathbf{R}_\alpha}\Phi_i(\mathbf{r};\mathbf{R})d\mathbf{r} \tag{3.8}$$

in (3.6) are assumed to be small and are set to zero.

$$\mathbf{d}_{ij}(\mathbf{R}) = 0 \tag{3.9}$$

$$D_{ij}(\mathbf{R}) = 0 \tag{3.10}$$

In this way a Schrödinger equation

$$\left[-\frac{\hbar^2}{2}\sum_{\alpha} M_{\alpha}^{-1}\nabla^2_{\mathbf{R}_\alpha} + E_j(\mathbf{R})\right]\Omega_j(\mathbf{R},t) = i\hbar\frac{\partial}{\partial t}\Omega_j(\mathbf{R},t) \tag{3.11}$$

describing the motion of the nuclei in a potential given by the instantaneous eigenvalues of the electronic Hamilton operator is obtained. It follows from Eqn. (3.11) that the $E_j(\mathbf{R})$ can be interpreted as potential energy surfaces for the motion of the nuclei, which are determined by the electronic wave function $\Phi_j(\mathbf{r};\mathbf{R})$.

Even so the solution of (3.11) still requires a tremendous computational effort because Eqn. (3.4) must be solved for every possible combination of positions of the nuclei $\mathbf{R}$. In practice, the dynamics of the nuclei are therefore often described classically

$$\sum_{\alpha} M_\alpha \ddot{\mathbf{R}}_\alpha(t) = -\sum_{\alpha}\nabla_{\mathrm{R}_\alpha} E_j(\mathbf{R}(t)). \tag{3.12}$$

This extremely reduces the computational cost because Eqn. (3.4) must only be solved for the $\mathbf{R}(t)$ on the trajectory.

3.2. Diabatic Representation

In the previous section the eigenstates of the Hamiltonian H_{el} were used to obtain a set of equations for the coupled motion of electrons and nuclei. In this way we arrived at the so called *adiabatic*, meaning non-crossing, description. As the electronic Hamilton operator becomes diagonal when expressed in terms of its eigenstates it becomes evident from (3.6) that transitions between potential energy surfaces are only caused by the coupling terms $\mathbf{d}_{ij}$ and D_{ij}. These terms are expressed in terms of the operator ∇_{R} which introduces the velocity of the nuclei into the equations. In the adiabatic representation, the cause of electronic excitations is thus the movement of the cores.

It is by no means necessary to use the eigenstates of H_{el} for the expansion (3.5), i.e., to use the adiabatic representation. Choosing a different basis leads to a different representation of (3.1) which might be closer to the actual physical problem. A so called

diabatic basis must therefore be carefully adjusted to the physical problem whereas the adiabatic basis is mathematically well defined by (3.4).

Had a different, normalized, but not necessarily orthogonal, and complete basis $\{\Phi'_\nu(\mathbf{r};\mathbf{R})\}$ of basis functions been used in Eqn. (3.6) a different set of equations

$$\begin{aligned}
i\hbar\frac{\partial}{\partial t}\Omega'_j(\mathbf{R},t) &= -\hbar^2\sum_i\sum_\alpha M_\alpha^{-1}\left(\int \Phi'^*_j(\mathbf{r};\mathbf{R})\left(\nabla_{\mathbf{R}_\alpha}\Phi'_i(\mathbf{r};\mathbf{R})\right)d\mathbf{r}\right)\nabla_{\mathbf{R}_\alpha}\Omega'_i(\mathbf{R},t)\\
&\quad-\frac{\hbar^2}{2}\sum_i\sum_\alpha M_\alpha^{-1}\left(\int \Phi'^*_j(\mathbf{r};\mathbf{R})\left(\nabla^2_{\mathbf{R}_\alpha}\Phi'_i(\mathbf{r};\mathbf{R})\right)d\mathbf{r}\right)\Omega'_i(\mathbf{R},t)\\
&\quad-\frac{\hbar^2}{2}\sum_i\sum_\alpha M_\alpha^{-1}\left(\int \Phi'^*_j\Phi'_i d\mathbf{r}\right)\nabla^2_{\mathbf{R}_\alpha}\Omega'_i(\mathbf{R},t)\\
&\quad-i\hbar\sum_{i\neq j}\left(\int \Phi'^*_j\Phi'_i d\mathbf{r}\right)\frac{\partial}{\partial t}\Omega'_i(\mathbf{R},t)\\
&\quad+\sum_i\left(\int \Phi'^*_j H_{\mathrm{el}}\Phi'_i d\mathbf{r}\right)\Omega'_i(\mathbf{R},t)\\
&= \hbar^2\sum_i \mathrm{d}'_{ij}(\mathbf{R})\nabla_{\mathbf{R}_\alpha}\Omega'_i(\mathbf{R},t)+\frac{\hbar^2}{2}\sum_i D'_{ii}(\mathbf{R})\Omega'_i(\mathbf{R},t)\\
&\quad-\sum_{i\neq j}S_{ji}(\mathbf{R})\left(\frac{\hbar^2}{2}\sum_\alpha M_\alpha^{-1}\nabla^2_{\mathbf{R}_\alpha}\Omega'_i(\mathbf{R},t)+i\hbar\frac{\partial}{\partial t}\Omega'_i(\mathbf{R},t)\right)\\
&\quad+\sum_{i\neq j}V_{ji}(\mathbf{R})\Omega'_i(\mathbf{R},t)\\
&\quad-\frac{\hbar^2}{2}\sum_\alpha M_\alpha^{-1}\nabla^2_{\mathbf{R}_\alpha}\Omega'_j(\mathbf{R},t)+E'_j(\mathbf{R})\Omega'_j(\mathbf{R},t)
\end{aligned}\tag{3.13}$$

for the time evolution and the coupling would have been found. Comparing (3.13) with its analog in the adiabatic description (3.6) it can be seen that two additional terms appear that lead to a coupling between states Ω'. The first term

$$-\sum_{i\neq j}\left[S_{ji}(\mathbf{R})\left(\frac{\hbar^2}{2}\sum_\alpha M_\alpha^{-1}\nabla^2_{\mathbf{R}_\alpha}\Omega'_i(\mathbf{R},t)+i\hbar\frac{\partial}{\partial t}\Omega'_i(\mathbf{R},t)\right)\right]\tag{3.14}$$

includes the direct overlap S_{ij} between the electronic wave functions and vanishes if the basis set is chosen to be orthogonal. The second term

$$\sum_{i\neq j}V_{ji}(\mathbf{R})\Omega'_i(\mathbf{R},t)\tag{3.15}$$

couples the wavefunctions of the nuclei by virtue of the interaction potential V_{ij} between electronic states.

Strictly speaking the Born-Oppenheimer approximation (3.9) may still hold in the diabatic basis while it becomes invalid in the adiabatic description. A short example will make the difference between the two representations clearer.

3.3. Two-state example

A simple two-state example introduced by Tully et al. demonstrates the difference between the diabatic and the adiabatic representation [Tul90]. For clarity, the diabatic states in this example can be seen as the neutral and ionic state of an adsorbing molecule. The example electron Hamiltonian matrix in the *diabatic* basis $\phi_i = \{\phi_1(x;X), \phi_2(x;X)\}$

$$H_{\text{el}} = \begin{pmatrix} V_{11} & V_{12} \\ V_{21} & V_{22} \end{pmatrix} \tag{3.16}$$

is defined trough its matrix elements

$$V_{11}(X) = \begin{cases} A\left(1 - \exp(-Bx)\right) & \text{if } X > 0 \\ -A\left(1 - \exp(Bx)\right) & \text{else} \end{cases} \tag{3.17}$$

$$V_{12}(X) = C \exp\left(-DX^2\right) \tag{3.18}$$

$$V_{21}(X) = V_{12}(X) \tag{3.19}$$

$$V_{22}(X) = V_{11}(X) \tag{3.20}$$

$$\tag{3.21}$$

which depend solely on the nucleus coordinate X. The corresponding wave functions $\phi_i(x;X)$ are not given explicitly but are assumed to be normalized and orthogonal. Additionally, they vary slowly as a function of the nucleus coordinate X, or in other words

$$\frac{d\phi_i}{dX} \approx 0. \tag{3.22}$$

To find the eigenvectors of H_{el} the secular equation

$$\|H_{\text{el}} - E\mathbb{1}\| = 0 \tag{3.23}$$

must be solved which has the solutions

$$E_\nu = \frac{1}{2}(V_{11} + V_{22}) \pm \sqrt{V_{21}^2 - V_{11}V_{22}}. \tag{3.24}$$

The corresponding eigenvectors ϕ_ν,

$$\phi_\alpha(x;X) = \frac{1}{\sqrt{2}}(\phi_1(x;X) + \phi_2(x;X)) \text{ and} \tag{3.25}$$

$$\phi_\beta(x;X) = \frac{1}{\sqrt{2}}(\phi_1(x;X) - \phi_2(x;X)), \tag{3.26}$$

form the basis used in the adiabatic representation. In general they are linear combinations

$$\phi_\nu(x;X) = \sum_i c_{i\nu}(X)\phi_i(x;X) \tag{3.27}$$

of the original wavefunctions ϕ_i. In order to calculate the Born-Oppenheimer coupling constants $d_{\nu\mu}$ the first derivatives

$$\frac{d\phi_\nu(x;X)}{dX} = \frac{d}{dX}\sum_i c_{i\nu}(X)\phi_i(x;X) \tag{3.28}$$

$$= \sum_i \frac{dc_{i\nu}(X)}{dX}\phi_i(x;X) + \sum_i c_{i\nu}(X)\frac{d\phi_i(x;X)}{dX} \tag{3.29}$$

have to be calculated. From (3.22) it can be seen that the second term in (3.29) must vanish. Thus the sole contribution to the $d_{\nu\mu}$ comes in through the change of the coefficients $c_{i\nu}$

$$d_{\nu\mu}(X) = M^{-1}\int \phi_\mu(x;X)\frac{d}{dX}\phi_\nu(x;X)dx \tag{3.30}$$

$$= M^{-1}\int \sum_i c_{i\mu}(X)\phi_i(x;X)\sum_j \frac{dc_{j\nu}(X)}{dX}\phi_j(x;X)dx \tag{3.31}$$

$$= M^{-1}\sum_i c_{i\mu}(X)\frac{dc_{i\nu}(X)}{dX}, \tag{3.32}$$

where the orthogonality of the original basis functions was used in the last step. A numerical calculation was carried out using a set of constants

$$\begin{aligned} A &= 0.01 & B &= 1.6 \\ C &= 0.005 & D &= 1.0. \end{aligned} \tag{3.33}$$

Figure 3.1 shows results from a numerical calculation using these constants. The lower panel shows the energy expectation values for the two diabatic states ϕ_i (dashed lines) and the energy eigenvalues for the adiabatic solutions ϕ_ν (solid lines). The adiabatic states are characterized by the fact that states originating from coupled states (like in this example) do not cross, hence *adiabatic*, in the sense that the energy eigenvalues do not cross as a function of the position of the nuclei. The upper panel shows the interaction potential V_{12} between the diabatic states and the middle panel shows the Born-Oppenheimer coupling parameter $d_{\alpha\beta}$. As expected, the adiabatic coupling strength is strong if the interaction potential is strong and if the adiabatic states show an avoided crossing.

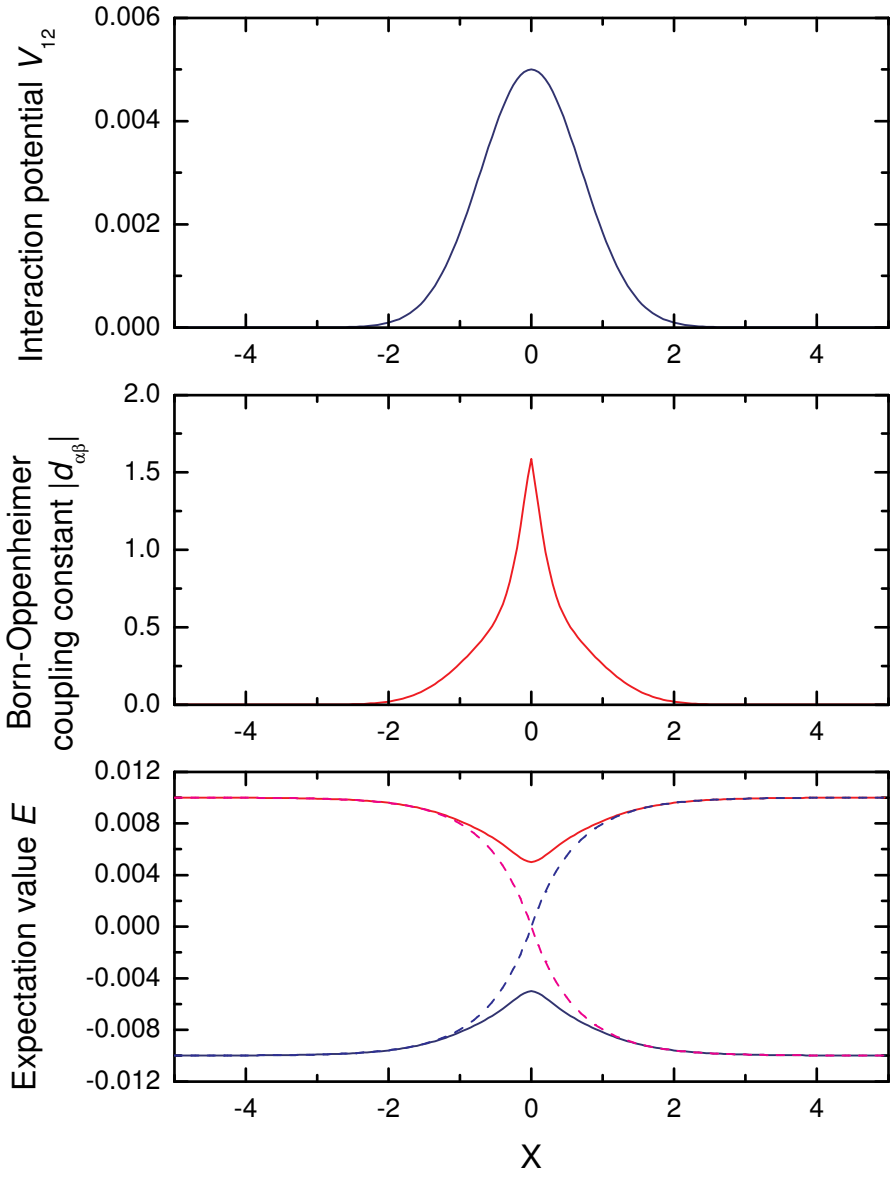

Figure 3.1.: Example calculations for a sample two-state problem in a diabatic representation. Upper panel: Coupling strength between diabatic electronic states V_{12}. Middle panel: Born-Oppenheimer coupling parameter $d_{\alpha\beta}$ between the adiabatic states. Lower panel: Energy expectation values for the diabatic states ϕ_i (dashed lines) and energy eigenvalues for adiabatic states ϕ_ν (solid lines).

3.4. Surface Molecular Orbitals: The Norskov-Newns-Lundquist Model

The reactions between electropositive metal surfaces and electronegative molecules from the gas phase have been widely studied in the context of the accompanying charge transfer and its implications for non-adiabatic behavior. Detailed experimental studies have been presented for the adsorption of halogen molecules as well as oxygen on alkali metals. In particular, interest into these reactions was sparked because they proceed strongly non-adiabatically showing exoemission of electrons as well as surface chemiluminescence.

Norskov, Newns and Lundquist (NNL) introduced a semi classical theory capturing the essentials of these charge transfer reactions in an effort to describe surface chemiluminescence spectra [NNL79]. The underlying idea is to describe the surface reaction in a similar way as one would describe gas phase reactions using molecular orbital (MO) correlation diagrams as shown in Fig. 3.2.

In panel 3.2 (a), the anti-bonding $\sigma^*_{X_2}$-orbital of a halogen X_2 molecule is depicted while crossing the one electron states of a metal's valence band as the molecule approaches the surfaces and forms a bond. The MO of the free molecule is diabatically, through its molecular symmetry, connected to the p_X surface bond between the metal and the halogen atom X. In the ground state, all single electron levels are occupied up to the Fermi level, as indicated by filled circles. Empty circles represent unoccupied states. Of course the picture simplifies the situation as the adsorbate state would really be broadened into a resonance, but the overall idea remains unaltered. From the one electron molecular orbitals total states, e.g, Slater determinants, can be constructed which, again, can be plotted in a correlation diagram (Fig. 3.2 (b)).

Far from the surface, the ground state is reached if the $\sigma^*_{X_2}$ MO remains unoccupied. By taking one or two electrons from the Fermi level and placing it on the molecule, indicated by $\varepsilon_F \rightarrow \sigma^*_{X_2}$, two excited states can be constructed. Clearly, the doubly occupied state connects diabatically to the ground state of the product state, while the other two connect to excited total states. By configuration interaction, the adiabatic states will avoid the crossing of the diabatic states, thereby connecting both sides on the ground state potential energy surface. If the reaction proceeds non-adiabatically, there will be a finite probability that the system does not proceed on the ground state potential but ends up in one of the excited states.

If the molecular orbital is pressed below the Fermi level, while the molecule approaches the surface on its trajectory, electrons from the surface may resonantly tunnel through

the potential barrier between the surface and the molecule. With the knowledge about the interaction matrix elements, NNL calculate the probability that the molecule remains neutral up to a time t on its trajectory

$$P_{\mathrm{h}}(t) = \prod_{t'<t} [1 - w(t')dt'] = \exp\left[- \int_{-\infty}^{t} w(t')dt' \right], \tag{3.34}$$

where $w(t)$ denotes the resonant lifetime of the molecular state. In an Anderson treatment of the surface reaction this would be the resonance lifetime

$$w(t) = \frac{2}{\hbar}\pi \sum_{k} |\langle k \,|\, V \,|\, a \rangle|^2 \, \delta(\varepsilon_a(t) - \varepsilon_k) \tag{3.35}$$

due to tunneling between the metal states ε_k and the adsorbate state ε_a.

Kasemo *et al.* extended the NNL model, that was originally indented for the explanation of photo emission, to the description of other non-adiabatic deexcitation pathways. In order for the chemisorption to occur, the anti-bonding MOs of the impinging molecule must be filled. Photons may be emitted if the intermediate hole state is filled by radiative decay (Fig. 3.3 (c)). By far most hole states, however, will be filled resonantly in a process refered to as "hot hole injection" leading to a cascade of electron-hole pair excitations (Fig. 3.3 (a)). Further relaxation of the hot holes occurs predominantly by electron-electron scattering in the conduction band. If the molecular hole state is injected deep below the Fermi level, sometimes referred to as *chemical hole diving* [Gre94, GFG$^+$94], sufficient energy may be transferred into a single electron like excitation, which may act as a source for exoelectron emission. The hole state may also be filled by direct Auger deexcitation (Fig. 3.3 (b)), which is a second source for exoelectron emission, provided the excitation energy of the initial hole becomes larger than the work function.

3.5. Harpooning and Chemical Hole Diving: Greber-Böttcher Model of Oxygen Chemisorption

Greber and Böttcher provide a model similar to the one proposed by NNL that describes the observed non-adiabatic effects in the oxidation of alkali metal surfaces [Gre94, GFG$^+$94]. In these reactions, regardless of whether the oxygen molecule is dissociatively adsorbed or not, the π^* MO of the oxygen molecule needs to be filled by two subsequent charge transfers from the surface. Figure 3.4 (a) depicts the first charge transfer which

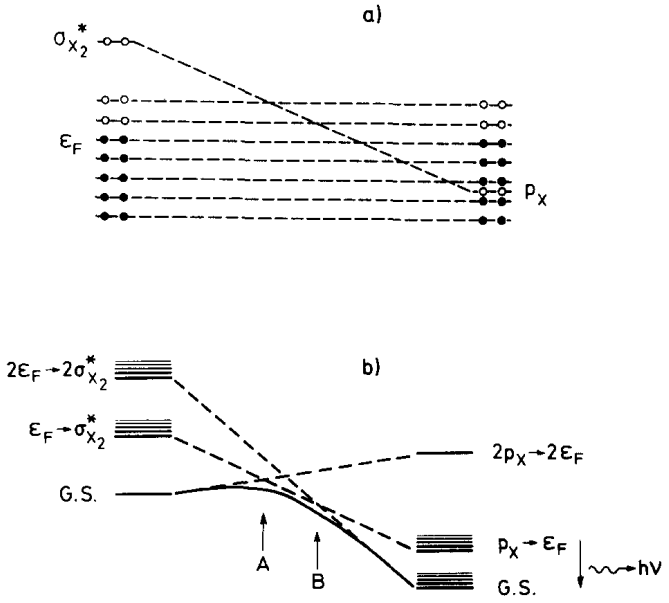

Figure 3.2.: Schematic one-electron orbital (a) and total energy (b) correlation diagrams for X_2 chemisorption on a metal with the Fermi energy ε_F (adapted from [NNL79]).

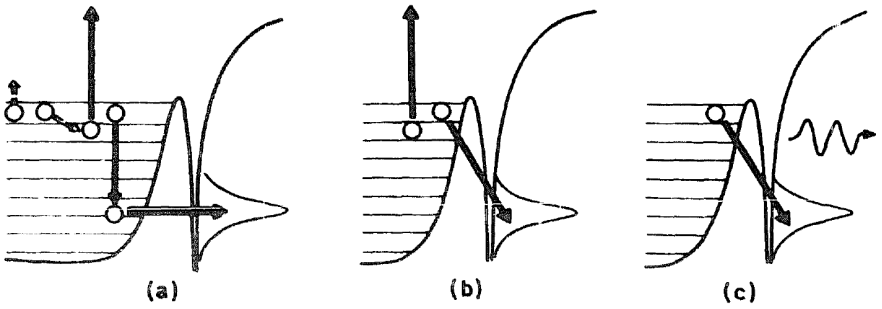

Figure 3.3.: Deexcitation processes for an intermediate hole state injected below the Fermi level resulting in (a and b) electron ejection and (c) photon emission (adapted from [KTNL79]).

is thought to occur quite far from the surface in a processes called *harpooning*[1]. Because of the slow velocity of the molecule there is enough time for the electron to tunnel resonantly into the affinity level of the O_2 molecule in spite of the large distance between the surface and the molecule. After the first charge transfer, the molecule accelerates on the potential energy surface of the singly charged ion which is dominated by the image force felt by the electron on the molecule. The second charge transfer $O_2^- \rightarrow O_2^{2-}$ occurs much closer to the surface but still remains adiabatic (Fig. 3.4 (b)).

In the following step the unstable O_2^{2-} is thought to dissociate into two O^- ions (Fig. 3.4 (c)), which, in rare cases, transfers sufficient kinetic energy onto one of the ions to eject them into the vacuum. Indeed, these ions have been observed experimentally, however, the probability of such an event is extremely small. It is the last step, depicted in Fig. 3.4 (d), that supposedly initiates the non-adiabatic processes leading to exoelectron emission. Just as the molecule did before, the O^- fragments of the oxygen accelerate further toward the surface. As a result the O 2p orbital is rapidly pushed below the Fermi level. This introduces a highly excited hole state which may relax through the mechanisms discussed earlier. In the case of exoelectron emission this would be an Auger transition involving two electrons from the metallic band and the molecular hole state. In a simple picture only those electrons may be detected which have sufficient energy to surmount the surface barrier.

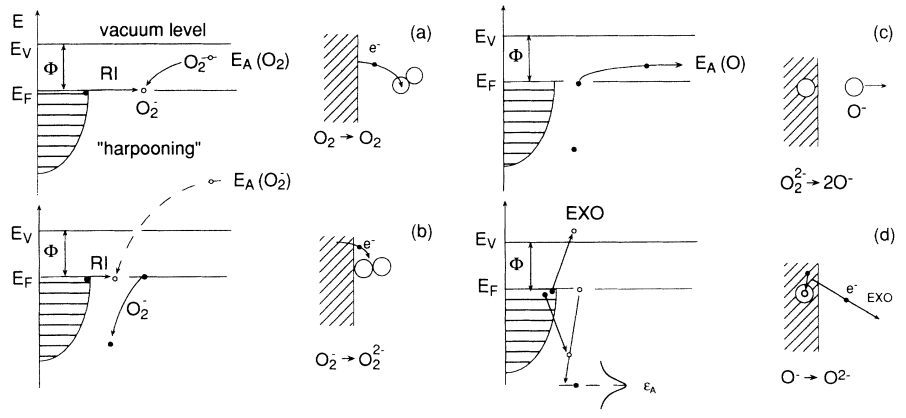

Figure 3.4.: Model for the oxidation of an alkali metal surface, i.e., lithium, including the dissociation of the oxygen molecule (adapted from [GFG+94]).

[1] *Harpooning* vividly refers to the picture of Captain Ahab hauling in the whale after shooting him with his harpoon.

3.6. Newns-Anderson-Model

The Newns-Anderson-Model has been used extensively over the past decades to describe features of the adsorbate-surface interaction, including the excitation of electron-hole pairs [BN89]. Recently, its time-dependent version has been applied to the adsorption of hydrogen atoms on metallic surfaces in order to model non-adiabatic excitations [MBPH05, MBPH07, MBPH08]. Numerical as well as analytical solutions of the problem in the wide-band limit given by the authors were able to produce single electron excitation spectra which were used to explain chemicurrents. Their results have been shown to be in reasonable agreement with more sophisticated theoretical approaches like time-dependent (TD)-DFT [BMLP08, TK09] on the one hand and with experimental results on the other hand [KNN07].

The picture of non-adiabaticity used in these kinds of treatment differs from the one introduced in the previous sections. The coupling between adiabatic electronic states was mediated through the motion of the nuclei, and a *time-independent* Schrödinger equation

$$H_{el}(\mathbf{r};\mathbf{R})\Phi_j(\mathbf{r};\mathbf{R}) = E_j(\mathbf{R})\Phi_j(\mathbf{r};\mathbf{R}) \tag{3.36}$$

for the electronic part of the full Hamiltonian had to be solved. The evolution of the electronic part of the wave function is therefore governed by Eqn. (3.13). In contrast, in the model described in the following section the dynamics of the electrons are determined by a *time-dependent* Schrödinger equation

$$H_{\mathrm{el}}\,|\phi(\mathbf{r},t)\rangle = i\frac{\partial}{\partial t}\,|\phi(\mathbf{r},t)\rangle \tag{3.37}$$

solely for the electrons. From now on, the label and the parameter $\mathbf{r}$ will be dropped because it should be clear that only electronic degrees of freedom are considered in this section.

Mean-field Newns-Anderson Hamiltonian The aim of the model is to solve the time-dependent Schrödinger equation using the following Hamiltonian

$$\begin{aligned} H = &\sum_{\sigma} \widetilde{\varepsilon}_{a\sigma}(t) c^{\dagger}_{a\sigma} c_{a\sigma} + \sum_{k,\sigma} \varepsilon_{k\sigma} c^{\dagger}_{k\sigma} c_{k\sigma} \\ &+ \sum_{k,\sigma} \left(V_{ak}(t) c^{\dagger}_{a\sigma} c_{k\sigma} + H.c. \right) \\ &- U n_{a\sigma}(t) n_{a-\sigma}(t), \end{aligned} \tag{3.38}$$

where a labels the adsorbate state, k the metal states, and σ the spin of the state. The interaction potential V_{ak} determines the coupling between the adsorbate and the substrate states, while the Coulomb energy U determines the interaction between the two spin states of the adsorbate. The last term in Eqn. 3.38 accounts for the double counting of the Coloumb repulsion in the mean-field treatment. The $c^{\dagger}_{\alpha\sigma}$ and $c_{\alpha\sigma}$ are fermion creation and annihilation operators for an electron in the state α having spin σ. The effective adsorbate energy $\widetilde{\varepsilon}_{a\sigma}$ is defined as

$$\widetilde{\varepsilon}_{a\sigma} = \varepsilon_a + U n_{a-\sigma}, \tag{3.39}$$

where $n_{a\sigma}$ denotes the mean field occupation of the adsorbate with spin $-\sigma$. No additional assumptions are made for the fermion states with the exception that they should form a complete and orthogonal basis set. Especially the adsorbate state $|a\rangle$ should be orthogonal to every substrate state $|k\rangle$.

Because it contains only quadratic terms in the fermion operators the Hamiltonian can be effectively written as a one electron matrix operator

$$H^{\sigma} = \begin{pmatrix} \widetilde{\varepsilon}_{a\sigma} & V_{ak} & V_{ak} & V_{ak} & \dots \\ V^{*}_{ak} & \varepsilon_{1\sigma} & 0 & 0 & \dots \\ V^{*}_{ak} & 0 & \varepsilon_{2\sigma} & 0 & \dots \\ V^{*}_{ak} & 0 & 0 & \varepsilon_{3\sigma} & \dots \\ \vdots & \vdots & \vdots & \vdots & \ddots \end{pmatrix} \tag{3.40}$$

which contains non-zero elements only on the first row, in the first column, and on the diagonal.

The time dependence of the Newns-Anderson model is introduced by varying the energy of the bare adsorbate $\varepsilon_a(t)$, the interaction potential $V_{ak}(t)$, and possibly the intra-adsorbate Coulomb repulsion $U(t)$ as a function of time. They can be obtained by fitting them to adsorbate projected densities of state from independent DFT calculations. This procedure makes use of the so called wide-band limit solution of the time independent Newns-Anderson model. In that case the adsorbate projected density of states is usually written as a Lorentzian

$$\rho_a(\varepsilon) = \frac{1}{\pi} \frac{\Gamma/2}{(\varepsilon - \varepsilon_a)^2 + \Gamma^2/4} \tag{3.41}$$

where Γ is the full width at half maximum (FWHM) of the Lorentzian. The interaction

potential V_{ak} is directly related to the FWHM by

$$\Gamma = 2\pi \left|V_{ak}\right|^2 \rho_m \tag{3.42}$$

where ρ_m is the density of states in the metal band. Earlier, in the discussion of the NNL model, this quantity was also label $w(t)$.

At an initial time t_0 the electronic eigenstates of the instantaneous Hamiltonian $|\nu_i^\sigma(t)\rangle$ are thought to be occupied following a Fermi distribution f_{ν,t_0}^σ. Accordingly, a density operator

$$\hat{\rho}^\sigma(t) = \sum_\mu |\mu_i^\sigma(t)\rangle \langle\mu_i^\sigma(t)| f_{\mu,t_0}^\sigma \tag{3.43}$$

can be defined where the $|\mu_i^\sigma\rangle$ are the time evolving wavefunctions with $|\mu_i^\sigma(t_0)\rangle = |\nu_i^\sigma(t_0)\rangle$ and $f_{\mu,t_0}^\sigma = f_{\nu,t_0}^\sigma$ which follow the one-electron Schrödinger equation

$$H^\sigma |\mu^\sigma\rangle = i\frac{\partial}{\partial t} |\mu^\sigma\rangle . \tag{3.44}$$

The density operator $\hat{\rho}(t)$ defines the electron distribution function (EDF)

$$n^\sigma(\varepsilon, t) = \sum_\nu \langle\nu_i^\sigma(t) \,|\, \hat{\rho}^\sigma(t) \,|\, \nu_i^\sigma(t)\rangle \, \delta(\varepsilon - \varepsilon_\nu) \tag{3.45}$$

$$= \sum_{\nu,\mu} \left|\langle\mu_i^\sigma(t)|\nu_i^\sigma(t)\rangle\right|^2 f_{\mu,t_0}^\sigma \delta(\varepsilon - \varepsilon_\nu) \tag{3.46}$$

which can be used to analyze the electronic spectrum caused by the time-varying Hamiltonian. In order to calculate the spectrum of electronic excitation the adiabatic counterpart of (3.46) must be subtracted. In the adiabatic case the time evolving wavefunctions $|\mu_i^\sigma(t)\rangle$ are equal to the eigenfunctions $|\nu_i^\sigma(t)\rangle$ of the Hamiltonian and therefore the adiabatic density operator $\hat{\rho}_{\mathrm{ad}}^\sigma$ is given by

$$\hat{\rho}_{\mathrm{ad}}^\sigma(t) = \sum_\nu |\nu_i^\sigma(t)\rangle \langle\nu_i^\sigma(t)| f_{\nu,t_0}^\sigma. \tag{3.47}$$

With these definitions the spectrum of non-adiabatic excitation

$$n_{\mathrm{ex}}^\sigma(\varepsilon, t) = \sum_\nu \langle\nu_i^\sigma(t) \,|\, \hat{\rho}^\sigma(t) - \hat{\rho}_{\mathrm{ad}}^\sigma(t) \,|\, \nu_i^\sigma(t)\rangle \, \delta(\varepsilon - \varepsilon_\nu) \tag{3.48}$$

$$= \sum_\nu \delta(\varepsilon - \varepsilon_\nu) \left(\sum_\mu \left(\left|\langle\mu_i^\sigma(t)|\nu_i^\sigma(t)\rangle\right|^2 f_{\mu,t_0}^\sigma \right) - f_{\nu,t_0}^\sigma \right) \tag{3.49}$$

can be calculated for every spin component.

It should be noted that the definition of the excitation free or adiabatic spectrum (3.47) differs from a Fermi distribution over the instantaneous eigenstates.

4. Experimental Techniques

4.1. Auger Electron Spectroscopy

Auger electron spectroscopy (AES) has been used to check the cleanliness and chemical composition of the substrates as well as of the samples used in this study [CCL+95]. Electrons ejected from a sample surface fired at with a high-energy beam of electrons are collected in an electron analyzer and filtered with respect to their kinetic energy. From the resultant spectrum, intensity vs. kinetic energy, conclusions can be drawn about the stoichiometry as well as the chemical state of surface atoms in the sample. In a usual setup, the kinetic energy is referenced with respect to the vacuum energy level of the spectrometer, which adds to some extend to the uncertainty of tabulated Auger energies.

In an Auger process an excited ion relaxes in the radiationless way depicted in Figure 4.1 [Aug25]. An initial process, e.g., an incident high energy electron, removes a K shell electron. A second electron neutralizes the hole state and transfers the energy gained in the process to a third electron. The Auger transitions are labeled by the energy levels of the electrons involved, e.g, the transition of Figure 4.1 would be a $KL_{II}L_{III}$, or simply KLL, transition. The first character labels the energy level of the initial core hole. The second and third correspond to the other energy levels involved. If one of the levels involved is the valence band of the solid, one usually writes the letter V instead of the X-ray spectroscopy label of the shell.

Because no two elements have the same binding energy for all electronic levels, the kinetic energy of the Auger electron can be used to identify elemental species. Additional information can be gained from the peak shape and, to limited extend, from the peak position of the Auger peaks. This is especially true for transitions including the valence band, e.g., the Si(LVV) transition, where reactions with adsorbates cause a drastic change of the valence band and thus of the Auger peak shape.

The surface sensitivity of AES, and of most other electron spectroscopic methods, has its origin in the limited lifetime of the emitted electrons in the solid. Depending on its

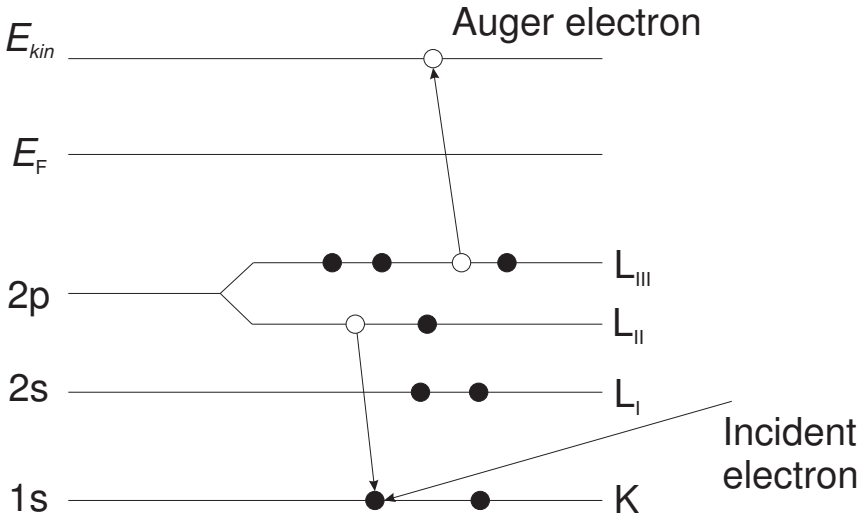

Figure 4.1.: Schematic diagram of a (KLL) Auger transition. Electrons from the incident beam remove an electron from the K shell (adapted from [CCL+95]).

kinetic energy the *escape depth*, or inelastic mean free path, may be only of the order of a few Angströms. It follows a general trend, often referred to as *universal curve* [SD79], valid for almost every material with a minimum escape depth at a kinetic energy of a hundred electronvolts. The universal behavior of the mean free path is a consequence of the similar mechanism causing the energy loss of the electrons: at fairly low energies up to one hundred electronvolts the dominant loss path is through electron-electron scattering, or electron-hole pair creation, while at higher energies the predominant loss mechanism is the excitation of collective electron vibrations, or plasmon.

4.2. Photo Electron Spectroscopy

Since its introduction into surface science in the 1960s photoelectron spectroscopy has been an invaluable tool in the characterization of sample surfaces and the *in situ* determination of reaction products. X-ray photoelectron spectroscopy (XPS) is widely used to identify the chemical state of adsorbates as well as for a quantitative analysis of the surface composition. In particular, XPS has been used to characterize the nature of the alkali metal films that were deposited during this study. Furthermore, quantitative results for the reaction kinetics of the oxygen oxidation of these very films at low tem-

perature could be obtained. Ultra violet photoelectron spectroscopy (UPS) was used as an additional tool to verify the molecular (or atomic) nature of the adsorbed oxygen.

X-ray Photo Electron Spectroscopy (XPS) In X-ray photo electron spectroscopy high energy photons from X-ray sources are used to ionize atoms by removing an electron from a core level. A schematic picture of the photo emission process and the energy labels used for its description have been included in Fig. 4.2. The ejected photo electrons will have a kinetic energy E_{kin} characteristic of the ionized energy level E_{b} and the photon energy $h\nu$ of the light source used in the experiment. Thus, from the measurement of the kinetic energy, which is referenced to the vacuum level of the spectrometer, the binding energy

$$E_{\mathrm{b}} = h\nu - E_{\mathrm{kin}} - \Phi_{\mathrm{a}} \tag{4.1}$$

can be calculated. Because the binding energy is usually referenced to the Fermi energy the analyzer work function Φ_{a} needs to be subtracted. The effective analyzer work function needs to be determined experimentally, which can be done by fitting known spectra with sharp emission lines. In addition to the photo electrons, Auger electrons from the relaxation of the (photo) excited ions in the sample are observed. Of course, these have the same kinetic energy as in AES, which is independent of the light source used in the experiment. Therefore, often two light sources emitting at different X-ray energies, e.g, Mg K_α and Al K_α, are used to easily distinguish between Auger and photo emission lines. This becomes particularly useful if many different, or heavy elements with many lines, are present in the spectrum and lines overlap. Then, the use of a different light source may move the position of an Auger line to a different binding energy where it does not interfere with other photo emission lines.

As in AES, the position and shape of the spectral lines are sensitive to the chemical environment of the ionized atom. This *chemical shift* can be used to, e.g., determine the charge state of an atom or molecule adsorbed at the surface. Every primary emission line is accompanied by a spectral background which is caused by additional losses experienced by the ejected electrons while they leave the solid. The actual shape of the background can contain valuable additional information about the environment of the elements present in the surface. Low energy losses, below a few electronvolts, in metals are often caused by electron-electron scattering and become visible as an asymmetrically shaped line. Additional, well defined peaks to the high binding energy side of the primary peak, are visible which often indicate plasmon losses. Of course, other

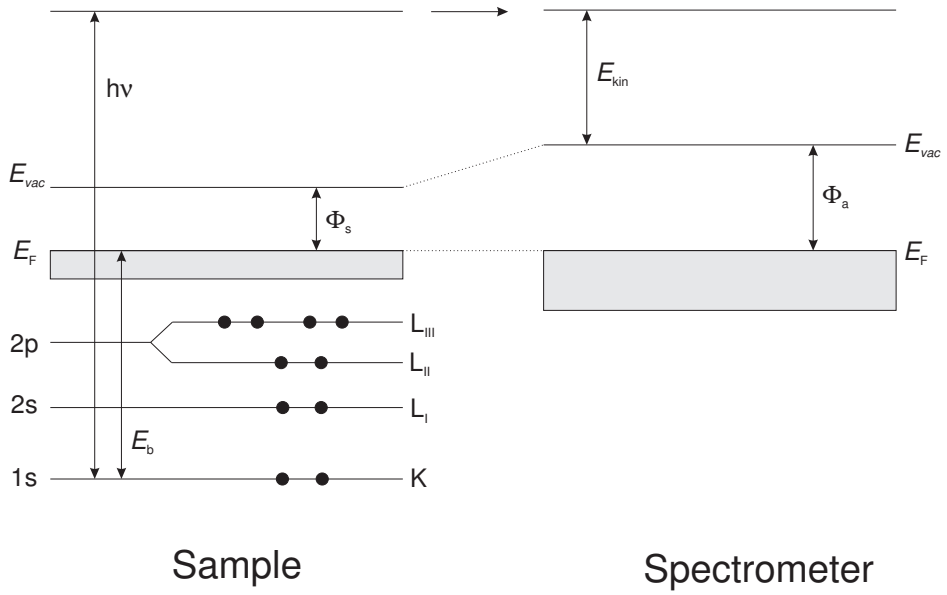

Figure 4.2.: Schematic diagram of the XPS principle. The incident X-ray photon $h\nu$ ionizes a surface atom by removing an electron from an inner shell.

loss mechanisms, like interband transitions or exciton excitations, may be present but the above are by far the ones most commonly encountered.

Ultraviolet Photo Electron Spectroscopy (UPS) Strictly speaking, there is no qualitative difference between XPS and UPS. The main difference lies in the energy range of the primary photons, which are X-rays in the case of XPS and UV light in the case of UPS. Usual UV light sources have photon energies of up to a few tens of electron volts, e.g., a He I gas discharge lamp emits at the primary energy of 21.218 eV.

While the energy levels in XPS are labeled by their single electron levels, it is often more suitable to use total states for the description of UP spectra because correlation effects between different spin configurations may play a role. Exploiting the low line width and the high intensity of UV lasers it is possible to study the photoelectron spectra of gas phase molecules in much detail. Regularly, the resolution of such systems in sufficient to easily discern between vibrational levels of, e.g., diatomic molecules. In combination with high accuracy quantum chemical calculations, the potential energy surfaces (PES) of many neutral molecules and stable anions can be determined.

As an example, the potential energy curves (PEC) of the ground states of the O_2 molecule and its anion are shown in Figure 4.3. For every electronic state vibrational

levels exist which can be calculated in the Born-Oppenheimer approximation. Transitions between these vibrational levels can be observed experimentally, e.g., by photo detachment and photo electron spectroscopy. Every pair of levels results in a line in the photo electron spectrum, like the one shown in Fig. 4.4, at an energy that is equal to the difference between the two. The intensity of the various lines in the band is determined by the overlap of the nuclear wave function, which is known as the Franck-Condon principle [FD26, Con26]. In an iterative process, the potential energy curves of the underlying electronic state can be reconstructed, e.g., by using schemes like the Rydberg-Klein-Rees (RKR) method [Ryd32, Kle32, Ree47].

The electron affinity is defined as the negative minimum energy required to attach an electron to a molecule or ion. In our example, the electron affinity of the neutral molecule $EA_0(O_2)$ is given by the energy difference between the $v = 0$ vibrational states of the $O_2\,X^3\Sigma_g^-$ and the $O_2^-\,X^2\Pi_g$ potential energy curves. For oxygen, the electron affinity is actually positive because the molecule gains energy by attaching an additional electron. This definition of the electron affinity differs from the so called adiabatic electron affinity $EA_a(O_2)$ which is given by the difference between the minimums of the PECs.

The vertical electron affinity EA_v is closely related to the Frank-Condon principle. From the observation that electronic transitions occur almost instantaneously when compared to the timescales of nuclear vibrations, it is reasonable to conclude that transitions occur *vertically*, i.e., at fixed nuclear positions, between potential energy curves. The vertical electron affinity is therefore defined as the difference between the ground state PECs at the minimum position of the neutral molecule. From the PECs of Fig. 4.3, the vertical affinity $EA_\mathrm{v}(O_2)$ can be determined which is negative, while the adiabatic electron affinity is actually positive.

In solid state UPS, vibrational levels cannot regularly be resolved because of the (in)homogeneous broadening of the electronic levels. Still, differences between transitions into excited electronic states are resolvable because the energy spacing between these states is often on the order of several electronvolts.

Electron Analyzer Among the most commonly encountered electron analyzer in surface science labs are the hemispherical energy analyzer (HSA) and the cylindrical mirror analyzer (CMA). In Auger electron spectroscopy, where high throughput is required, the CMA is regularly used while the HSA is usually used for photo emission experiments.

The energy dispersion in a CMA is achieved by applying a voltage between two concentric cylinders (Fig. 4.5). The sample, the electron detector, and the electron gun

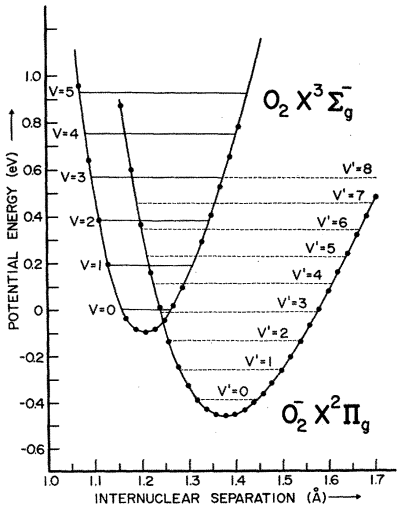

Figure 4.3.: Potential energy curves for the ground states of the free oxygen molecule and the O_2^- anion. The data for the O_2 $X^3\Sigma_g^-$ state were deduced from vibrational spectra using the RKR method. The potential energy curve of the O_2^- $X^2\Pi_g$ was calculated [BS70].

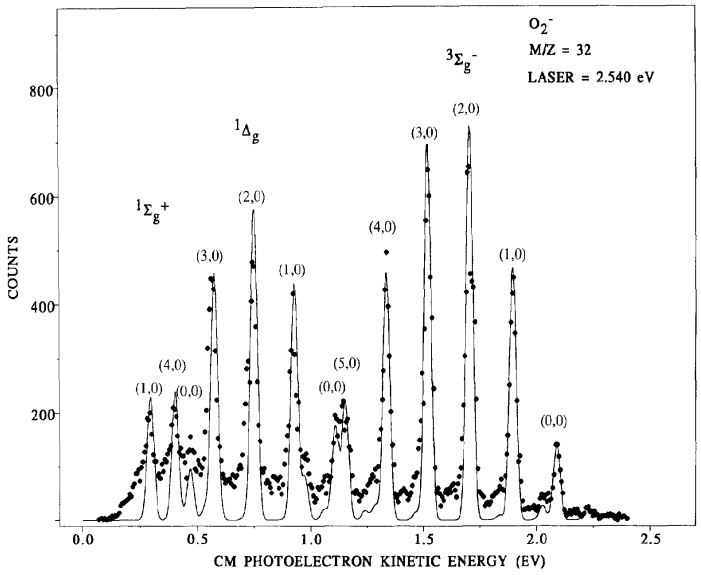

Figure 4.4.: Photo electron spectrum of O_2^-. Transitions from the O_2^- $^2\Pi_g$ state into three O_2 states ($^3\Sigma_g^-$, $^1\Delta_g$, and $^1\Sigma_g^+$) and their vibrational levels are observed. The solid line is a Frank-Condon fit [TCE89].

reside on the CMA axis. The exit slit of the analyzer determines the energy resolution of the analyzer. The CMA acts as a band pass filter whose resolution varies proportionally with the analyzer voltage. Therefore, the resolution $\Delta E/E$ of the CMA remains constant throughout the spectrum.

Its sensitivity on the sample position makes the CMA less suitable for XPS analysis where chemical shifts of a few hundred meV must be resolved. If the sample is not placed accurately at the focal position of the analyzer, the measured energy E_m differs from the nominal analyzer energy E_a ,which is proportional to the voltage applied between the cylinders. This dependence, $\Delta E_\mathrm{m} \propto E_\mathrm{a}\Delta z$, of the measured energy on the distance of the sample from the focal plane can easily be on the order of an electronvolt per micrometer. This is remedied by measuring the peak of elastically reflected electrons at a fixed energy and changing the sample position until the nominal and measured energies coincide.

Figure 4.6 shows the typical schema of a hemispherical energy analyzer used for photo emission. An electron lens system consisting of a number of electrostatic lenses projects the electrons emitted from the sample onto the entrance slit of the hemispherical capacitor section. Electrons on a trajectory in the middle between the outer and inner hemisphere may pass through the analyzer and can be detected at the detector. The resolution of the hemispherical energy analyzer depends on the energy of the electrons passing through the hemispheres. To achieve a maximal resolution, the analyzer is often operated in the fixed analyzer transmission (FAT) mode. In this mode the electrons are decelerated to a fixed pass energy at the entrance slit.

Light Sources In the lab, the most common light source used in XPS setups consists of a water cooled copper anode which is bombarded by electrons of a few kilo electronvolts. A suitable electrode material is deposited as a thin film of a few micrometer thickness on the tip of the anode. In this way, only X-ray radiation from the electrode material gets emitted while ensuring good thermal contact with the enforced water cooling. Usually, different materials are deposited on either side of the anode's beveled head. In a typical combination of materials one uses a magnesium anode in combination with an aluminum electrode because these combine a reasonably low line width, below one electronvolt, with primary photon energies of 1253.6 eV and 1486.6 eV, which give access to most relevant energy levels.

In recent years, the use of synchrotron radiation sources has become more and more important because of the much higher photon flux these machines may generate and the

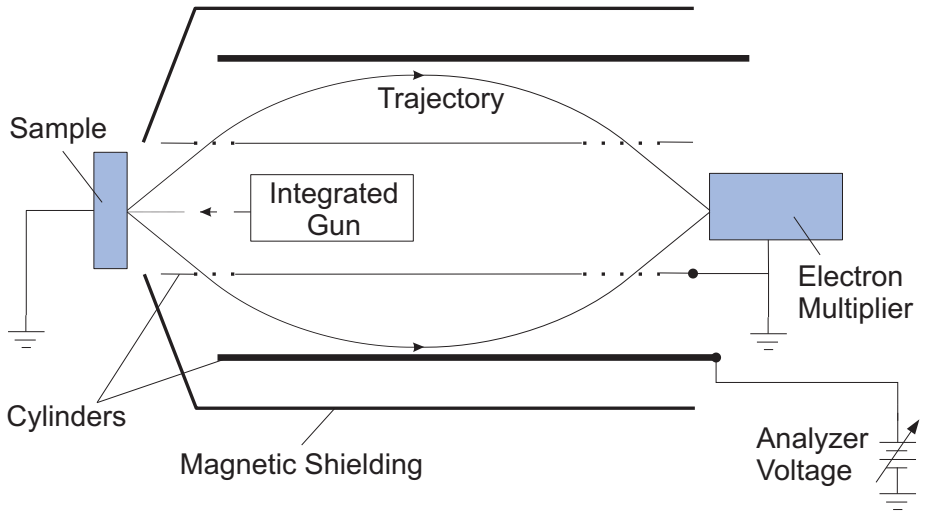

Figure 4.5.: A schematic diagram of a cylindrical mirror analyzer (CMA).

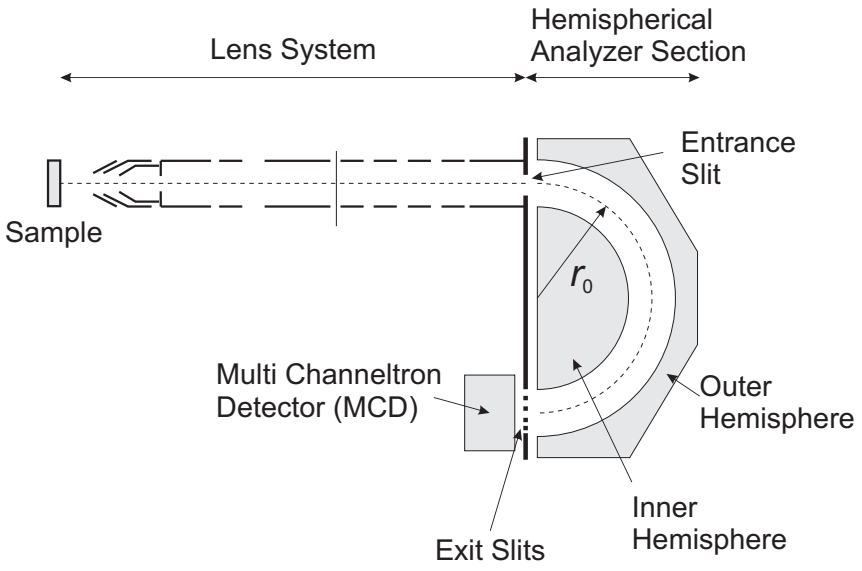

Figure 4.6.: A schematic diagram of a hemispherical energy analyzer (HSA). Picture similar to a SPECS Phoibos 100 analyzer.

ease of altering the photon energy.

Gas discharge lamps are used as light sources for UPS. Most commonly, a low pressure helium discharge in the vacuum is started which provides the UV light. He I at 21.2182 eV and He II at 40.8138 eV are the primary emission lines which are frequently used in the experiment. Because all window materials are opaque at these photon energies, the discharge chamber and the UHV system are directly connected through a glass capillary. A two staged differential pumping system is used to lower the pressure at the low pressure side of the capillary to a level compatible with UHV. For this purpose, two orifices are cut into the capillary which connect to a rotary vane pump in the first stage and a turbo molecular pump in the second stage.

4.3. Electron Exoemission

In general, an electron spectrometer could be used for all electron exoemission experiments. For energy resolved exoemission the setup is therefore quite similar to the one used in UPS. The only difference lies in the way of excitation. Although valuable information about the spectrum of excitation can be gained from such a setup, the time need to achieve a reasonable signal to noise ratio limits its use for time-dependent studies. Therefore, the very simple setup shown in Fig. 4.7 is used: the sample is placed at a distance of a few centimeters in front of a *naked* channeltron detector. Electrons emitted from the sample may reach the first dynode, a metal mesh, of the channeltron detector. Secondary electrons are created at a specially coated surface inside the detector and a pulse of electrons is generated by the high voltage applied to the detector. The pulse can be extracted at the far end of the channel and fed into suitable electronics for the amplification of the signal and the counting of individual pulses.

Because the sample surfaces in exoemission experiments have a work function Φ_S which is regularly much smaller than the one of the first dynode Φ_C, the electron needs to work against the electric field in between the sample and the detector. Only those electrons with kinetic energies larger than Φ_C may reach the detector. To remedy this problem, an additional voltage ΔV is applied to the first dynode which reverses the field in the field region such that the electrons only need to surmount the work function of the sample. Usually, a voltage in greater excess of the work function difference is applied because the sensitivity of the channeltron increases as a function of the primary kinetic energy of the incident electrons. Although the maximum sensitivity is reached at around 100 ev, much smaller voltages are necessary (< 10 V) to reach good signal to

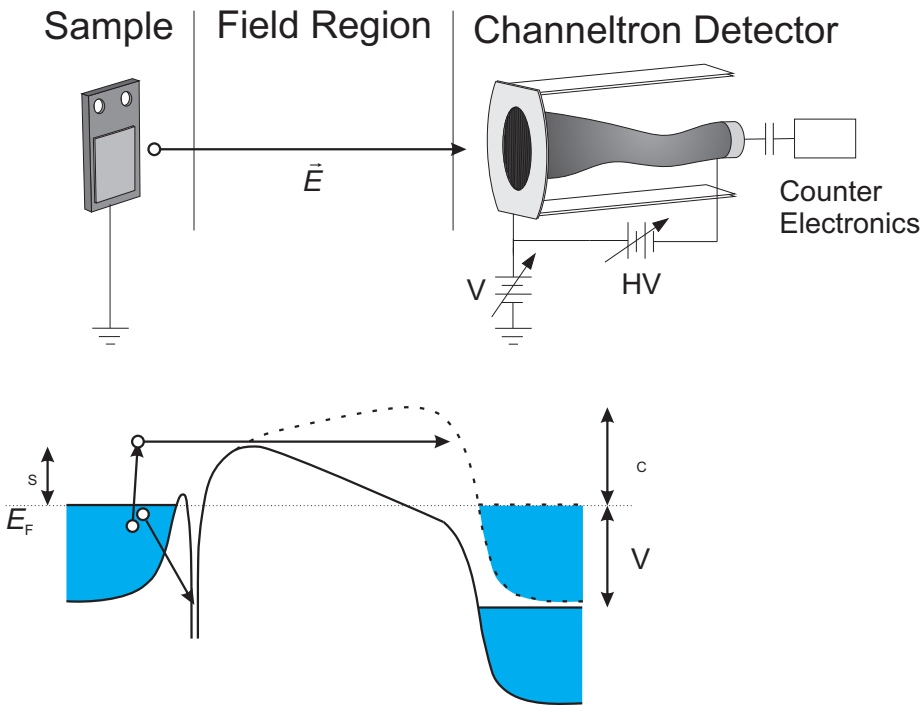

Figure 4.7.: A schematic diagram of a setup for exoelectron collection.

noise ratios. Indeed, if the bias voltage is chosen too high, there is a chance of saturating or even damaging the channeltron.

4.4. Work Function Measurement: Kelvin Probe

The Kelvin method utilizes a vibrating probe to measure the work function of metals, semiconductors, and liquid interfaces [McA04]. A typical Kelvin probe configuration consist of parallel plate capacitor comprising the sample and a reference electrode suspended above the sample surface. In a simplified version of the electric connections to the Kelvin probe, see Fig. 4.8, the sample is regularly held at ground potential, while a variable (DC) voltage is applied to the reference electrode. If the coil drive is at rest, both inputs of the difference amplifier see an equal voltage and the output voltage is zero. Changing the capacitance, e.g., by varying the distance between the electrodes, between the reference and the ground electrode generally causes a displacement current to flow. As a consequence the potential at the one input of the amplifier also changes and

a corresponding voltage for every capacitance change can be measured at the output.

Even if no voltage is applied, an electric field is present between the electrodes which is caused by the contact potential difference (CPD) between either sides. Obviously, the presence of this field requires that charges Q of equal amount but opposing signs must be present on the electrodes. For a parallel plate capacitor of area A, the capacitance is given by the well known formula

$$C = \varepsilon\varepsilon_0 \frac{A}{d}, \tag{4.2}$$

where d is the distance between the plates. In the general case of an applied voltage V_{back}, the sum $\Delta V = V_{\text{back}} + V_{\text{CPD}}$ must be used to calculate the displacement current

$$I = \frac{dQ}{dt} = \Delta V \frac{dC}{dt} \tag{4.3}$$

of the vibrating capacitance. If the backing potential equals the contact potential difference $e_0 \times V_{\text{CPD}} = \Phi_s - \Phi_r$, the displacement current vanishes. The contact potential difference can, therefore, be easily measured by changing the applied backing potential until the displacement current vanishes.

For the actual measurement, the reference electrode is put into a harmonic oscillation

$$d = d_0 + d_1 \sin(\omega t + \phi) \tag{4.4}$$

around an equilibrium position d_0 at an amplitude d_1. The frequency ω can be freely chosen to fit the experimental requirement, usually approximately 100 Hz, and ϕ is an arbitrary phase. The usual routine is to measure the current

$$I = -\varepsilon\varepsilon_0 \Delta V \frac{d_1 \omega \cos(\omega t + \phi)}{(d_0 + d_1 \omega \cos(\omega t + \phi))^2} \tag{4.5}$$

using a lock-in amplifier and changing the backing potential until the lock-in signal vanishes. The alternative method, employed here, is to deliberately apply a number of backing voltages around the expected contact potential difference and measure the respective signal amplitude [McA04]. The data points of current versus applied voltage result in a straight line whose intercept with the voltage axis is just at the position of the desired contact potential difference.

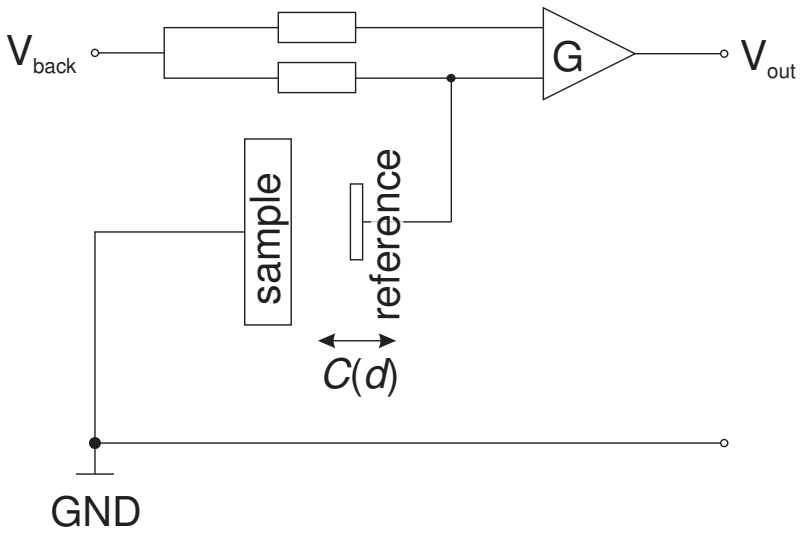

Figure 4.8.: Kelvin probe setup: if V_{back} equals the contact potential difference between the sample and the reference electrode, the AC component of the output voltage vanishes.

5. Experimental Setup

5.1. Ultra High Vacuum Chamber

Parts of the work performed for this study were carried out under ultra high vacuum (UHV) conditions. The ultra high vacuum system comprises three chambers: an electron spectroscopy chamber, a preparation chamber and a quick load-lock system. Every chamber can be vented separately without affecting the pressure in the others.

5.1.1. Electron Spectroscopy Chamber

The UHV chamber used for electron spectroscopy holds a hemispherical electron spectrometer and the light sources used for ultra-violet electron spectroscopy (UPS) and X-ray electron spectroscopy (XPS). The chamber is evacuated by a turbo molecular pump backed by a rotary vane pump. The vacuum reaches a base pressure of typically 1×10^{-10} mbar or better as determined using an uncalibrated Bayert-Alpert gauge. A quadrupole mass spectrometer can be used for residual gas analysis. The samples can be transfered from the preparation chamber to a pocket cooled by a liquid nitrogen cryostat. The minimum temperature that could be reached was 120 K as measured using a thermocouple attached to the sample holder. The sample position could be altered using a manipulator.

A SPECS Phoibos 100 hemispherical energy analyzer was used for X-ray and UV photoelectron spectroscopy as well as for energy resolved exoemission (EREE). A custom built dual anode X-ray gun could be switch between MgK_α and AlK_α radiation. A SPECS UVS 10/35 UV lamp was used for valence band spectroscopy using He I light.

5.1.2. Preparation Chamber

The preparation chamber was used for the deposition of metal films on the substrates as well as for the film characterization using Auger electron spectroscopy (AES), Kelvin probe (KP) and for the chemicurrent and exoemission measurements. The chamber was

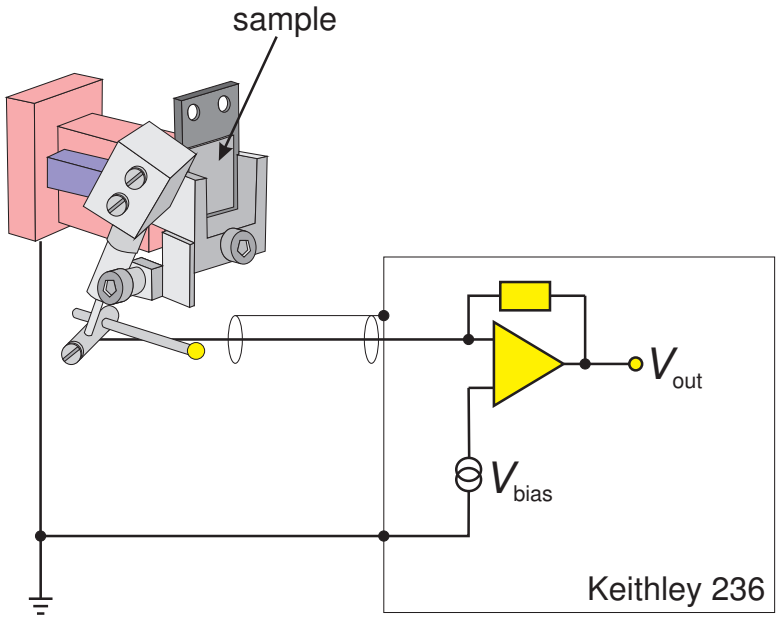

Figure 5.1.: Sample holder with pivoted front contact to be mounted on a liquid nitrogen cryostat. Sketch of the electrical contacts used for chemicurrent measurements as well as for I/V characterization.

pumped using an ion getter pump, a titanium sublimation unit and a non-evaporable getter pump. The total pressure was determined using an uncalibrated inverted magnetron gauge and a Bayert-Alpert hot filament gauge. Regularly a base pressure better than 1×10^{-10} mbar could be reached. Samples were characterized for cleanliness and film thickness using a CMA with an integrated electron gun for AES and a commercial KP for work function measurements.

The sample manipulation system was designed to allow *in situ* sample growth, characterization and chemicurrent/exoemission without the need of transferring and possibly warming the sample in between steps. It comprises a liquid nitrogen cryostat capable of controlling the sample temperature between 100 K and 600 K and a pivoted mechanism to contact the metal films for electrical measurements. A sketch of the sample holder mounted on the liquid nitrogen cryostat is shown in Figure 5.1. The rotatable front contact can be flipped in the vacuum, and thereby the metal film can be contacted using the gold ball attached at the tip. Using the manipulator the sample could be placed in

front of the metal sources, the CMA, the KP and in front of a *naked* secondary electron multiplier needed for exoemission experiments.

Palladium was deposited onto the silicon substrate from a thermal evaporator (Knudsen cell) whose flux was determined using a quartz balance. A standard SAES alkali metal dispenser was used for the deposition of alkali metals. To reduce the amount of contaminations during the deposition of the alkali metals the dispensers were mounted into a shroud cooled with liquid nitrogen.

5.1.3. Electric Characterization: IV-Curves, Chemicurrents

After depositing the metal electrodes the metal films were contacted by flipping the gold front contact onto the sample surface. A Keithley 236 source-measure unit (SMU) was used for the DC measurements in chemicurrent experiments and for I/V characterization of the Schottky devices alike. Figure 5.1 shows a sketch of the analog part of the measuring circuit. Inside the chamber unshielded signal wire was used, while regular coax cables were used on the air side. Regularly the back contact was fixed at ground potential and only the front contact was attached to the SMU. For chemicurrent measurements the metallic side of the samples was usually kept at zero bias with respect to ground. Current-voltage characteristics were obtained by applying the potential to the front contact and keeping the back contact grounded.

5.1.4. Electron Multiplier: Exoemission

A Burle Series 4800 channeltron was used to collect electrons emitted in the exoemission experiments. The electron multipliers first dynode was biased at +10 V with respect to the sample surface to counteract the work function difference between the collector front and the sample. At a multiplier voltage of 2050 V the channeltron pulses are sufficiently high to be detected using a custom build amplifier-discriminator electronic. A detailed description of the measurement circuitry can be found in Appendix C.

5.2. Sample Preparation

Single crystalline silicon wafers cut in the (001) direction were used throughout this work. The wafers were cut into pieces of $11 \times 10\,\mathrm{mm}^2$ and were polished on the front side. The back side of the samples was made ohmic by ion implantation and subsequent annealing at the Fraunhofer-Institute for Microelectronic Systems and Circuits (IMS).

After this treatment the samples carry a thick protective oxide layer which requires further wet-chemical etching steps to be removed.

The as-received samples were cleaned using ultrasonic cleaning in water and isopropanol to wash away dust and organic contaminations on the oxide surface. In a second step the oxide was striped in a solution of 5% hydroflouric acid (HF). Then the samples were re-oxidized in a 1:1 mixture of sulfuric acid and hydrogen peroxide. Afterwards the samples were again rinsed in water and cleaned in an ultrasonic bath of isopropanol. In a final step the chemical oxide including any contaminations from previous treatments was removed by etching in 5% HF.

The procedure effectively removes carbon contaminations from the surface and yields a flat, but atomically rough, hydrogen passivated silicon surface. Afterward, the samples were transfered into vacuum and regularly checked for chemical contaminations. Using Auger electron spectroscopy traces of oxygen were found on the surface whose origin are to be sought in the last HF treatment step. All other contaminations, especially carbon, were below the detection limit of AES and XPS. Additional cleaning steps like sputtering-annealing were not used so that the hydrogen passivation layer remains intact.

5.3. A Word on Pressure Measurement

Because oxygen readily adsorbs on all clean surfaces in the UHV chamber, all pressure readings, and therefor all exposure ratings, must be considered with some care. In particular liquid nitrogen cooled surfaces have a large getter capacity whose pumping rate may easily exceed those of the vacuum pumps. Especially for the photo emission experiments and the energy resolved exoemission this poses quite a problem because the pressure gauge used for the pressure measurements is located in the preparation chamber.

6. Alkali Metal Oxides

The alkali metals form a large variety of oxides when brought in contact with an oxygen atmosphere [GE03, SLC+83]. In general they may be divided into atomic oxides and molecular oxides. In the *regular* oxides, the oxygen is bound in the form of an O^{2-} ion carrying a doubly negative charge. In the peroxides M_2O_2 and superoxides MO_2 the anions are oxygen molecules which are singly or doubly charged. These oxides can be obtained for all five alkali metals under appropriate conditions. Additional oxides and stable suboxides exist, especially for the heavier metals [Lid95, GE03].

During the oxidation of thin metal films under UHV conditions a variety of oxides can be formed depending on the reaction conditions. Film thickness, temperature, oxygen pressure and time of exposure have a crucial influence on the reaction products. The different alkali metals behave differently under oxygen exposure although similarities exist. In general the prepared oxides are not pure but consist of a mixture of different molecular and atomic species.

6.1. Thermodynamical Data

From the thermodynamical point of view all alkali oxides, the peroxides as well as the superoxides, are stable compounds under standard conditions, i.e., at $T^\circ = 298.15\,\mathrm{K}$ and $p^\circ = 1\,\mathrm{bar}$ and unit activities. Table 6.1 lists a number of thermodynamical parameters for the most important alkali metal oxides [Lid95, LM]. Under standard conditions the Gibbs free energy ΔG° is negative for all compounds giving the necessary condition for stability.

Given the tabulated data the temperature and pressure dependence of the Gibbs free energy of formation can be calculated [Atk98]. The Gibbs free energy is defined as

$$G(p,T) = H(p,T) - TS(p,T) \tag{6.1}$$

where $H(p,T)$ is the enthalpy and $S(p,T)$ the entropy at a temperature T and a pressure

Table 6.1.: Thermodynamical data of the stable alkali metal oxides including the standard enthalpy of formation ΔH° from the elements, the standard entropy S° and the Gibbs free energy ΔG° [Lid95, LM]. Standard conditions refer to $T^\circ = 298.15\,\mathrm{K}$ and $p^\circ = 1\,\mathrm{bar}$.

	ΔH_f° (kJ/mole)	S° (J/K mole)	ΔG_f° (kJ/mole)
Lithium			
Li	0	29	-8.6
Li_2O	-599	38	-562
Li_2O_2	-636	45	-571
Sodium			
Na	0	51	-15.2
Na_2O	-418	75	-379
Na_2O_2	-510	95	-447
NaO_2	-260	116	-218
Potassium			
K	0	65	-19.4
K_2O	-363	94	-322
K_2O_2	-495	113	-429
KO_2	-285	123	-241
Rubidium			
Rb	0	77	-23.0
Rb_2O	-337	109	-293
Rb_2O_2	-427	105	-351
RbO_2	-263	59	-197
Cesium			
Cs	0	85	-25.3
Cs_2O	-320	126	-276
Cs_2O_2	-404	118	-327
CsO_2	-278	65	-211
Oxygen			
O_2	0	205	-61.1
O	249	161	201

p. Standard enthalpies of formation ΔH_f° and entropies ΔS_f° are tabulated for a wide range of substances and can be combined to find the Gibbs free energy of formation $\Delta G_f^\circ = \Delta H_f^\circ - T\Delta S_f^\circ$. If the pressure and temperature conditions of interest are not listed estimates of the thermodynamical potentials can still be calculated. It follows directly from the definition of the heat capacity C_p, that the change of enthalpy when changing the temperature from T_1 to T_2 is given by

$$H(T_2) = H(T_1) + \int_{T_1}^{T_2} C_p dT, \tag{6.2}$$

when the pressure is kept constant during the heating (cooling). Equally, the entropy change is given by

$$S(T_2) = S(T_1) + \int_{T_1}^{T_2} \frac{C_p}{T} dT. \tag{6.3}$$

To find the Gibbs energy when changing the pressure of a system at a fixed temperature the volume work done on the system has to be considered. It follows that

$$G(p_2) = G(p_1) + \int_{p_1}^{p_2} V dp. \tag{6.4}$$

Equations (6.2) to (6.4) are exact by definition. To further equate their value model assumptions have to be taken. For the elements all necessary data at standard pressure are tabulated, and therefore only their pressure dependence has to be considered. As the volume change of solids is small the Gibbs free energy can be treated as constant for the alkali metals as well as for the oxides. Oxygen can be treated as an ideal gas under the experimental conditions. Its state function therefore is $V = RT/p$, or if substituting into (6.4)

$$G(p_2) = G(p_1) + RT \int_{p_1}^{p_2} \frac{dp}{p} = G(p_1) + RT \log(\frac{p_2}{p_1}). \tag{6.5}$$

The temperature dependence of the alkali metal oxides can be approximated using the Debye model of specific heat [AM76, Kit96]. At low temperatures $T < T_D$ only the acoustic branches of the phonon spectrum contribute to the heat capacity, and one finds

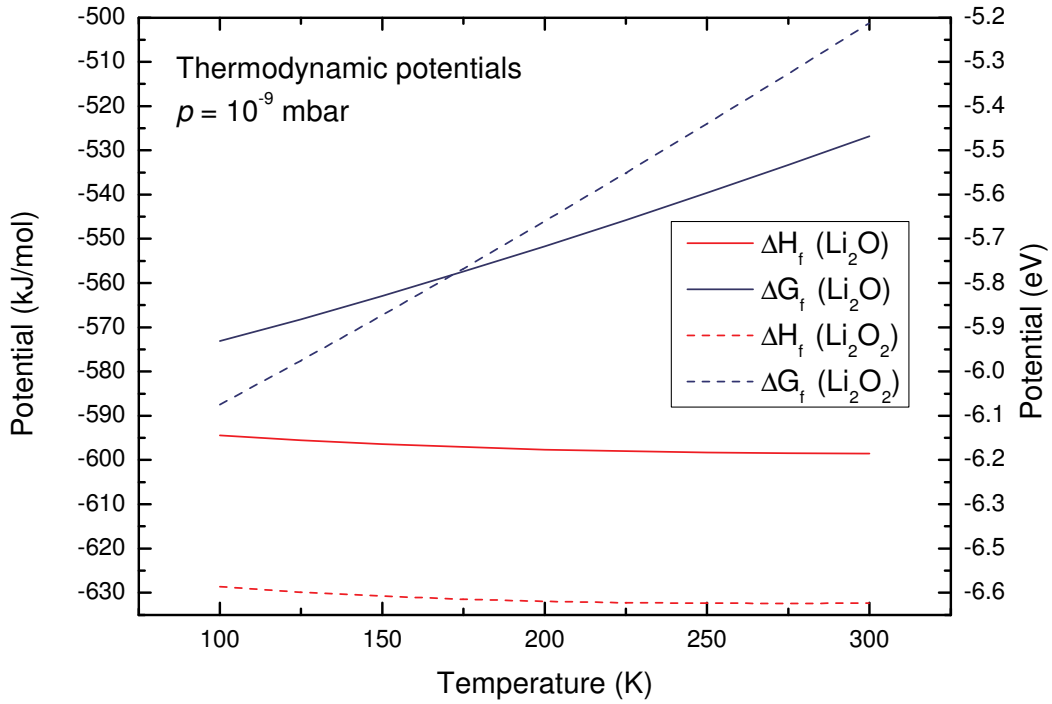

Figure 6.1.: Thermodynamical potentials of Li_2O and Li_2O_2 at $p = 10^{-9}$mbar as a function of temperature. Lithium peroxide was treated as a Debye solid with $T_D = 930\,\mathrm{K}$ and oxygen as an ideal gas [JB51, Ser09, LM]

$$C_p \approx C_V = 9NR\left(\frac{T}{T_D}\right)^3 \int_0^{T_D/T} \frac{\tau^4 e^\tau}{(e^\tau - 1)^2} d\tau, \tag{6.6}$$

where T_D is the Debye temperature and N is the number of atoms in the unit cell.

Figure 6.1 shows the temperature dependence of the enthalpy and the Gibbs energy of formation of lithium oxide and lithium peroxide at a pressure typical for UHV experiments, $p = 10^{-9}\,\mathrm{mbar}$. The data for lithium oxide were computed from tabulated values obtained from low temperature experiments [JB51] using only the pressure dependence as given by Eqn. (6.5). The lithium peroxide data were obtained by extrapolating data above room temperature using a Debye model. A Debye temperature of $T_D = 930\,\mathrm{K}$ was chosen in accordance with total energy calculations [RS01, Ser09]. It is quite obvious that the temperature dependence of ΔG_f is dominated by the entropy term $-T\Delta S^0$, whereas the temperature dependence of ΔH_f is negligible.

A clear trend can be observed for the difference of the standard enthalpy of formations between the normal oxide and the peroxides for lithium, sodium and potassium. Therefore an analysis similar to the one for Li (Fig. 6.1) was carried out for K and Na as well, which is presented in Figure 6.2. The enthalpy difference $\Delta H_f^\circ = 37\,\mathrm{kJ/mol}$ between the regular lithium oxide and the peroxide is much smaller than for the other alkali metals. The respective literature values for sodium and potassium , 95 kJ/mol and 130 kJ/mol (Tab. 6.1), are nearly trice as high. As has been shown, virtually the entire

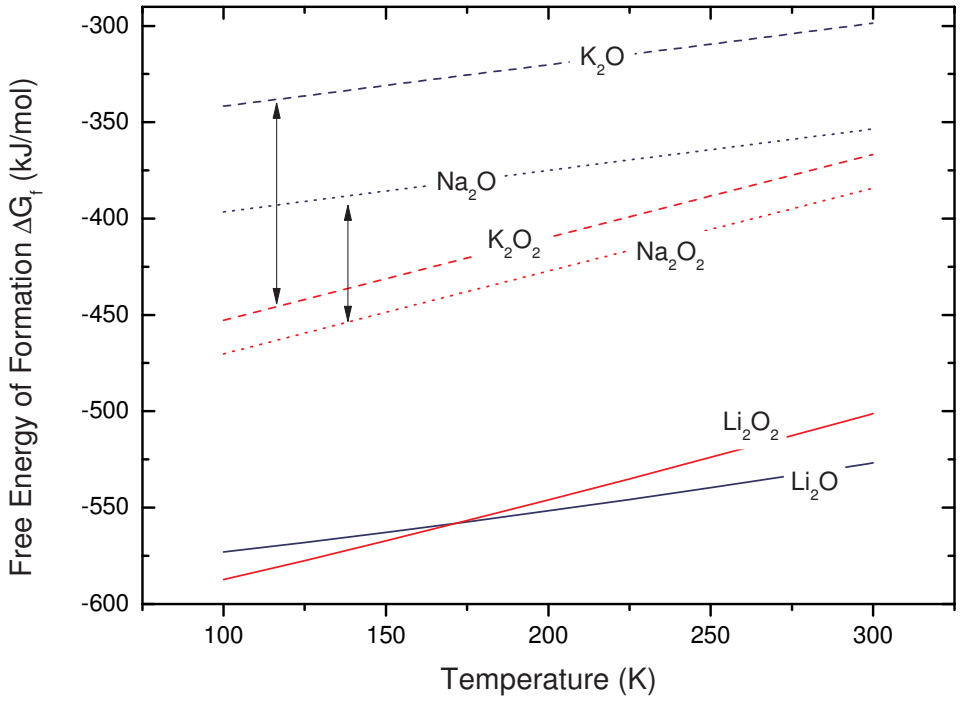

Figure 6.2.: Thermodynamical potentials of alkali metal oxides and peroxides at $p = 10^{-9}$mbar and $T = 125\,\mathrm{K}$.

temperature dependence of ΔG is due to the entropic term introduced by the oxygen gas. For the purpose of this study, all other terms can therefore be safely neglected in the analysis. The result of the calculations reveals that the trend suggested by the difference in reaction enthalpy holds also for the Gibbs free energy: while for Na and K the Gibbs free energy is more negative for the peroxides in the relevant temperature regime, the driving force toward the formation of the peroxide is missing in the case of lithium.

6.2. Electronic Structure of the Oxygen Ions

Elemental oxygen under standard conditions is a diatomic molecule O_2 with an electron configuration of $3\sigma_g^2 1\pi_g^4 1\pi_u^2$. A corresponding molecular orbital (MO) schema following the method of linear combination of atomic orbitals (LCAO) is shown in Fig. 6.3. In the ground state the electrons are found in the $O_2\,X^3\Sigma_g^-$ state, i.e., in accordance with Hund's rules two electrons with parallel spin-moment occupy the anti-bonding $1\pi_u^*$ orbital. The singly charged superoxide ion O_2^- has the electron configuration $3\sigma_g^2 1\pi_g^4 1\pi_u^3$. In the gas phase its ground state is $O_2^- X^2\Pi_g$. The peroxide ion O_2^{2-} has a filled outer $1\pi_u^*$ shell corresponding to the $O_2^{2-}\,X^1\Sigma_g$ state, which is unstable in the gas phase.

Atomic oxygen has four valence electrons in the O 2p-shell. To fill the valence shell two more electrons are therefore needed. In a compound with alkali metals atomic oxygen is therefore usually found as a doubly negative ion O^{2-} with a filled 2p-shell.

For the interpretation of UV spectra it is helpful to compare the experiment with

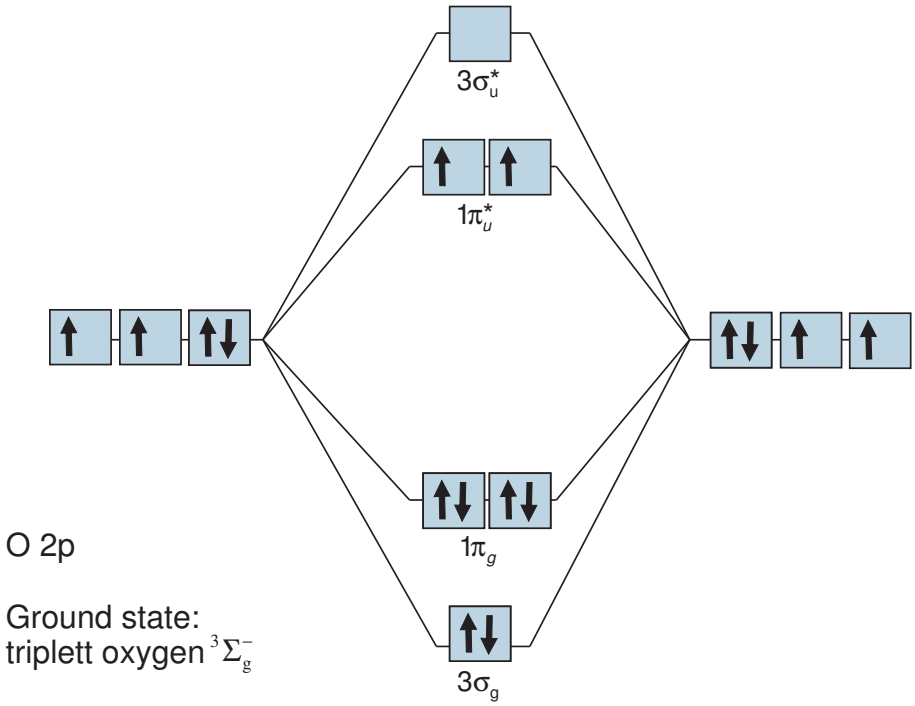

Figure 6.3.: In an oxygen molecule the atomic 2p orbitals are split into two binding ($3\sigma_g$ und $1\pi_g$) and two anti-bonding ($3\sigma_u$ und $1\pi_u$) orbitals. Their occupation in the ground state is determined according to Hund's rules. The ground state therefore is the triplett state $X^3\Sigma_g^-$.

theoretically computed spectra. Potential energy curves for the different electronic states of the oxygen molecule as well as the superoxide ion are available for the gas phase [SL77, KNW$^+$73, LM] and can be used for this purpose. From these the vertical energy differences between the electronic states can be extracted for specific O-O separations which need to be adjusted to the intra molecular bond length in the solid. The spacing between states is often similar to the spacing between features corresponding to different final states in photoemission experiments.

Table 6.2 lists the energy differences between electronic states of the oxygen molecule and the superoxide molecule which can be reached by photoemission from the ground state of the superoxide and peroxide molecule [Atk98]. The energies of the O_2 molecular states are given relative to the $O(^3P) - O(^3P)$ configuration of oxygen atoms. With the exception of the $B^3\Sigma_u^-$ state, which is connected to the $O(^1D) - O(^3P)$ configuration, all the states are adiabatically connected to this configuration. The energies of the superoxide ion states are given relative to its $O_2^-\ X^2\Pi_g$ ground state.

For the photoemission from the $O_2^{2-}\ X^1\Sigma_g^+$ ground state the interpretation of the final states is quite simple because the spin direction does not play a role in closed shell molecules. It is the emission of one electron from the π_u^*, the π_g or the σ_g molecular orbital leaving the O_2^- ion in the $O_2^-\ X^2\Pi_g$, the $O_2^-\ ^2\Pi_u$ and the $O_2^-\ ^2\Sigma_g$ state.

The photoionization of the superoxide ion on the other hand is complicated by the alignment of the spin moment in different O_2 final states. The MO representations of various low lying states of the oxygen molecule presented in Fig. 6.4 help to understand these transitions. All of these states are adiabatically connected to the $O(^3P) - O(^3P)$ atomic states of the dissociated oxygen atoms and are stable or metastable in the gas-phase.

Although the oxygen ions are tightly bound in the molecular alkali oxides it has been shown that surprisingly good agreement between the theoretical predictions and the experiment [JDB92] is found if only energy separations are considered. This indicates that the overall symmetry of the molecular ions is preserved and shall help to identify possible molecular species during the adsorption of oxygen on alkali films.

Table 6.2.: Vertical energy separations between molecular states for the oxygen molecule and the superoxide ion; the values were computed using configuration-interaction methods for an O-O separation of 1.37Å and 1.59Å[SL77, KNW$^+$73]. Energies of the oxygen states are relative to the $O(^3P) - O(^3P)$ configuration, energies of the superoxide states are relative to the O_2^- $X^2\Pi_g$ ground state.

Superoxide ion O_2^-		Oxygen molecule O_2		
Molecular state	ΔE	Molecular state	E	ΔE
$X^2\Pi_g$	0	$X^3\Sigma_g^-$	-4.49	0
$^2\Pi_u$	3	$a^1\Delta_g$	-3.51	0.97
$^2\Sigma_g$	4.4	$b^1\Sigma_g^+$	-2.93	1.55
		$c^1\Sigma_u^-$	-0.65	3.84
		$C^3\Delta_u$	-0.42	4.06
		$A^3\Sigma_u^+$	-0.31	4.18
		$B^3\Sigma_u^-$	1.92	6.42
		$1^3\Pi_g$	2.01	6.50

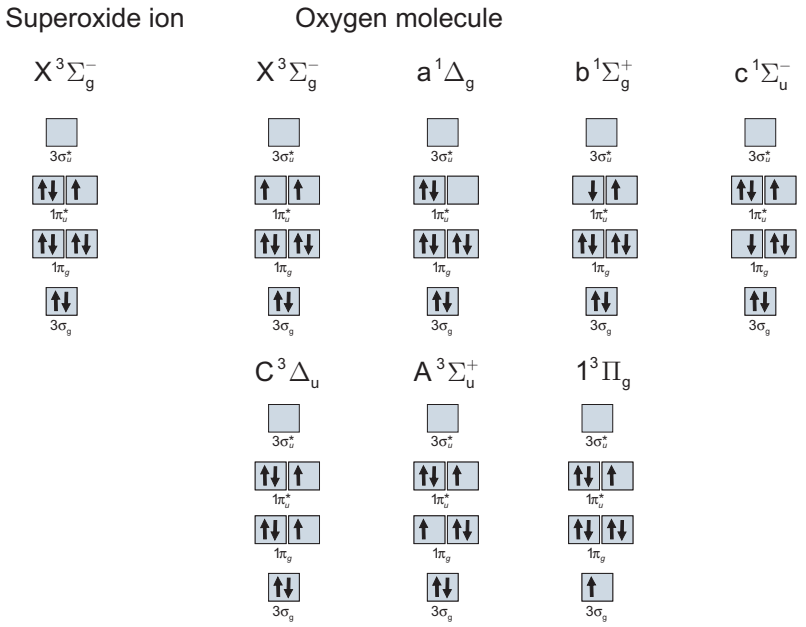

Figure 6.4.: Molecular orbital diagrams for the states involved in the photoionization of a superoxide ion. Only oxygen molecular orbits adiabatically connected to the $O(^3P) - O(^3P)$ are shown.

7. Experimental Results

The knowledge of the barrier height of the used Schottky diodes is of crucial importance because it determines the sensitivity of the devices for weak electronic excitations. In the first part of this chapter, Schottky contact I/V-characteristics are presented that were used, if possible, to determine the homogeneous barrier height of the ideal interface. Where proper IV-curves, that could be fitted using thermionic emission theory, were not available the barrier height was calculated using the MIGS-and-electronegativity concept [Mön01].

For the second part of this chapter, X-ray photoelectron spectroscopy (XPS) was used to determine the composition of alkali metal films while they were exposed to oxygen. The earliest investigations on non-adiabatic energy release using the chemicurrent method assumed a constant efficiency of the current generation. This assumption led to the conclusion that the chemicurrent traces directly reflect the reaction rate, i.e., $j_{\mathrm{CC}}(t) = \alpha \times R(t)$, [GN04]. To test this assumption, the reaction rate, or equivalently the oxygen uptake, must be measured separately. In this way, the reaction mechanism could be determined and compared to the outcome of the combined exoemission and chemicurrent experiments.

The third section contains a brief study of the work function change of potassium films under oxygen exposure which was measured using the Kelvin probe method.

In the following section results from exoemission and chemicurrent experiments are presented. Both were recorded simultaneously as a function of time in a combined experiment during the oxidation of alkali metal surfaces. A comparison between the resultant chemicurrent and exoemission traces, and the reaction rate shows that the simple assumption of a constant efficiency does not hold for the systems that were investigated in this study.

In the last section a model incorporating the previously shown findings will be presented.

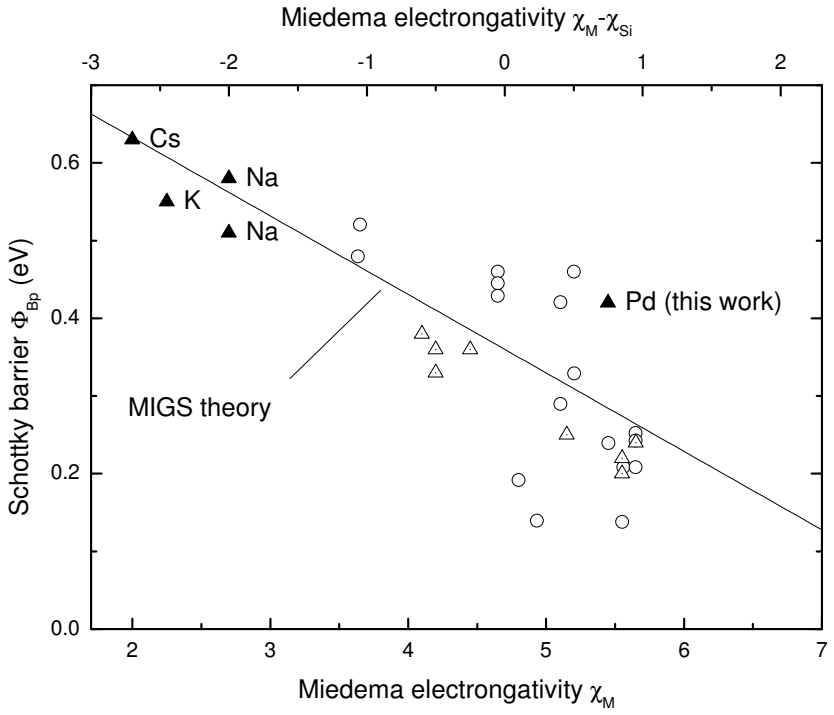

Figure 7.1.: Barrier heights laterally homogeneous silicon Schottky contacts as a function of the Miedema electronegativity of the metal. Triangles are data for abrupt metal-semiconductor contacts, the open circles represent data from silicide interfaces [Mön01, HKMN09]. Filled symbols are for metals used in this study.

7.1. Schottky Contacts

Two different kinds of Schottky contacts were used for the experiments in this study: either the alkali metal was directly deposited on the semiconductor substrate or an intermediate layer of palladium was deposited on the silicon surface.

7.1.1. Palladium-Silicon Schottky Contacts

Figure 7.2 (a) shows I/V curves recorded at a number of temperatures in the range of 120 K to room temperature (RT) in steps of 5 K. In thermionic emission theory the current through a Schottky diode is given by Eqn. (2.22). The total current measured is given by the sum of (2.22) and the photo current due to infrared radiation in the chamber. For Figure 7.2 (b) theoretical curves calculated with the help of (2.22) are used to fit I/V curves in the temperature range between 125 K to 155 K. To reduce

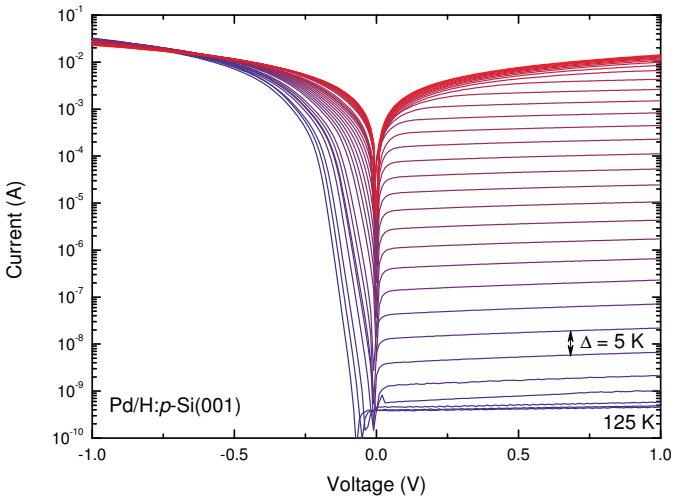

(a) Full temperature range.

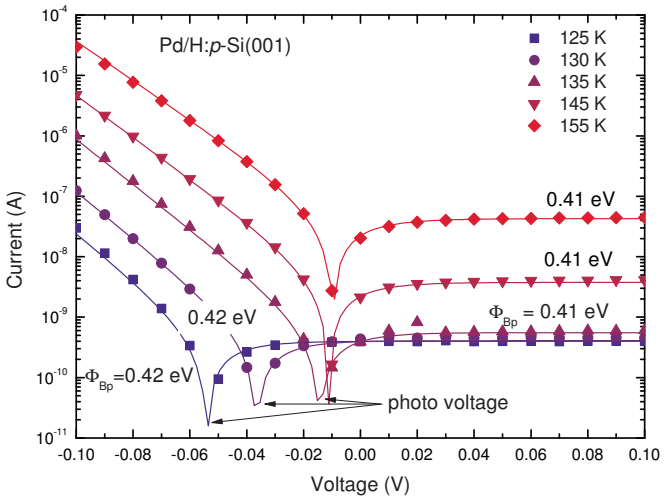

(b) Temperature range around 120 K. Lines indicate fits according to the thermionic emission theory.

Figure 7.2.: I/V curves recorded at various temperatures in the range of 120 K to RT in steps of 5 K for a Schottky diode with a 1.2 nm Pd metal electrode on H-terminated *p*-type Si(001) substrate.

effects of the series resistance of the thin film, the voltage range used for the fits was restricted to a range of $-0.1\,\mathrm{V}$ to $0.1\,\mathrm{V}$. The data can be fitted with a Schottky barrier $\Phi_p \approx 0.41 \pm 0.01\,\mathrm{eV}$ and an ideality factor $n = 1.01$, taking into account the image force lowering of the Schottky barrier.

The theory of metal-induced gap states (MIGS) and electronegativity relates the homogeneous barrier height Φ_{Bp} with the electronegativity difference of a given metal-semiconductor pair [CK96, Mön01]. Figure 7.1 compiles a number of barrier heights for metal contacts on p-doped silicon which were obtained using various techniques like ballistic electron microscopy, photo emission and I/V characterization. Data sets for reactive silicide-silicon (open circles) and abrupt metal-silicon interfaces (triangles) were plotted. Barriers for contacts used in this study are marked by filled symbols. In the case of metal-p-Si contacts, an empirical formula has been derived which predicts the barrier height

$$\Phi_{\mathrm{Bp}} = (0.36 - 0.101 \times (\chi_{\mathrm{M}} - \chi_{\mathrm{Si}}))\,\mathrm{eV}, \tag{7.1}$$

where χ_{M} and $\chi_{\mathrm{Si}} = 4.7$ are the Miedema electronegativities [MdCdB80] of the metal and the silicon substrate [HKMN09]. Although (7.1) is strictly valid only for abrupt interfaces, reasonable agreement with barrier heights of silicide-silicon interfaces has been shown [Mön01]. For Pd_2Si diodes, the model predicts a homogeneous barrier height $\Phi_{\mathrm{Bp}} = 0.28\,\mathrm{eV}$ ($\chi_{\mathrm{Pd}} = 5.45$) whereas the barrier height found for our diodes is markedly higher than this. Similarly discrepancies have been observed for numerous metals on hydrogen passivated surfaces and were explained by an extrinsic dipole layer caused by hydrogen remaining at the interface which adds to the dipole introduced by the MIGS at the interface [KM95, HKMN09]. At defected transition metal silicide interfaces, deviations from the ideal behavior of the MIGS-and-electronegativity concept must also be expected which are caused by dangling d orbitals [FA94, Mön01]. They lead to additional charging of the interface and hence an altered barrier height which depends on the exact structure of the interface.

Because of their low barrier palladium Schottky diodes are very efficient light sensors even in the infra red. The additional current simply adds to the thermionic current and establishes a shift of the I/V curves which can be seen in panel 7.2 (b). For a surrounding environment at 300 K this photo current is already of the order of a nanoampere which is close to the current strength regularly observed for chemicurrents. This would not pose a problem if the photo current remained constant throughout the chemicurrent experiment. In fact, this is not so because the optical properties of the film (absorption, reflectivity) change during the an oxygen exposure. So, in spite of their low barrier

which results in a high sensitivity to low-energy electronic excitations, palladium based diodes are not especially suitable for the study of small chemicurrents ($\approx 1\,\mathrm{pA}$).

7.1.2. Alkali-Silicon Schottky Contacts

Alkali-silicon Schottky interfaces are in particular interesting because of their dissimilar I/V-characteristics on p-doped and n-doped silicon. Whereas the p-doped diodes have excellent diode characteristics, Ohmic contacts form on negatively doped substrates. At the same time, photo emission data show Schottky barriers $\Phi_{\mathrm{Bn}} \approx 0.6\,\mathrm{eV}$ for sodium on silicon which is in good agreement with the MIGS theory. A direct validation of the MIGS-slope from I/V characteristics is therefore only possible using p-doped diodes.

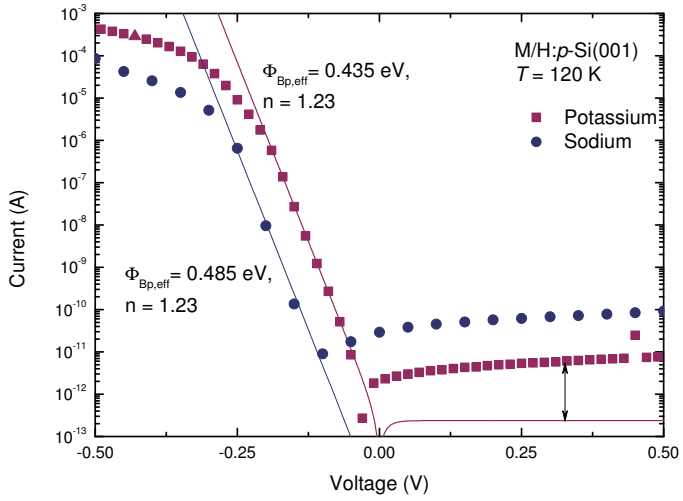

Figure 7.3.: Sample I/V-characteristic of a K/H:p-Si(001) and Na/H:p-Si(001) Schottky diode.

A comprehensive study of potassium-silicon Schottky diodes has been published recently by Huba *et al.* [Hub08, HKMN09] who analyzed the same diodes also used for this thesis. In agreement with the general behavior, n-doped Schottky diodes showed Ohmic characteristics and could not be used for chemicurrent experiments. In contrast, the barrier height of a homogeneous potassium contact on p-doped silicon could be determined as $\phi_{\mathrm{Bp}} = 0.55\,\mathrm{eV}$. Accordingly, a reduction of the residual photo current by two orders of magnitude could be reached in comparison with the photo current in palladium based diodes. Sample I/V characteristic for a sodium diode and a potassium diode have been included in Fig. 7.3. Fit curves according to Eqn. 2.22 have been including

Table 7.1.: Schottky barrier height Φ_{Bp} of laterally homogeneous Schottky contacts on silicon.

Metal	Interface structure	Φ_{Bp}(eV)	$\Phi_{\mathrm{Bp}}^{\mathrm{MIGS}}$(eV)	Data source
Li	N/A	N/A	0.55	-
Na	(7×7)-Si(111)	0.58 (PES)	0.56	[Mön01, PNHH98]
	(3×1)-Si(111)	0.51 (PES)	0.56	
K	(1×1)-H:Si(001)	0.54 (IV)	0.61	[HKMN09], this work
Rb	N/A	N/A	0.62	-
Cs	(7×7)-Si(111)	0.62	0.64	[Mön01]
Pd	(1×1)-H:Si(001)	0.42	0.28	this work

in the figure. Ideality factors far greater than $n = 1$ have to be used to satisfactorily fit the currents in the exponential forward direction, which indicates to a very inhomogeneous interface. The I/V characteristics are quickly dominated by the serial resistance of the films, which is due to the spread resistance of the extremely thin metal layer. Several factors contribute to the current in the reverse direction and are responsible for its deviation from the ideal behavior. They include: (a) photocurrent at a much lower level then for palladium based diodes, (b) ohmic current paths parallel to the diodes, (c) charging of the diodes according to $I = C\frac{dV}{dt}$.

Table 7.1 includes a compilation of the barrier heights of laterally homogeneous Schottky contacts on p-doped silicon substrates for metals that were used in this study. For potassium and palladium reliable experimental data are available for Schottky diodes fabricated using hydrogen passivated silicon whereas the experimental foundation for the other alkali metals is rather weak. If necessary the MIGS theory value $\Phi_{\mathrm{Bp}}^{\mathrm{MIGS}}$ computed from the Miedema electronegativities were used [MdCdB80].

7.2. Photoelectron and Auger Spectroscopy

7.2.1. Silicon

The wet-chemically etched silicon wafers were regularly checked for cleanliness and complete oxide removal. Figure 7.4 shows representative Auger and X-ray spectra of an *as prepared* sample after quick insertion into the UHV. Both methods are capable of detecting contaminations as low as approximately one surface contamination atom in a hundred substrate atoms.

The Auger and XP spectra in Fig. 7.4 show that the initial silicon surface is essentially free of hydrocarbon contaminations. In comparison with previous studies, that reported an appreciable amount of hydrocarbon adsorbates on the wet chemically cleaned silicon surfaces, this must be seen as a large improvement of the cleanliness of the sample preparation with regard to carbon contaminations [Gla04]. The crucial step toward the reduction of these contaminations was the intermediate etching in the $H_2SO_4 : H_2O_2$ solution. Spurious oxygen contaminations on the order of one percent of a monolayer are visible which were introduced in the last step of the wet chemical preparation. Most probably, these are caused by residual hydroxyl groups bonded to the surface.

7.2.2. Lithium

Metallic Lithium Films

Metallic lithium films were deposited on hydrogen passivated, clean, and n-doped silicon wafers. An example X-ray spectrum of a lithium film deposited on a wet-chemically prepared Si(001) surface is presented in Fig. 7.5. In Figure 7.6, Auger spectra of the clean silicon surface, the metallic lithium film as it was deposited, the lithium film at elevated temperatures, and an oxidized film at room temperature are shown. Samples using negatively doped substrate were used for all spectroscopic measurements because their Ohmic contacts effectively prevent the metallic film from charging.

The upper panel of Figure 7.5 shows a survey spectrum of a multi-layered ($\approx 10\,\mathrm{ML}$) Li film that was deposited at a temperature of 120 K and was kept at that temperature afterward, with the exception of a brief period of time during the transfer into the electron spectroscopy chamber. Two features dominate the spectrum: the Li 1s photoemission line and a broad loss spectrum starting at a binding energy of 100 eV. In particular, there is no clear photoemission visible from the Si 2s and Si 2p lines in the spectrum. Instead a large background loss signal is seen at that position. A thor-

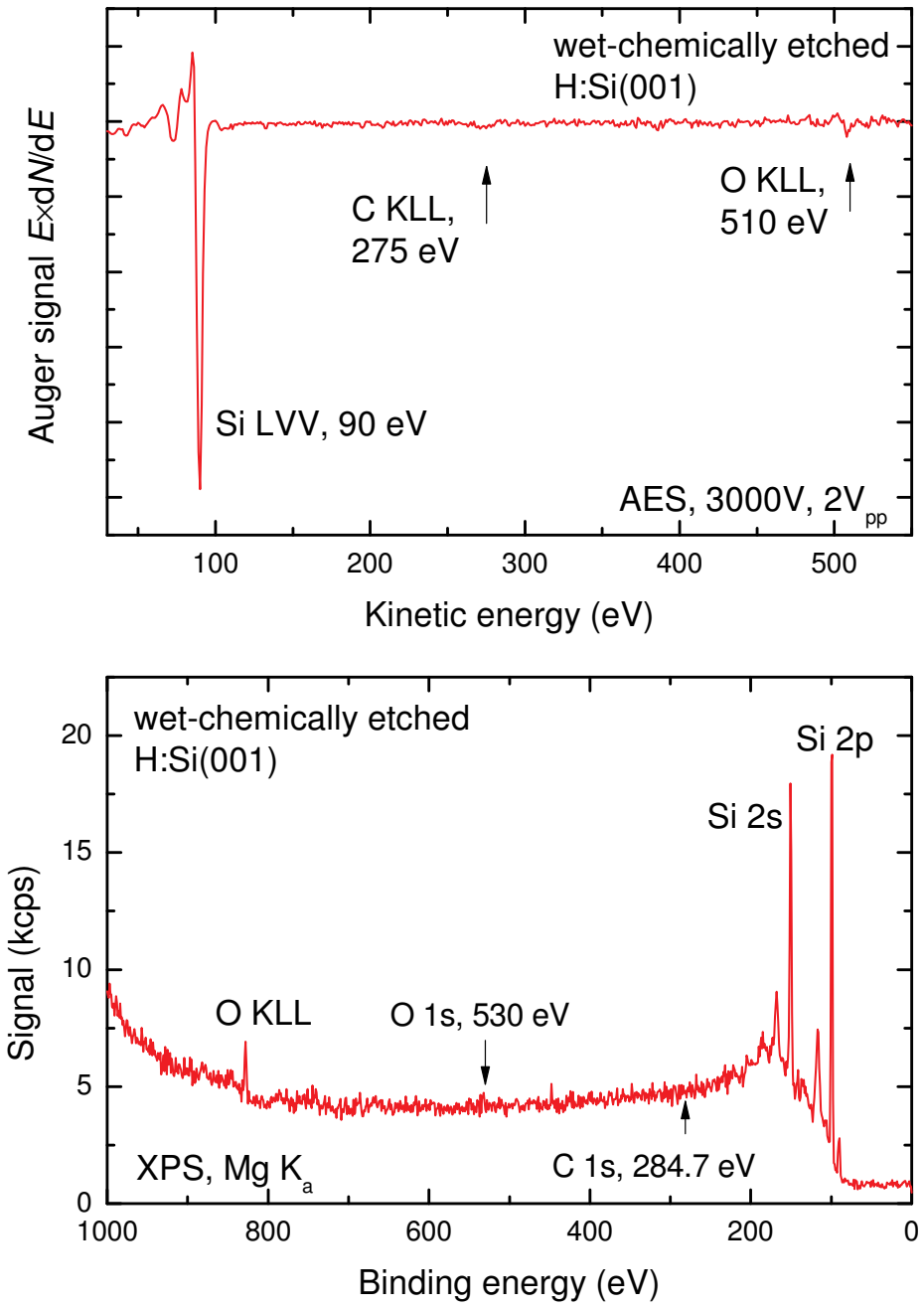

Figure 7.4.: AES and XPS spectra of wet-chemically prepared H:Si(001) surfaces.

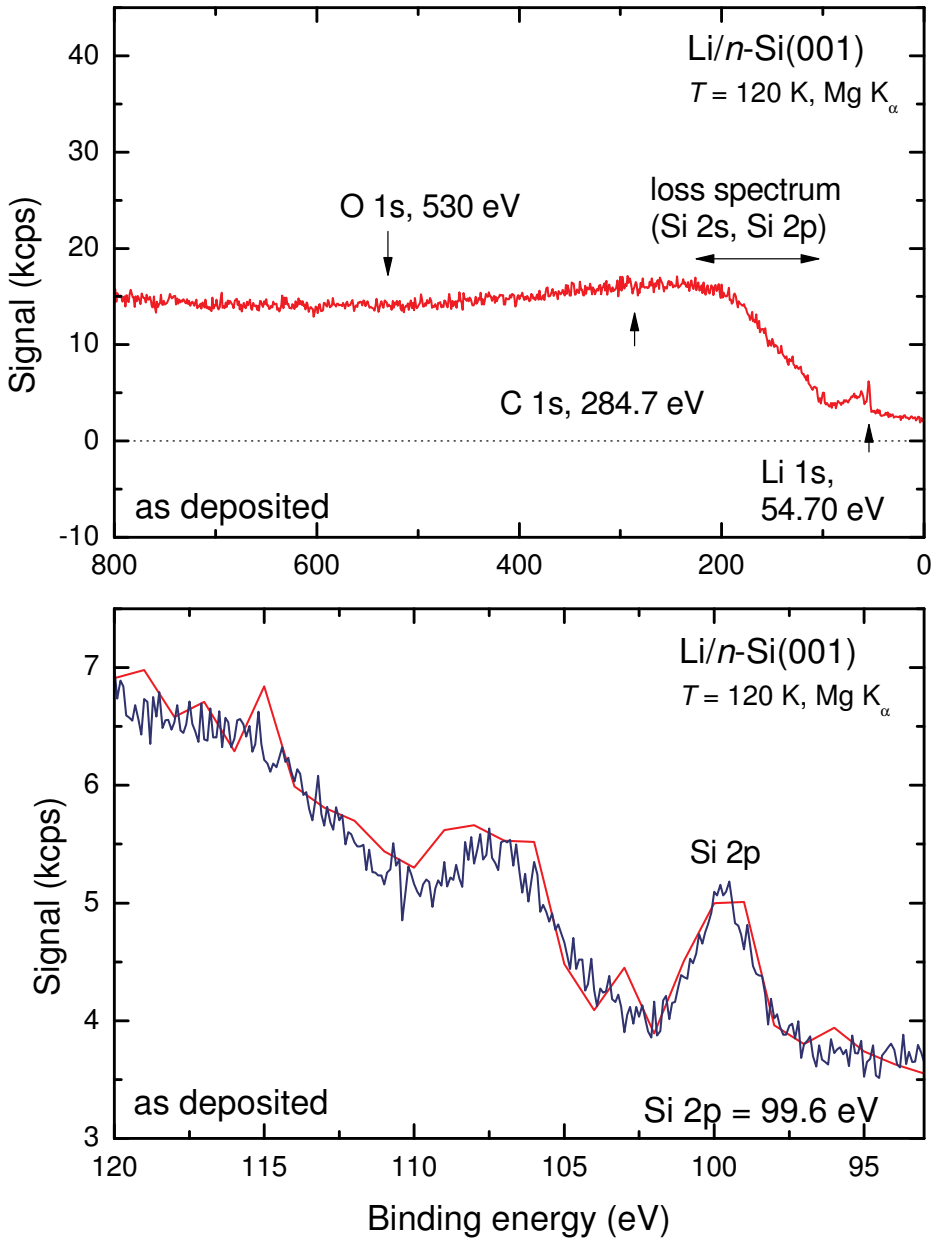

Figure 7.5.: Multi-layered Li film deposited on n-Si(001) at a temperature $T = 120\,\mathrm{K}$ - Survey spectrum. The spectrum is dominated by a broad loss feature at the position of the Si 2s and Si 2p lines.

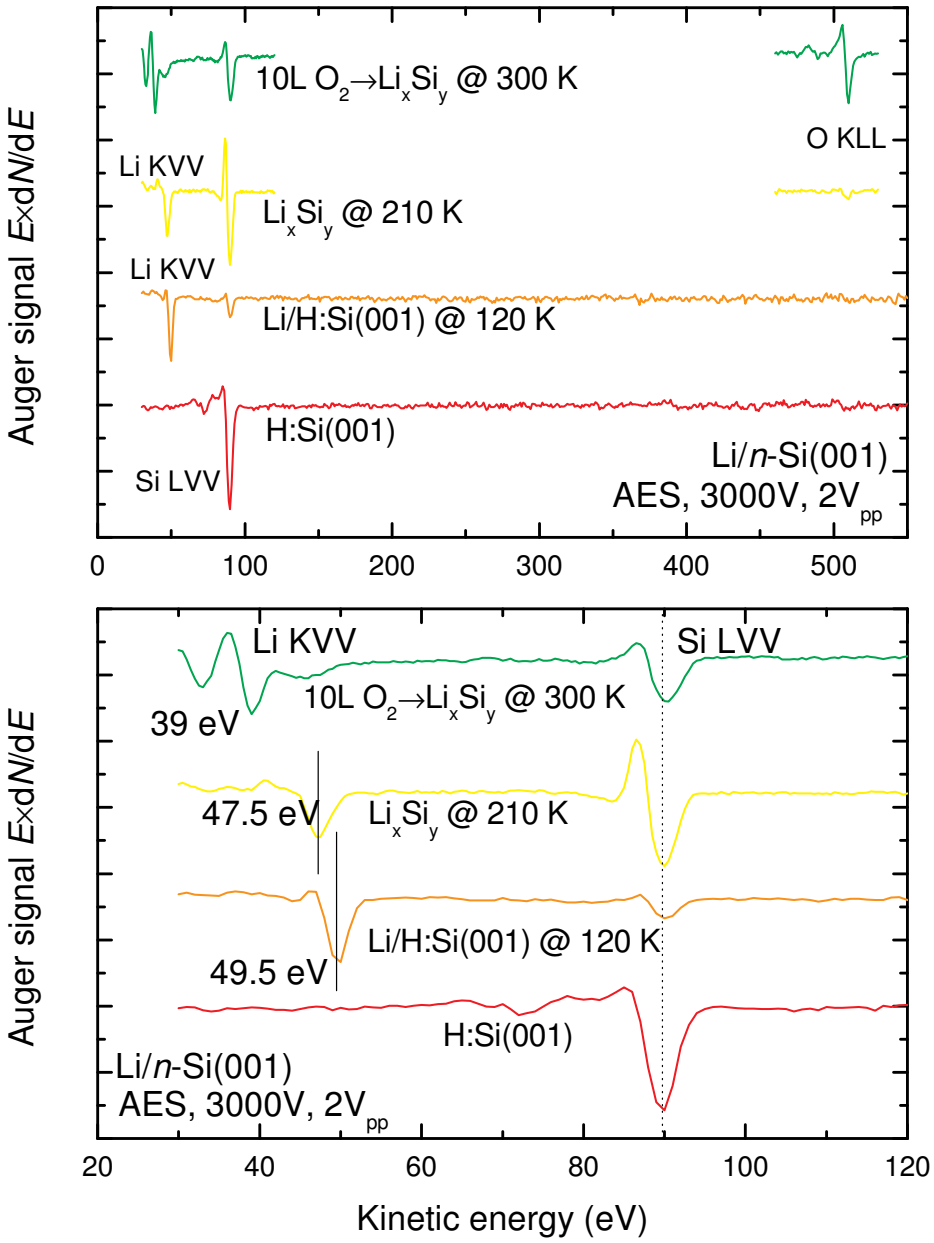

Figure 7.6.: Auger spectra at varying temperatures of an approximately three monolayer thick lithium deposit on a hydrogen passivated Si(001) surface.

ough explanation of this result has yet to be established but from its position it may be concluded that this feature is due to silicon photoelectrons undergoing losses in the lithium film on top. For this reason reliable thickness data could not be established for the lithium samples when recording XPS spectra, because the intensity decrease of the Si 2p peak cannot be determined. Oxygen and carbon contaminations were below the detection limit of XPS.

The films are stable if held at a temperature of 120 K. Spectra with higher resolution were recorded in the Si 2s and Si 2p region as shown in Fig. 7.5. Data from the same sample which were recorded earlier (10 min) in the session are included in red. The composition of the film's surface does not change during this time. Also radiation damage from the X-ray beam was neither expected nor found experimentally. Likewise the emission from the Li 1s line does not change during that time (see Fig. 7.8). The metallic character of the film can be seen from the high intensity plasmon losses starting at 7.7 eV below the primary Li 1s line [Ale71].

Lithium-Silicon Interdiffusion

Lithium readily dissolves into the bulk of silicon substrates even at cryogenic temperatures. The effect can be observed by X-ray photoemission at temperatures as low as 200 K as presented in Fig. 7.7. The blue curve shows a Li film deposited at 120 K right after transferring it into the analysis chamber, while the red line shows the same sample after it was held at 200 K for five minutes. In both curves the Si 2s, the Si 2p, and the Li 1s peak at 54.9 eV are clearly visible. But while the silicon photoemission lines are initially weak they become much more pronounced after the thermal treatment. Great care must therefore be taken to hold the temperature of the sample below 130 K at all times.

Auger spectroscopy data confirm the diffusion of lithium into the silicon substrate. Figure 7.6 compiles Auger spectra of lithium films that were deposited on a hydrogen passivated Si(001) substrate. The spectra were recorded with a primary excitation voltage of 3000 V and a peak-to-peak modulation of 2 V. The difference between the stable metallic film and the silicide film are easy to discern. The position of the Li KVV line shifts from 49.5 eV for the metallic film to 47.5 eV in the silicide, and the peak of the Si LVV line changes from an asymmetric appearance to a symmetric shape. The metallic film remains stable for hours at the deposition temperature of 120 K, even though a silicide interface has already been formed.

At higher temperatures the spectrum gradually changes to the typical lithium silicide

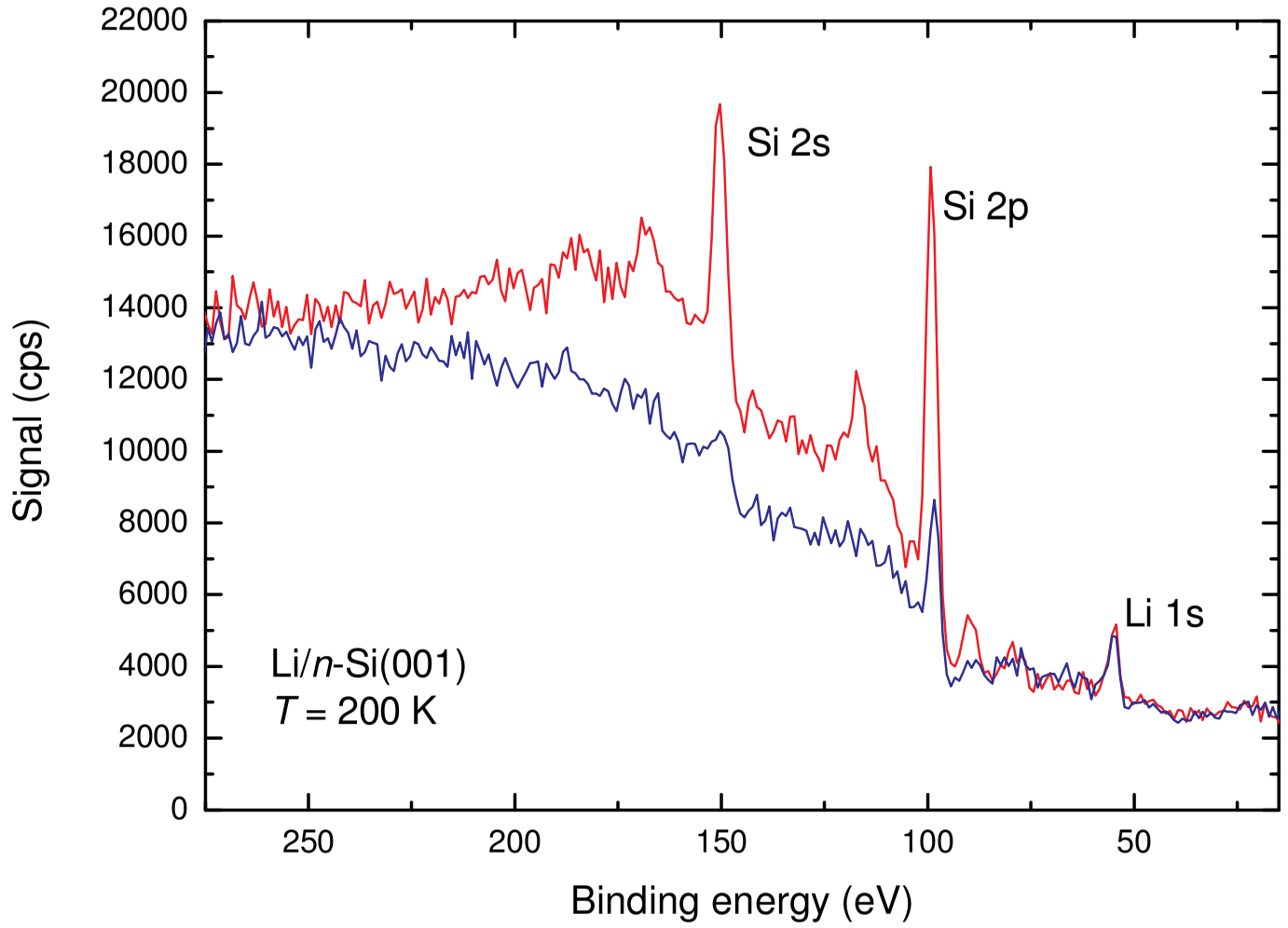

Figure 7.7.: Multi-layered Li film on n-Si(001) at an elevated temperature $T = 200$K - Photo emission spectrum of the Si 2s, Si 2p region

composition, leading to a gradual increase of the silicon peak height. The thickness of the film was approximately three monolayers, which was determined by the attenuation of the Si LVV peak through the metallic film.

Lithium Oxidation and Oxides

During the oxidation of lithium thin films mainly lithium oxide Li_2O is formed. UPS data show a single peak originating from atomic O 2p orbitals at low exposures and a subsequent development of additional features that can be attributed to molecular orbitals. Figure 7.9 shows a plot of the valence band region of a lithium film on a silicon substrate during an exposure to O_2 at a partial pressure $p(O_2) = 10^{-8}$ mbar. In the upper part of the panel UP spectra recorded with a He I light source at different exposure are shown. The lower panel shows a contour plot of the same exposure. The oxidation starts with the production of O^{2-} as in Li_2O which is eminent in the appearance of a large peak at 5.3 eV which shifts slightly toward higher binding energies with increasing exposure. The peak is caused by the ionization of the O^{2-} ion with a transition into the ^2P state of the singly charged oxygen atom. Obviously, the initial film already contained a small amount of oxygen which stems from the deposition itself.

Two additional features start to develop at higher exposures at 12 eV and around 7.9 eV. A comparison with spectra obtained for molecular alkali oxides shows that the peak at 12 eV cannot be explained by O 2p related orbitals from peroxide or superoxide ions [JDB92]. A straight forward explanation is reached if bonds between oxygen and silicon are considered: the O 2p-Si 3s,3p orbitals indicate that silicon from the substrate is also oxidized to form SiO_2 during the reaction [FPDG77, SGBF02, WOW$^+$05]. The peak at 7.9 eV can be explained as either being due to emission from non-bonding O 2p orbitals from oxygen incorporated into SiO_2 or due to emission from molecular Li_2O_2 orbitals. Both explanations are compatible with previous observations from the literature [JDB92, WOW$^+$05]. The appearance of molecular orbitals also accounts for the apparent shift in the position of the lithium oxide peak when the molecular peaks start to overlap with the emission from atomic states.

A further close-up of the valence band region around the Fermi edge during the oxidation is presented in Fig. 7.10. While data were obtained for the same oxidation experiment already shown in Fig. 7.9, they reveal the change of the lithium conduction band much better than the UP survey spectrum. Remarkably, no distinguished Fermi edge expected for a metallic surface could be observed for the as deposited films and the Li valence band does not show the expected triangular shape typical for the alkali metals

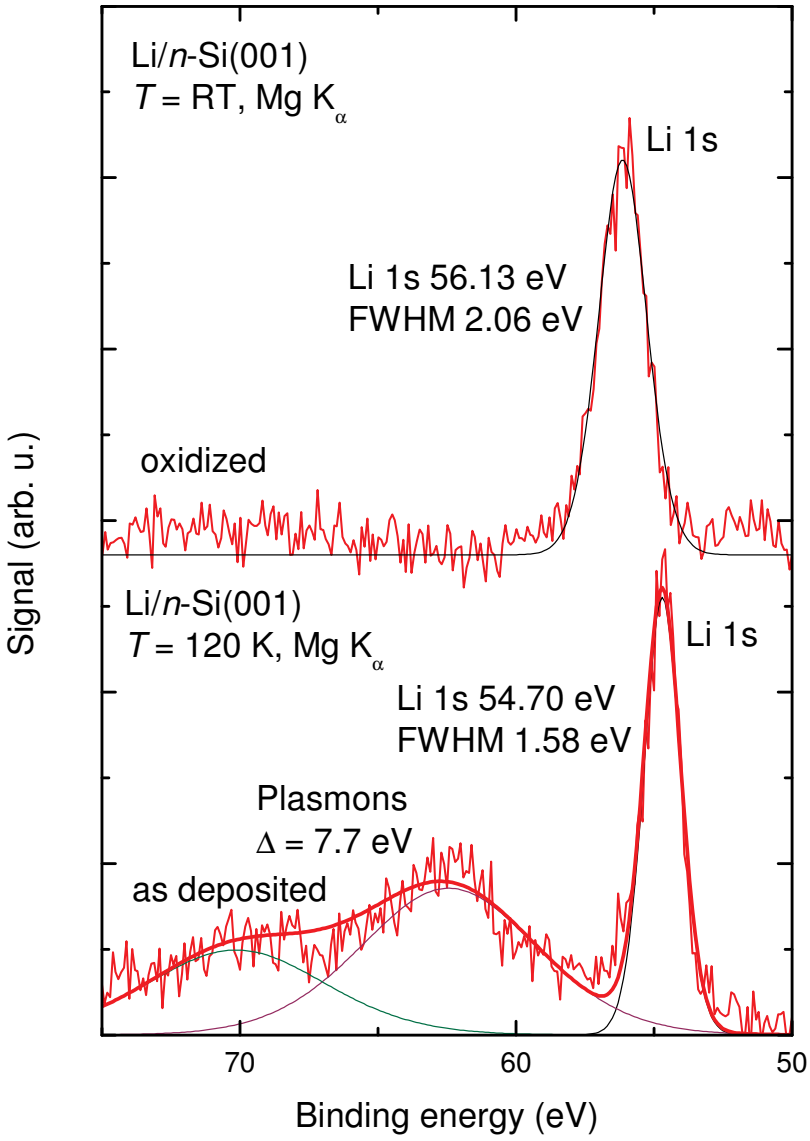

Figure 7.8.: Multi-layered Li film on n-Si(001) at a temperature $T = 120$K - Photo emission spectrum of the Li 1s region

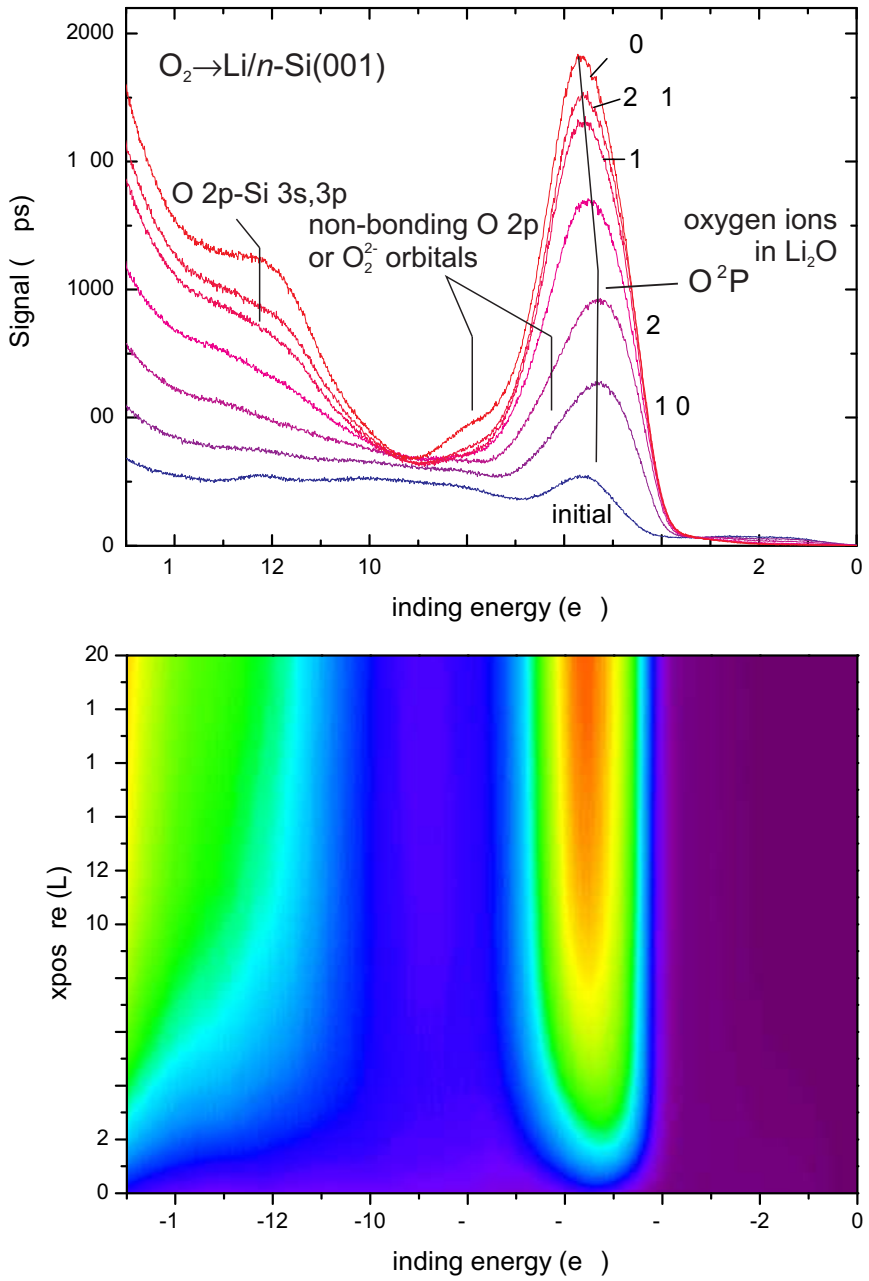

Figure 7.9.: Multi-layered Li film on n-Si(001) at a low temperature of $T = 120$K - Valence band region during oxidation at 120 K.

[KLM$^+$73]. Because of its higher surface sensitivity compared to X-ray photoemission UPS probes a few atomic layers of the film which may already be partly oxidized at the start of the experiment. A film that appears metallic in XPS may therefore appear non-metallic in UPS. For the same reason surface oxygen may be detected using UPS even if only small amounts of oxygen were visible in XPS.

Two peaks appear within the region of the Li conduction band at binding energies of 1.45 eV and 2.65 eV whose origins are not clear. Possibly, these indicate that this particular film was built up from lithium silicide which might have formed during the transfer of the sample. This would also explain the appearance of silicon oxide related peaks in the oxide spectra and the lack of a sharp Fermi edge.

After oxidation of lithium silicide at room temperature, the Li KVV peak splits into a doublet structure shifted to a kinetic energy of 39 eV (Fig. 7.6).

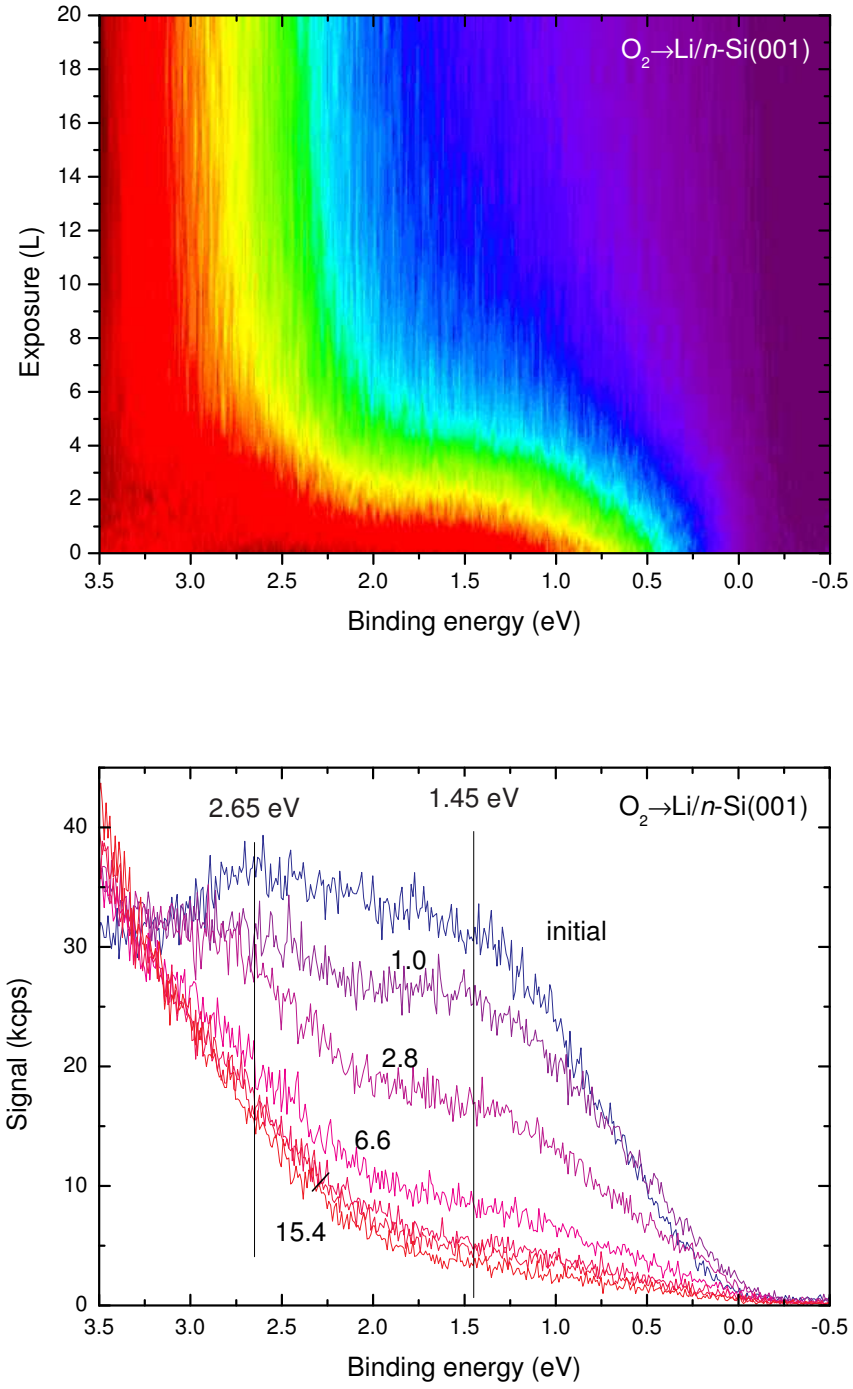

Figure 7.10.: Multi-layered Li film on n-Si(001) at a low temperature of $T = 120$K - Valence band region around the Fermi edge during oxidation at 120 K.

7.2.3. Potassium

Over the last decades, the exact mechanism underlying the oxidation of potassium in an oxygen atmosphere has been the subject of numerous studies. While some agreement has been established in the literature on the identification of the various potassium oxide species [PK77, JDB92, LSR95] little is known about the reactions kinetics during the oxide formation. In particular, the confusion in this subject is caused by the sensitivity of the reaction on the experimental conditions, especially on the temperature employed. Early studies on the subject stated that the oxidation of a cooled surface (77 K) follows a nucleation and growth mechanism [KW78] - much the same as is observed for the oxidation of magnesium [GN04]. However, due to the method of the investigation, the authors were not able to tell which kind of oxide was formed. In later studies, the growth and chemical composition of oxidized potassium layers could be clarified in more detail which revealed that molecular adsorption dominates at low oxygen pressures and proceeds in a layer-by-layer fashion [LSR95]. However, a general model for the reaction kinetics as a function of temperature is still not available.

Metallic Potassium Films

Figure 7.11 shows the photoemission in the K 2p region of a thick (multi-layered) film of potassium on n-Si(001) before and after oxygen oxidation. Non-monochromatized MgK_α radiation was used for the XPS-spectra and spectra were recorded in normal emission. The upper panel shows the as deposited film while the lower panel shows the film after exposing it to 40 L of oxygen at 120 K. The spectrum of the as deposited film shows a large loss structure due to plasmon scattering at the high binding energy side of the K 2p-doublet. This indicates the metal like electronic structure of the film which is lost during the oxidation. Hence the plasmon losses vanish for the oxidized films.

The data were fitted using a sum of multiple Voigt profiles employing a standard Levenberg-Marquard fitting routine. The spin doublet structure of the 2p peaks was reproduced by requiring a 4 : 2 ratio for the peak areas, a peak-to-peak distance of 2.80 eV and equal line widths (FWHM). Each photoemission line gives rise to multiple plasmon loss features which are reproduced for a plasmon energy of 3.4 eV. The position of the K $2p_{3/2}$ peak was found to be 294.5 eV.

After the oxidation only a slight shift of the K $2p_{3/2}$ peak toward a binding energy of 294.8 eV is observed. In contrast to the strong chemical shift observed for the O 1s line, surprisingly little information about the oxidation state, e.g., peroxide vs. atomic oxide,

can be extracted from the potassium photoemission lines.

Potassium Oxidation and Oxides

In contrast to the spectra that were obtained for thin lithium films, the O1s line in potassium is highly structured. This can be exploited to distinguish between the various oxide species appearing in the potassium film. As can be seen from the photoemission data presented in Figures 7.12 and 7.13 the O 1s line splits into three peaks. The splitting of these peaks is caused by the different oxidation states of the oxygen bound in the film and they are ordered with respect to the number of electrons residing on the oxygen atoms. The lowest binding energy peak (527.9 eV) is interpreted as a marker for dissociatively adsorbed oxygen O^{2-}. Peroxide like oxygen molecules O_2^{2-} are identified by a peak at 532.1 eV and the superoxide species O_2^- shows a peak at 534.0 eV[PK77, JDB92, LSR95]. The total oxygen uptake shown in Fig. 7.14 has been plotted as a function of exposure. Assuming an initial sticking coefficient of unity, the initial slope can be used to scale the equivalent plots for other metals which will be presented throughout this chapter.

Under the chosen conditions molecular adsorption is preferred over dissociative adsorption. Figures 7.15 and 7.16 (for higher exposures) show the intensities of the oxide (red squares), the peroxide (blue triangles) and the superoxide (purple circles) peaks as a function of oxygen exposure Φ_E. Initially, some oxygen dissociates at defect sites on the clean surface thus forming O^{2-} ions. Aside from the defect induced adsorption, oxygen is predominantly adsorbed as molecular ions. In a first step oxygen is bonded as K_2O_2 and at later stage incorporated as KO_2. The oxides grow in a layer like manner, the later oxide growing on top of the earlier oxides. Peroxide grows on top of the layer of atomic oxide. Likewise the peroxide layer becomes covered by a superoxide layer.

The peroxide intensity follows an exponential law

$$I_{\mathrm{K_2O_2}} \propto 1 - \exp\left(-\Phi_\mathrm{E}/\tau_1\right) \tag{7.2}$$

typical for Langmuirian adsorption with a rate proportional to a number of free adsorption sites. Φ_E designates the exposure. At large exposures the peroxide intensity decreases due to the afore mentioned covering of the peroxide layer with superoxide growing on top.

Because of the large intensity of the peroxide peak it seems implausible that the adsorption is restricted to a single molecular layer on top of the surface. The description

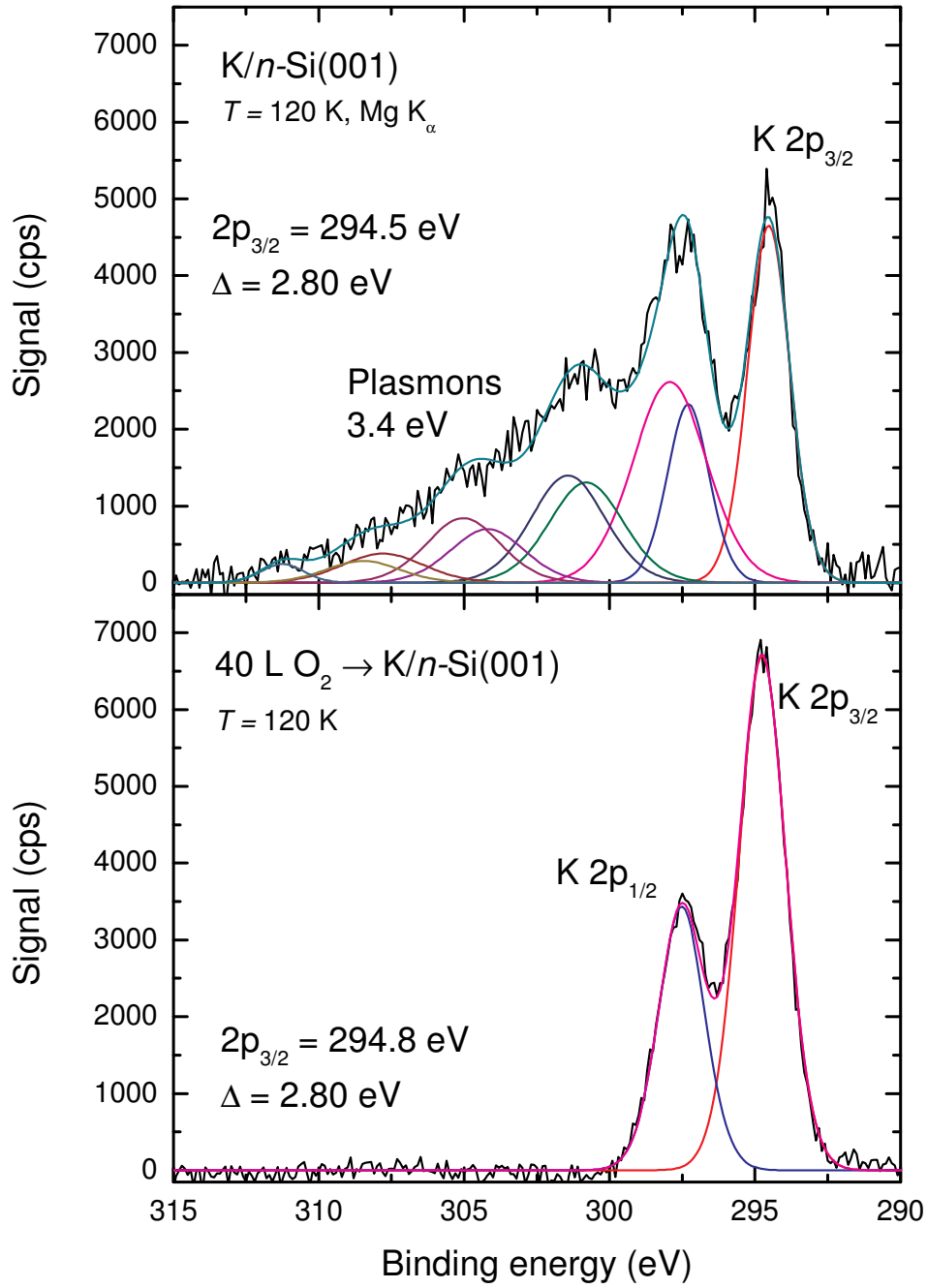

Figure 7.11.: Potassium multi-layered film deposited on n-Si(001) at 120 K - Photo emission in the region of the K 2p line before and after oxygen oxidation at 120 K.

of the molecular reaction therefore differs from simple Langmuir adsorption kinetics in the sense that the number of available reaction sites cannot be identified simply by the number of surface sites. Therefore some transport of either potassium atoms to the surface or diffusion of oxygen molecules into the bulk must be considered. In this sense the fixed number of adsorption sites required by the Langmuir model can be identified by metal atoms in a thin layer near the surface which can reach the surface through diffusion. This process must be much faster than the impinging rate to ensure that the concentration of potassium atoms is constant within this layer and that it remains in thermal equilibrium with the surface.

In contrast, the superoxide growth must be described by a square root law

$$I_{\mathrm{KO_2}} \propto \sqrt{\Phi_{\mathrm{E}}} \tag{7.3}$$

which is observed for diffusion limited processes. Potassium diffuses through an already existing oxide layer and reacts either with oxygen from the gas phase or oxygen already physisorbed on the surface. A detailed discussion of the model, its implications and a derivation of (7.3) can be found in Appendix A.

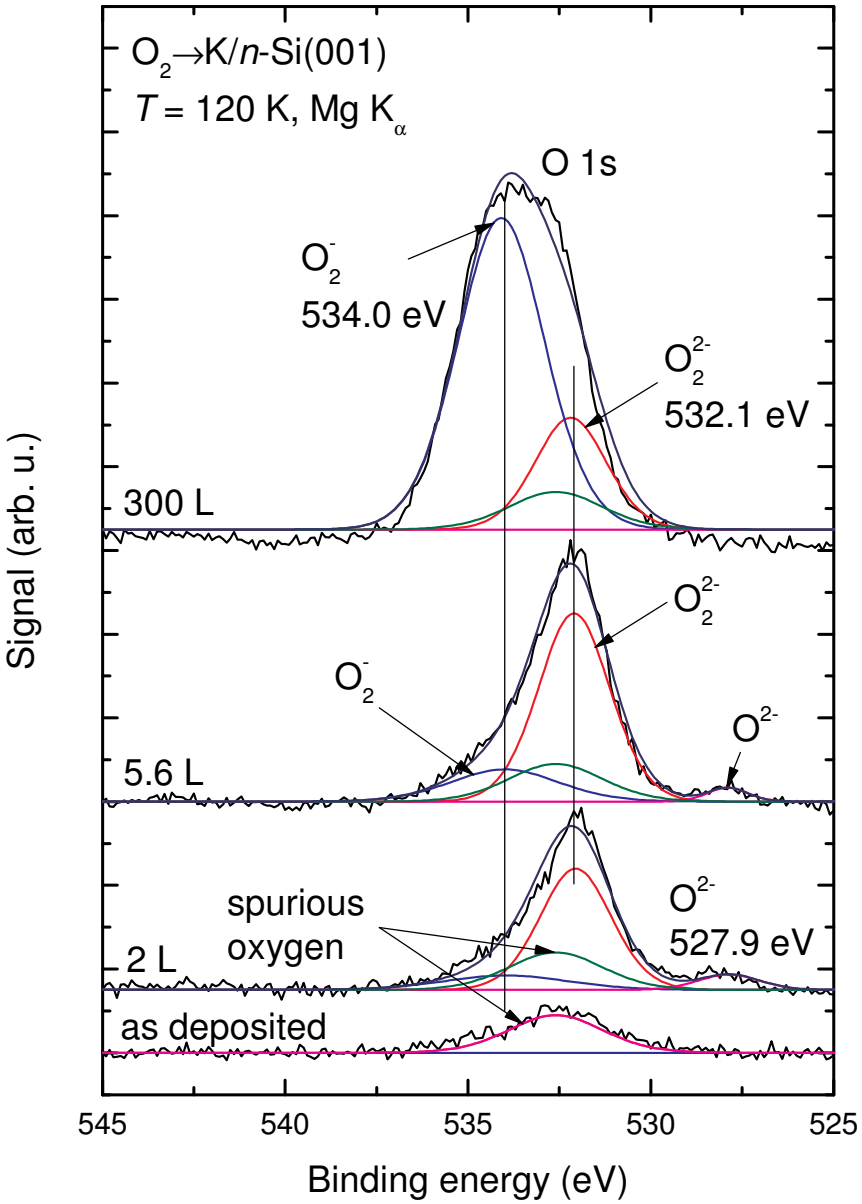

Figure 7.12.: Potassium multi-layered film deposited on n-Si(001) at 120 K - Photo emission in the region of the O 1s line during the oxygen oxidation at 120 K.

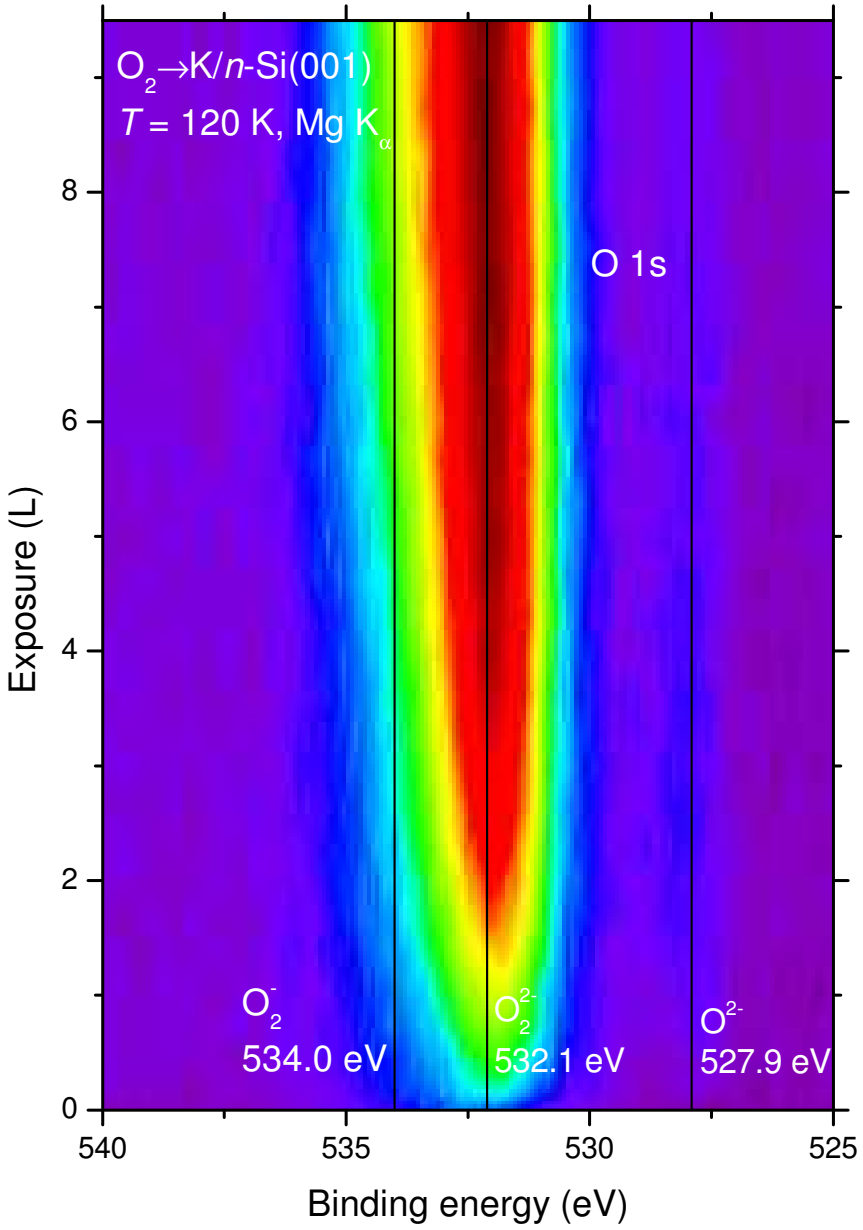

Figure 7.13.: Potassium multi-layered film deposited on n-Si(001) at 120 K - Photo emission in the region of the O 1s line during the oxygen oxidation at 120 K.

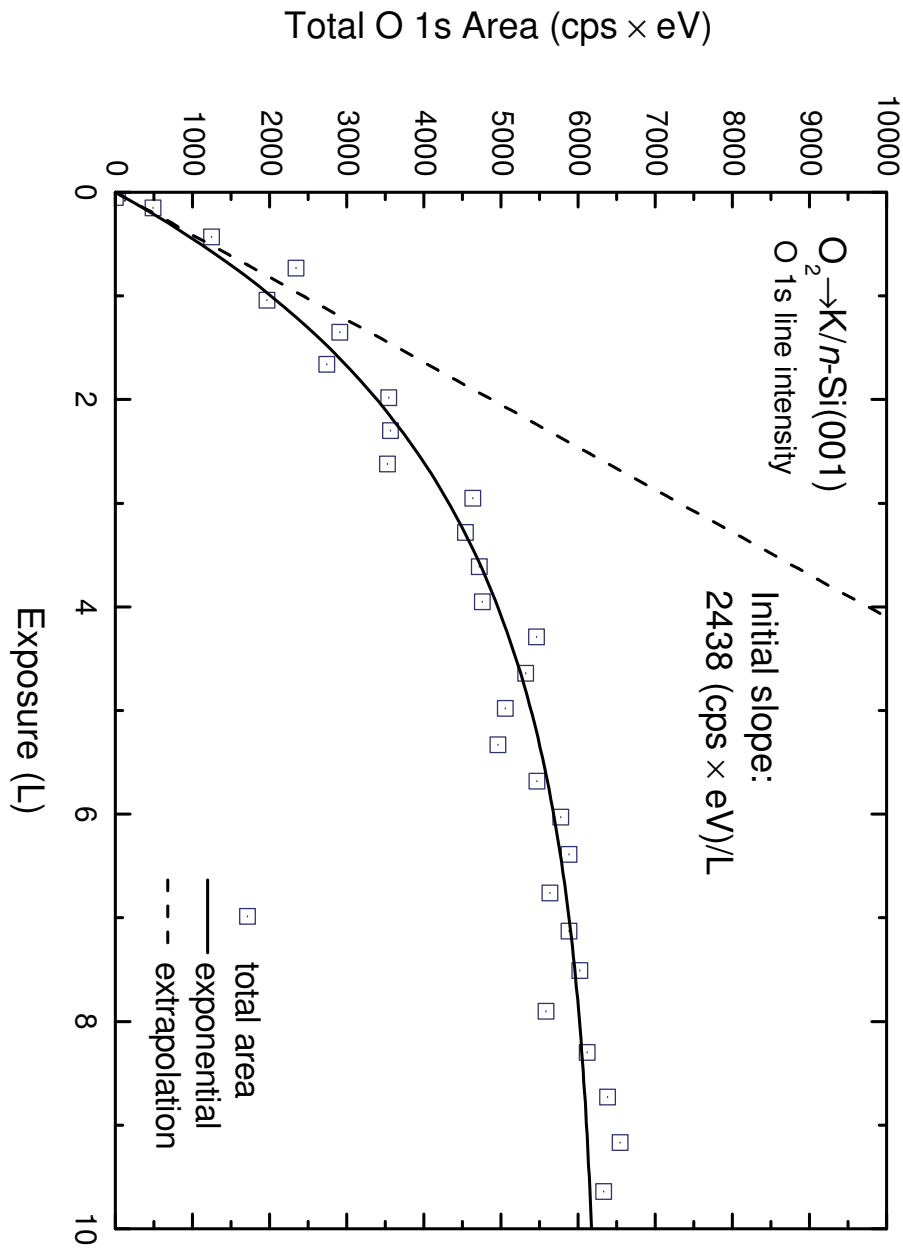

Figure 7.14.: Potassium multi-layered film deposited on n-Si(001) at 120 K - Increase of the O 1s line intensity during the oxygen oxidation at 120 K.

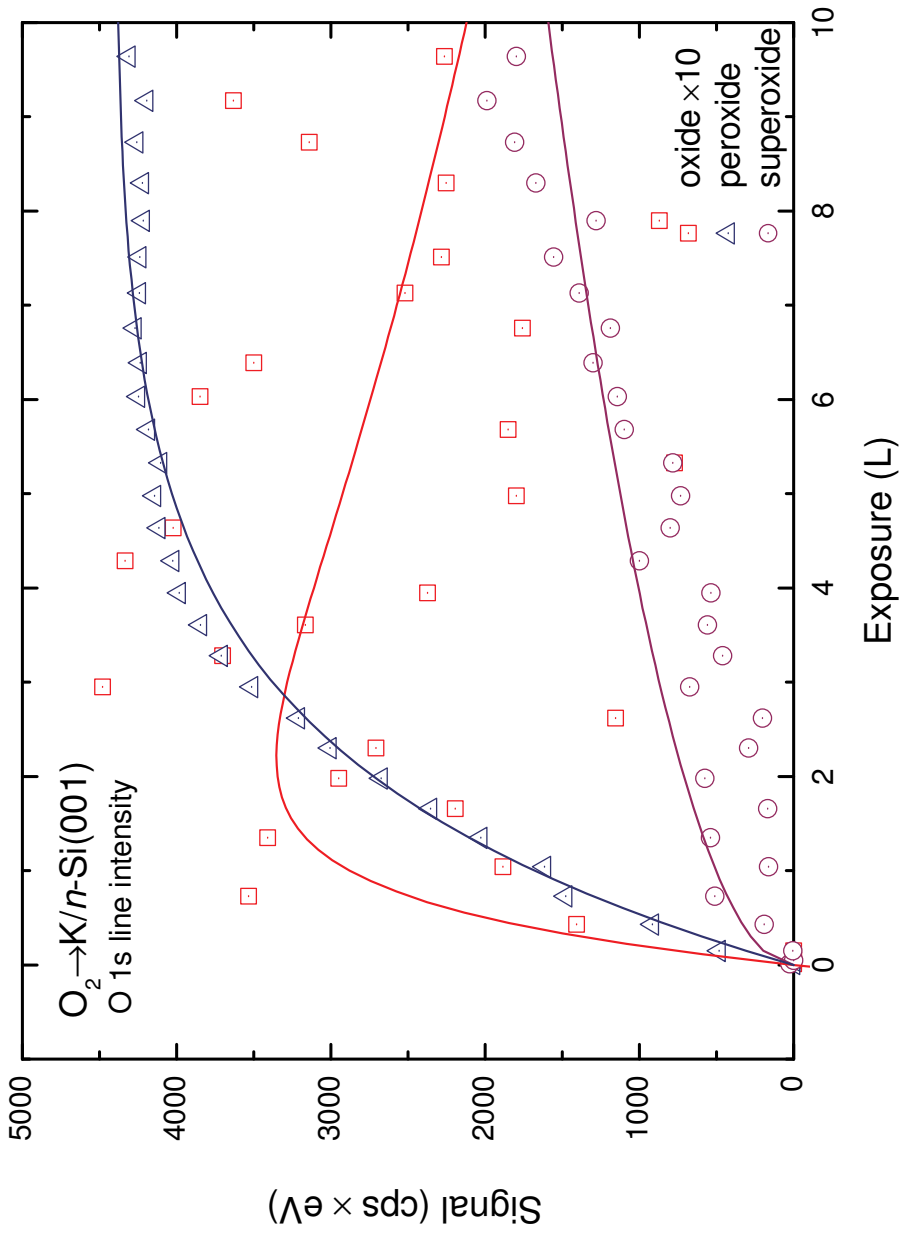

Figure 7.15.: Potassium multi-layered film deposited on n-Si(001) at 120 K - Increase of the O 1s line intensity during the oxygen oxidation at 120 K.

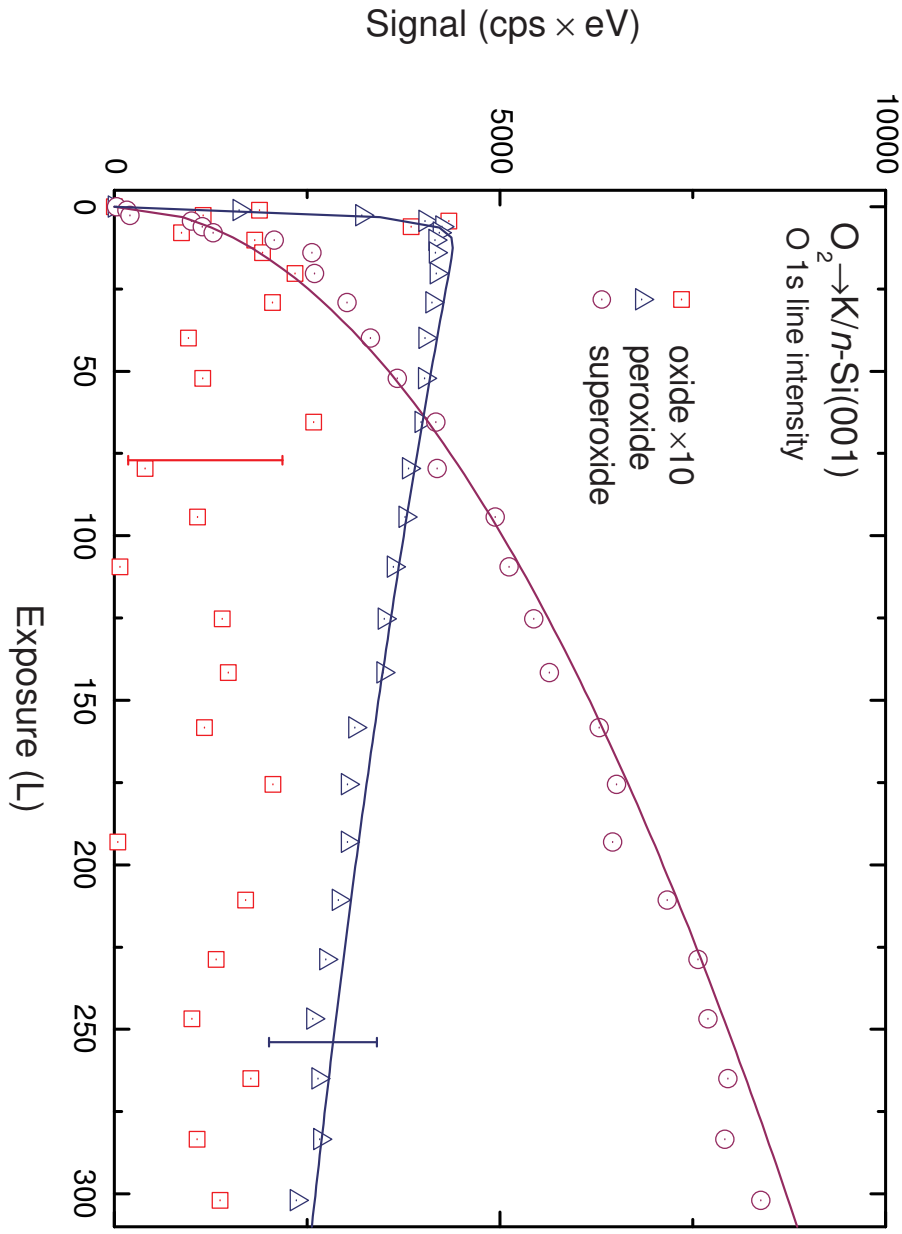

Figure 7.16.: Potassium multi-layered film deposited on n-Si(001) at 120 K - Increase of the O 1s line intensity during the oxygen oxidation at 120 K.

Valence Band Spectroscopy

The UPS valence band spectrum using a He I light source shown in Fig. 7.17 is dominated by O 2p related peaks which can be identified as molecular orbitals. Oxygen was adsorbed on a thick layer of potassium at a temperature of 120 K. The results compare well with the findings of Petersson and Karlsson [PK77] and with the interpretation of Jupille *et al.* [KNW$^+$73, JDB92]. For the initial deposit, the M_3VV Auger peak at 3.9 eV (corresponding to a kinetic energy of 17.3 eV) and valence band plasmon losses at 7.2 eV and around 11 eV are visible. The K 3s valence band itself has a much lower intensity and will be discussed separately (see Fig. 7.19).

At very low coverages some oxygen is presumably adsorbed as a O^{2-} species. The feature corresponding to the O ^{2}P state is found at a binding energy of 2.7 eV, which is in agreement with the low intensity 527.9 eV peak seen in the XPS spectra. During the next phase, two peaks which relate to the $O_2^-\,{}^2\Sigma_u^+$, the $O_2^-\,{}^2\Pi_u$ and the $O_2^-\,{}^2\Pi_g$ final states appear. While the transition into the $O_2^-\,X^2\Pi_g$ ground state can be clearly resolved, the $O_2^-\,{}^2\Sigma_u^+$ and the $O_2^-\,{}^2\Pi_u$ could not be resolved as single peaks. They rather appear as one broad peak because of their overlap with features related to the ionization of superoxide ions, i.e., transitions into O_2 states. For the same reason the position of these peaks can not be accurately determined here. The relative distances between the peaks given by Krauss *et al.* [KNW$^+$73] for an O-O bond length of 1.59 Å were used to describe the spectrum in agreement with the interpretation of Jupille *et al.*. Given the uncertainties in the measurement as well as in the theoretical values assigning the weakly visible peak at 8 eV to the $O_2^-\,{}^2\Sigma_u^+$ final state transition seems also possible.

The increasing oxygen coverage leads to a transition from a peroxide dominated spectrum to a spectrum typical for superoxide adsorption. The high energy structure around 2.7 eV vanishes and a new peak at a binding energy of 11 eV appears. In the literature, the high energy peak is explained by excitations into the nearly degenerate $O_2\,{}^3\Sigma_u^-$ and $O_2\,{}^3\Pi_g$ and the $O_2\,{}^1\Sigma_u^-$, $O_2\,{}^3\Delta_u$ and $O_2\,{}^3\Sigma_u^+$ states. Again, the distances between these states as shown in Fig. 7.17 are equivalent to the vertical separations between these states calculated by Saxon *et al.* for the free molecule at a binding distance of 1.37 Å [SL77, JDB92]. The structure formerly assigned to the $O_2^-\,{}^2\Pi_u$ excitation grows further in size because of an overlap between peroxide excitations and excitations into the $O_2\,{}^1\Sigma_u^+$, $O_2\,{}^1\Delta_g$ and $O_2\,X^3\Sigma_g^-$ final states of the ionized superoxide ion[1].

A close up of the valence band in the region of the Fermi edge is given in Fig. 7.18. The

[1]These are the lowest lying states singlet and triplet states of the neutral oxygen molecule. The $O_2\,X^3\Sigma_g^-$ is the ground state of the free molecule.

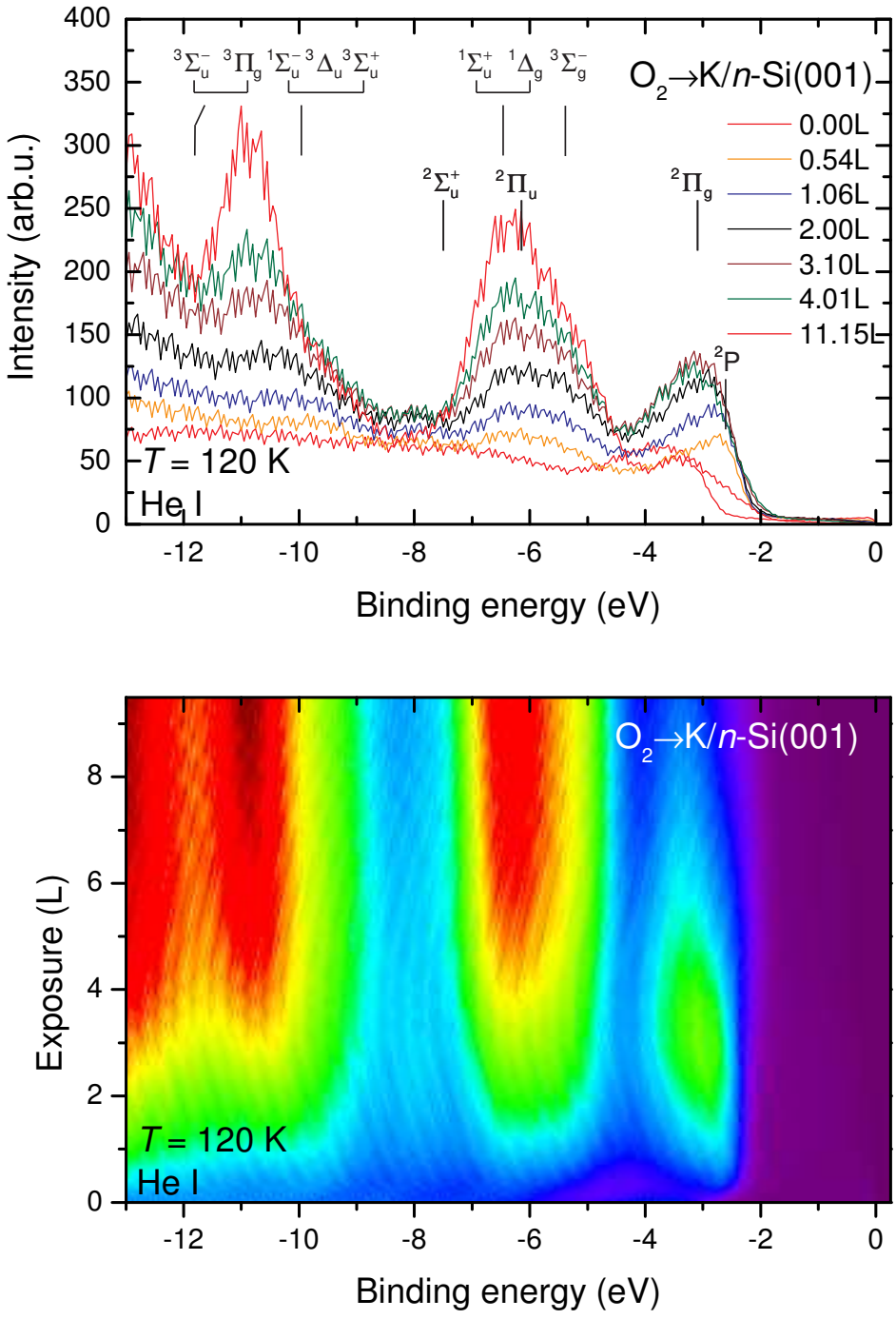

Figure 7.17.: Multi-layered K film on n-Si(001) at low temperature $T = 120$K - Valence band region and emission from O 2p related levels during oxidation at 120 K.

photoemission of the clean surface is dominated by a narrow conduction band. During the oxidation the intensity near the Fermi edge (see Fig. 7.19) decreases exponentially as free electrons of the metal are bound into the oxide. For low to moderate oxygen exposures additional peaks located within the conduction band become visible. They can be attributed to metastable molecular species bound in a metallic environment. Their binding energy is lessened compared to the bulk oxides discussed above because of the missing Madelung energy that stabilizes the oxides in their bulk environment.

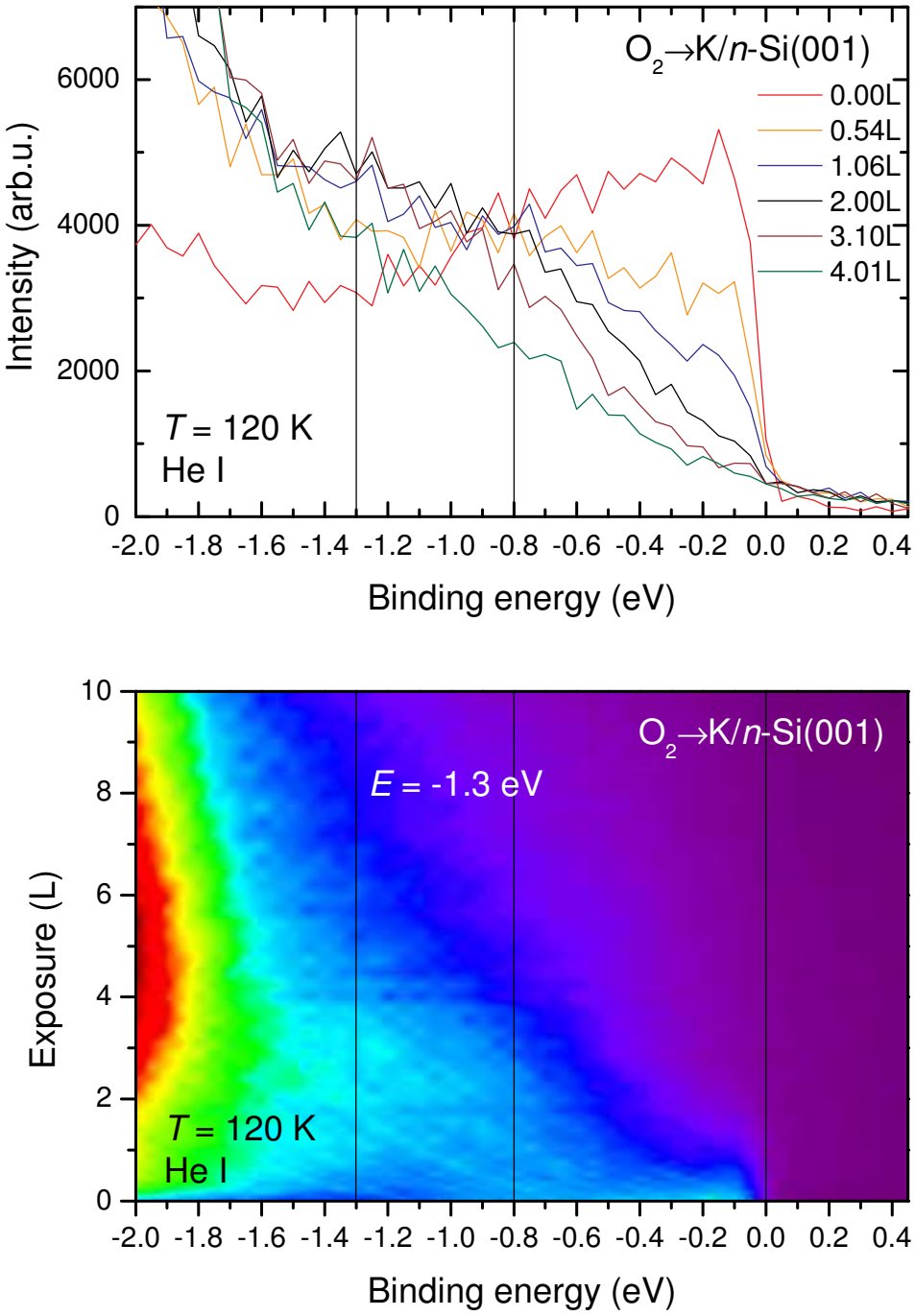

Figure 7.18.: Multi-layered K film on n-Si(001) at low temperature $T = 120$K - Valence band region near the Fermi edge during oxidation at 120 K.

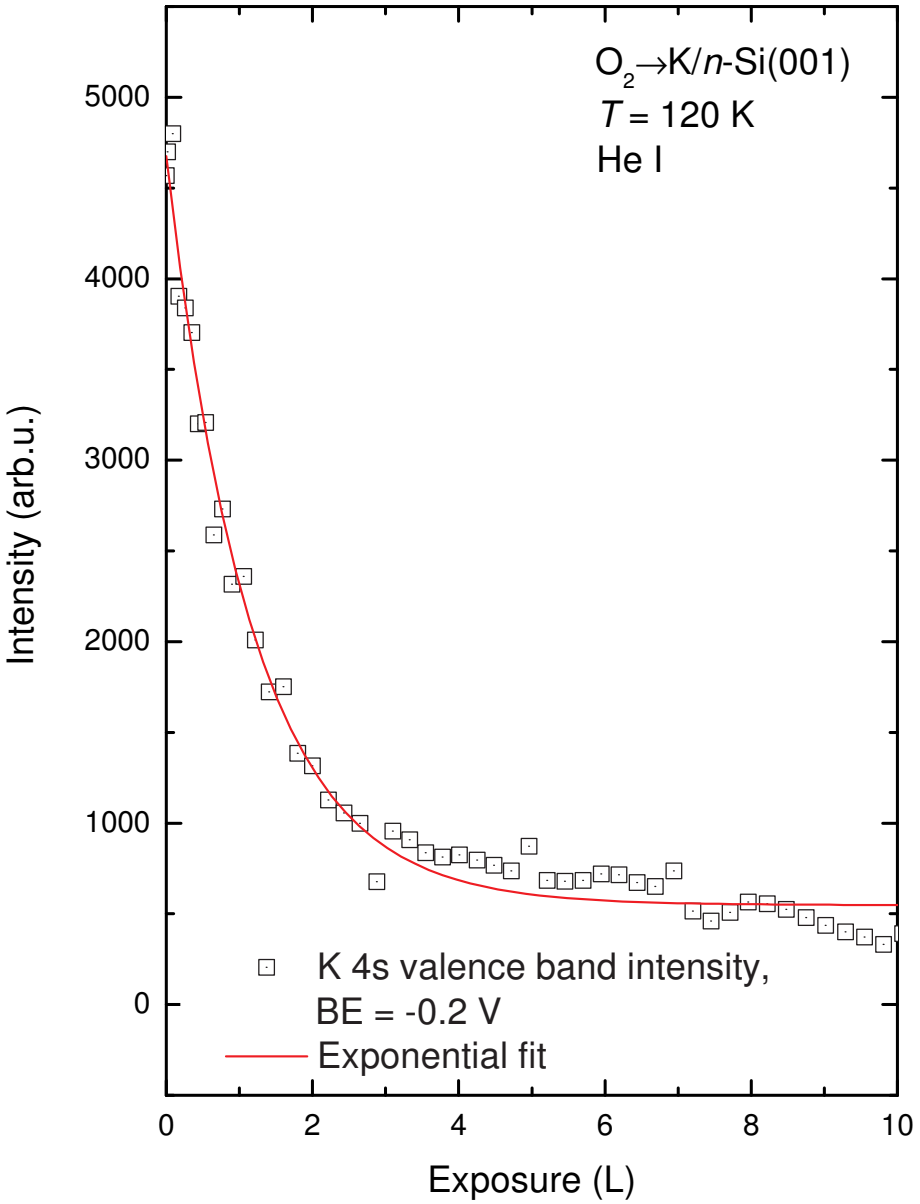

Figure 7.19.: Multi-layered K film on n-Si(001) at low temperature $T = 120$K - Valence band depletion near the Fermi edge during oxidation at 120 K.

7.2.4. Sodium

Sodium can be deposited on silicon at low temperatures around 120 K to form thick bulk like layers. Like in the case of potassium, two oxide species form during the oxidation of sodium films when they are exposed to low pressure oxygen at a temperature of 120 K. The oxide films comprise a mixture of atomic oxide, which forms through the dissociation of oxygen molecules, and of molecularly adsorbed oxygen, which is present in a peroxide state.

The O 1s spectra shown in Fig. 7.20 and Fig. 7.21 show clearly distinguishable peaks at 529.2 eV and at 533.0 eV which are signatures of the regular and the peroxide. In Figure 7.23 the total oxygen uptake has been plotted as a function of exposure. Apparently, both peaks shift toward higher binding energies of the oxygen covered surface which may be a sign for a higher binding energy for the bulk oxides vs. oxides that are adsorbed at the surface. The much narrower line width of the atomic oxygen feature, ≈ 1.5 eV vs. a FWHM of ≈ 2.5 eV for the peroxide, could lead to the wrong impression that the early stages of the oxidation might be dominated by dissociative adsorption. This is not true as can be seen from the area integrated intensity which has been plotted in Fig. 7.22 as a function of oxygen exposure. Indeed, the initial reaction rate for both processes is approximately the same. The dissociative reaction rate is constant up to an exposure of approximately 5 L where it abruptly turns to zero. Afterward the atomic oxygen signal becomes attenuated by the peroxide layer growing on top of it. The molecular signal shows a smoothly curved intensity which approximately follows a first order exponential decay of the reaction rate.

Dissociative adsorption occurs only on the metallic surface and is a spontaneous process which does not require the diffusion of sodium atoms to the surface. Its constant reaction rate is puzzling because it implies that the concentration of the metallic reaction partner does not play a role in the reaction kinetics. The peroxide reaction on the other hand seems to follow regular Langmuir adsorption kinetics in a process similar to the potassium films.

It is peculiar that no superoxide species was observed on sodium films in these experiments as reports of such a species exist in the literature [BNRS89, BGG$^+$93]. Whether this is due to an insufficiently long exposure, which would imply that sodium superoxide would be observable at this temperature, or whether sodium superoxide is thermodynamically unfavorable at this temperature cannot be told from these data. A final answer to this problem can only be found through additional measurement, preferentially using a molecular beam setup which allows a better control of the gas flux.

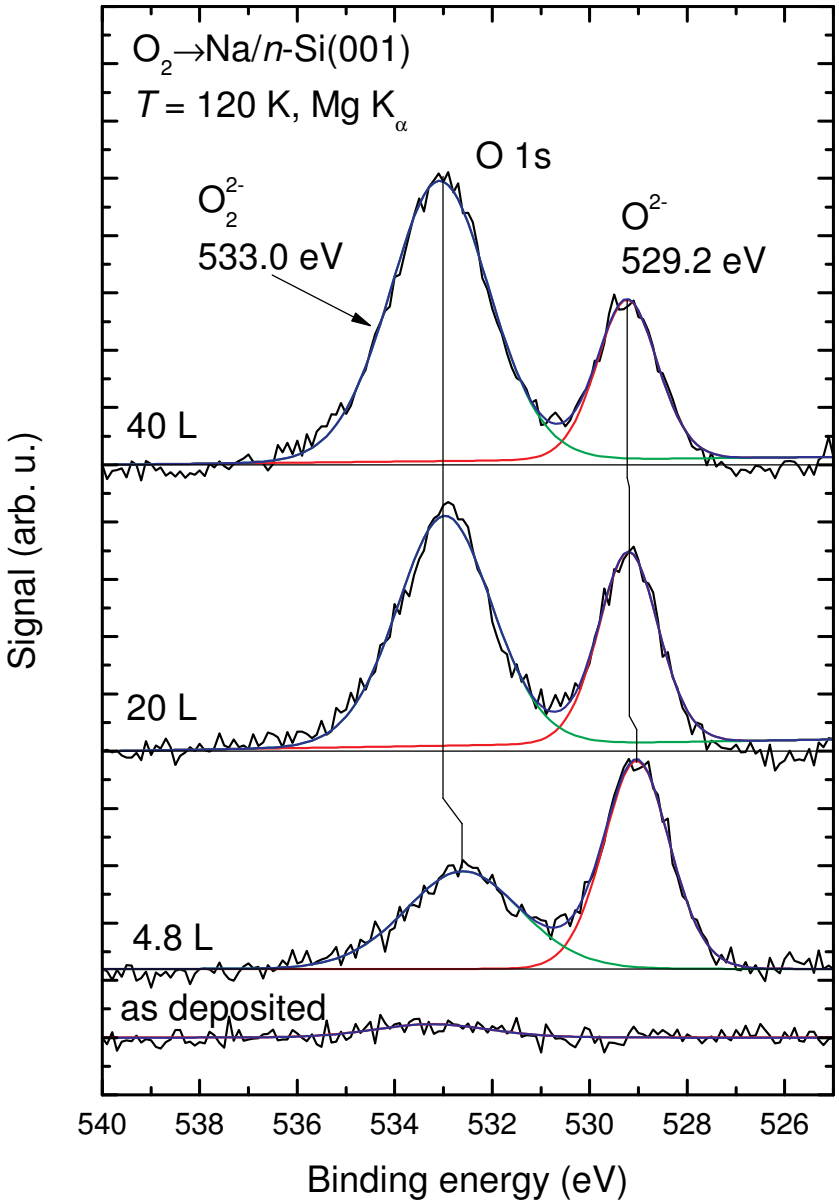

Figure 7.20.: Sodium multi-layered film deposited on n-Si(001) at 120 K - Photo emission in the region of the O 1s line during the oxygen oxidation at 120 K.

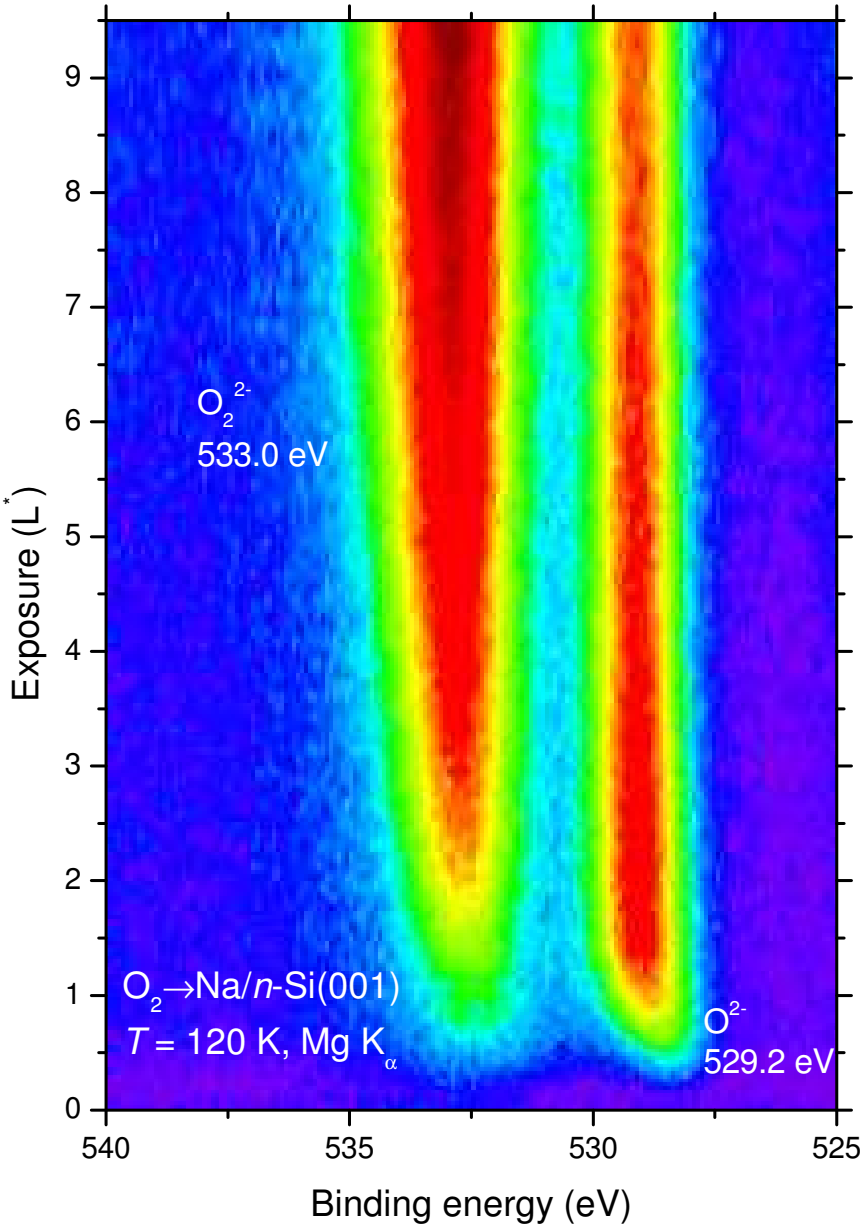

Figure 7.21.: Sodium multi-layered film deposited on n-Si(001) at 120 K - Photo emission in the region of the O 1s line during the oxygen oxidation at 120 K.

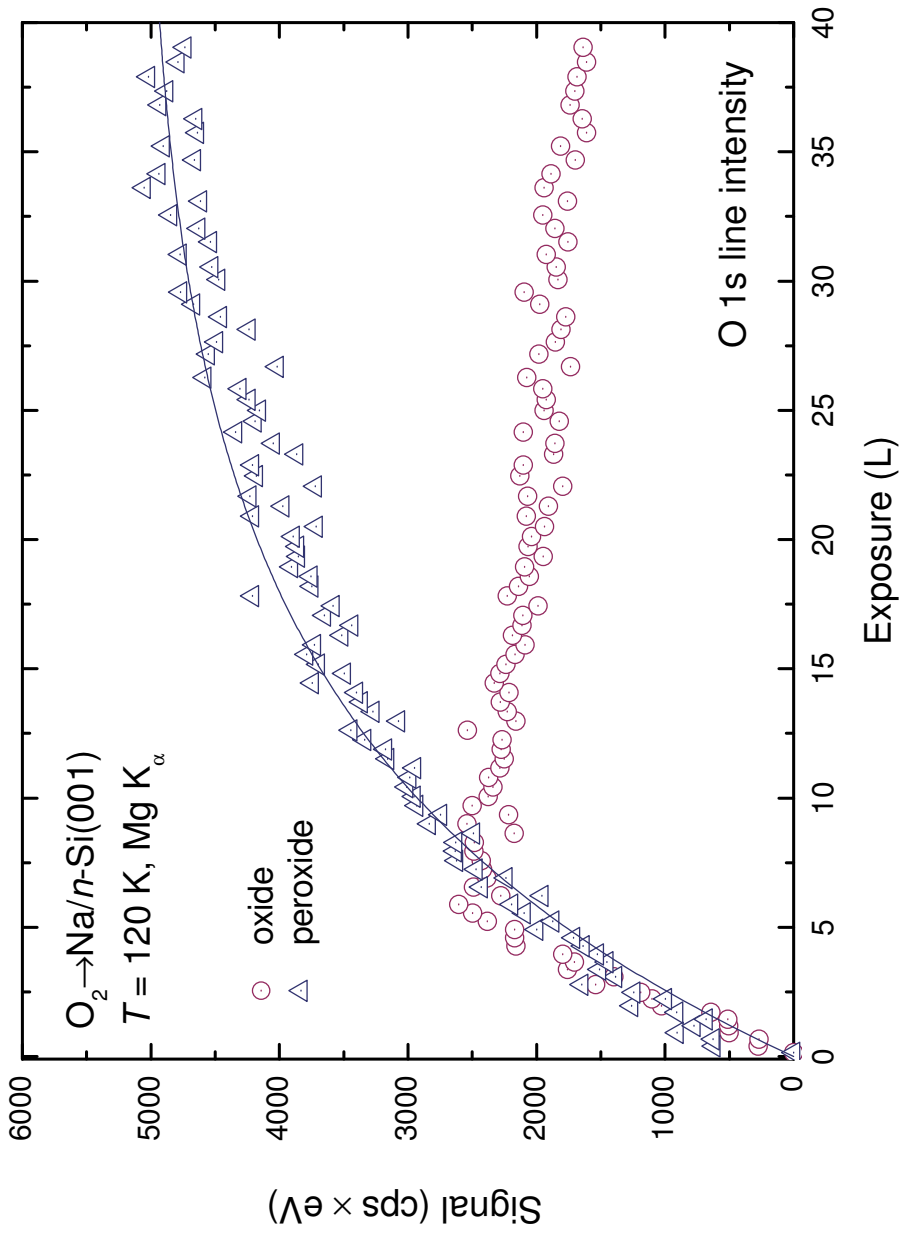

Figure 7.22.: Sodium multi-layered film deposited on n-Si(001) at 120 K - Intensity of the O 1s transition during the oxygen oxidation at 120 K.

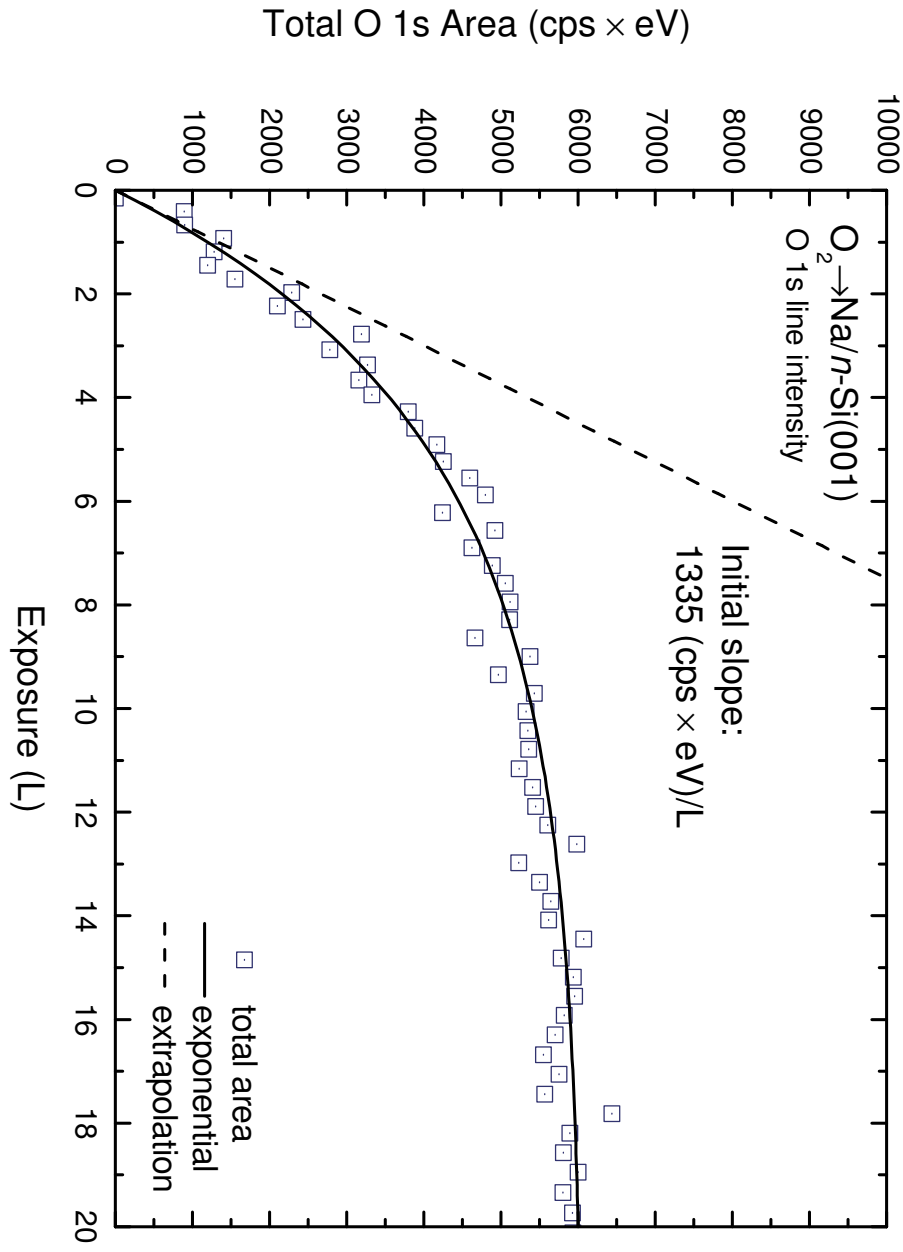

Figure 7.23.: Sodium multi-layered film deposited on *n*-Si(001) at 120 K - Intensity of the O 1s transition during the oxygen oxidation at 120 K.

7.2.5. Rubidium

X-ray photoemission spectra of the Rb 3d line before and after the oxidation are shown in Fig. 7.24. A thick layer of rubidium of approximately 10 ML was deposited on an *n*-Si(001) substrate at a temperature of 120 K. After subtracting a linear background the Rb $3d_{5/2}$ peak position was found at a binding energy of 111.5 eV for the as deposited film. The metallic nature of the film can be deduced from the strong plasmonic loss structure of the as deposited film. Although the loss peaks are too broad to determine the plasmon energy from this measurement the spectra are well reproduced by multiple bulk plasmon losses using the literature value of 3.3 eV [MSSB95, FBG$^+$94].

After oxidizing the film the Rb $3d_{5/2}$ line shifts slightly toward a lower binding energy of 111.2 eV which is in accordance with the general trend of this line in rubidium compounds [MSSB95]. In favor of an increasing intensity of the primary photoemission lines the intensity of the plasmon losses is drastically reduced and vanishes for a completely oxidized film. Instead and in addition to the photoemission lines, a small feature from shake-up processes appears in the spectra.

The development of the O 1s line was monitored while the film was exposed to molecular oxygen. Figure 7.25 shows the region of the XP spectrum containing the O 1s line for exposures of 5 L and 10 L. While it was not possible to determine the reaction kinetics from the data, four oxygen components are visible for all exposures. The regular oxide, peroxide and superoxide peaks are found at binding energies of 527.7 eV, 531.5 eV and 535.0 eV. In addition, a fourth component can be observed that shows up as a shoulder at the high binding energy (533.0 eV) side of the peroxide peak. Similar components have been observed regularly for potassium as well as cesium layers [LSR95, SLC$^+$83] and are commonly interpreted as originating from a sesquoxide species M_2O_3.

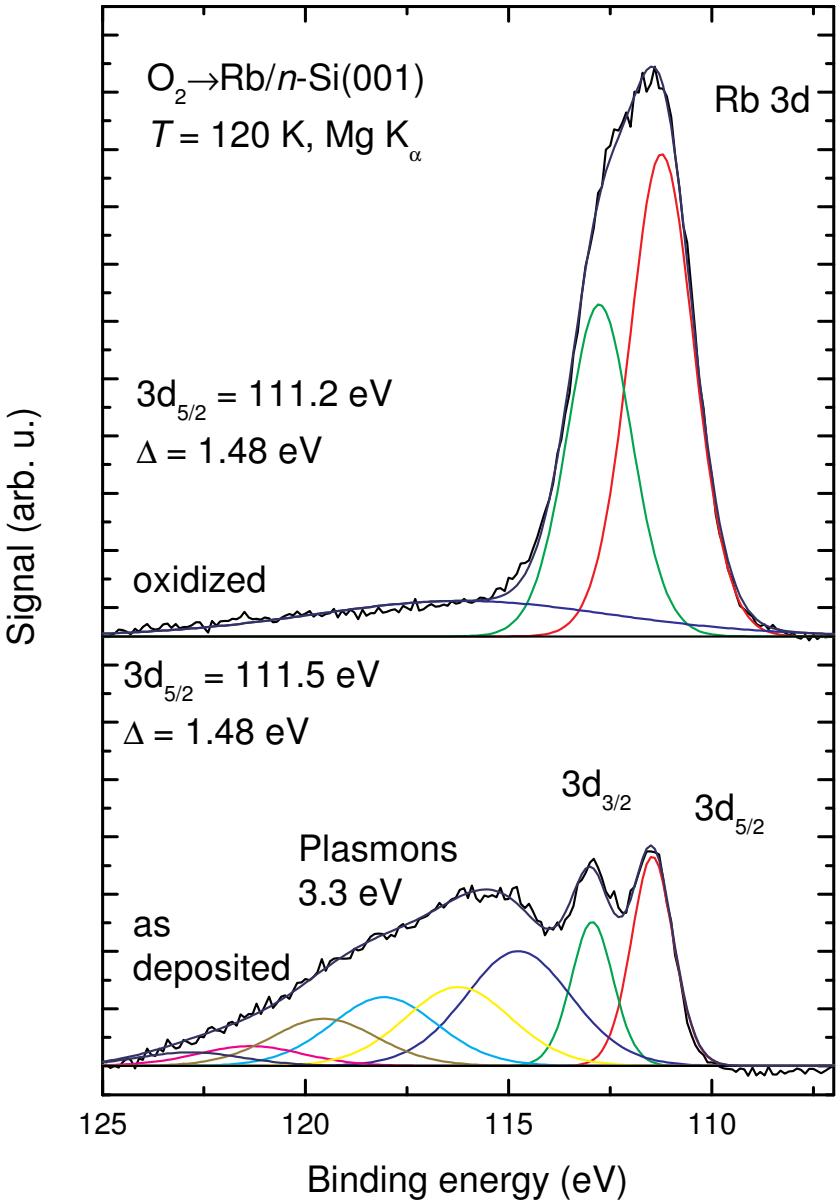

Figure 7.24.: Rubidium multi-layered film deposited on n-Si(001) at 120 K - Photo emission in the region of the Rb 3d line during the oxygen oxidation at 120 K.

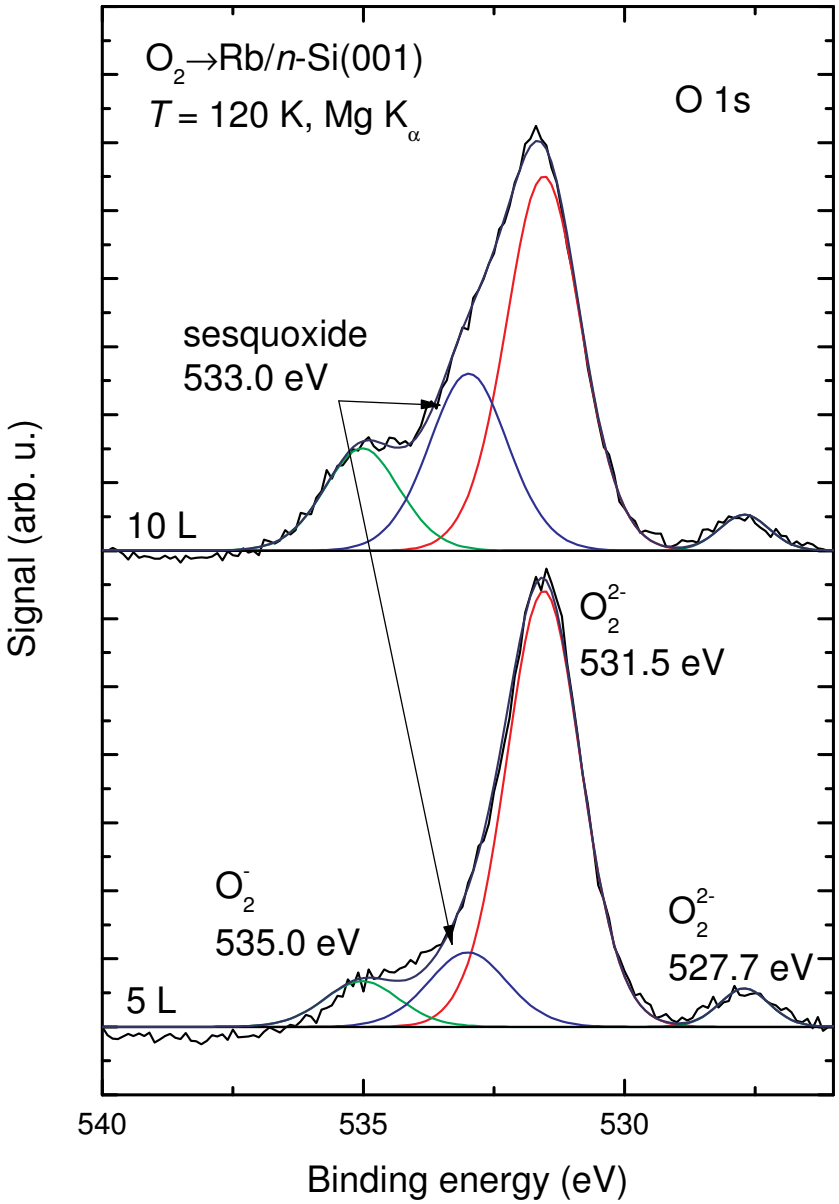

Figure 7.25.: Rubidium multi-layered film deposited on n-Si(001) at 120 K - Photo emission in the region of the O 1s line before and after oxidizing the film at 120 K.

7.2.6. Cesium

Layers of cesium were deposited on an *n*-Si(001) substrate in the thickness range of 10 ML as was determined by the attenuation of the Si 2p core level emission. The films were deposited on the cooled sample surface at 120 K. From the large contribution of plasmon losses to the photoemission in the Cs 3d shown in the lower panel of Fig. 7.26 the metallic nature of the surface is obvious. The location of the Cs $3d_{3/2}$ and the Cs $3d_{5/2}$ were found to agree with the literature values of 726.4 eV and 740.4 eV for bulk cesium and the data were fitted after subtraction of a linear background using Voigt profiles assuming multiple plasmon losses with the bulk plasmon energy of 2.3 eV [MSSB95].

On oxidation the film looses its metallicity and the intensity of the primary photoemission lines increases as the plasmon losses vanish. A shift toward lower binding energy in accordance with the observations made for rubidium is also seen for the Cs 3d photoemission lines.

The region around the O 1s line shown in Fig. 7.27 is highly structured showing contributions from three different oxygen species. The assignment is straightforward and follows the lines of the other alkali metals. An atomic oxide species is found at 527.7 eV, the peroxide and superoxide lines are seen at 531.2 eV and 533.8 eV. Reports of additional oxide species can be found in the literature but could not be observed under the experimental conditions of this study. The total oxygen uptake has been plotted in Fig. 7.29.

Figure 7.28 shows the intensity of the different oxide peaks as a function of oxygen exposure. The red squares, the purple circles and the blue triangles mark the absolute peak area of the regular oxide, the superoxide and the peroxide peak. The superoxide and regular oxide signal have been scaled by an appropriate factor to facilitate the comparison between the differing reaction kinetics. The black line is an exponential fit to the peroxide data. At the conditions of the experiment most of the oxygen is incorporated in a peroxide phase with some superoxide contributions. The fraction of superoxide with respect to the peroxide content in the film remains constant over the whole exposure regime, which can be seen from the normalized curves. On the other hand there is only a small contribution of regular oxide at the very beginning of the reaction up to an exposure between 2 L and 3 L where the normalized curve for the regular oxide deviates from the one for the molecular species.

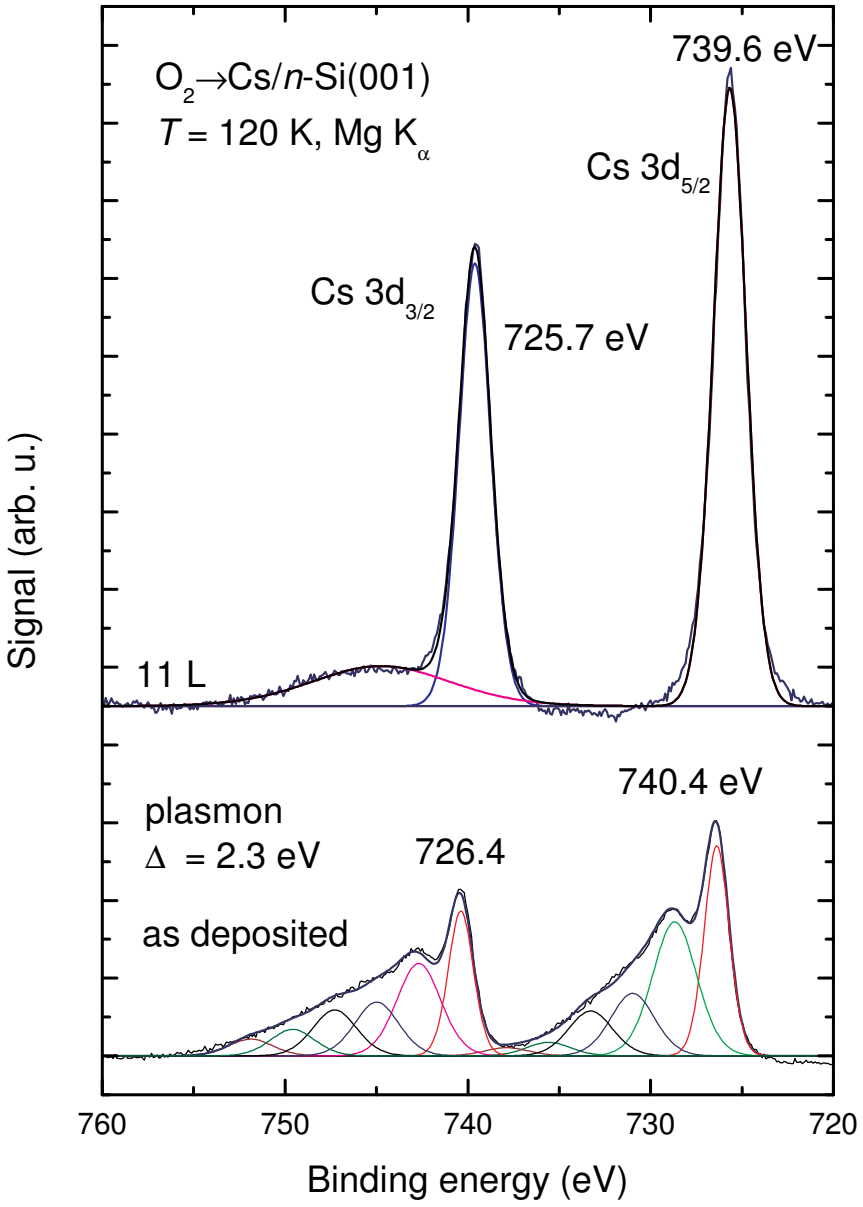

Figure 7.26.: Cesium film deposited of ≈ 10 ML thickness on n-Si(001) at 120 K - Photo emission in the region of the Cs 3d doublet before and after oxygen oxidation at 120 K.

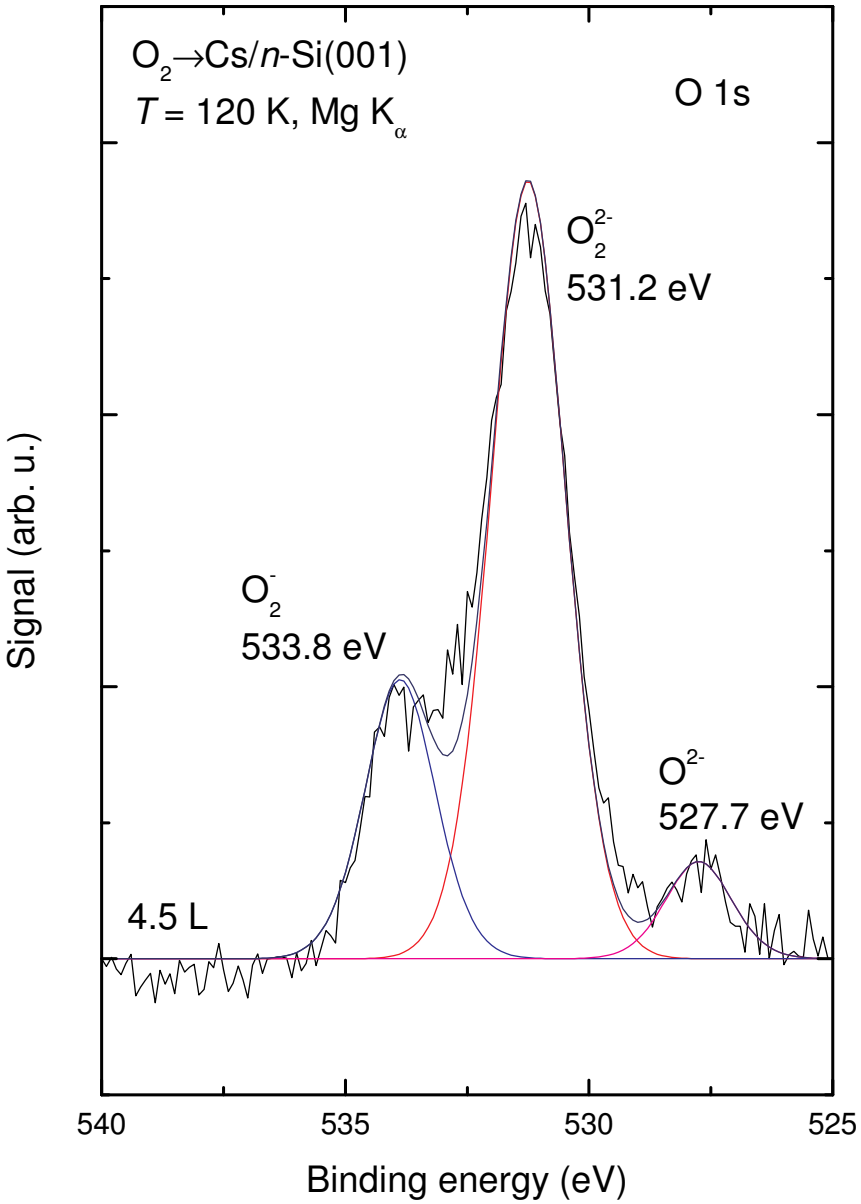

Figure 7.27.: Cesium film deposited of ≈ 10 ML thickness on n-Si(001) at 120 K - Photo emission in the region of the O 1s line during the oxygen oxidation at 120 K.

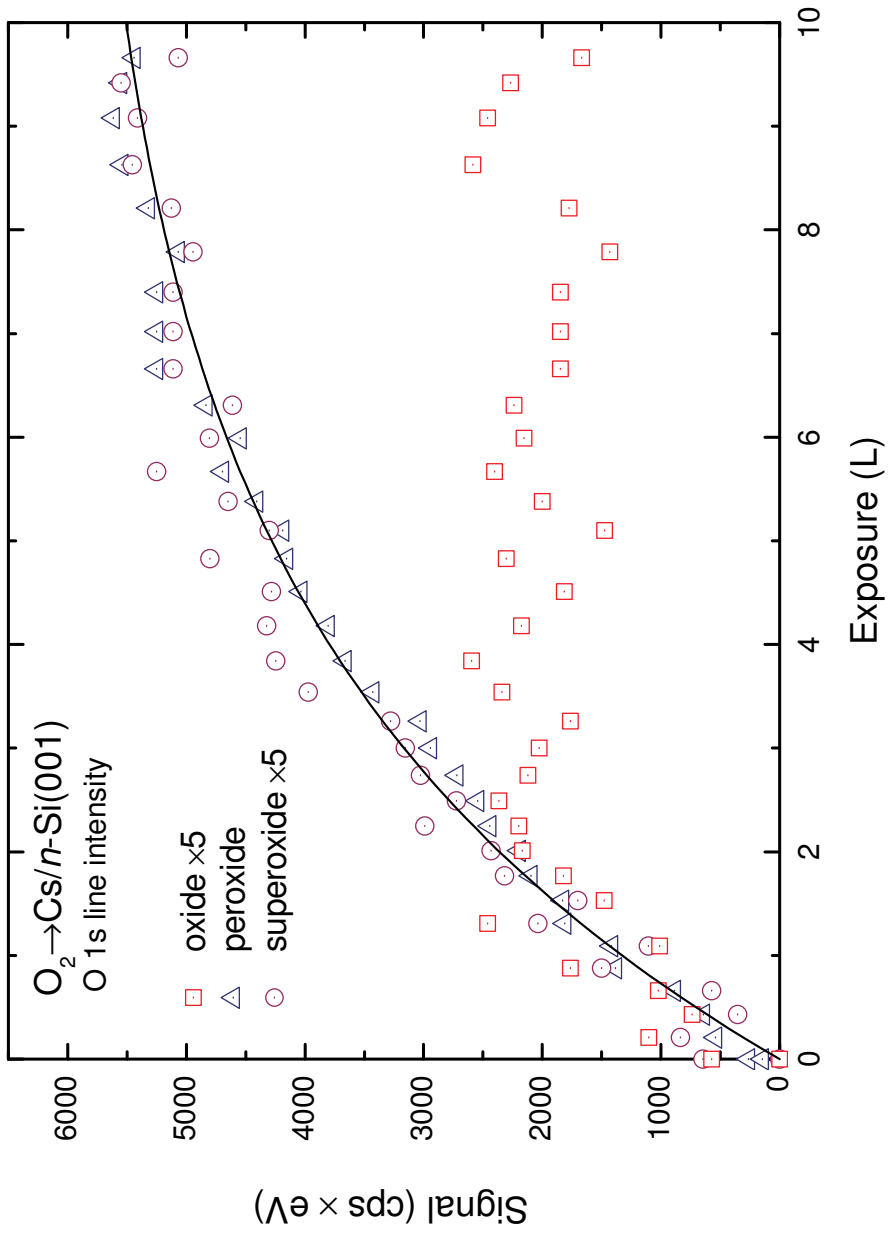

Figure 7.28.: Cesium film deposited of ≈ 10 ML thickness on *n*-Si(001) at 120 K - Intensity of the O 1s transition during the oxygen oxidation at 120 K.

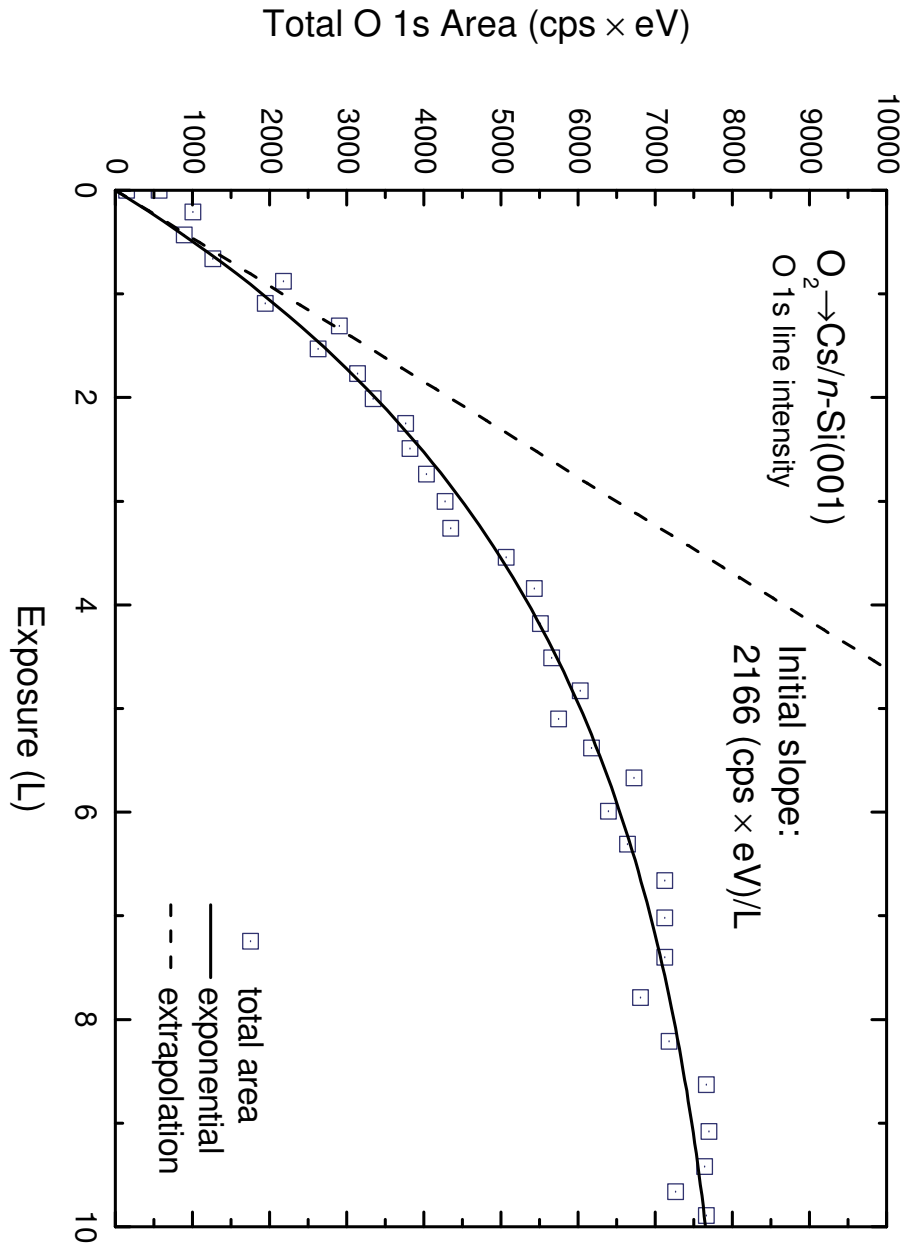

Figure 7.29.: Cesium film deposited of ≈ 10 ML thickness on n-Si(001) at 120 K - Intensity of the O 1s transition during the oxygen oxidation at 120 K.

7.2.7. Chemical Trend

Table 7.2.: Binding energies and assignments of the O 1s XPS peaks of the various oxide species occurring during the oxidation of alkali metal films.

	Atomic	Peroxide	Superoxide	
Lithium	530.7 ± 0.2			this work
Potassium	527.1 ± 0.2	530.3 ± 0.2	534.7 ± 0.2	[JDB92]
	527.2	531.0	534.3	[LSR95]
	528.3			[LSR95]
	528.2 ± 0.3	531.9 ± 0.3	534.5 ± 0.3	[PK77]
	529.7	531.5	534.6 ± 0.3	[HSSX92]
	527.9	532.1	534.0	this work
Sodium	529.2	533.0		this work
Rubidium	527.7	531.5	535.0	this work
Cesium	527.7	531.2	533.8	this work

A clear chemical trend toward dissociative adsorption shows when going upward in the periodic system (Fig. 7.31). Whereas the dissociative adsorption seems to be defect related or at least limited to the very early oxidation for cesium, rubidium and potassium, it is an intrinsic property of the oxidation of sodium and lithium thin films. Still, this result should not be considered as a general feature of the oxidation. It should rather be emphasized that strictly speaking this behavior is only true in the temperature regime around 120 K and might be entirely different at a higher (or lower) temperature. Especially the dissociation of the oxygen molecule may be an activated process which would then be very sensitive to the temperature of the experiment.

As a second result, the binding energy of the O 1s electrons of the oxide species as a whole shift toward higher binding energies when going upward in the periodic system (see Table 7.2 for a comparison). At the same time, it shows that the relative position of the oxide, peroxide and superoxide peaks remains essentially the same for all alkali metals. This leads to yet another unambiguous identification of the chemical nature of these species which is independent of the previously mentioned UPS results.

Figure 7.30 shows the shift of the O 1s binding energy as a function of Miedema's electronegativity for the alkali oxides (circles), peroxide (triangles) and superoxides (squares) which were prepared for this study. The nearly linear relation between the binding energy and the electronegativity is to be expected because the underlying reason for the

chemical shift is the charge transfer from the metal onto the oxygen ion.

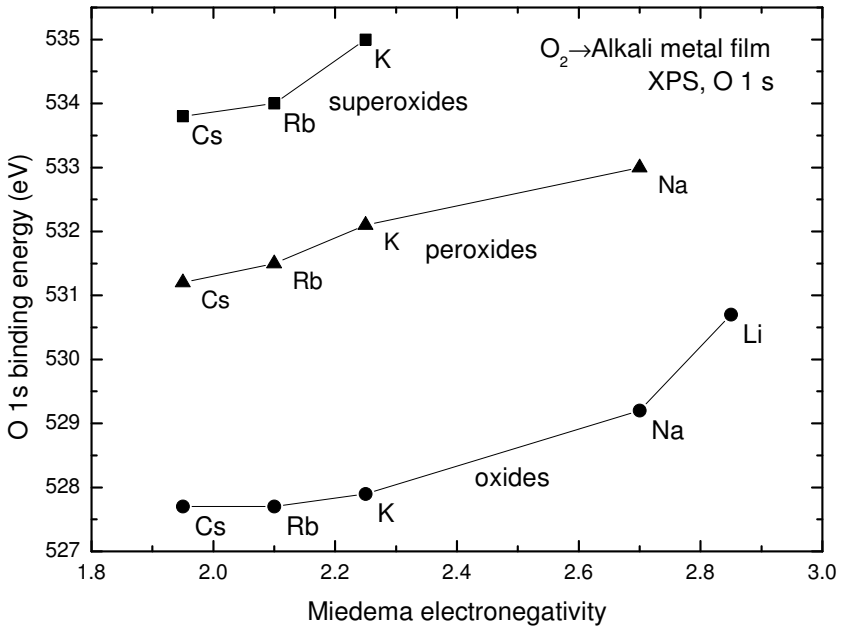

Figure 7.30.: Binding energies of the O 1s photoemission line for the alkali oxides (circles), peroxide (triangles) and superoxides (squares) as a function of Miedema's electronegativity [MdCdB80].

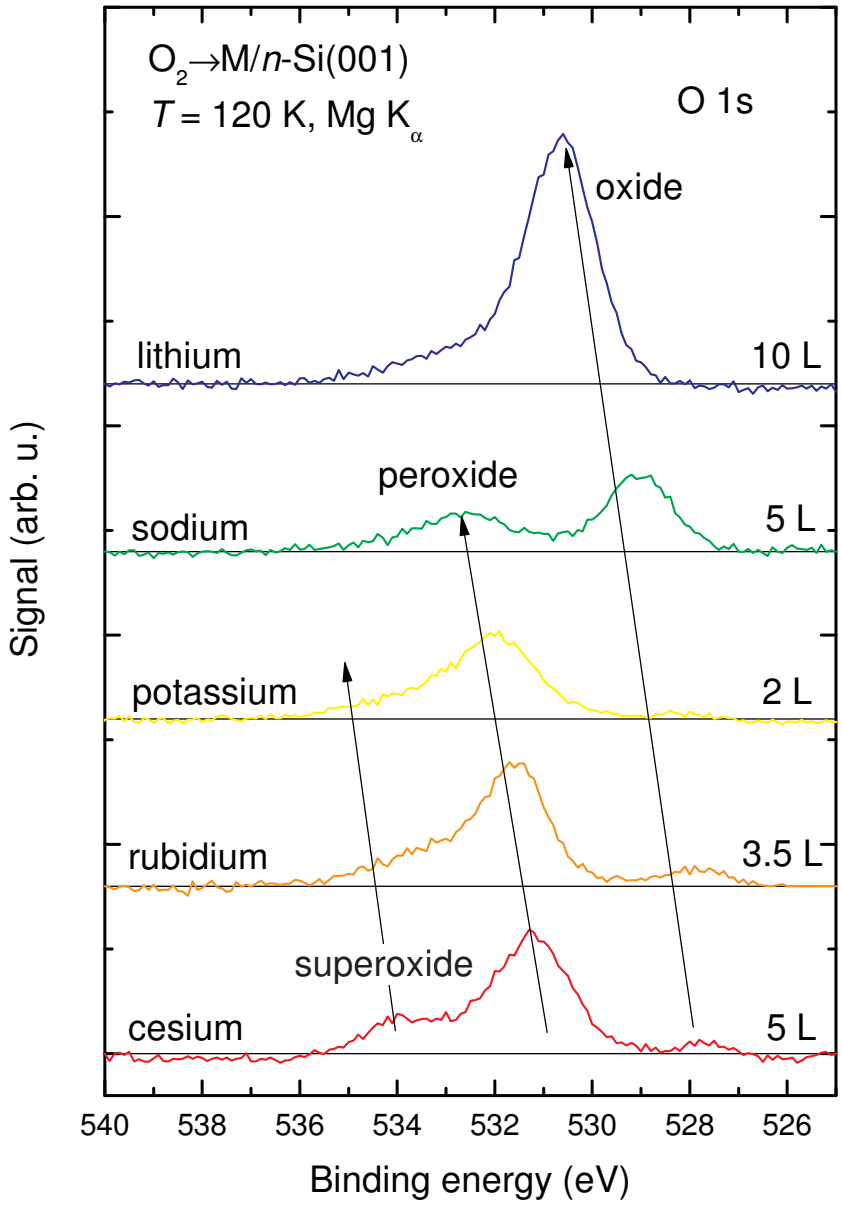

Figure 7.31.: Chemical trend in the oxidation of alkali metal films under UHV conditions and low temperatures. Shift of the O 1s binding energy for the alkali metal oxides.

7.3. Work Function Changes

The response of the work function of potassium covered palladium diodes under oxygen exposure was determined using the Kelvin probe method. Figure 7.32 shows the work function change resulting from an exposure of thick K adlayers to molecular oxygen. The potassium layer was deposited on a thick palladium film. Although the work function is initially the same for all coverages shown here, its evolution upon oxygen exposure is highly dependent on the amount of deposited potassium. For low coverages ($d_K \approx 2\,ML$) the work function initially decreases by 50 meV but eventually increases monotonously by more than 1 eV. For high coverages d_K the work function change is quite different: the work function decreases to a broad but shallow minimum (100 meV). After some critical O_2 exposure it rises to a value only 0.2 eV above the initial work function.

These observations are typical for alkali modified transition metal surfaces and are also commonly seen for alkali multilayers [PC73, PBB80, SRK87, WSK$^+$87]. It is commonly believed that at first oxygen is preferentially incorporated into the bulk of multilayered alkali films. The adsorbed oxygen diffuses into the bulk and forms an oxide layer just underneath the uppermost potassium layer. The surface on the other hand essentially remains free of oxygen for low exposures. This causes an initial decrease in work function, presumably because of a change of potassium from a metallic to an ionic state. Once the potassium layer is saturated, further oxygen is adsorbed on top of the surface effectively causing the observed increase in the work function.

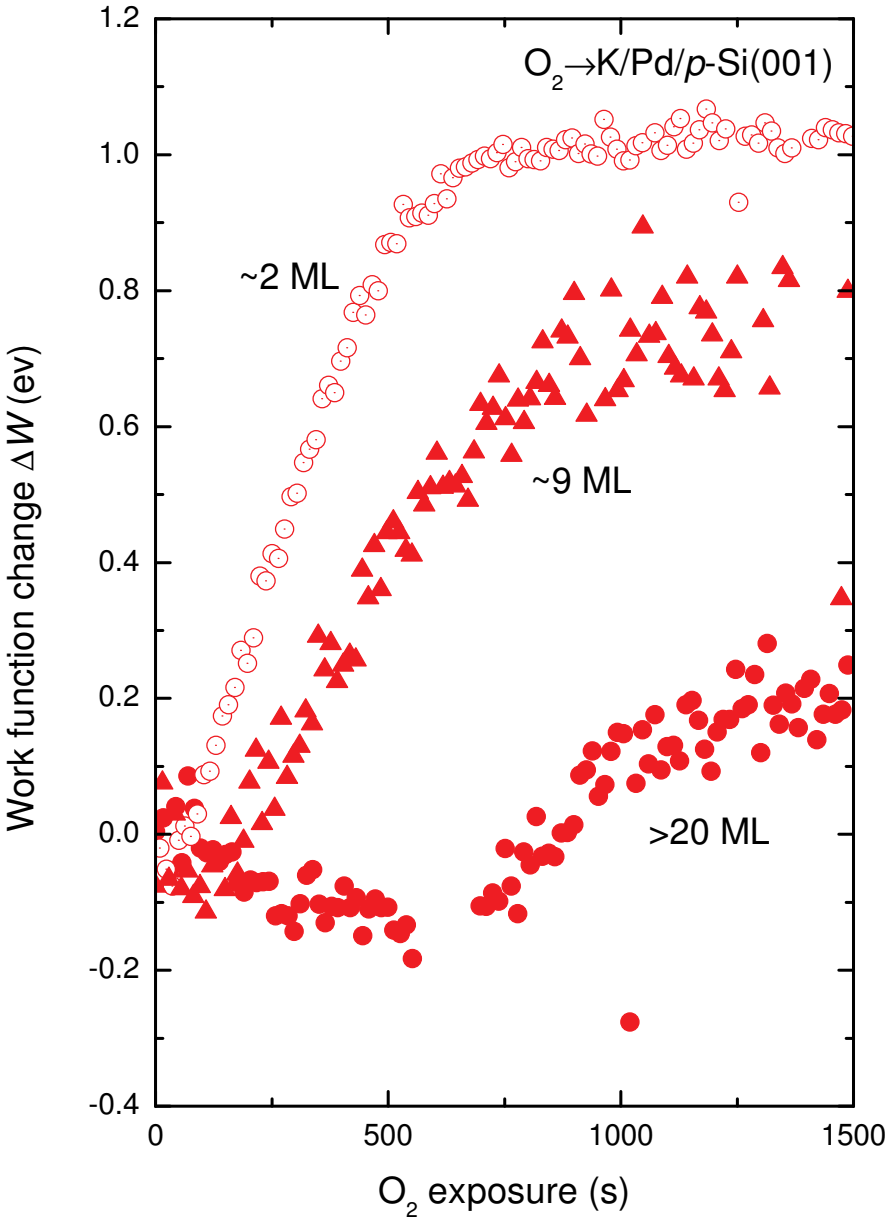

Figure 7.32.: Work function change while exposing potassium films on palladium to oxygen at $T = 120\,\mathrm{K}$ [KHN09].

7.4. Chemicurrent and Exoemission

Chemicurrent experiments were performed for a number of alkali metal surfaces. Apart from depositing the pure metals, i.e., lithium, sodium, potassium, rubidium, and cesium on silicon directly, potassium modified palladium surfaces were also investigated. The virtue of using metallic support films lies in their electrical stability during the chemical reactions. Depending on whether palladium diodes were used or not the investigation focused on the low coverage regime of ≤ 1 ML or on thick samples with alkali metal films 1 nm or thicker. Chemicurrent experiments were only possible on p-doped because only these show diode behavior.

7.4.1. Lithium

Thin lithium films were deposited directly on hydrogen passivated silicon substrates. The metal was deposited at a substrate temperature of below 120 K which prevented the formation of lithium silicide phases. All exposures were carried out under the same temperature conditions if not stated otherwise. Figure 7.33 shows the chemicurrent (blue curve) and the total exoemission (red curve) during an exposure at an oxygen pressure of 10^{-8} mbar. The chemicurrent is dominated by a rapidly decaying transient that shows a broad shoulder at around 3 L of oxygen exposure. The maximal intensity is seen right at the beginning of the exposure. The exoemission on the other hand reaches its maximum value only after an induction period of 3 L.

In Figure 7.34 exoelectron spectra and the integrated exoemission yield from an energy resolved experiment are shown. The lower panel shows the exoemission yield as calculated from the spectra shown in the upper panel. The result in Fig. 7.34 compare well with the results obtained from the combined exoemission and chemicurrent measurements which were presented in Fig. 7.33. The upper part gives an impression of the spectral features of the exoemission during the exposure. In Fig. 7.35 the same spectra are presented in a different form. Similar spectra and exoemission yields have been reported on earlier by Greber *et al.* [GFG$^+$94]. The overall emission is restricted to a narrow region above the vacuum level. From a fit to the exponential tail (Fig. 7.36) of the data a characteristic energy of $\Delta E = 0.18$ eV is found.

The onset of the exoemission / the work function decreases during the exposure starting from a value of 2.7 ± 0.1 eV. As can already be seen from Fig. 7.34, the work function decreases in two distinct regions each showing a different slope. In Fig. 7.37 the onset of the exoemission spectra has been plotted as a function of the oxygen exposure. From

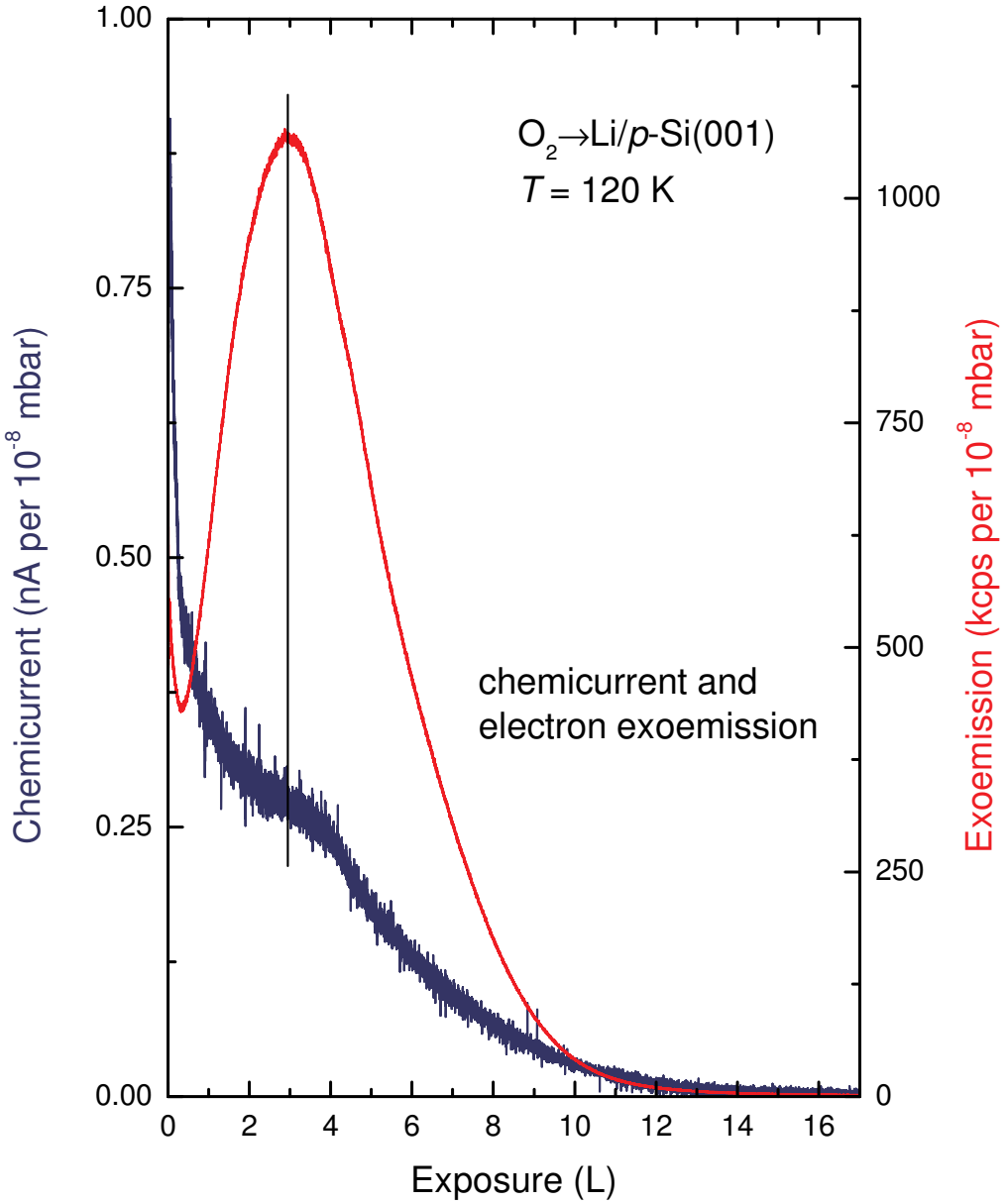

Figure 7.33.: Chemicurrent vs. exoemission for a thick sample of lithium on silicon

these data a slope of $215 \pm 20\,\mathrm{meV/L}$ for the initial region and $55 \pm 8\,\mathrm{meV/L}$ for the high-exposure region has been extracted by a linear regression. After an exposure of 6 L no further change of the work function can be observed. This is mainly so because the intensity of the exoemission is reduced to a level at which it becomes impossible to determine the onset of the emission.

Discussion

It is a striking feature of these results that the exoemission and the chemicurrent show different exposure dependencies. In addition, it cannot be seen as a coincidence that the maximum of the exoemission and the shoulder of the chemicurrent occur at the same exposure. It is rather suggestive to appoint these two to the same chemical process. This is also supported by the observed kink in the work function which occurs in the same exposure regime. All of this points to changed reactions conditions on the surface.

Earlier studies explained the decreasing work function by the incorporation of oxygen below the first alkali layer. The negatively charged oxygen ions below the surface results in a dipole layer which effectively reduces the work function [GFG$^+$94, KHN09]. The kink in the work function therefore indicates a change from subsurface incorporation of oxygen to a different mechanism of oxidation. Possible mechanism include (a) the diffusion of lithium to the surface formation additional oxide layers and (b) the molecular adsorption of precursor oxygen on the oxide surface [GFG$^+$94].

The photo emission data and the available thermo chemical data show that atomic oxygen is formed by dissociation on the surface during the oxidation. At the start of the reaction a strong chemicurrent but no significant exoemission of electrons can be observed. Exposure dependent exoemission and chemicurrent efficiencies must be considered because the respective yields are not directly proportional to each other. Several reasons for the delayed onset of the exoemission may be found from the experiment: (a) the work function is greatly lowered during the oxidation and thereby the emission over the barrier is eased, (b) the kink in the work function suggests a second reaction mechanism that sets in after the saturation of a first oxide layer, and (c) chemicurrent and exoemission show a maximum at the same exposure also indicating a different reaction mechanism or a slowed reaction rate after the formation of the first oxide layer.

These results may be explained in the picture of the NNL model which takes into account the lifetime of excited hole states on the impinging molecule. This lifetime is itself depending on the instantaneous state of the surface. Apart from the work function the later may be described by the electron density right at the surface. The electron

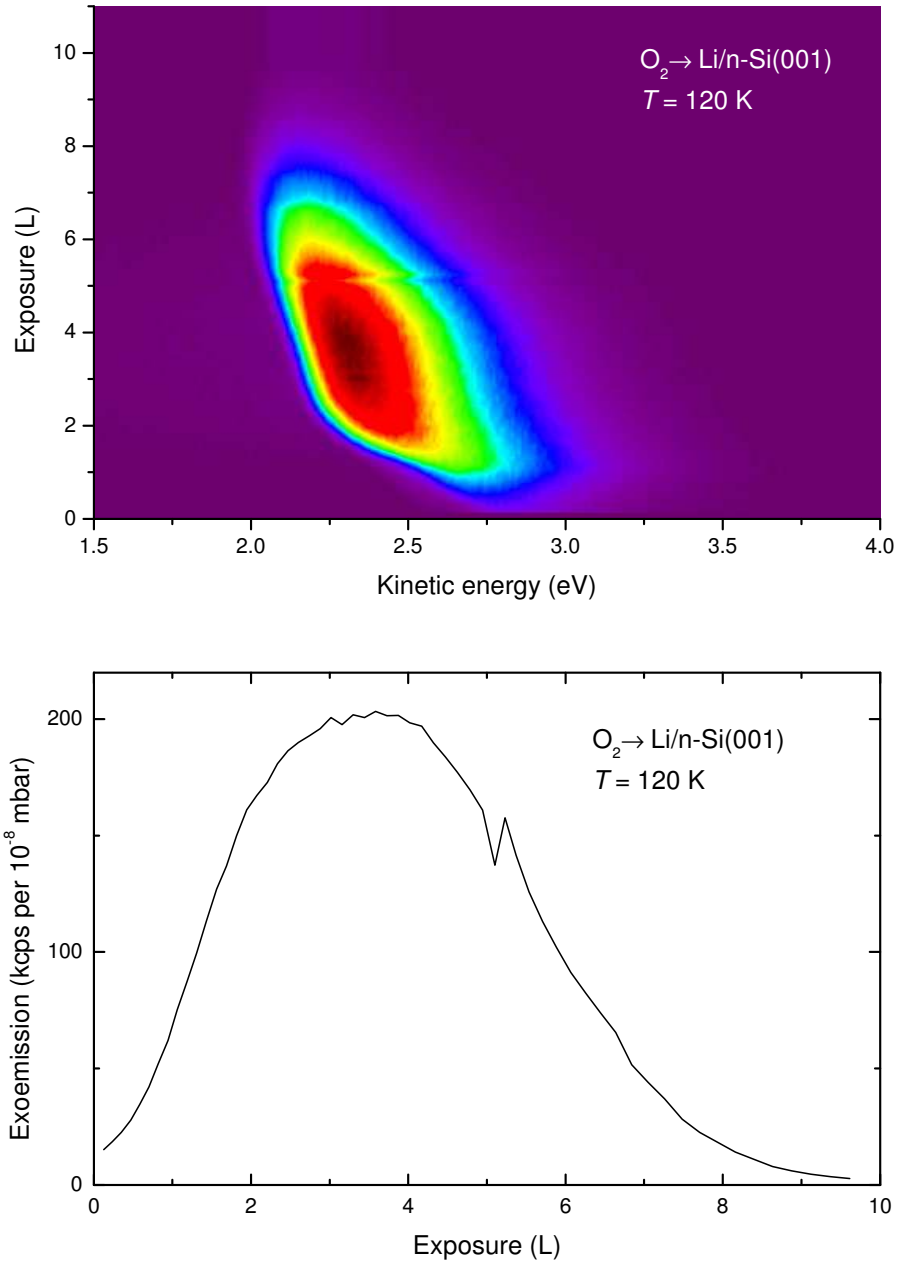

Figure 7.34.: Energy resolved electron exoemission from a thick sample of lithium on silicon under oxygen exposure. Upper panel: contour plot of the exoemission as a function of exposure. Lower panel: integrated exoemission as a function of exposure.

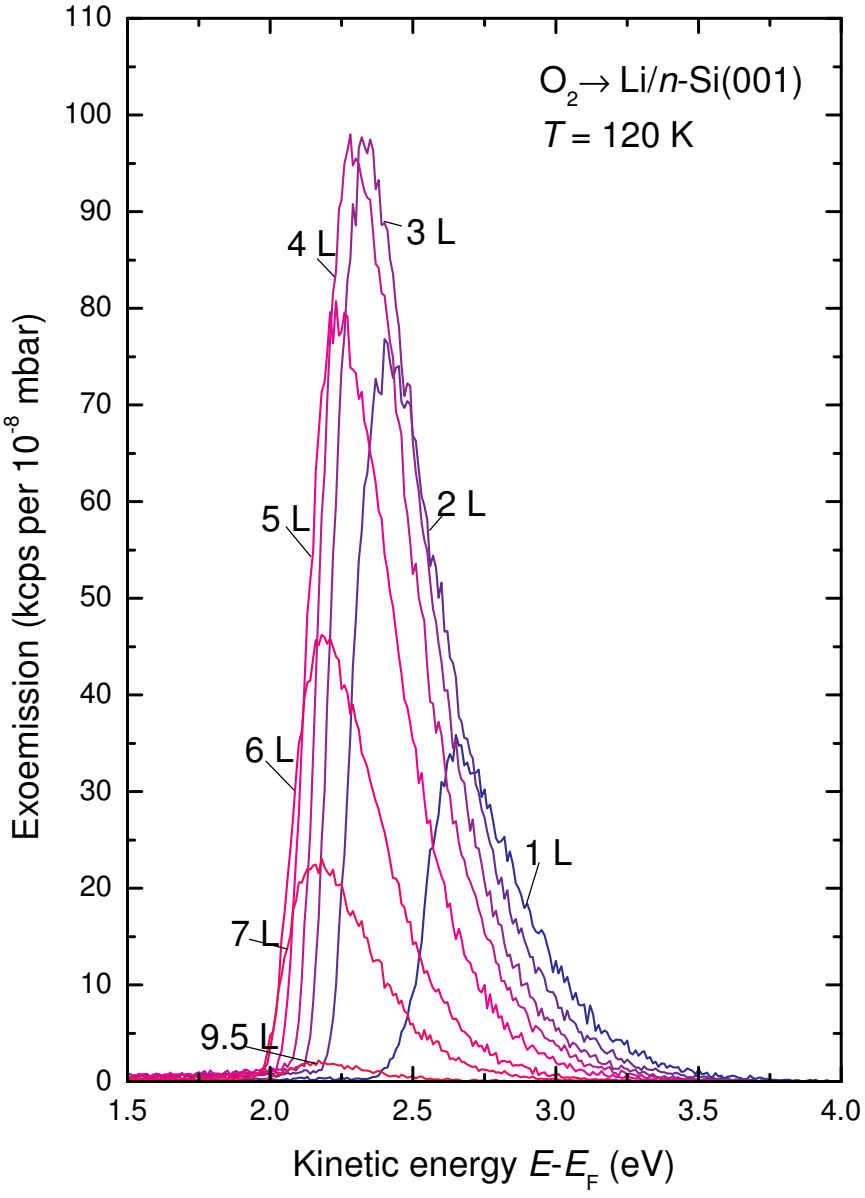

Figure 7.35.: Energy resolved electron exoemission from a thick sample of lithium on silicon under oxygen exposure. Exoemission at selected exposure times.

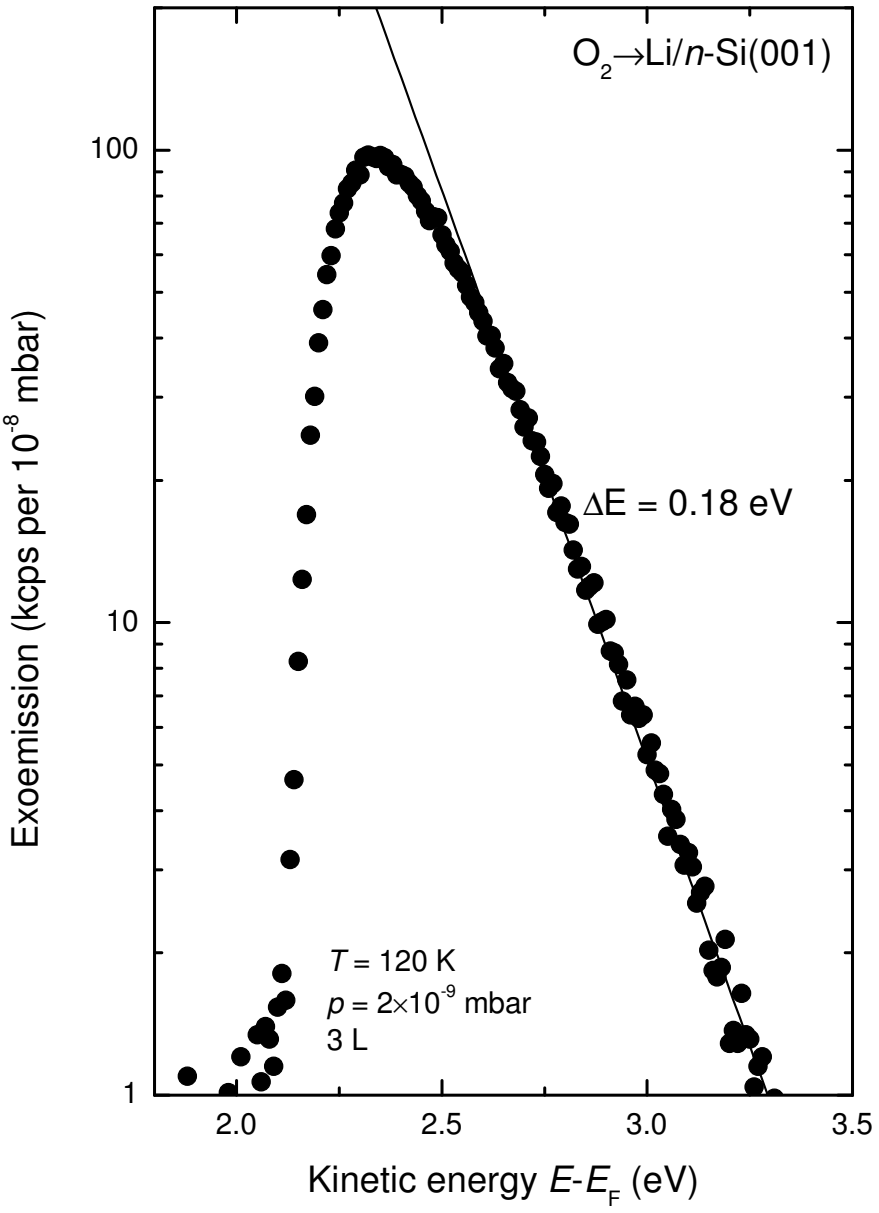

Figure 7.36.: Thick lithium film deposited on n-Si(001) at 120 K - Exoemission spectrum at constant oxygen partial pressure at 120 K and an exposure of 3 L.

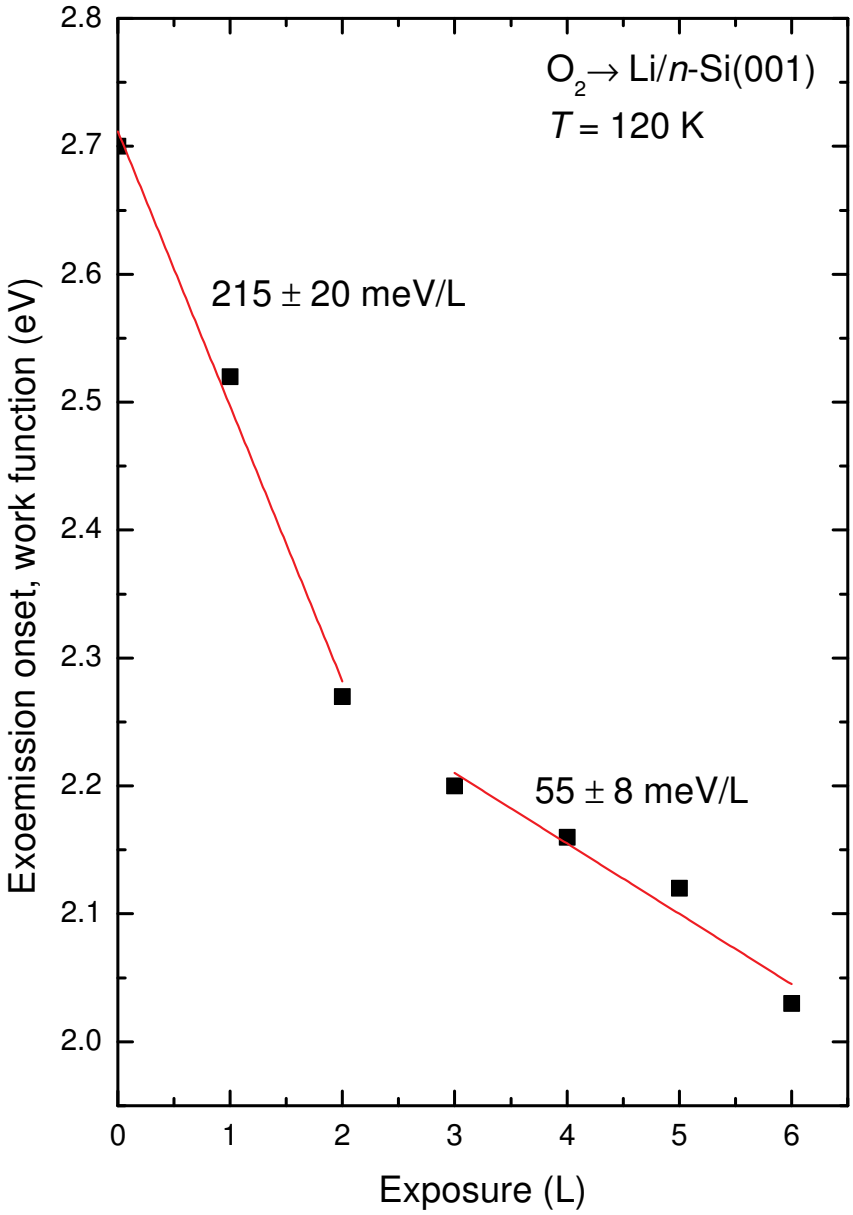

Figure 7.37.: Change of the onset of the exoemission/work function change of a thick, metallic lithium film on a silicon substrate

density is high during for the freshly deposited metal film and during the first stage of the oxidation. Hence the chemically excited holes have a short lifetime because the ionization probability in front of the surface is high. Still the lifetime is sufficiently long to produce excitations that can be detected in a chemicurrent experiment. On the other hand the energy of the excitations is insufficient to provide the energy for any electrons to move over the surface barrier. Once the surface is covered with an oxide layer there are far less electrons available for the reaction which (a) reduces the reaction rate and (b) delays the charge transfer from the surface to the molecule and thereby increases the non-adiabaticity of the reaction.

In the literature the exoemission during the oxidation of lithium films has been explained to occur during the dissociation of the oxygen molecule [GFG$^+$94]. This conclusion was justified by cluster calculations which showed a deexcitation energy (4.5 eV) for the transition $O^- \rightarrow O^{2-}$ which were compatible with the maximum energy of the observed exoelectrons. On the other hand some doubt must be stated if these results are applicable also for the oxidized surface - especially because the main exoemission stems from the oxidized surface. In this light it cannot be ruled out that the charge transfers to the *molecule* which must precede its dissociation are responsible for parts of the chemicurrent signal and for the exoemission peak.

7.4.2. Sodium

Chemicurrent and Integrated Exoemission

The chemicurrent traces that were recorded for thick sodium films show features similar to the ones seen for lithium. Figure 7.38 shows a typical trace of the chemicurrent and the exoemission during the oxidation at 120 K. In an initial region the chemicurrent decays rapidly from an initial maximum value while no exoemitted particles can be detected. Around an exposure of 1.2 L, a local maximum of the chemicurrent is seen. The exoemission steeply increases in a similar way to reach is maximum shortly after the observed maximum of the chemicurrent. The absolute value of the exoemission can not be directly compared with the results of the other alkali metals because a different counting electronic was used, which was not able to capture all the emitted electrons.

Like for lithium, the dissociative adsorption during the initial phase of the reaction creates sufficiently energetic holes for the detection of a chemicurrent but lacks the high energy electrons observed as exoemitted electrons. The chemicurrent tails off exponentially as the surface becomes saturated with sodium oxide and the reaction rate levels off. The local maximum of the chemicurrent is due to the molecular adsorption of a peroxide species.

Temperature Programmed Exoemission (TPEE)

After exposing them to oxygen at low temperatures the samples were heated to above room temperature at a constant rate. While heating the samples the exoemission of electrons was monitored. Figure 7.39 shows the resulting exoemission for two thick sodium samples that were exposed to 8 L of oxygen when they were heated from 120 K to 350 K at a constant rate of $\beta = 50\,\mathrm{mK/s}$. The curves show two maxima at 179 K and around 300 K.

Similar observations have been made for Cs monolayer film on Ru(0001) substrates by Grobecker *et al.* [GGBE94] where they attributed the thermally activated exoemission to the dissociation of preadsorbed oxygen molecules. In general this may explain the thermal emission from sodium surfaces, yet additional data on the chemical transformation in the temperature regime of this study are necessary. Indeed, the second peak around 300 K marks that at least two processes lead to thermally activated exoemission which makes an explanation solely on the dissociation questionable.

The analysis of TPEE spectra is quite similar to the analysis of temperature programmed desorption (TPD) data [Red62]. In the simplest approximation of first order

reaction kinetics, the activation energy E_a of the two processes can be calculated from their peak position T_p alone:

$$\frac{E_a}{RT_p^2} = \frac{\nu}{\beta} \exp\left(-\frac{E_a}{RT_{T_p}}\right). \tag{7.4}$$

The attempt frequency ν could be evaluated by changing the ramp rate β, which has not been done for this study. Instead a typical phonon frequency $\nu = 10^{13}\,\mathrm{Hz}$, and indeed the one found by Grobecker *et al.*, has been used for the analysis. The high energy peak with $E_a = 0.9 \pm 0.1\,\mathrm{eV}$ is in agreement with the literature data. From the low energy peak at 179 K, which has not been observed so far, an activation energy of $E_a = 0.55 \pm 0.1\,\mathrm{eV}$ is derived. Possibly, the low energy peak is due to the thermally activated diffusion of Na from the bulk to the surface.

Pressure Dependence

The influence of the oxygen partial pressure on the reaction parameters of the oxidation was tested in the pressure range between $10^{-9}\,\mathrm{mbar}$ and $10^{-7}\,\mathrm{mbar}$. Essentially, no influence of the partial pressure on the reaction dynamics was found in this pressure range. Figure 7.40 shows the variation of the maximum current density and the time to reach the local maximum as a function of pressure on a double logarithmic scale. A direct proportionality between the maximum current density and the pressure and an inverse proportionality between the time to reach the second maximum and the oxygen flux was observed.

Especially, these results show that the mutual interaction between possibly physisorbed oxygen on the surface has no effect on the chemicurrent. Indeed, they show that the surface reaches thermodynamical equilibrium in between reaction events. This requires that all rate constants, e.g., desorption rate or diffusion constants, must be much larger than the impingement rate which is directly proportional to the partial pressure.

Discussion

On the fresh surface the molecular adsorption does not efficiently create hot holes nor electrons and consequently does not produce a chemicurrent nor does it show any exoemission. Again, as more parts of the surface oxidize the more non-adiabatic the reaction becomes. Two possible mechanism may explain this behavior. Firstly, the charge transfer that finally leads to the electronic excitation may be delayed because the surface

electron density of states is reduced. This in turn reduces the coupling between absorbate and metallic states and therefore leads to an increased lifetime of an induced empty state. Secondly, additional stabilization effects due to neighboring sodium peroxide cells may effectively increase the adsorption energy and therefore increase the energy that is available for the excitation of electronic degrees of freedom.

Böttcher *et al.* report similar exoemission results for sodium films on metallic substrates in conjunction with MDS and work function data [BGG+93]. While their data on the non-adiabatic reaction pathway is limited to exoemitted electrons, which require much higher excitations than chemicurrents, their interpretation agrees with the one presented in this study: the lowering of the surface density of states leads to an increased non-adiabaticity during the oxidation. They however attribute the exoemission to the formation of superoxide like oxygen molecules. This is thought to occur through the reaction of an oxygen molecule from the gas phase with an activated $Na_2O_2^*$ species on the surface. This differs from the observation in this study in two respects: (a) no superoxide signal was observed in the XPS data, and (b) the potassium data suggest that the superoxide formation leads to exoemission only when the metal film is thoroughly oxidized and therefore two peaks in the exoemission are usually observed.

However, the authors used thinner sodium film (5 ML in their case) and a higher sample temperature (230 K vs. 120 K) than in this study. They may, therefore, have missed the second peak resulting from the superoxide formation and therefore could not discern between the two processes.

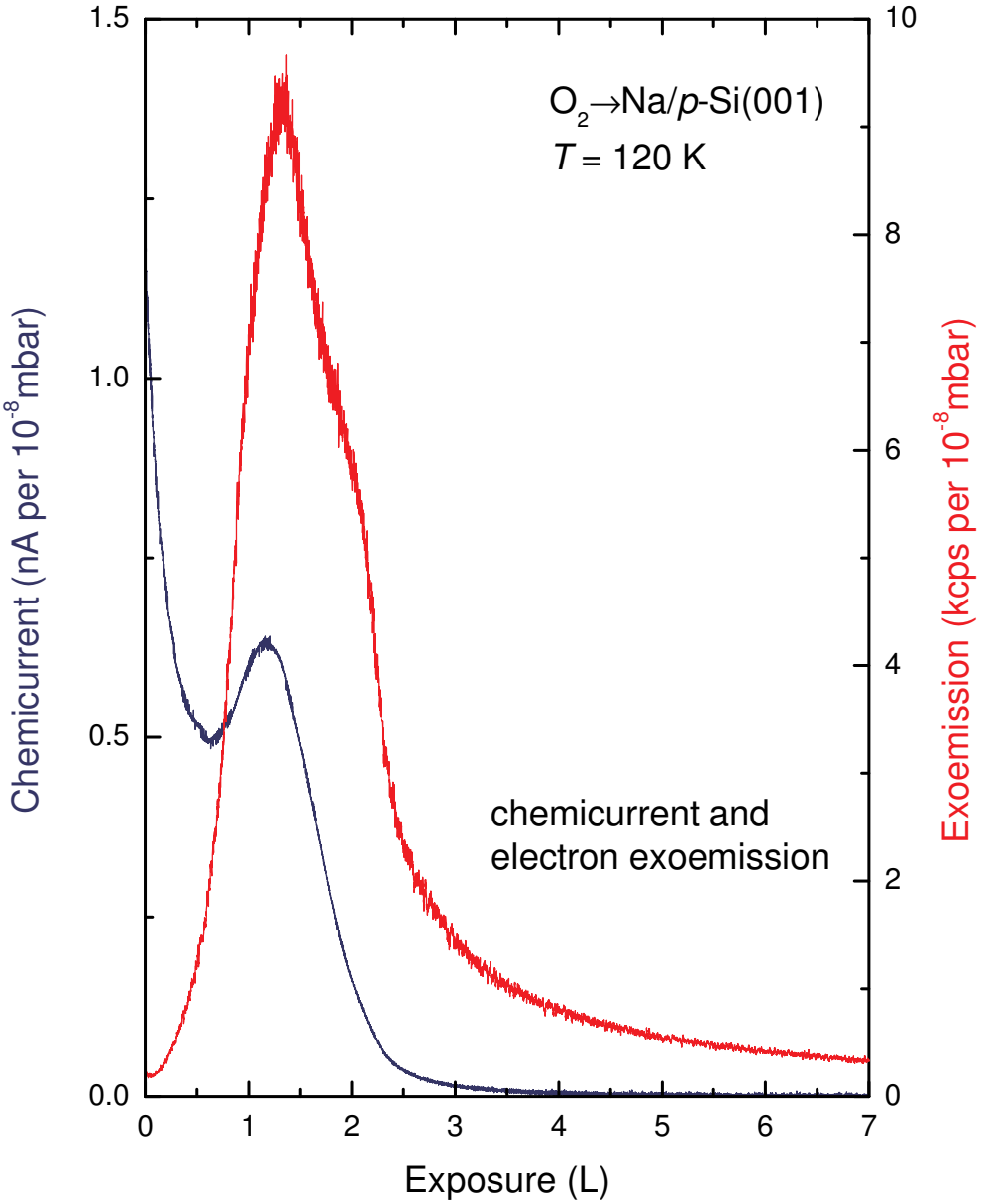

Figure 7.38.: Chemicurrent vs. exoemission for a thick sodium layer on silicon.

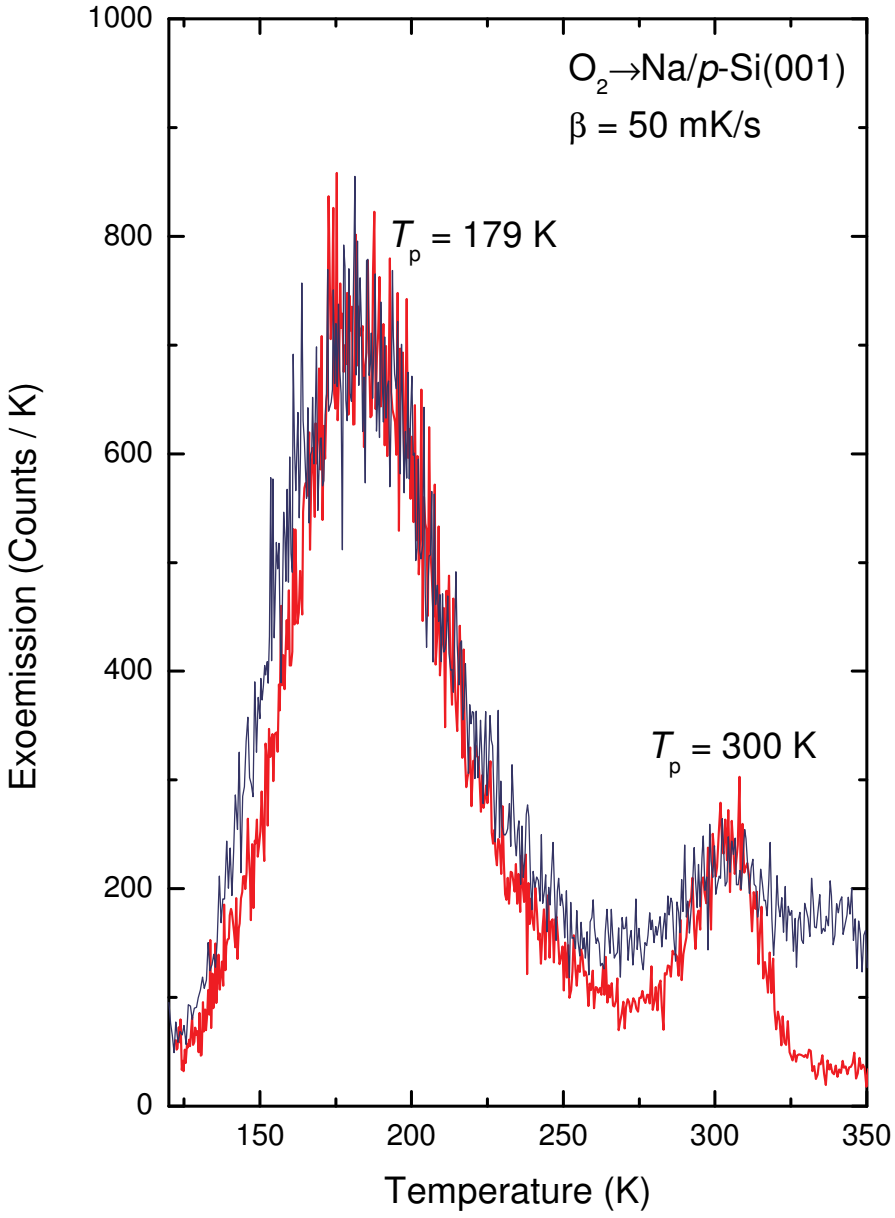

Figure 7.39.: Temperature programmed exoemission from a multi-layer thick sodium film that was exposed to oxygen at an initial temperature of $T = 120\,\mathrm{K}$.

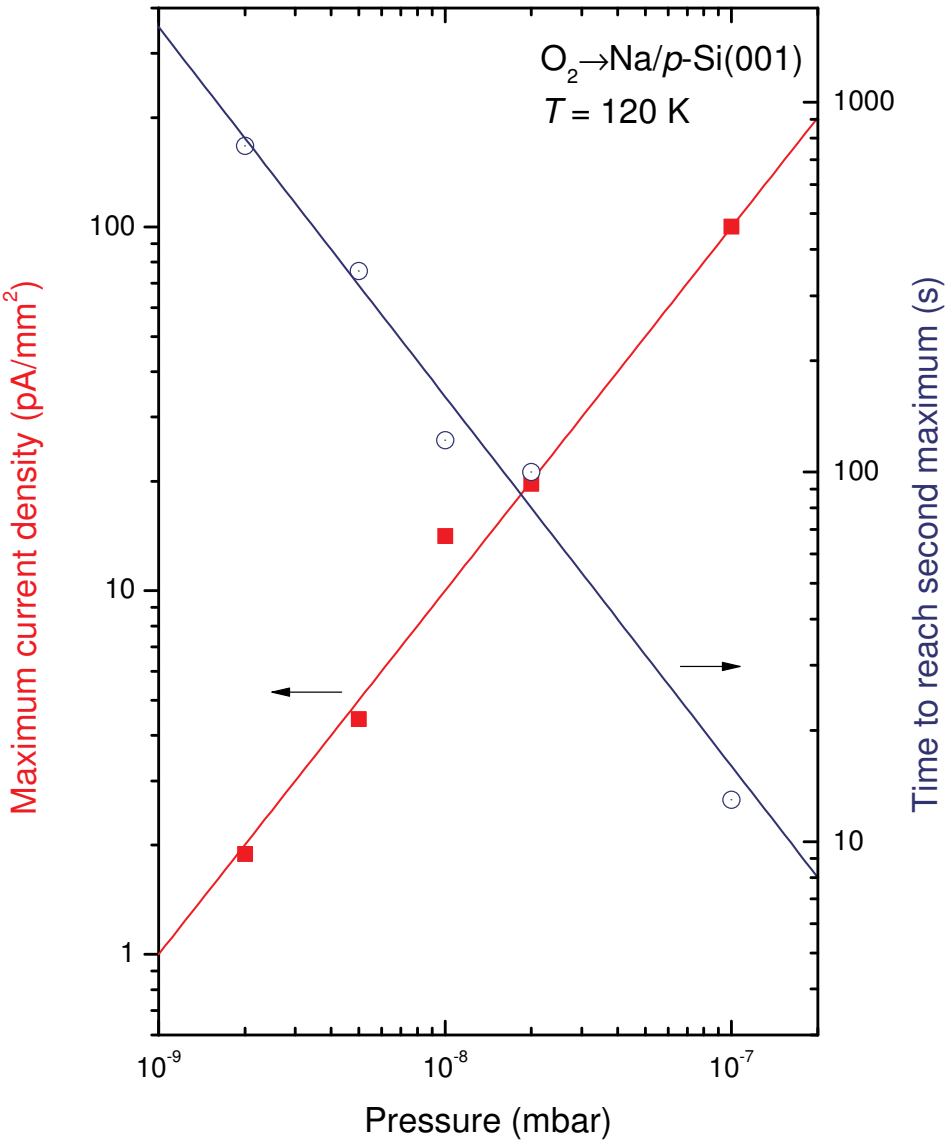

Figure 7.40.: Multi-layered sodium films deposited on p-Si(001) exposed to oxygen at $T = 120\,\mathrm{K}$. Pressure variation of the reaction speed: linear relation for the chemicurrent yield and inversely linear reaction speed.

7.4.3. Potassium on Palladium-Silicon Diodes

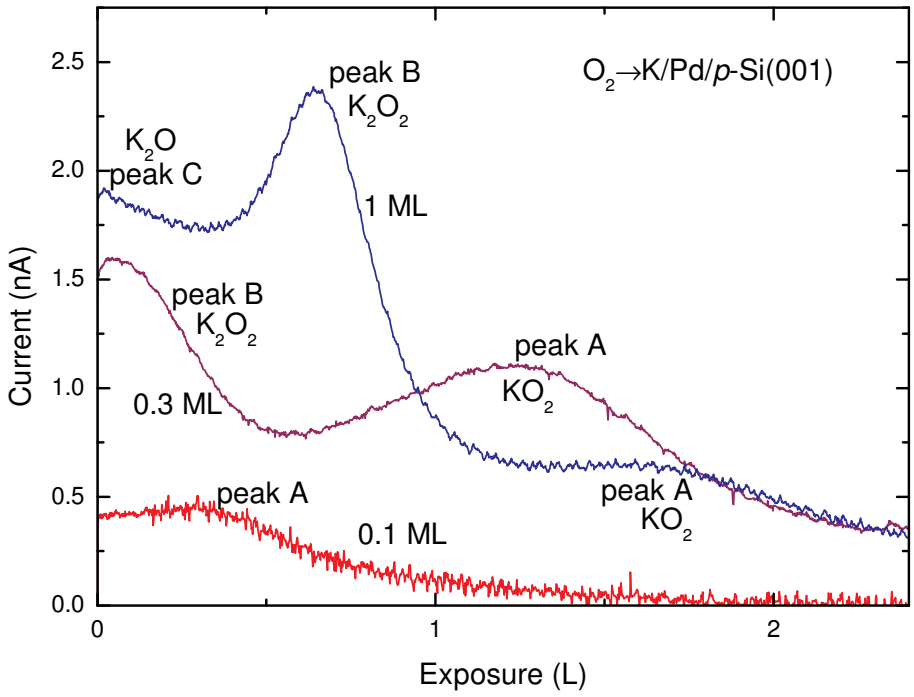

Figure 7.41.: Chemicurrent traces recorded on K/Pd/p-Si(001) Schottky diodes during the oxidation of the surface in a continuous beam of molecular oxygen.

Figure 7.41 shows typical chemicurrent traces recorded while the samples were exposed to a continuous beam of molecular oxygen ($p = 10^{-8}$ mbar). The samples were based on silicon substrate which held a thin layer of palladium ($d = 1.2$ nm). Potassium was deposited on the surface of the palladium electrode which activated the non-adiabatic processes. The measurements were performed at a sample temperature of $T = 120$ K which reduced the thermionic backward current below the detection limit. Due to the low Schottky barrier of the Pd diodes a residual photo current of approximately 1 nA had to be subtracted for clarity. It is quite obvious that the amount of potassium deposited on the surface has a strong effect on the shape of the chemicurrent traces. Three distinct features are present which are labeled by the letters A, B and C in the plot. The feature labeled A is present for all coverages, while B and C are only observed when the surface is fully covered[2]. Apparently the film has to be in a certain condition to support the

[2]The coverage unit used is relative to the amount of surface atoms of the substrate. The surface is fully covered for a potassium coverage of 0.25 ML.

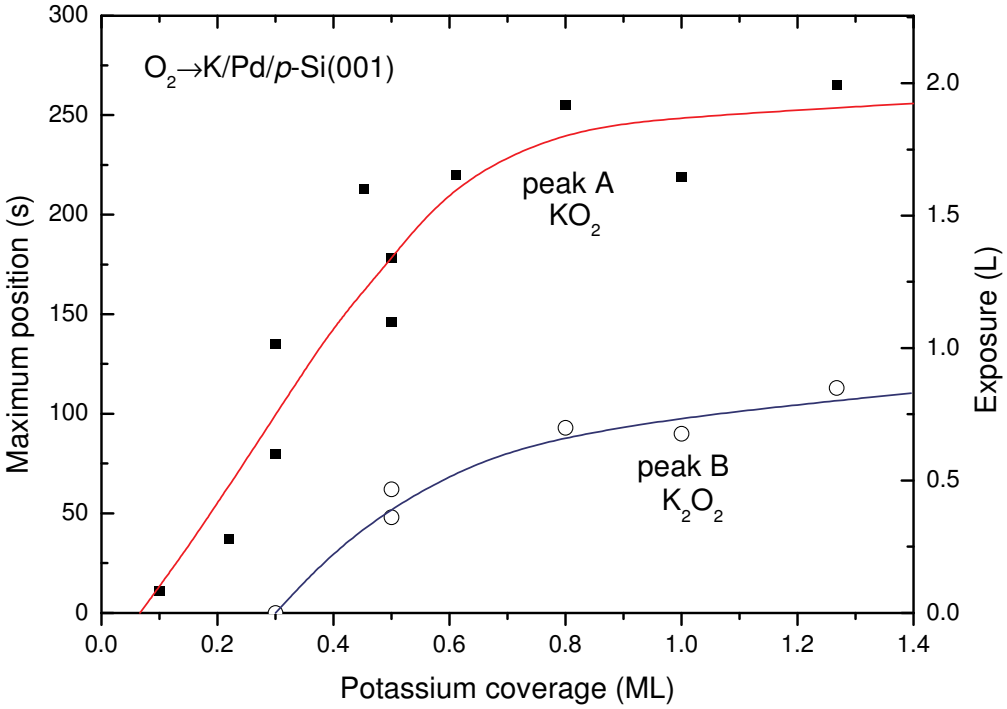

Figure 7.42.: Position of the main features in the chemicurrent observed for a number of K/Pd/p-Si(001) with varying potassium coverage while exposed continuous beam of molecular oxygen.

generation of chemicurrent. Figure 7.42 shows how the maximum positions of A and B shift with increasing potassium coverage. Before discussing the reasons it must be certain that the current observed is a ballistic chemicurrent.

Figure 7.43 shows chemicurrent traces as well as the total charge carried by the chemicurrent as a function of an increasing thickness of the palladium electrode. As expected for a ballistic current an exponential attenuation is observed while the general shape of the current traces remains the same [Nie02, GN04]. According to Beer's law (2.3) an attenuation length was determined by an exponential fit

$$Q_{\mathrm{cc}}(\mathbf{d}) \approx \exp\left(-\frac{d}{\lambda}\right) \tag{7.5}$$

of the total charge Q_{cc} as a function of film thickness d. The attenuation length $\lambda = 1.2\,\mathrm{nm}$ for palladium as compared to the values for other electrode materials found in

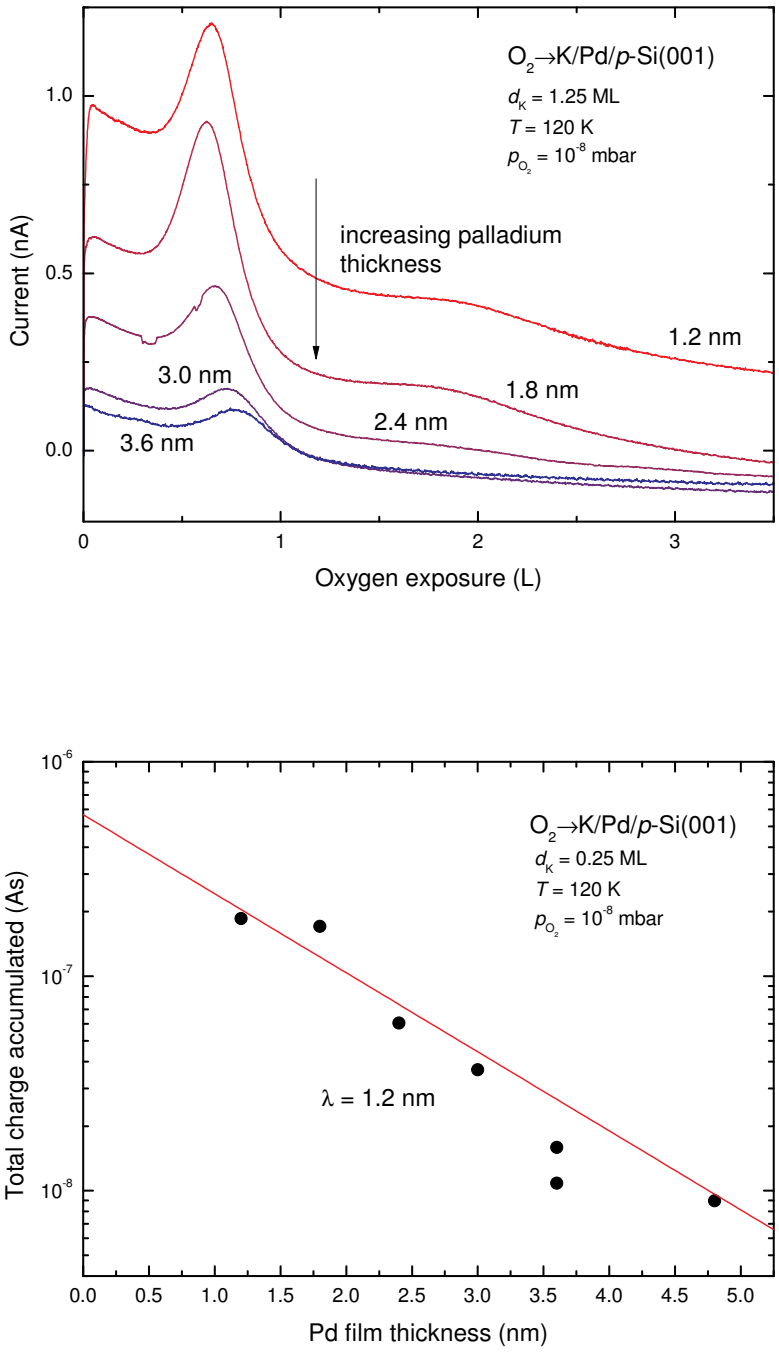

Figure 7.43.: Increasing the palladium film thickness attenuates the chemicurrent signal. The total charge accumulated during the reaction falls of exponentially with the Pd thickness with an attenuation constant $\lambda \approx 1.2\,\mathrm{nm}$

the literature can be explained by scattering of the hot electrons with the palladium d-bands which leads to a drastic reduction of carrier lifetime [LHPAD04].

Curves resembling Fig. 7.41 have been observed for the reaction $O_2 \rightarrow Mg/p-Si(111)$ and have been attributed to a changing reaction rate [GN04, Gla04]. The variations of the chemicurrent

$$j_{CC}(t) = \alpha(t)\frac{dN}{dt}(t) \tag{7.6}$$

were thus interpreted as due to a changing reaction rate while the chemicurrent efficiency α was assumed to be constant. A similar approach was taken by Böttcher *et al.* who explained their experimental results on the oxidation of cesium by a complicated rate equation model. These interpretations do not fit the photo emission data that were presented in section 7.2. There it was found that the oxidation rate of the alkali metals under the conditions used in the chemicurrent experiments is monotonously decreasing with increasing exposure. In particular the uptake curves that were recorded do not show an S-like shape which would be an indication of a transiently increased reaction rate. Therefore it has to be concluded that in the case of alkali metals the chemicurrent does not follow the simple behavior (7.6) that was observed in previous chemicurrent studies. It is therefore mandatory to make use of the full equation

$$j_{CC}(t) = \sum_i \alpha_i(t) R_i(t), \tag{7.7}$$

considering time dependent chemicurrent efficiencies, where the summation goes over every reaction step. If we assume that there is no conversion between oxide (there are no reactions of the form $K_xO_y \rightarrow K_uO_w$), the summation in (7.7) runs over every produced oxide species, i.e., regular oxide, peroxide and superoxide.

In the presence of excess potassium at low oxygen exposures and high potassium coverages it is most likely that K_2O is produced. Feature C therefore is attributed to the dissociation of oxygen and its incorporation as K_2O into the film. At slightly higher oxygen concentrations the production of K_2O_2 becomes dominant and gives rise to peak B. Increasing the oxygen exposure even further favors the production of the oxide with the least potassium content. Thus peak A can be attributed to the formation of a superoxide species. This is also confirmed by the fact that it is the feature that becomes first visible even at low potassium coverages.

7.4.4. Potassium

Potassium - in contrast to lithium and sodium - absorbs oxygen predominantly as molecules and therefore serves as a model system of the associative chemisorption of oxygen molecules. This opens up the opportunity to investigate the non-adiabaticity of the charge transfer mechanism without the interference caused by the breaking of the O-O bond during dissociative absorption. In section 7.4.3 chemicurrent traces for ultra-thin potassium films on a metallic substrate were presented which showed a profound influence of the specific reaction conditions, as there are temperature, oxygen partial pressure, and alkali film thickness, on the non-adiabatic processes. Similar effects must be expected if the initial potassium films are deposited directly on the semiconductor substrate.

Dependence on Potassium Deposition

Figure 7.44 shows the chemicurrent and exoemission for a number of potassium films directly deposited on hydrogen passivated silicon. Four films of varying thickness were prepared and exposed to oxygen at the same pressure level of 10^{-8} mbar and to the same total exposure of 20 L. After exposing the films the thickness of the resulting oxygen film was determined from the attenuation of the Si 2p features using XPS. The chemicurrent is governed by two features: a broad peak-like feature that broadens with increasing film thickness and an additional signal at the beginning of the exposure featured by the thick films. The broad maximum is due the adsorption of oxygen as peroxide ions, while the initial feature is related to the dissociative adsorption of oxygen presumably at defect sites.

Depending on the film thickness up to three features can be discerned in the corresponding exoemission data plotted in the lower panel of Fig. 7.44. A broadly peaked maximum slightly below an exposure of 1 L corresponding to molecular adsorption of peroxide ions, a shoulder at the high exposure side of the exoemission that shifts to higher exposures for thicker films in the superoxide region, and initial exoemission related to adsorption at defect sides can be made out.

Because of their relative importance in the oxidation of potassium, peroxide and superoxide related effects shall be the focus of a close investigation. The lower panel in Fig. 7.45 shows the position of the peaks seen in the exoemission and the chemicurrent during the peroxide formation. While the maximum position of the chemicurrent is constant in the thickness range investigated, the maximum of the exoemission shifts

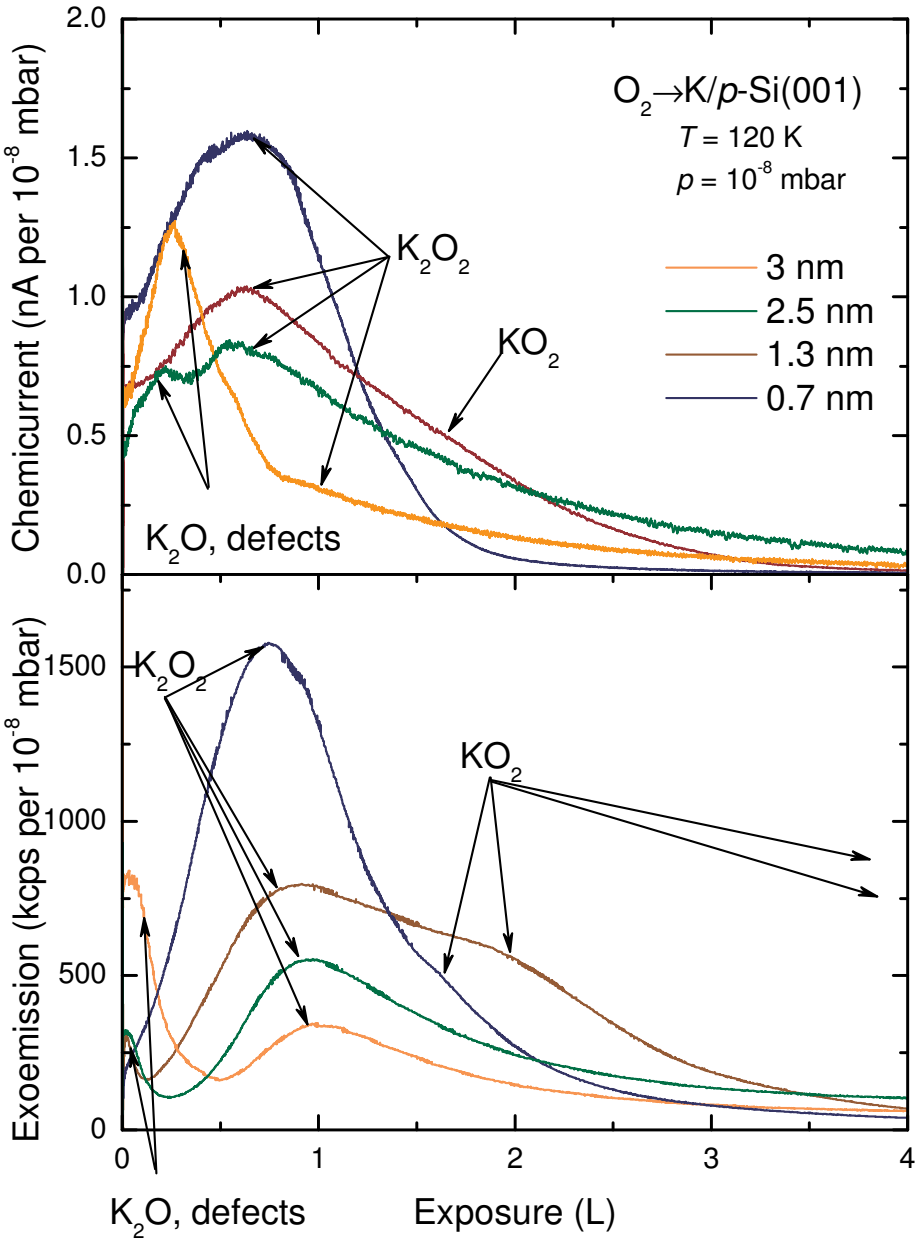

Figure 7.44.: Chemicurrent vs. exoemission for potassium samples of varying thickness on silicon. Both signals show a profound dependence of the signal shape and amplitude on the thickness.

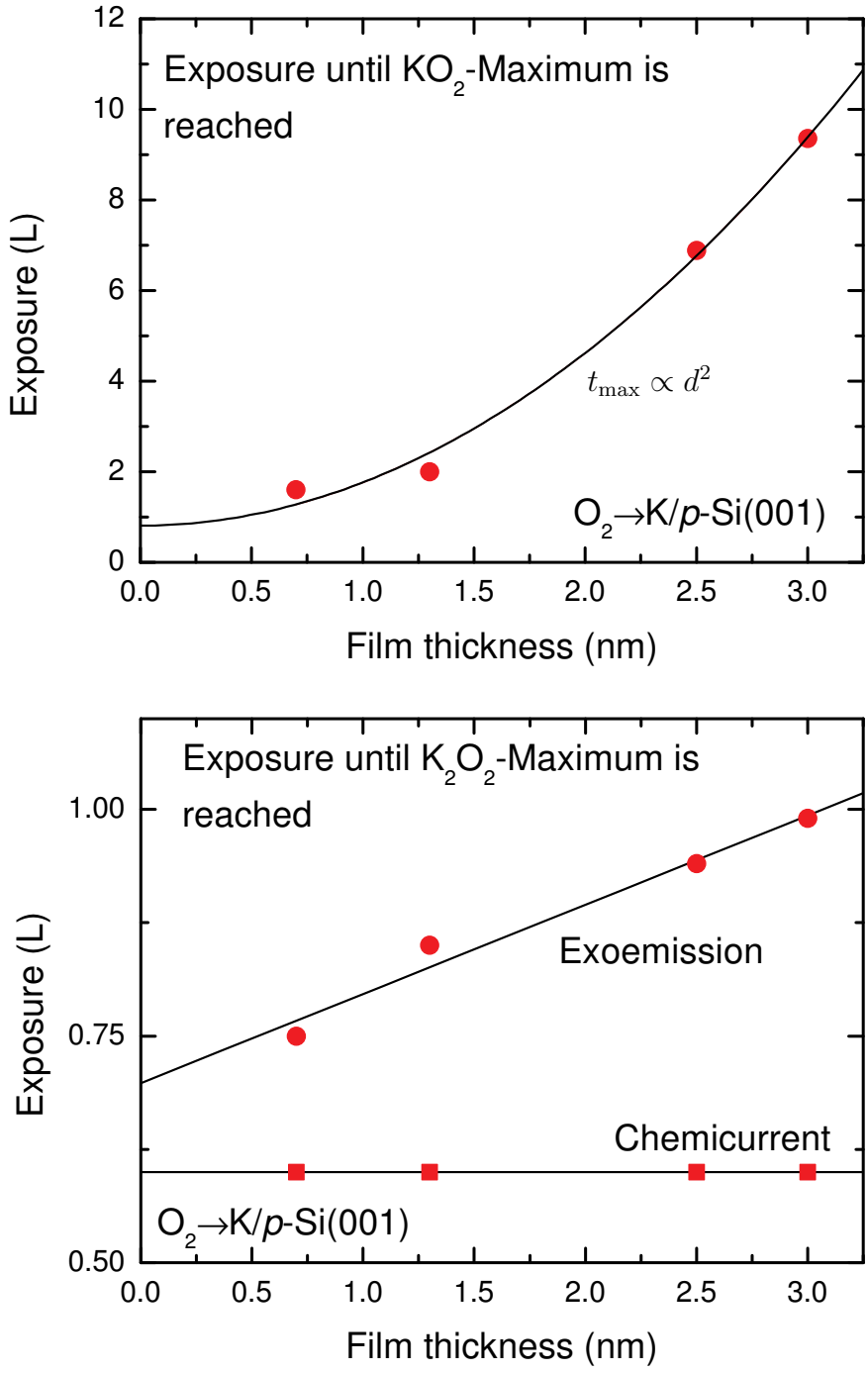

Figure 7.45.: Chemicurrent vs. exoemission for potassium samples of varying thickness on silicon. Both signals show a profound dependence of the signal shape and amplitude on the thickness.

linearly toward higher exposures with increasing film thickness. The upper panel shows the position of the last maximum of the exoemission as a function of film thickness. In contrast to the linear dependence we found for the peroxide related peak, a quadratic dependence is found for the position of the superoxide peak.

A close relation between the observed features in the chemicurrent and the exomission and the reaction products can be established. Figure 7.46 shows X-ray photo emission spectra in the O 1s region after exposing the samples shown in Fig. 7.44 to 20 L of oxygen. For the lowest thickness only peroxide and superoxide are present on the surfaces. This corresponds to the broad peak in the exoemission and the chemicurrent as well as to the shoulder present in the exoemission data. The peroxide feature is strongest for the lowest thicknesses because peroxide is only formed while the surface remains unoxidized. Subsequently offered oxygen becomes incorporated on top of the peroxide layer thus suppressing the peroxide signal slightly. This is only possible if potassium atoms diffuse through the oxide film. The X-ray spectrum for the 3 nm differs distinctively from the other spectra seen so far. While the molecular species follow the trend described earlier, there is a strong peak due to the presence of an atomic oxygen species on the surface. Its presence on the surface is caused by the dissociation of oxygen at defect sites that were introduced during the deposition of the potassium films. The number of defect site is not directly related to the thickness of the film but rather to the exact conditions of the dispenser and the silicon substrate. As a consequence they can not be controlled in a systematic manner. Yet, in spite of their presence they do not seem to have a direct influence on the two other processes. Possibly the other two processes occur in parallel on areas unaltered by the defects.

Interrupting the Oxygen Exposure

An additional interesting fact that helps to understand the origin of the shifts in the exoemission spectra is shown in Fig. 7.47. The exposure was interrupted well after the maximum of the chemicurrent was reached and switched back on later. The chemicurrent as well as the exoemission after the interruption is found to be lager albeit the oxygen pressure was constant. In section 7.2.3 on photo emission from oxidized potassium layers it was shown that the oxidation does not stop after the first monolayer. It was rather observed that the whole potassium film becomes oxidized essentially forming a thick superoxide film. This and the observed behavior of the chemicurrent gives evidence for the diffusion of potassium atoms through the oxide film thereby increasing the concentration of unreacted potassium on the surface. This is equivalent to stating

that the reaction conditions are set back to a previous state. As the signal was decreasing at the time of the interruption an increased signal is found when switching the oxygen supply back on.

Bias Dependence

Figure 7.48 shows the I/V-characteristics of a potassium diode under oxygen exposure. A diode characteristic with an additional current offset is observed. The forward bias region is dominated by the thermal emission current found in Eqn. (2.22). Due to the relatively high Schottky barrier of the alkali metal diodes photo currents are usually below 1 pA and cannot account for the high reverse current seen in the diagram. The usual chemicurrent is measured under zero bias conditions $V = 0\,\mathrm{V}$ in order to minimize the influence of capacitance related effect. Here, the dependence of the chemicurrent on the applied reverse bias voltage was explicitly checked and is found to be negligible. The absence of any bias dependence of the chemicurrent in the reverse direction indicates that emission over the barrier is the primary mechanism of chemicurrent generation. Voltage assisted tunneling and displacement currents do not seem to play a role as they would be highly sensitive to the applied voltage.

Spectrally Resolved Exoemission

The energy spectrum of the emitted electrons during an exoemission experiment was recorded. Figure 7.49 shows these spectra at different exposures for a thick potassium film during the first stages of the oxidation. As with the integral exoemission, cryogenic temperatures of 120 K were maintained in order to prevent dissociative adsorption. During the experiment the oxygen partial pressure was kept constant at $2 \times 10^{-9}\,\mathrm{mbar}$.

In general, the exoemission sets in sharply above the work function and shows an exponential tail off at higher energies. Depending on the energy of the primary excitation a shift between the work function and the maximum of the exoemission might be expected. Respective results have been shown for the oxidation of thin sodium films [BGG+93]. Indeed, the work function of the oxidized surface of 2.5 eV is only slightly less than the $\approx 2.7\,\mathrm{eV}$ binding energy of the $1\pi^*$ electrons in the peroxide. Within the resolution of this experiment ($\approx 250\,\mathrm{meV}$) it is therefore difficult to distinguish if the exoemission spectrum is peaked at an energy higher than the vacuum level cut off or not.

A maximum energy for the exoemission cannot be given because the signal tails of exponentially as depicted in Fig. 7.50. The data were fitted to a single exponential with

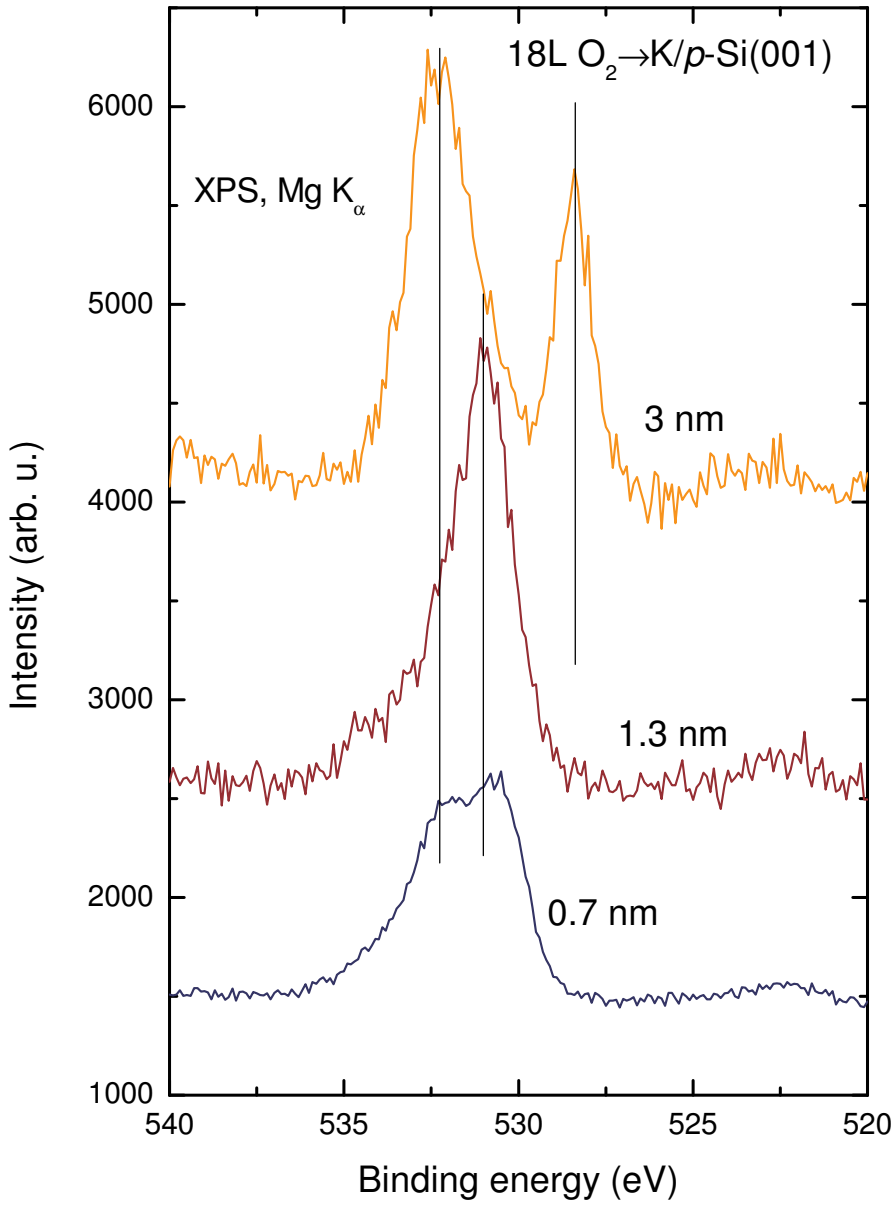

Figure 7.46.: The O 1s region of XPS spectra taken from the samples shown in Fig. 7.46) after an exposure to 18 L of molecular oxygen.

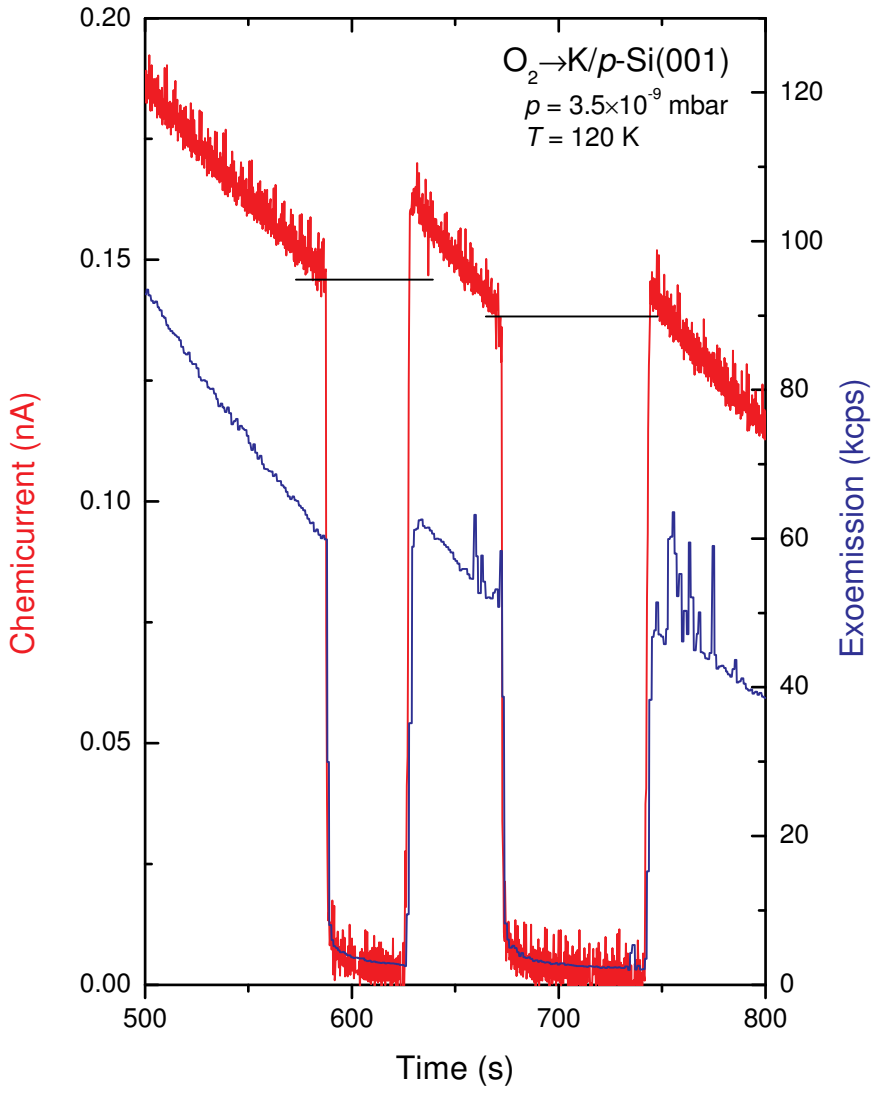

Figure 7.47.: Chemicurrent of a potassium film under oxygen exposure. When the oxygen supply is interrupted and switched back on later the chemicurrent sets in at a higher level than expected. The same effect is observable for the exoemission

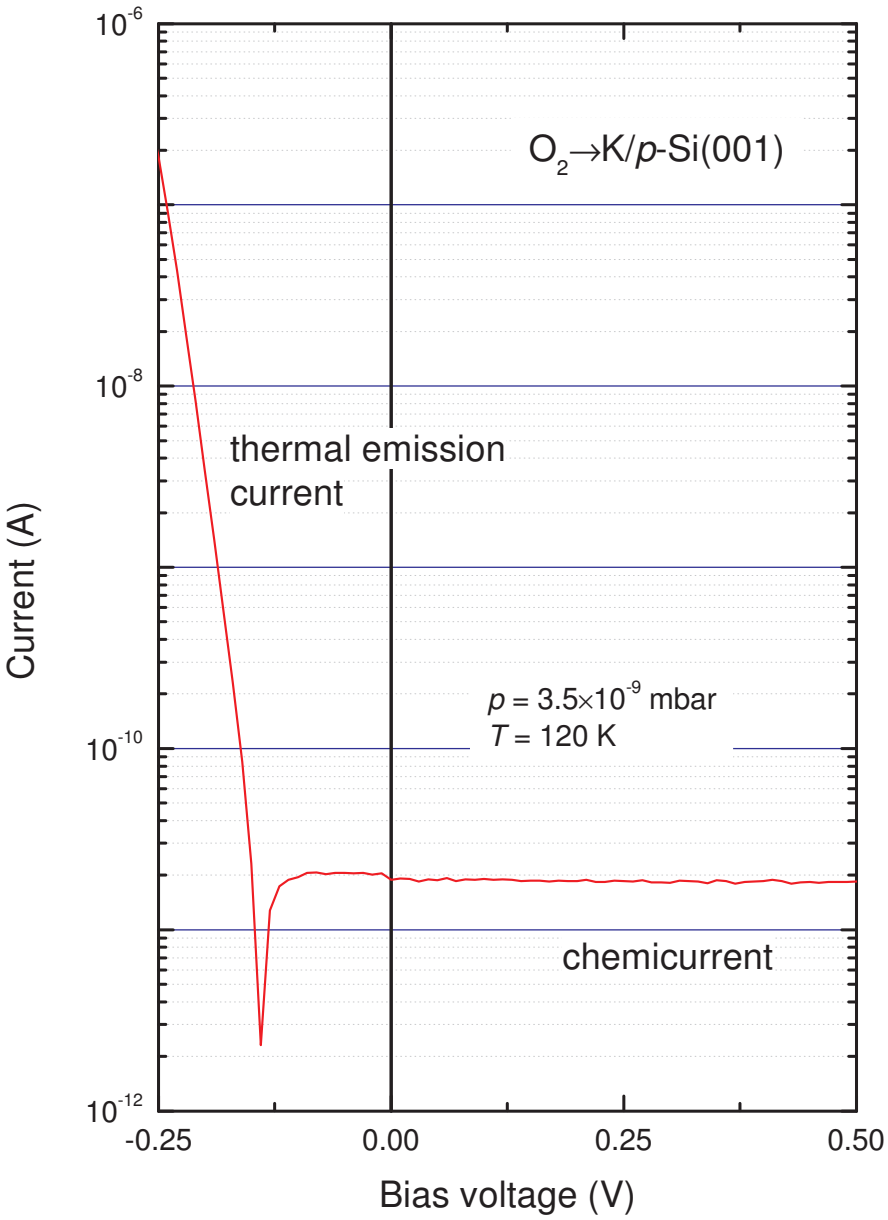

Figure 7.48.: Chemicurrent of a potassium film under oxygen exposure. The bias dependence of the chemicurrent under reverse-bias in negligible.

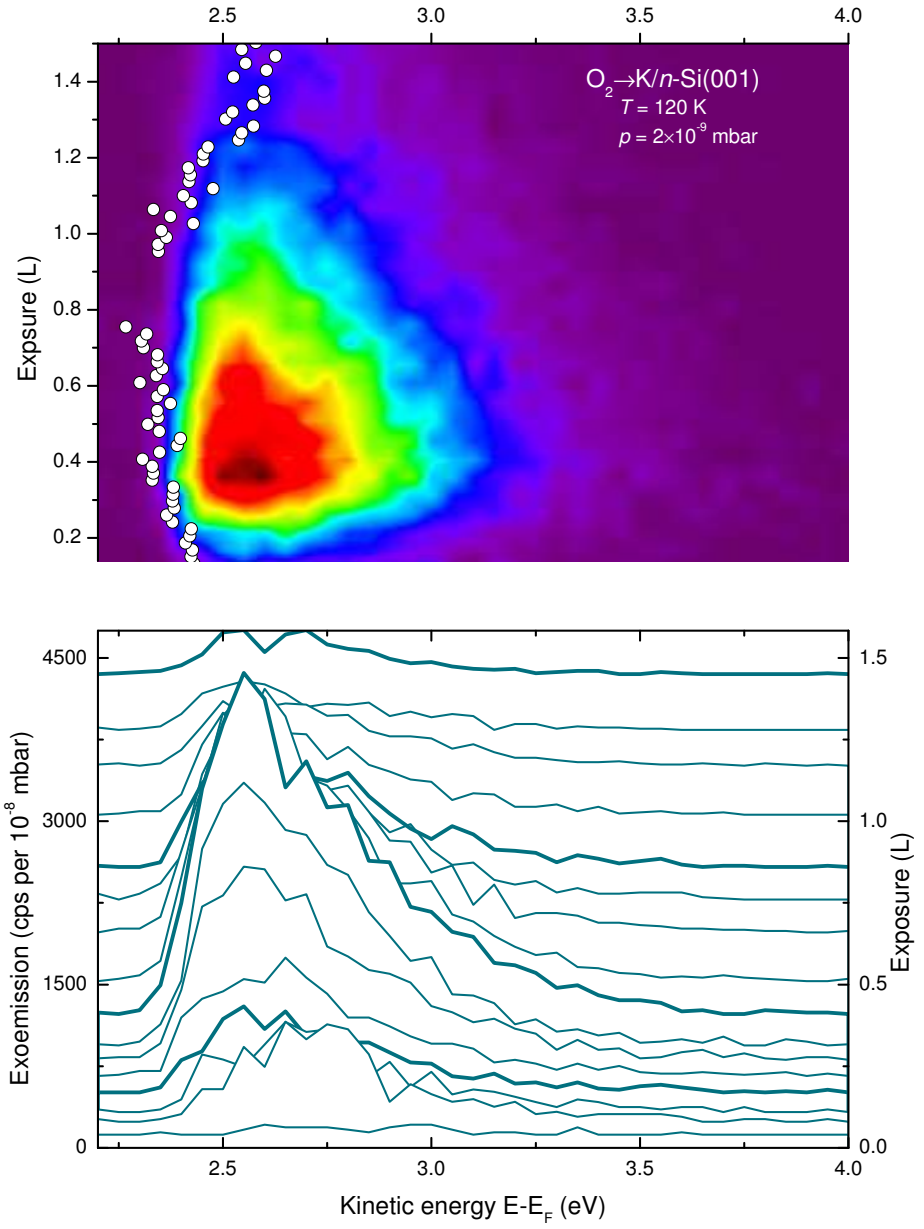

Figure 7.49.: Multi-layered potassium film deposited on n-Si(001) at 120 K - Exoemission spectra at a constant oxygen partial pressure of 2×10^{-9} mbar at 120 K. Circles are for comparison with Kelvin probe data.

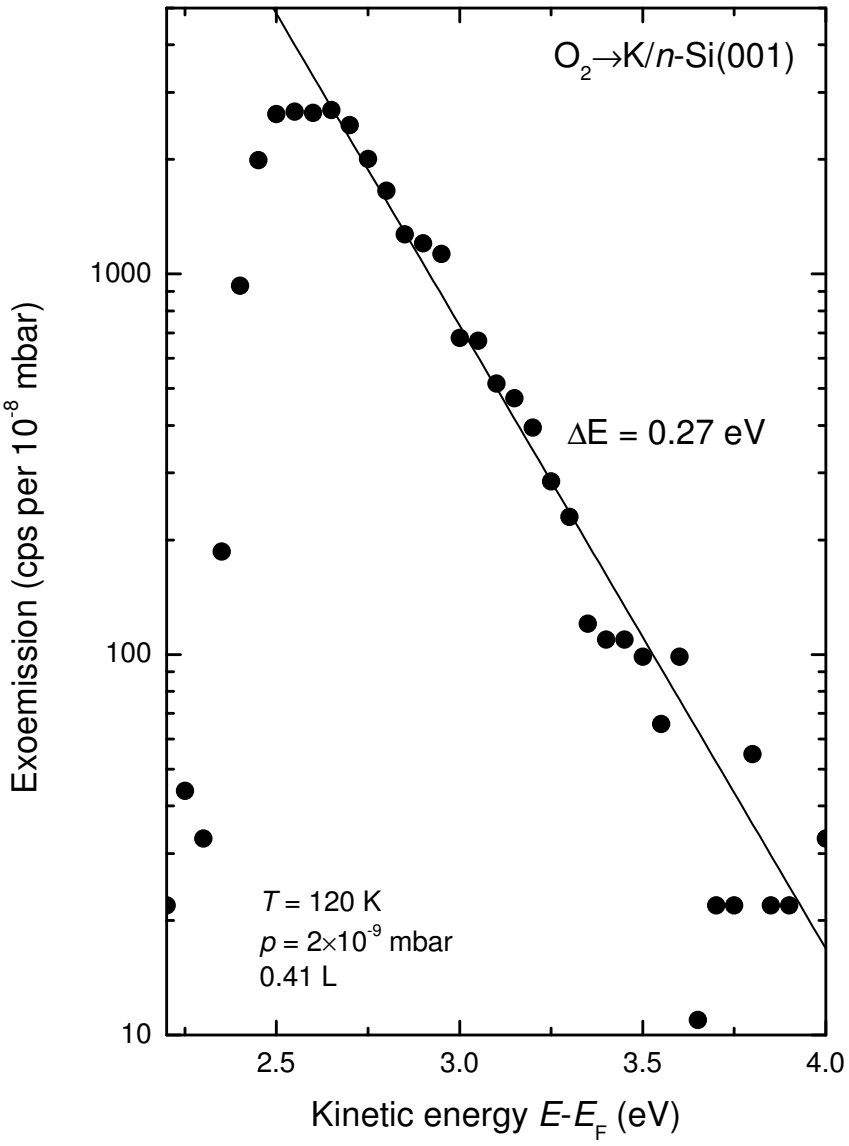

Figure 7.50.: Multi-layered potassium film deposited on n-Si(001) at 120 K - Exoemission spectrum at a constant oxygen partial pressure of 2×10^{-9} mbar at 120 K and an exposure of 0.41 L.

a slope of 270 meV which reproduces the data for a wide range of energies up to 4 eV above the Fermi level.

This seems to some extend be surprising because the electron binding energy is much less than that (≈ 2.7 eV in peroxide). On the other hand the enthalpy for the reaction is -495 kJ/mole or -5.13 eV per oxygen molecule which is well above the observed 4 eV. Still these results raise the question of how energy conservation should be introduced into theoretical calculation of exoemission and chemicurrents, e.g., can there be a hundred percent transfer of the available chemical energy into a single electron excitation.

Discussion

The chemicurrent and exoemission results fit the chemical trend that was observed in the photo electron spectra and was expected from the thermochemistry data. The dissociative adsorption increases in strength when moving upward in the periodic table. It is strongest for the lithium oxide which results in a large and rapidly decaying background in the chemicurrent. On the other hand the molecular adsorption is the strongest for potassium. Accordingly the chemicurrent is dominated by a single large maximum and shows only a small background transient. Finally, the chemicurrents observed on sodium films resemble a mixture between lithium and potassium as they show a large contribution from atomic oxygen as well as a peaked contribution from a molecular peroxide adsorption.

If the total reaction is dominated by a single process j, the exoemission and the chemicurrent are directly proportional to the reaction rate. In the ratio between the exoemission yield and the chemicurrent the reaction rate therefore cancels and an expression for the ratio

$$\frac{Y_{\mathrm{EE}}(t)}{I_{\mathrm{CC}}(t)} = \frac{\sum_i R_i(t)\alpha_{\mathrm{EE},i}(t)}{\sum_i R_i(t)\alpha_{\mathrm{CC},i}(t)} \approx \frac{\alpha_{\mathrm{EE},j}(t)}{\alpha_{\mathrm{CC},j}(t)} \tag{7.8}$$

can be determined experimentally. Figure 7.51 shows a normalized version $\zeta(t) = Y_{\mathrm{EE}}/I_{\mathrm{CC}}$ calculated from the traces shown earlier in this section. In the peroxide dominated region all the curves follow a general relation which can be modeled by the simple

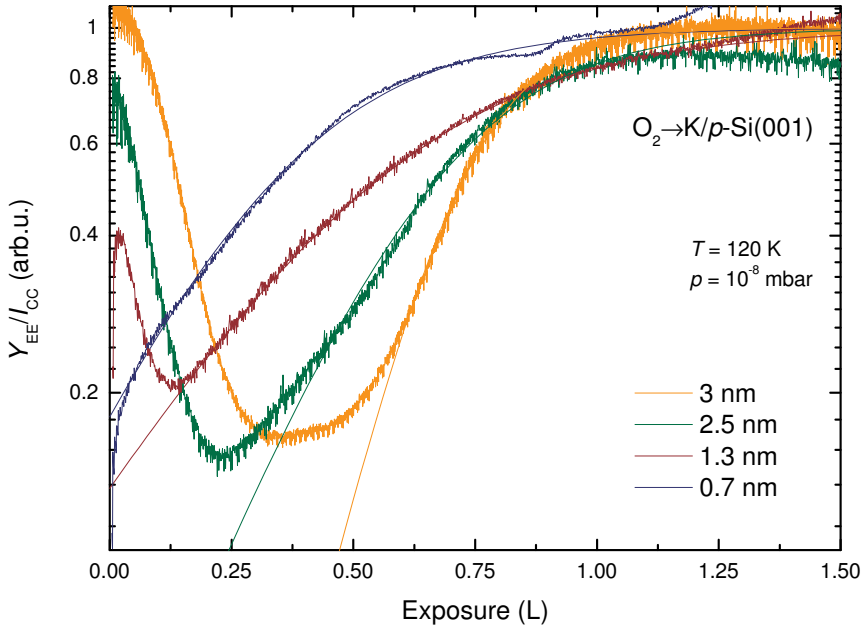

Figure 7.51.: Ratio between exoemission yield and chemicurrent normalized to its saturation value as a function of exposure.

function

$$\zeta(t) = \frac{Y_{\mathrm{EE}}(t)}{I_{\mathrm{CC}}(t)} = \frac{\zeta_{\mathrm{sat}}}{1 + \left(\dfrac{\zeta_{\mathrm{sat}}}{\zeta_0} - 1\right) \exp\left(-t/\tau_r\right)} \tag{7.9}$$

$$\approx \zeta_0 \exp\left(t/\tau_r\right) \text{ for small } t \text{ and } \zeta_0 \ll \zeta_{\mathrm{sat}}. \tag{7.10}$$

The later approximation is especially valid for thick potassium samples where the initial exoemission intensity is low and hence ζ_0 is small.

The quantity thus calculated may not have a direct physical meaning but it could be a useful check for theoretical calculations.

7.4.5. Rubidium and Cesium

The oxygen chemistry of rubidium as well as cesium is distinctly different from the lighter elements. They support a large variety of oxides which results in highly structured chemicurrent traces. The metal films were deposited directly onto the hydrogen passivated silicon substrate at a constant sample temperature of 120 K. The film thickness was chosen such that the metallic nature of the films could be verified in photo emission experiments which corresponds to a thickness of 5 ML to 10 ML.

Integral Exoemission and Chemicurrent

Figure 7.52 shows representative chemicurrent and exoemission traces for low exposures that were gathered while the films were exposed at an oxygen partial pressure of 10^{-8} mbar. As has been observed previously, the exoemission is initially suppressed on the cesium films [BGI+95]. A chemicurrent in contrast can be measured right from the beginning of the exposure. Two maximums are observable for the chemicurrent: a small one that is reached quickly after the start of the exposure and a large one that is reached around an exposure of 2 L. Interestingly, the exoemission is only significant at exposure levels at which the chemicurrent is already diminished significantly. On the other hand the chemicurrent tails of at a much larger rate than the exoemission.

The rubidium films show a much shorter induction period of the exoemission. The exoemission traces splits into a pronounced maximum that tails of in a similar manner as is seen for the cesium films and a second contribution that is seen as a shoulder to the left of the exoemission maximum. Likewise the chemicurrent traces show two features seen as a maximum that is reached quickly after the start of the experiment and a smaller maximum at around 1 L.

Fig. 7.53 presents exoemission yields and chemicurrent for a long term exposure of a thick cesium film. At higher oxygen exposures a second maximum of the exoemission is observed. The second maximum occurs well in the region of saturation of the surface and therefore at a time in the reaction where only superoxide forms. A tiny maximum in the chemicurrent can be observed which was not initially expected.

Spectrally Resolved Exoemission

The spectrum of the emitted electrons in the low exposure regime was monitored in more detail. Figure 7.54 shows spectra recorded during the exposure of a thick ceasium film. During the experiment the oxygen partial pressure was kept constant at 2.1×10^{-9} mbar.

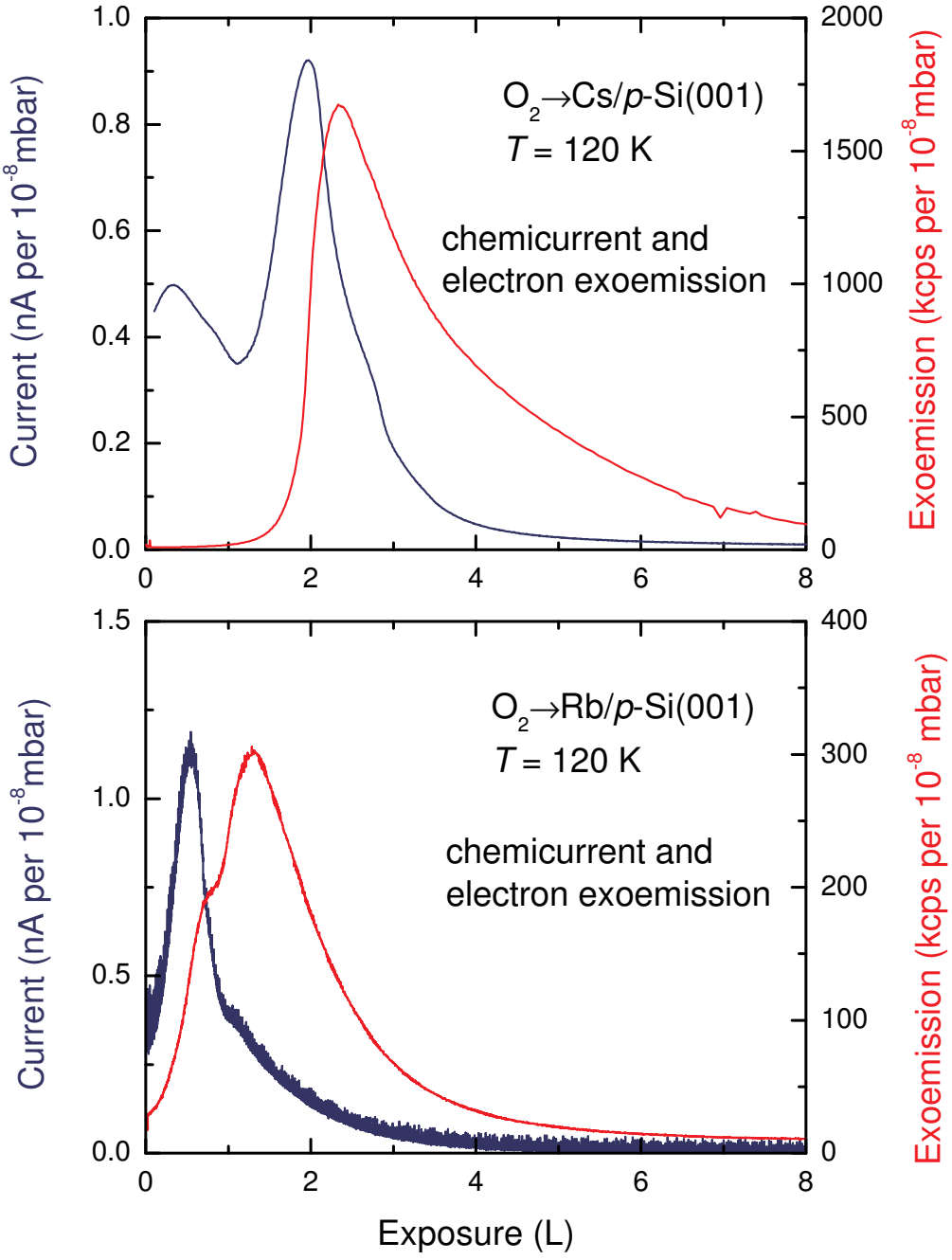

Figure 7.52.: Chemicurrent vs. exoemission for thick samples of cesium and rubidium on silicon.

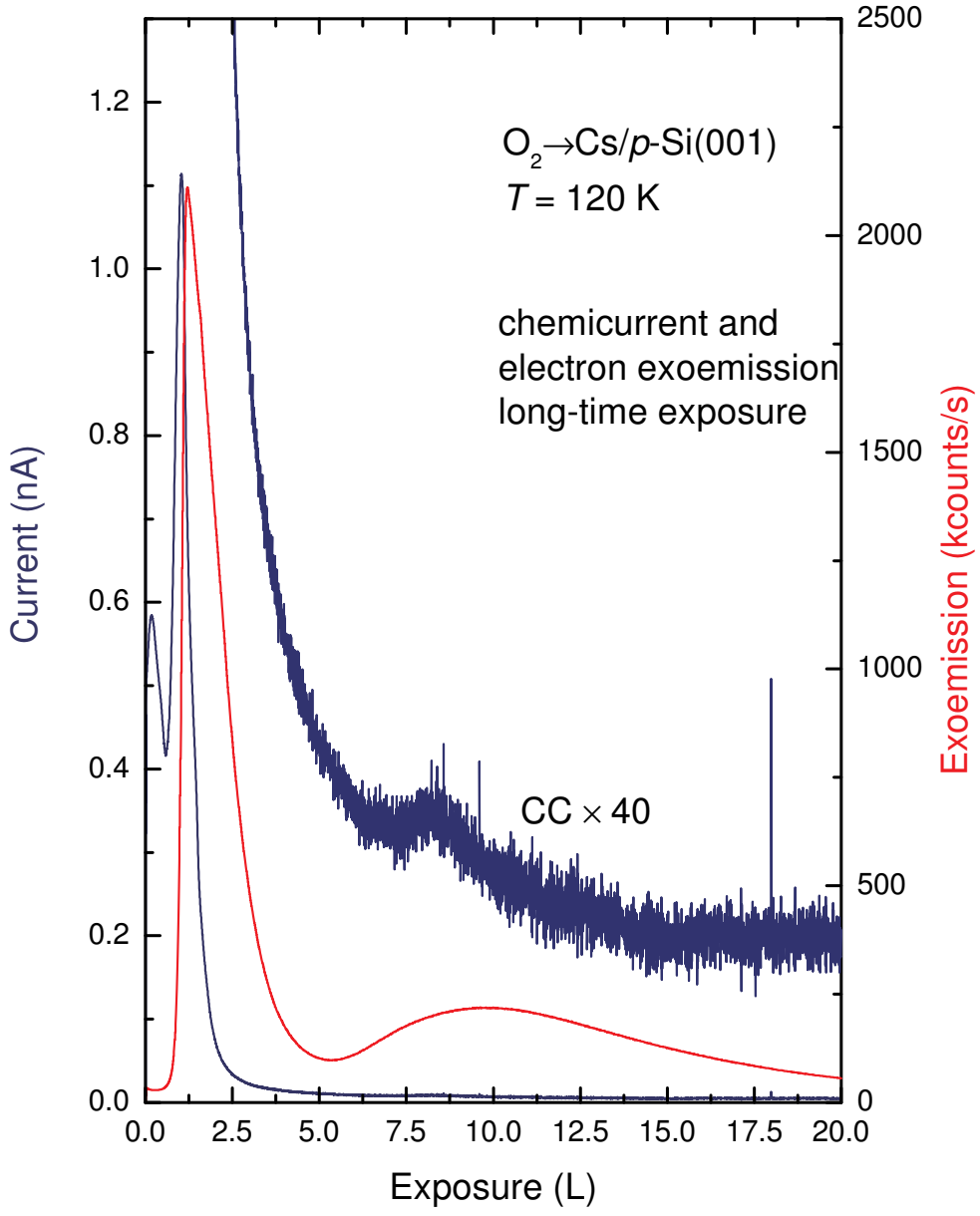

Figure 7.53.: Chemicurrent vs. exoemission for a thick sample of cesium on silicon. High exposure regime.

The sample temperature was 120 K.

The spectra are quite similar to the ones obtained for potassium. They set in sharply at the surfaces work function and tail off exponentially at higher energies (Fig. 7.55). However, the maximum of the exoemission does not coincide with the vacuum level for very low exposure. This observation is probably due to an inhomogeneous oxidation of the surface. Low work function patches on the partly oxidized surface spread the inset of the work function which causes the apparent shift of the maximum to higher energies. Another possibility is that energy in excess of the work function is truly transferred to a single electron. Indeed, the O^{2-} binding energy from UPS shows a peak at $E_B = 2.8\,eV$ [BGI+95, WSK+87], which is larger than the average work function.

Discussion

Rubidium and cesium have in common that the maximum of the chemicurrent as well as of the exoemission is located in a region where the surface changes from predominantly peroxide like to superoxide like [GFG+94]. At this point of the reaction the second charge transfer into the $O_2\pi^*$ is increasingly suppressed. It is therefore suggestive to appoint the non-adibatic effect to the first charge transfer $O_2 \rightarrow O_2^-$. However, it becomes apparent from the exoemission at high exposures that this cannot be entirely true: from the high exposure data shown it can be deduced that the second maximum of the exoemission is due to this first charge transfer as it occurs at a time in the reaction where no peroxide formation, and therefore no second charge transfer, is observed.

It could be argued that the first charge transfer is also responsible for the exoemission and the chemicurrent in the early reaction. This seems implausible because the same chemical process - the intermediate superoxide generation - would be inefficient in generating hot electrons in between two regions where it is very efficient.

A comparison between chemicurrent and exoelectron yield again shows a delayed emission of electrons. The maximum of the chemicurrent in the peroxide region precedes the exoemission maximum. The conclusion is the same as for potassium and sodium: the maximum of the chemicurrent as well as of the exoemission occur when the reaction rate already declines. The increase in non-adiabaticity (and thereby the chemicurrent and exoemission probability) exceed the decline in reaction rate and leads to the observed maxima.

It is not clear if the second maximum in the current is due to a regular chemicurrent. As was discussed in the theory section the interface between film and silicon substrate is also accompanied by a space charge. If the chemical environment of the interface

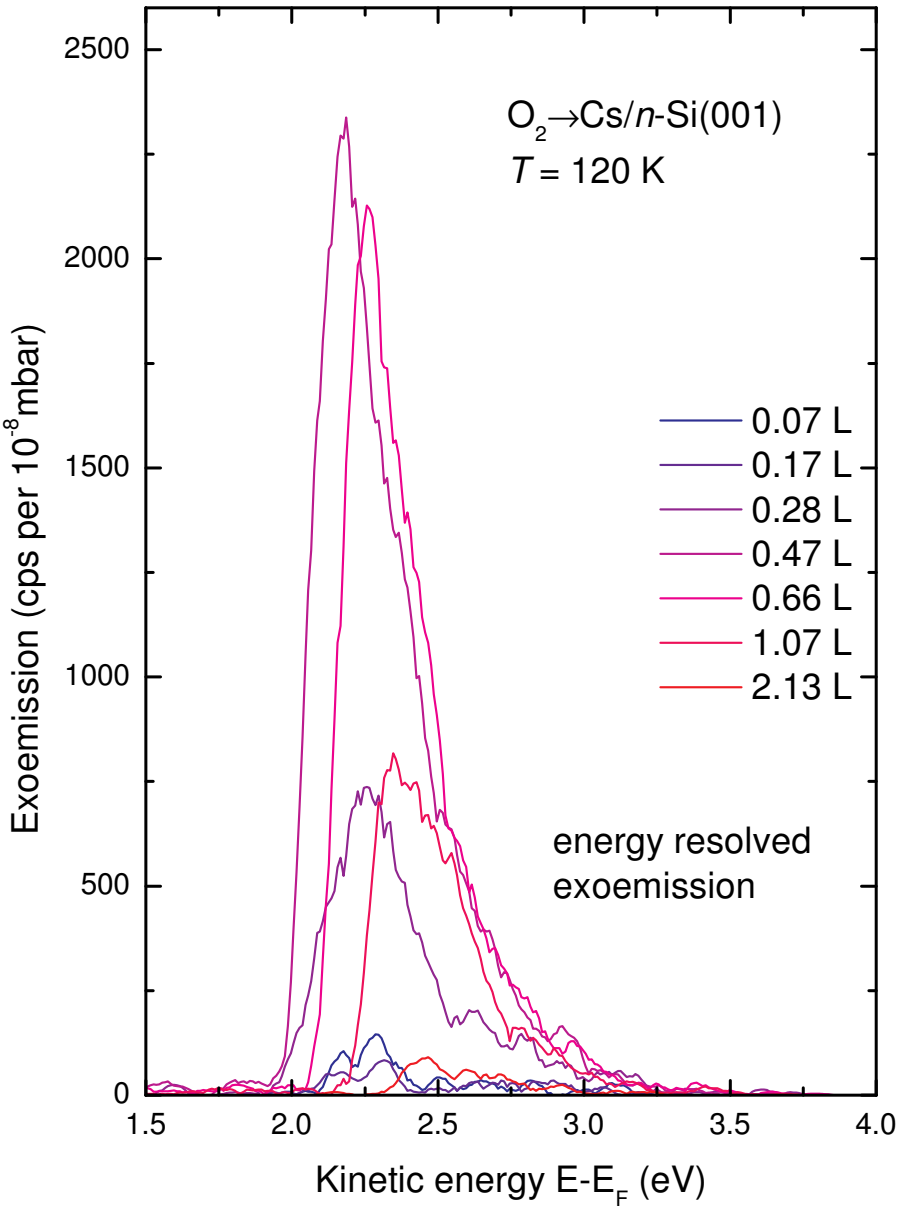

Figure 7.54.: Energy resolved electron exoemission from a thick sample of cesium on silicon under oxygen exposure. Exoemission at selected exposures.

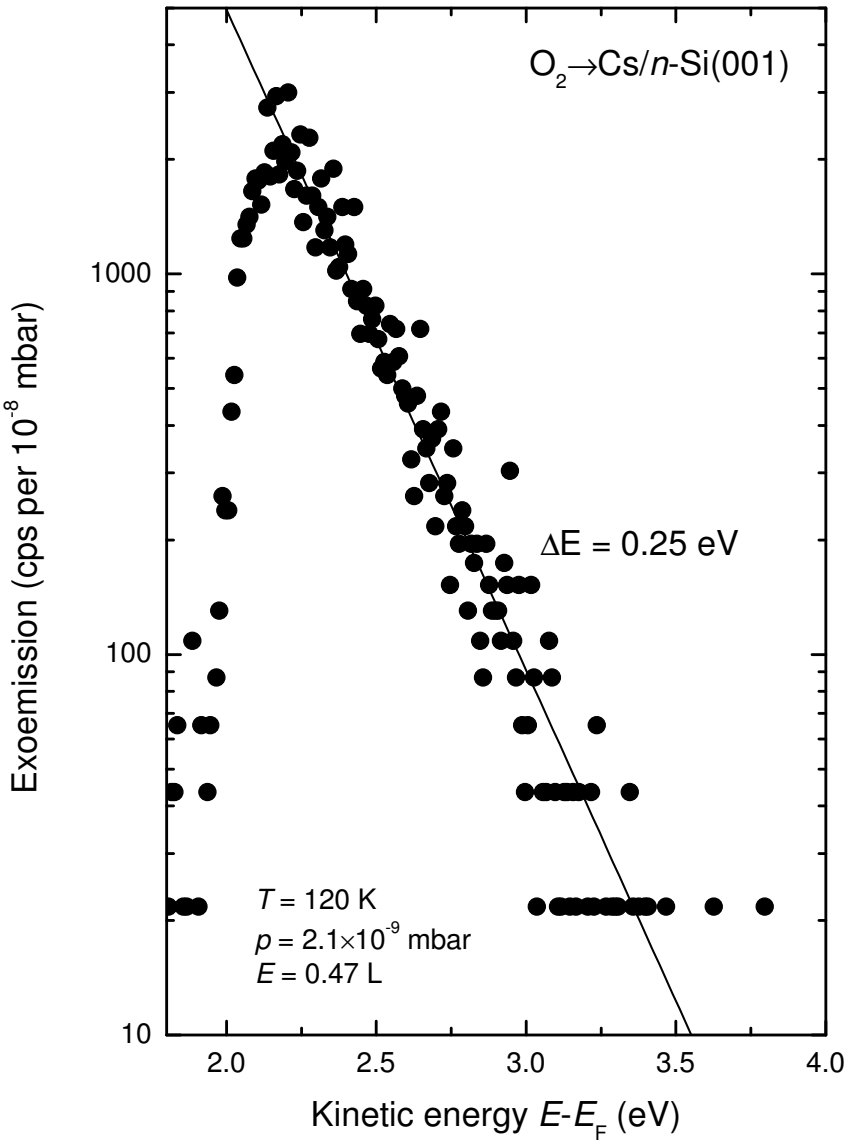

Figure 7.55.: Multi-layers cesium film deposited on n-Si(001) tt 120 K - Exoemission spectrum at a constant oxygen partial pressure of 2.1×10^{-9} mbar at 120 K and an exposure of 0.47 L.

is changed, so is the charge content of the space charge layer. Consequently a current through the device may be observed. A similar effect has been discussed by Hagemann *et al.* in a recent publication where a currentdue tot he formation of the Schottky barrier was superimposed on a regular chemicurrent due to non-adiabatic adsroption of magnesium atoms on a magnesium surface [UKN10a, UKN$^+$10b].

7.4.6. Chemical Trend

In Figure 7.56 an overview of typical chemicurrent and exoemission traces are presented. The detailed shape of the curves is quite different for every alkali metal. Still, similarities between the traces can be found. Pronounced maximums in both chemicurrent and exoemission show for all metals that were investigated. With the exception of lithium, these occur when the reaction products change from peroxide dominated to superoxide like. At this stage of the reaction the concentration of electrons at the surface drops below a certain limit. At this concentration of electrons the stable production of superoxide species becomes possible. It has been shown that this process is gradual and the concentration of electrons at the surface decreases exponentially (for UPS data, refer to Fig.7.19). In the figure, a vertical line marks the exoemission maximum that has been attributed to this region of electron depletion.

From these data, and in particular for the heavy alkali metals, is can be seen that the maximums of the exoemission of electrons and the chemicurrent do not occur simultaneously. Rather, the chemicurrent shows its maximum intensity before the exoemission reaches its maximum. As a figure of merit Γ[3], the ratio between chemicurrent at the time when the exoemission reaches its maximum value $I_{CC}(t_{max,EE})$ and the maximum chemicurrent intensity $I_{CC,max}$ is used. The use of such a relative unit reduces the error introduced through the uncertainty of the pressure calibration. Additionally, all contributions from transport losses cancel out making a comparison between different samples possible.

Figure 7.57 shows Γ as a function of the bulk bandwidth of the metal layer [Gre97]. As was observed in the previous sections, Γ is unity for metals with a large bandwidth, as in the case of Li. The chemicurrent maximum and the maximal exoemission occur at the same time. For metal surfaces with a small bandwidth, Cs and Rb, the chemicurrent has already decreased to almost half its maximum value when the emission of electrons is most pronounced. A line has been included as a guide to the eye that separates the

[3]This must not be confused with the resonance width describing the interaction of the adsorbate with the metal surface in the Newns-Anderson model.

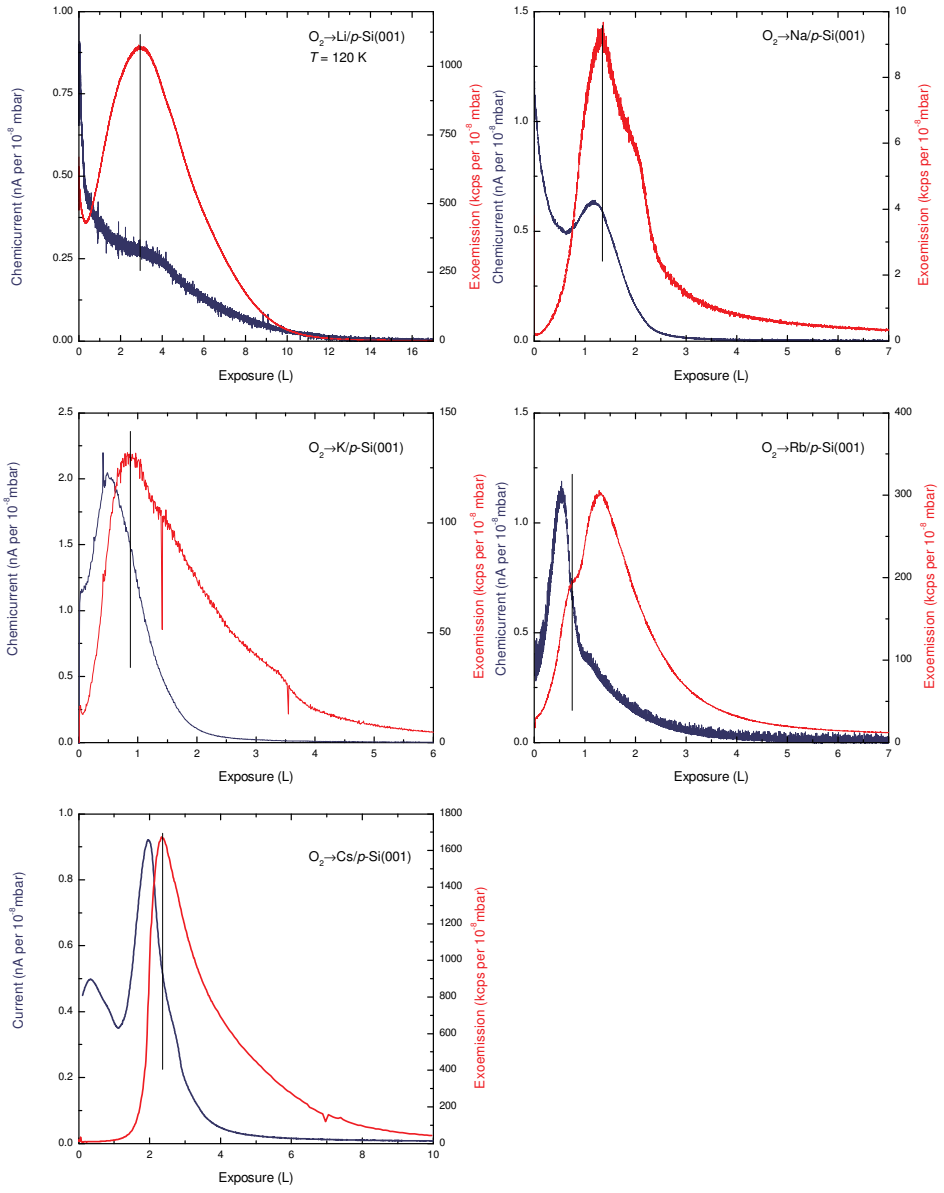

Figure 7.56.: Overview of exoemission and chemicurrent data for the alkali metals studied in this work. Apparently, the maximum of the exoemission is seen at higher exposures than the one of the chemicurrent.

region of possible values of Γ and the region of Γ values that have not been observed. Secondly, data points for extremely thin potassium films have been included into the plot. For thick, bulk like films Γ is substantially less than unity and follows the trend observed for the other alkali metals. Decreasing the film thickness leads to a shift toward higher Γ values approaching unity.

A possible explanation for the chemical trend seen in this shift starts from the observation that the bandwidth of the conduction band increases when going downward in the periodic table. While the bandwidth is almost 5 eV for lithium, it reduces to 1.5 eV for cesium. Figure 7.58 refers to the chemical hole injection picture used for the description of the exoemission process. Auger processes are responsible for the ejection of exoelectrons while the chemicurrent is sustained by resonant hole injection.

For metals with a large bandwidth, the possibility of a resonant charge transfer into the conduction band is present at all times. For this reason exoemission and chemicurrents in lithium can be observed at the same time. If the conduction band is quite narrow, the unoccupied adsorbate state must be injected below the band bottom for exoemission to be efficient. The resonant ionization mechanism does not work if the adsorbate state is pressed below the band bottom. The Auger process responsible for the emission of exoelectrons on the other hand is unaffected by the reduced bandwidth.

Considering the statistical nature of the adsorption process this leads to a simple explanation of the delayed maximum of the exoemission: the maximum of the exoemission is only reached if the surface conditions allow the adsorbate state to be pressed far below the band bottom. Resonant processes being the most efficient process for chemicurrents cannot occur under these conditions, hence, the chemicurrent efficiency is already reduced.

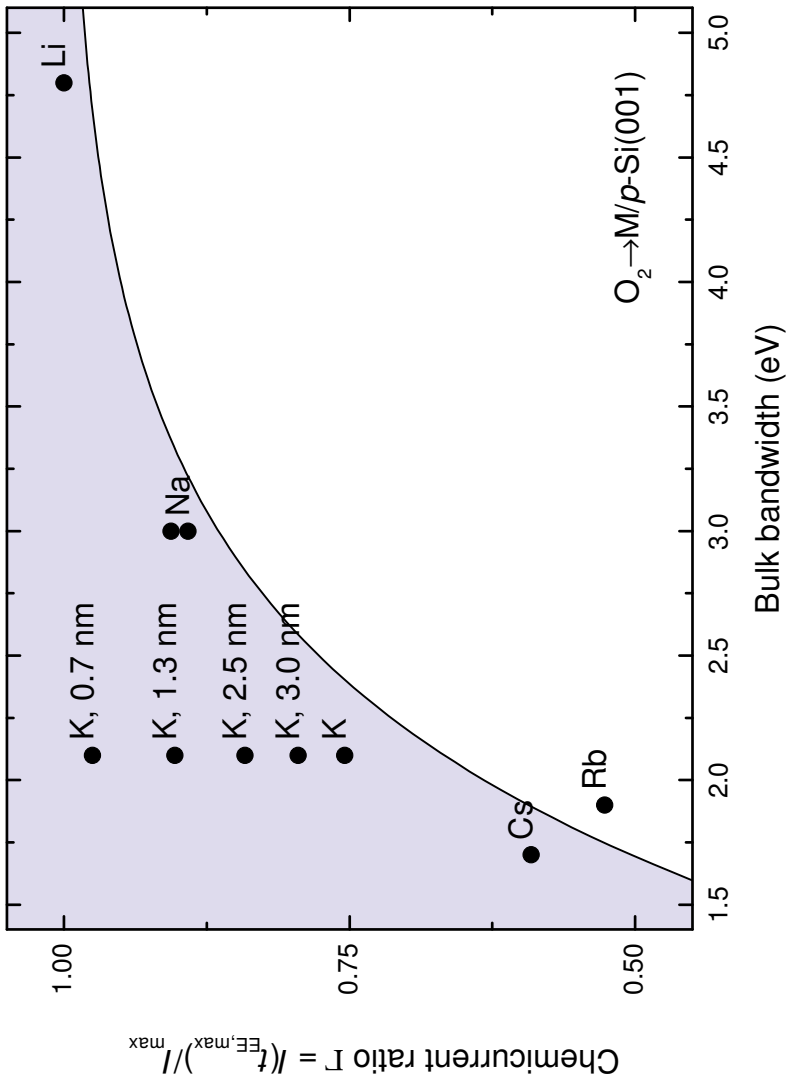

Figure 7.57.: The ratio between chemicurrent at the time when the exoemission reaches its maximum value $I_{CC}(t_{max,EE})$ and the maximum chemicurrent intensity $I_{CC,max}$ plotted as a function of the bulk bandwidth of the deposited metal.

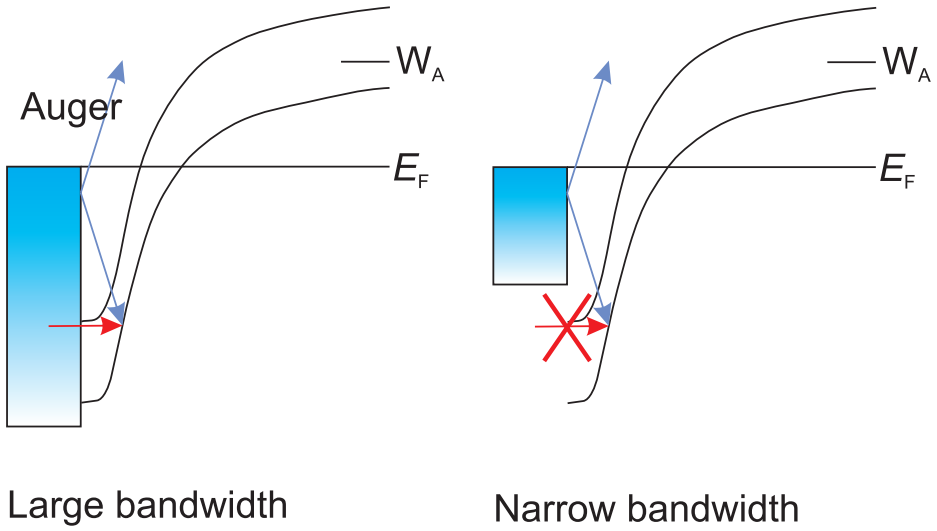

Figure 7.58.: Model of non-adiabatic excitation during the adsorption of oxygen on an alkali metal surface. Influence of the bandwidth of the underlying metal on the possible relaxation mechanism.

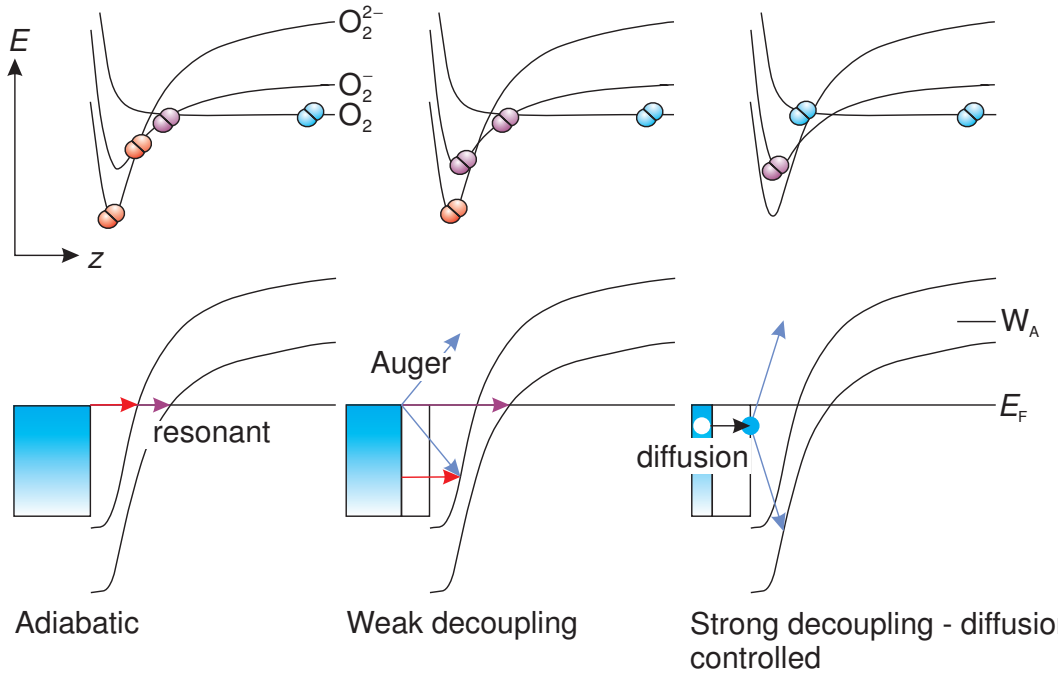

Figure 7.59.: Model of non-adiabatic excitation during the adsorption of oxygen on an alkali metal surface. Influence of the changing surface conditions on the non-adiabaticity of the charge transfer.

7.5. A Model of Chemicurrent and Exoemission Transients

A thorough description of the non-adiabatic effects in the alkali oxidation must include both the reaction kinetics and the dynamics of the single process. While the former can be accessed by standard surface science methods, the later is much more difficult to handle. In the previous chapters experimental data for the non-adiabatic dynamics of the reaction were presented using the methods of chemicurrent and electron exoemission. From these data it became apparent that a simple proportionality between the chemicurrent and the reaction rate is insufficient to explain the experimental results. Most theoretical methods cannot solve this problem easily because they require a detailed knowledge of the surface geometry which is clearly not available even if the experiment started out with a single crystalline surface.

The oxide formation in the reaction $O_2 \rightarrow K$ serves as a model for the molecular adsorption of oxygen on an alkali metal film. It has been shown that there is a continuous

progression from the initial peroxide formation on the clean film toward the production of potassium superoxide if the surface is already covered with oxygen. Two charge transfers are therefore involved in the reaction: a first one forming the superoxide species and a second one which is responsible for the peroxide formation. The first charge transfer is seen even for highly oxidized surfaces while the later process can only be observed for the clean surface.

In Fig. 7.59 the underlying excitation mechanisms are depicted for different states of the surface. In the upper panel, diabatic potential energy surfaces representing the chemisorption well of the oxygen molecule in its neutral, singly charged and doubly charged states are shown. The lower panel contains the corresponding single electron picture comprising the continuum of metal states to the left and two single electron states located on the molecule crossing the Fermi level. From left to right the oxygen coverage is thought to increase as depicted by the white bar between the molecular states and the metal.

In the preceding section it was shown that the chemicurrent can be explained by the resonant transfer of electrons from the metal onto the molecule effectively giving rise to a hot hole current into the semiconductor. Two parameters determine the chemicurrent efficiency (a) the effective interaction potential and (b) the maximum binding energy of the one-electron adsorbate states. In the extreme if the interaction potential is quite large the electronic states will be filled right at the Fermi level and neither a chemicurrent nor exoemission will be observed if one neglects the small contributions from the electronic friction mechanism.

For potassium peroxide the situation on the clean surface is as such that the hole survival probability for the second charge transfer is large enough to contribute a substantial chemicurrent but not to generate exoemitted electrons. The time to fill the hole is small compared to the time that is needed for the nuclei to reach their equilibrium position because the surface can easily provide the necessary electrons. Therefore the maximum excitation energy is much smaller than the equilibrium binding energy of the electrons. Hence the reaction cannot provide the necessary energy for the exoemission of an electron via an Auger process.

If during the course of the reaction the surface becomes oxidized two effects will contribute to an increased non-adiabaticity

- some of the surface atoms will already be close to the distorted structure of the peroxide unit cell. It will therefore be easier for an impinging oxygen molecule to find an adsorption place that releases the equilibrium chemical energy.

- the existing oxide layer decouples the metal states from the surface thereby reducing the interaction potential with the oxygen molecule.

Both effects lead to a reduction of the ratio between the time needed to reach the adsorption position and the average time to fill the molecular hole state. While this also has an influence on the chemicurrent efficiency the effect on the exoemission yield is much more pronounced (the exoemission yield increases exponentially with respect to the chemicurrent). Eventually, the energy level of the adsorbate state will drop below the band bottom while it is still substantially unoccupied which suppresses the resonant charge transfer. From this point on the chemicurrent efficiency should start to decrease because less charge is directly injected into the band. The only way for the hole state on the molecule to relax is through an Auger process which increases the probability of exoemission.

At highest exposures diffusive transport of potassium atoms to the surface must be considered as the driving force of the reaction. Because the oxide layer is too thick for the electrons to tunnel through, zero-valent alkali atoms have to diffuse through the layer thus providing the necessary electrons at the surface. At this point the reaction becomes similar to a gas phase reaction of isolated atoms because of the extremely low density of reaction partners for the oxygen molecules. Obviously this leads to the point at which the first charge transfer onto the molecule becomes strongly non-adiabatic leading to exoemitted electrons. The chemicurrent on the other hand is quenched because the transport through the non-conduction oxide film is suppressed.

8. Model Calculations

8.1. Density Functional Calculations: Potassium Peroxide

A potassium surface with an O_2 adsorbate impinging at the K(100) hollow site was simulated in a slab model using density functional theory (DFT) on the Kohn-Sham level. All calculations were carried out in the framework of the Vienna Ab-initio Simulation Package (VASP) [KH93, KH94b, KH94a]. Potentials for the projector augmented wave (PAW) method employing the Perdew-Burke-Ernzerhof generalized gradient approximation which were supplied with the DFT package were used for both the potassium as well as the oxygen atoms [Blö94, PBE96, KJ99]. The K potential treated the 2s, 2p, and 3s states as valence states. A cutoff energy of 300 eV was used for the dynamic as well as for the static calculations.

Static Calculations The surface was modeled by a 6-layer K slab in a $7 \times 3 \times 3$ super cell using a potassium lattice constant of 5.33 Å. The oxygen molecule was placed in parallel to the surface and on top of the K(100) hollow site. The molecular axis was pointing toward its corners. A 5×5 k-point mesh including the gamma point was used during the relaxation runs.

The anion position was determined by relaxing the oxygen atoms, the four potassium atoms surrounding the hollow site and the potassium atom directly under the molecule. The found position determines a local minimum of the total energy. Figure 8.1 shows the resulting adsorption geometry of the oxygen molecule. As has been expected from the much larger density of the oxides a substantial rearrangement of the potassium atoms surrounding the oxygen ion takes place. Its rhombohedral structure resembles the bulk structure of potassium peroxide. The identification of the ionic state as peroxide like is confirmed by the large intra molecular distance of 1.51 Å which is typical for an adsorbed peroxide. Additionally, a Bader charge analysis which showed a total charge of $1.7\,e_0$ on the molecule which is only slightly short of the expected two additional charges [HAJ06].

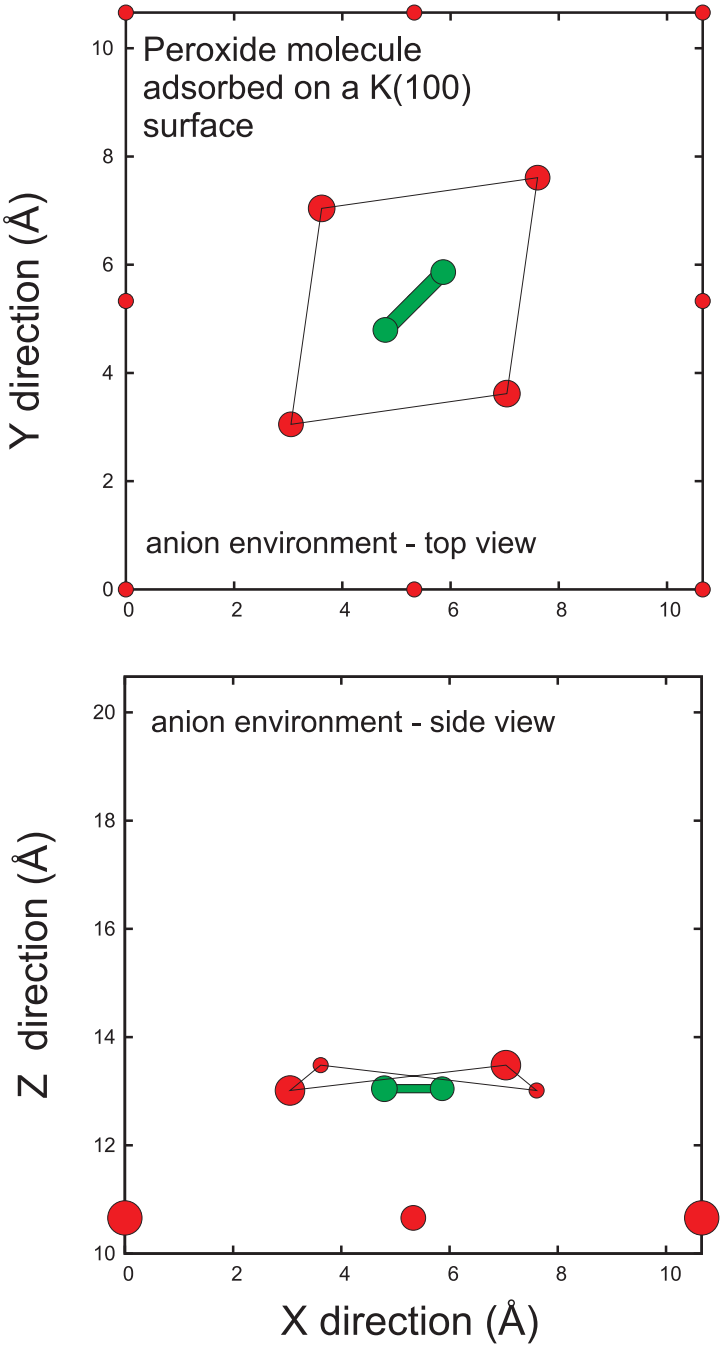

Figure 8.1.: Peroxide like adsorption site of an oxygen molecule on a K(100) surface. The four potassium atoms surrounding the hollow site and the second layer atom underneath the oxygen molecule were allowed to relax into their equilibrium position.

Adiabatic Molecular Dynamics Simulation Keeping in mind that the surface needs to undergo a substantial reconstruction, it seems unlikely that a potential energy surface with a rigid surface should adequately reflect the physics of the peroxide adsorption on a potassium surface. Out of the many possible trajectories one should be chosen that reflects the typical processes as there are

- molecular adsorption
- restructuring of the surface
- charge transfer
- stretching of the O-O bond

For the adiabatic molecular dynamics simulation the system size was reduced to a $7 \times 2 \times 2$ super cell and a $3 \times 3 \times 1$ grid of k-points. Again the highly symmetric position above the K(100) hollow site was used as a starting point. To speed up the calculations the oxygen molecule was placed 4 Å above the top-most layer and was given an initial kinetic energy of 476 meV. This assumes that far away from the surface most of the binding energy is transformed into kinetic energy of the molecule. Only the four potassium atoms and the potassium atom directly under the hollow site were allowed to move in the simulation. Because of the initial symmetry of the supercell no angular momentum can be transferred onto the molecule.

Figure 8.2 shows snapshots at intervals of 25 fs while the oxygen molecule impinges on the surface. The upper panel of Fig. 8.3 shows the total potential energy (black line) in the supercell and the kinetic energy (orange line) while the molecule penetrates the surface layer and undergoes a hard collision with the subsurface potassium atom. The middle and lower panel show the oxygen-oxygen bonding distance and the distance between the molecules center of mass and the subsurface potassium atom.

Far from the surface most of the potential energy is converted into translational energy of the oxygen molecule while it is attracted due to its image potential. While charge is transferred from the surface into the anti-bonding π^* orbital the oxygen-oxygen bond is weakened and the bonding distance increases monotonously. Nearer to the surface, the top-layer potassium atoms are accelerated toward the oxygen molecule which reduces the size of the surface cell. Finally, the molecule penetrates the top surface layer and collides with the a subsurface potassium atom. Due to the nearly equivalent mass of the molecule and the atom most of the kinetic energy is transferred directly onto the atom. The molecule stretches even further and starts to oscillate on its way back.

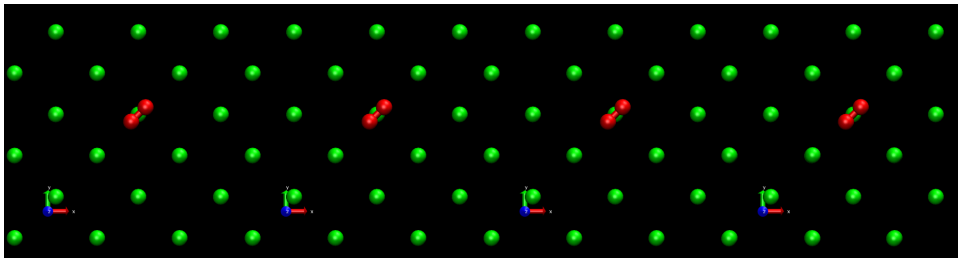

(a) 0 fs (b) 25 fs (c) 50 fs (d) 75 fs

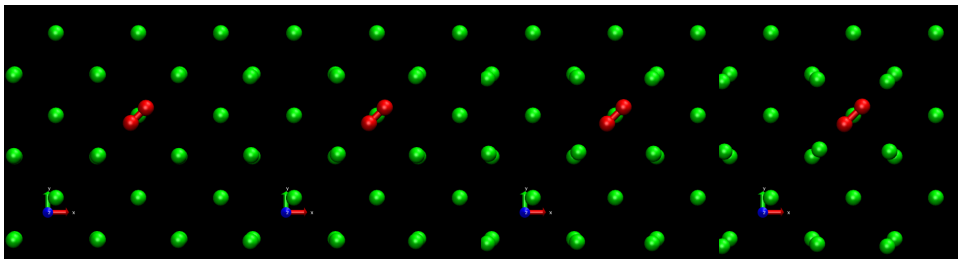

(e) 100 fs (f) 125, fs (g) 150 fs (h) 175 fs

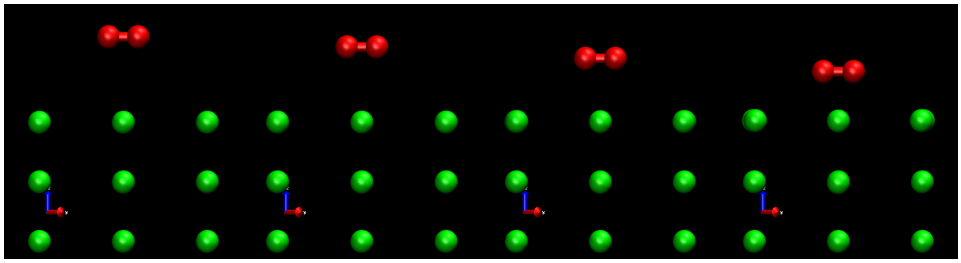

(i) 0 fs (j) 25 fs (k) 50 fs (l) 75 fs

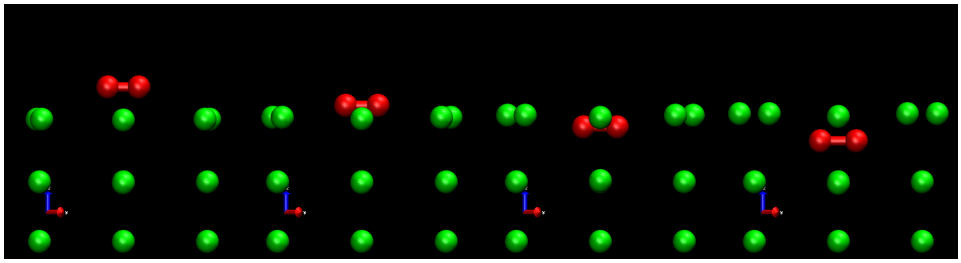

(m) 100 fs (n) 125 fs (o) 150 fs (p) 175 fs

Figure 8.2.: Still images of the molecular dynamics simulation of an oxygen molecule impinging on top of the hollow site of a K(100) surface. The molecular axis lies parallel to the surface plane and points toward two of the potassium atoms surrounding the hollow site. The molecular dynamics simulation starts at a molecule-surface plane distance of 4 Å.(Additional data in the electronic version)

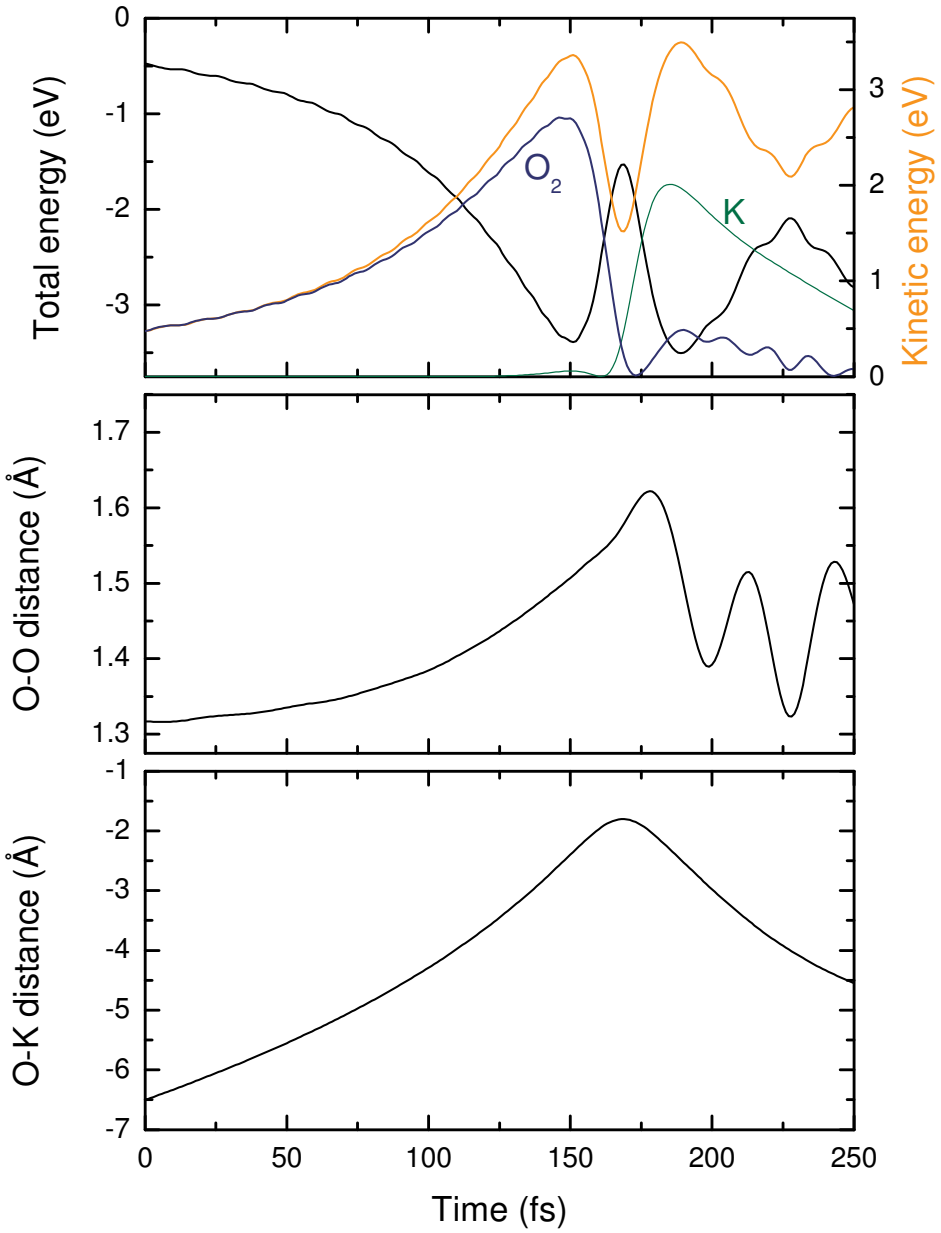

Figure 8.3.: Total energy, oxygen bond length and distance between sub-hollow site K atom and the molecule for an O_2 molecule impinging at the hollow site of a K(001) slab.

Figure 8.4 shows the evolution of the Kohn-Sham eigenvalues relative to the Fermi energy during the simulation. In general, formerly occupied states tend to shift upwards in energy, whereas formerly unoccupied states shift downward as they are filled. Because of its localized nature, it is easy to recognize the oxygen related molecular states. Initially they are located close to the Fermi edge and are therefore only partly occupied. On the way to the surface they shift slowly toward higher binding energies as they are attracted by the image potential. Likewise, the metallic states of the potassium film shift upwards as they become less occupied.

As the peroxide ion contains two additional electrons in an anti-bonding orbital it is not stable in the gas phase. In contrast, the surrounding potassium ions stabilize a doubly charged oxygen configuration when it is embedded in the crystal. In addition, the oxygen molecule itself needs to expand to lower the Coulomb repulsion between these electrons. Surprisingly, the later process seems responsible for quickly pushing down the electron levels, a process which can be observed as a steep descent of the energy around 150 fs.

Although a spin-polarized solution would be expected from the gas phase configuration of the oxygen molecule, and which is indeed reached by DFT for a molecule in a single supercell, the DFT results remain spin-unpolarized for all molecule surface distances. This should be considered a failure of the current implementation of DFT and cannot be easily mended. A possible solution to this problem, that at the same time allows the calculation of diabatic PES, is the decoupling of the molecular states from the metal by imposing constraints on the allowed basis functions for the two subsystems [Beh04]. In addition, constraints on the number of allowed electrons as well as the number of spins on the molecule may be kept fixed while calculating a self-consistent potential and the corresponding wave functions. This approach has been used to successfully describe the oxidation dynamics on aluminum surfaces and have been implemented into commercially available ab-initio packages. While theses schemes may be installed reasonably easy in all electron codes using atomic basis functions [Beh04], an implementation into plain waves codes as in VASP requires a larger afford because of the conceptually different approach.

A diabatic description in this sense may lead to reasonably correct results for the alkali-oxygen system if the weak mixing between the molecular and metallic states are considered. Unfortunately, the artificial decoupling between the molecular and metallic states renders the results less useful for the intended non-adiabatic description of electron-hole excitations. Mostly this is because of the lack of mixing that the interac-

tion matrix elements cannot be extracted from the projected density of states but must be computed explicitly from the potential and the diabatic wave functions. Although this does not pose as much of a problem for more detailed calculations that rely on the direct calculation of the Hamiltonian, it strongly diminishes the virtues of a simple model calculation.

For the use of this study the spin-unpolarized solution will be considered as *good enough for the purpose* and will be used further on.

The steep descend of the electronic levels caused by the expansion of the molecule is particularly interesting because experimental work by White *et al.* showed an efficient coupling between large amplitude molecular vibrations and electronic degrees of freedom, e.g., they observed exoemission of electrons for highly vibrationally excited NO molecules impinging on a cesiated gold surface [WCM$^+$05]. Recently the underlying mechanism has been attacked theoretically using an extension to Tully's surface hopping algorithm which included single electronic excitations [Tul90, RST09]. This mechanism may be of more general relevance as the impinging molecule is set into a highly excited vibrational state ($\nu \approx 4$ for the MD run shown above) by the very collision with the surface itself. Even if the vibration itself is not responsible for the excitations (The KS eigenstates do not cross the Fermi level again and the molecule does not work as an actual charge pump.) it accelerates the descent of the electronic levels. This is because the motion in the chemisorption well caused by the image charge potential is much slower than the motion caused by the vibration of a light molecule. One could see this mechanism as an intermediate between molecular and dissociative adsorption as the dissociation can be seen as being caused by an extremely large vibrational excitation. In this light the proposed influence of the vibrational motion on the non-adiabaticity of the reaction can be understood as an intermediate step toward previously proposed mechanism of exoemission from dissociative chemisorption [GFG$^+$94]

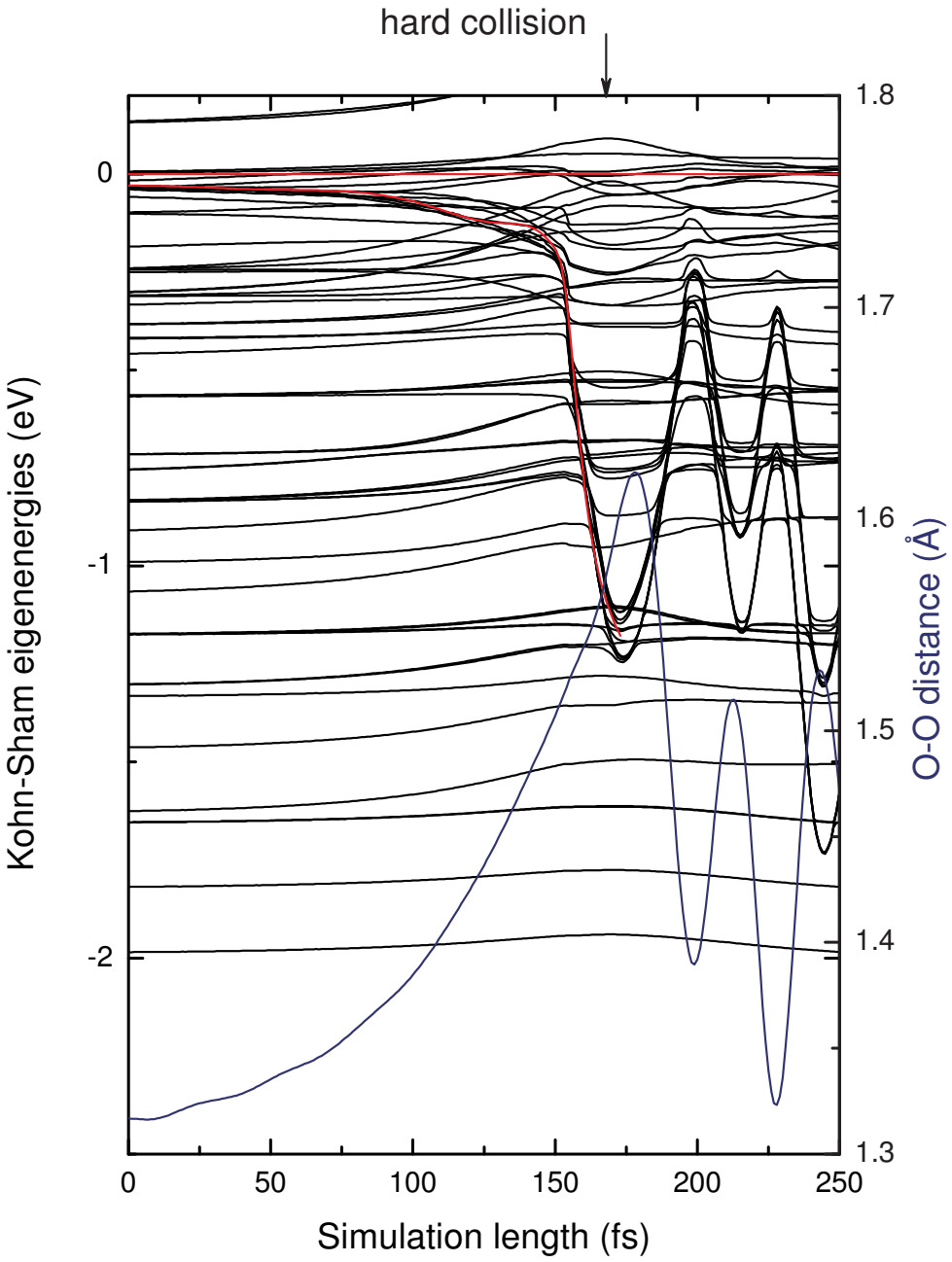

Figure 8.4.: Kohn-Sham eigenenergies for an O_2 molecule impinging at the hollow site of a K(001) slab.

8.2. Non-adiabatic Model

The underlying mechanism of both chemicurrent and exoelectron emission is the non-adiabatic charge transfer of electrons from the metal substrate onto the molecule and possibly back to the metal. A Newns-Anderson model Hamiltonian has been parameterized using the numerical results from the MD-DFT calculations presented in the previous section. The method cannot be expected to yield quantitative results for the chemicurrent (or exoemission) yield but must be seen as a tool to describe general features of non-adiabatic excitations. At the same time, the model describes the physical processes accurately enough to go beyond a mere rate-equation based description as it explicitly includes quantum mechanical mechanisms [Hag54]. Especially, it may help to understand the origin of the often assumed and calculated *temperature like* excitation spectra [TGB$^+$02, KNN07, TK09].

Parameterization

The upper panel in Figure 8.5 shows the density of states projected onto the p_x or equivalently the p_y orbitals of one of the oxygen atom. Lorentzians given by Eqn. 3.41 were used to fit the projected density of states from DFT on a logarithmic scale. The fitting procedure yields the parameters V_{ak} by virtue of (3.42) and the center of the surface resonance ε_a plotted in Fig. 8.5.

Because of the ionic nature of the bond, and therefore the lack of mixing between the wave function of the molecule and the metal states the width of the ad-atom resonance Γ is only of the order of 20 meV even in close vicinity of the surface. Determining such narrow resonance widths is only possible by using an dense distribution of k-vectors and a small smearing parameter in the calculations. As this significantly increases the required amount of memory and computation time it was only calculated for selected points on the trajectory and in a non-selfconsistent calculation which used the charge density of the molecular dynamics run.

The metallic states were distributed evenly over a width of 5 eV with the band bottom at -2.5 eV. Convergence of the numerical results was reached when using 511 metal states per spin direction and a total number of 512 electrons which results in an approximately half filled band. Further details on the numerical integration of the Schrödinger equation can be found in Appendix B.

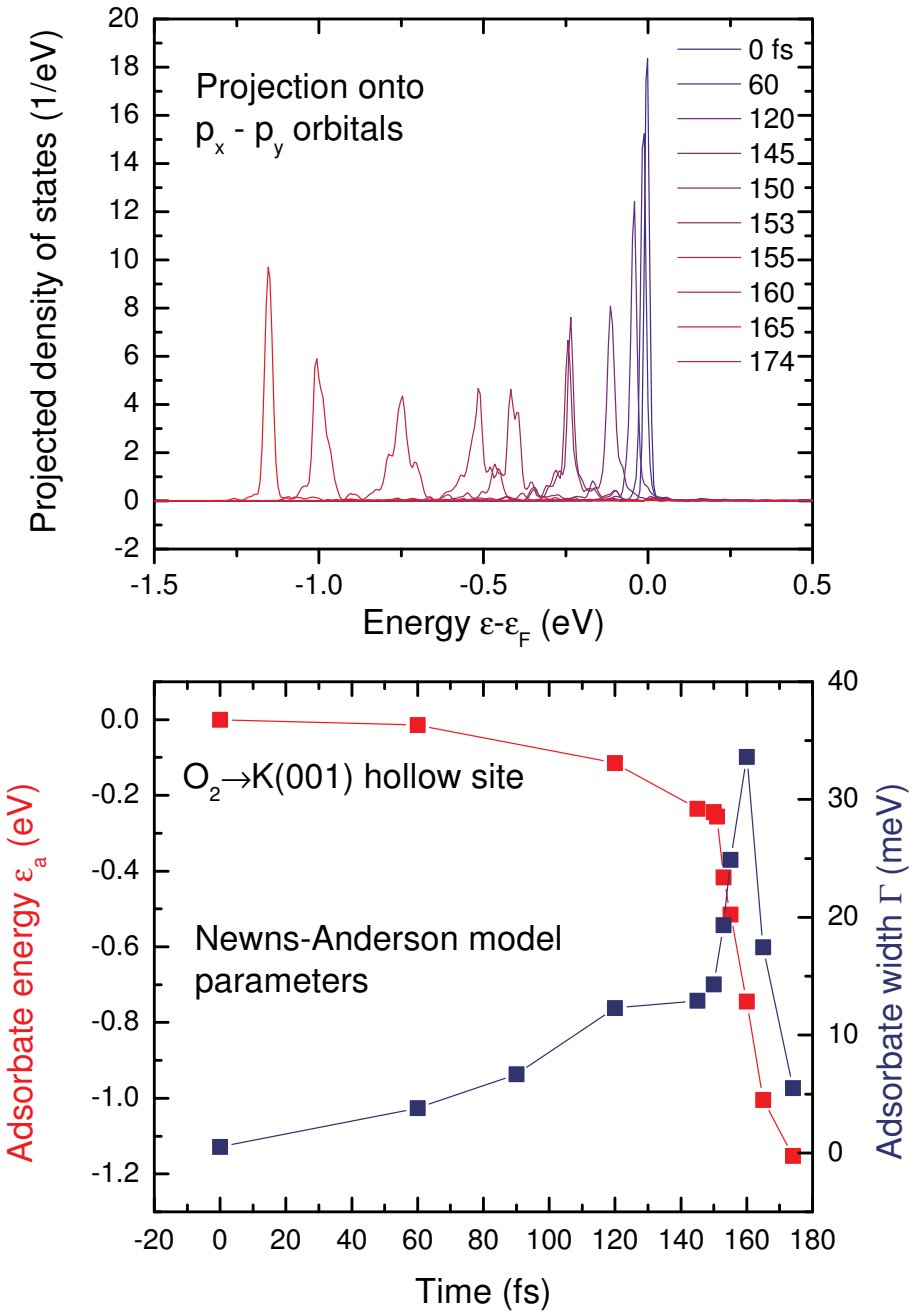

Figure 8.5.: Upper panel: Kohn-Sham density of states projected onto p_x (or equivalently p_y) orbitals of one of the oxygen atoms in the molecule. Lower panel: Parameters for the Newns-Anderson model Hamiltonian that were extracted from from the data in the upper panel.

Excitation Spectra

Figure 8.6 shows snapshots of the excitation spectra $n^{\mathrm{ex}}(t)$ calculated for the system parameters given in Fig. 8.5. Both panels show the same dataset on a linear (upper panel) and on a logarithmic scale (lower panel). The dotted line shows the Gaussian with a root mean square deviation of 20 meV used to approximate the δ-distribution introduced in the definition of excitation spectrum (see Eqn. (3.49)). Areas of the spectrum with an excess of electrons point upwards, hot holes are indicated by negative numbers. The initial electron temperature was set to 120 K, close to the experimental conditions.

Because the total number of electrons must be conserved in the simulation the same number of electrons and holes are excited. There is no rule that fixes the sum of electron hole-pairs to a special number or requires the spectra to be symmetric. In the case of oxygen on potassium where the interaction matrix elements are small and negative charge is transferred onto the molecule this results in a sharp distribution of electrons around the Fermi edge and a spread out distribution of hot holes.

The general features of the hot hole distribution can be understood based on the classical picture of charge transfer and *chemical hole diving*. Because the molecular states are initially located at the Fermi edge they are half filled. As the states are pushed down below the Fermi edge hole density is transfered from the molecule to the metal proportional to the number of holes n_{ha} in the molecular state at the given time. If the rate of change of the adsorbate energy is small and fairly constant the exponential decrease of the transfer rate translates from the time domain into the spectra:

$$\frac{dn_{ha}}{dt}\frac{dt}{dE} = \text{const.} \times \exp\left(-t/\tau\right)\frac{dt}{dE} \tag{8.1}$$

$$= \text{const.} \times \exp\left(-E/k_{\mathrm{B}}T_{\mathrm{eff}}\right) \tag{8.2}$$

In the range between -0.5 eV and the Fermi edge, which is swept by the adsorbate state on the incoming trajectory in the chemisorption well, an effective temperature like distribution according to (8.2) is well reproduced in the calculated spectra. The sharp drop of the electron energy when the molecule hits the surface on the other hand leads to a nearly constant distribution of hole density. Because the rate of change of the one electron energy is high the occupation of the molecular state remains fairly constant while the energy sweeps the range between -1.25 eV and -0.5 eV. As a consequence the probability of a hole transfer remains constant throughout and a constant distribution of hot holes is generated.

The electron distribution cannot be understood in the light of these semi-classical considerations. The electron spectrum features a sharp distribution near the Fermi edge which are caused by the additional density of states that was introduced into the band by the adsorbed molecule. In thermal equilibrium this must result in a slight shift of the Fermi energy. A similar effect appears in the adiabatic distribution which needs to be subtracted from the non-adiabatic case. As a result a term proportional to $df/d\varepsilon$ appears in the spectra which is only significantly different from zero near the Fermi edge.

On the logarithmic scale appreciable quantum mechanical contributions at energies far from the resonance center become apparent. The level broadening leads to excitations which are otherwise not possible and which are small compared to the dominant features discussed above which have classical counterparts. Some of the contributions are probably caused by the oversimplification of the wide band limit (constant V for all $|k\rangle$) and the constant density of states employed in this simulation.

Total energy

A theory relying on a trajectory based approach relies heavily on the assumption that the trajectory used for the calculation of the electronic Hamiltonian is also a good approximation of the trajectory associated with the non-adiabatic electron density. Especially, this can be checked by comparing the total energy of the adiabatic system to the energy transferred into electron hole pairs. If the later is small compared to the former one may conclude that this assumption may be a good one. In Figure 8.7, the total energy change $\Delta E = \langle\langle \sum_i h_{\mathrm{el}} \rangle\rangle - \langle\langle \sum_i h_{\mathrm{el}} \rangle\rangle_{t0}$ of the electronic system[1] has been plotted as a function of time. The red squares represent the adiabatic solution while the green circles denote the non-adiabatic total energy. The difference between the two is the energy transferred into electron-hole pairs and is plotted as blue triangles.

The adiabatic and the non-adiabatic solution reveal total energies which differ by approximately 10%.

Fermi edge shifting

Especially in the limit of a vanishing resonance width the sharply pointed distribution of electrons at the Fermi edge can be understood by the renumbering of states as the adsorbate state crosses the metallic energy levels. Figure 8.8 depicts the physical situation in this case. Initially, the states μ_i in this example are thought to be eigenstates

[1] As always, the spin index has been dropped because of the spin degenerated solution.

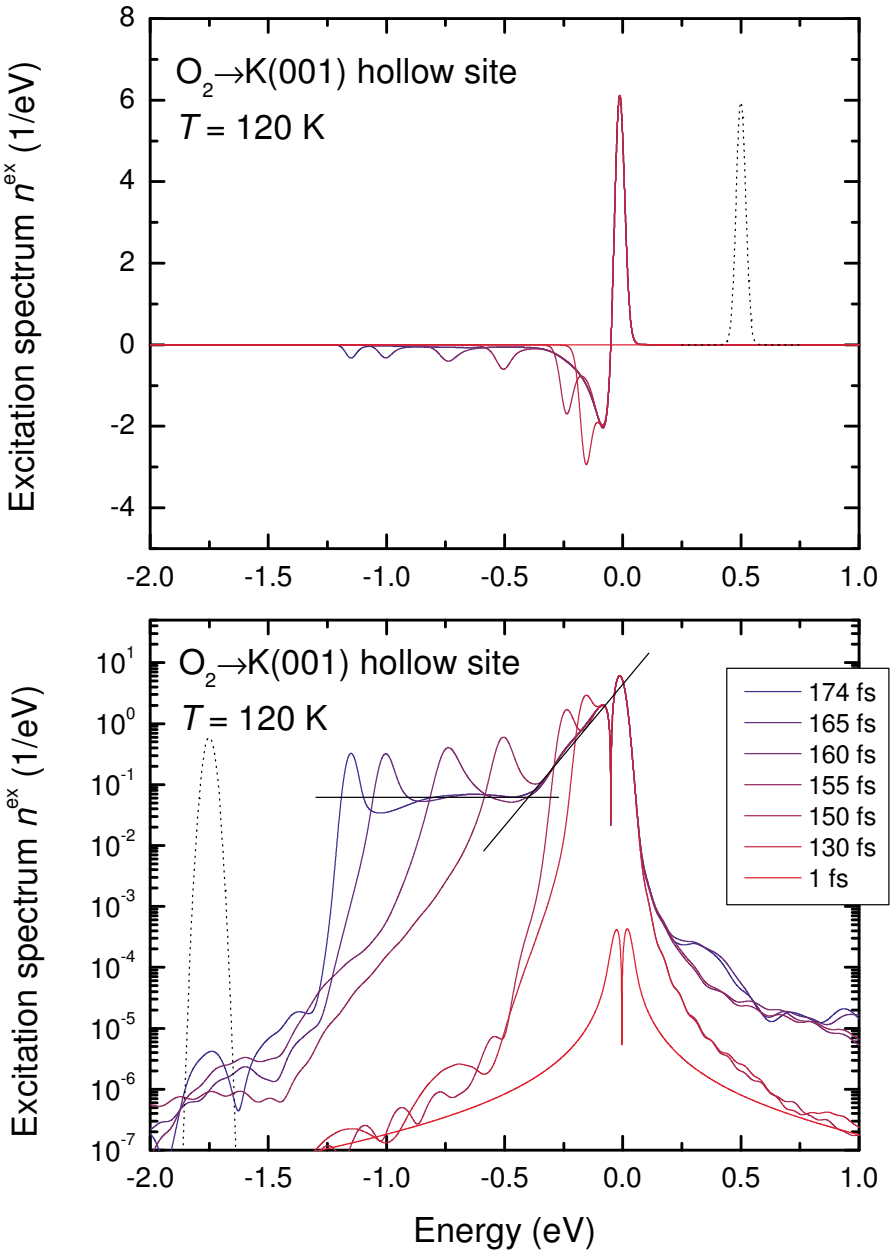

Figure 8.6.: Upper panel: Excitation spectra n^{ex} at different time steps on the adiabatic trajectory calculated as a difference to an equilibrium Fermi distribution of $T = 120\,\mathrm{K}$. Lower panel: same as in the upper panel, but plotted on a semi-logarithmic scale.

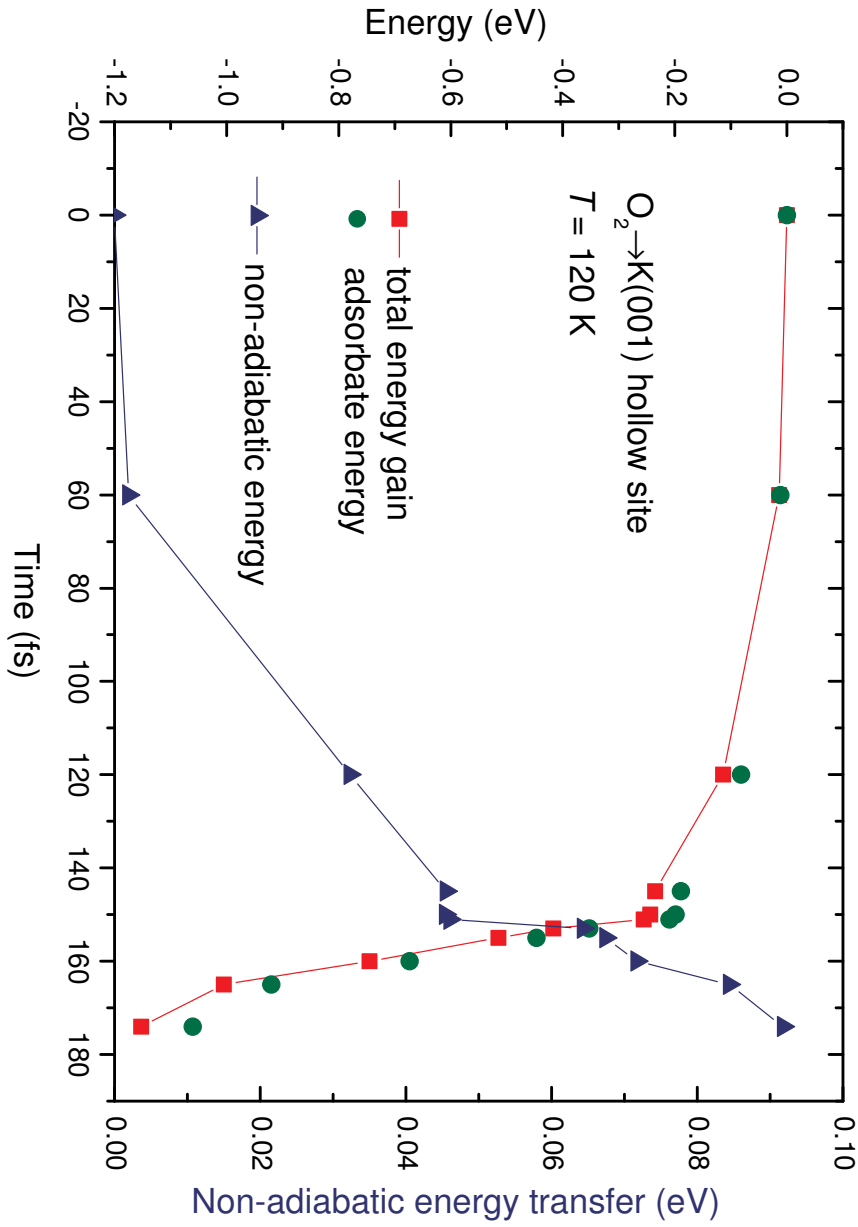

Figure 8.7.: Adsorbate induced energy gain of the electronic system (red squares), electronic resonance position (green circles), and the energy transfer into non-adiabatic excitations (blue triangles).

of the instantaneous Hamiltonian at a time t_1 as depicted in the left part of the figure. They are given numbers $i = 1..N$ according to their one particle energy. Likewise, each state is a assigned an initial occupation number f_i which can be a Fermi distribution and remains fixed at all times. The density operator $\hat{\rho}$ on the other hand will evolve in time as the states change under the influence of the electronic Hamiltonian as depicted on the right. Because the non-diagonal matrix elements of the Hamiltonian are all zero the initial states remain eigenstates of the instantaneous Hamiltonian even if the energy of the adsorbate is changed. Yet, the order of the states with respect to their eigenenergy may change.

It is straightforward to write down the occupation numbers of these states in the adiabatic and the non-adiabatic case. In the adiabatic case the number of the electronic states are ordered with respect to their instantaneous eigenenergy such that the ordering of eigenenergies and the occupation numbers are the same. In the non-adiabatic case this is not the case because the occupation of a particular state does not change while it evolves with time. A simple example will make this clearer.

In Figure 8.8 the adsorbate state initially has the occupation number f_5 because it has the fifth lowest eigenenergy. Subject to the Hamiltonian it will evolve over time but its occupation probability will remain f_5. So although its eigenenergy has been reduced to the second lowest value, its occupation number has not changed to f_2 as it should have in the adiabatic case.

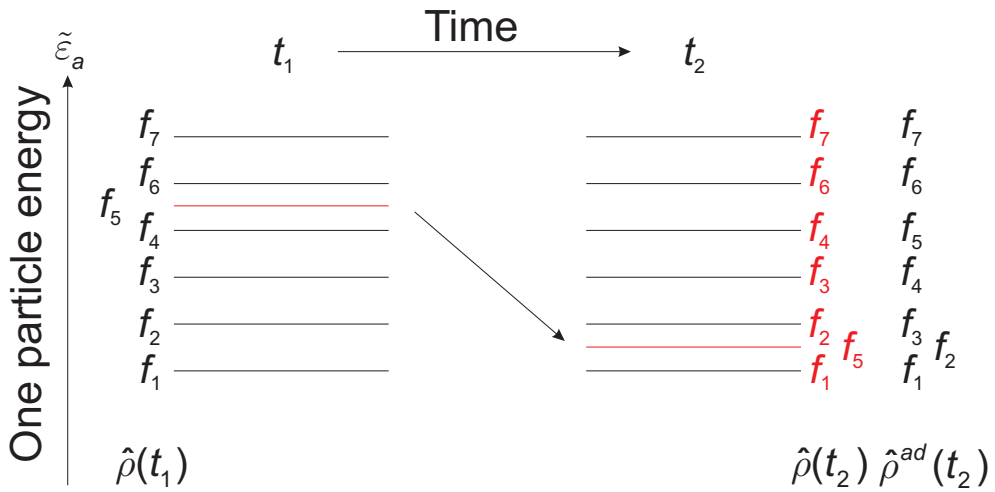

Figure 8.8.: Renumbering of the one-particle states if the energy of the adsorbate state changes.

9. Summary and Outlook

The results presented in this study answer open questions arising in connection with the non-adiabatic effects present in the reaction of molecular oxygen with alkali metal surfaces. Theoretical as well as experimental approaches were used to study these systems. Experimentally, the reaction kinetics were studied using photoelectron spectroscopy confirming predictions from thermodynamical calculations. This knowledge was used to interpret chemicurrent as well as exoelectron emission data which were recorded as part of this thesis. On the theoretical side, electronically non-adiabatic model calculations based on input from density functional theory were presented for the adsorption of molecular oxygen on a potassium surface.

9.1. Summary

9.1.1. Photoelectron Spectroscopy

Photoelectron spectroscopy was used to determine the kinetics of molecular oxygen reacting with alkali metal surfaces. Typical experiments were conducted under UVH conditions (base pressure $\approx 10^{-11}$ mbar) and at low surface temperatures (typically < 120 K). The samples were exposed to a low pressure atmosphere ($\approx 10^{-8}$ mbar) of oxygen while XPS and UPS spectra were recorded. A rich variety of oxide species was found to form under these conditions: regular oxide, peroxide and superoxide species could be identified in agreement with previously published data. They were identified by using the chemical shift of the O 1s photoemission line in XPS. Emission from molecular orbitals observed using UPS confirmed the assignment of these peaks. The chemical shift of the O 1s line was explained by the increased charge that is transfered onto the oxygen atoms in their different oxidation states. The regular atomic oxides show the lowest binding energy, followed by the peroxides and the superoxides at the highest binding energies. A chemical trend toward higher binding energies can be observed when going upward in the periodic system (Cs $\rightarrow$ Rb $\rightarrow$ K $\rightarrow$ Na $\rightarrow$ Li). Pronounced differences

between the relative contribution of the various oxide species are found for the specific elements:

- Lithium forms the regular oxide LiO_2 with dissociatively bound oxygen atoms when exposed to molecular oxygen in the UHV and at surface temperatures as low as 100 K.
- Sodium oxidizes to form NaO_2 as well as Na_2O_2, which were shown to exist simultaneously and in approximately equal contribution (UHV, ≤ 120 K).
- The oxidation of potassium is dominated by molecular adsorption, first as peroxide K_2O_2, later as potassium superoxide KO_2. Some dissociation of oxygen and the formation of regular oxide K_2O has been found at very low exposures which seems to be defect related (UHV, ≤ 120 K).
- Rubidium and cesium films show a rich variety of oxides. Clear reaction kinetics could not be determined from the available photoemission data (UHV, ≤ 120 K).

The reaction kinetics of potassium were studied in more detail: the initial oxidation is dominated by the direct adsorption of peroxide ions on the surface which leads to a simple exponential saturation of the peroxide concentration (Langmuir adsorption). On top of the peroxide layer a superoxide films grows, whose growth is driven by the diffusion of zero-valent potassium atoms from the bulk to the surface. The final thickness of the superoxide layer therefore depends on the initial thickness of the potassium layer.

The successive oxidation of the oxide film causes a reduction of the electron density that is available at the surface. UPS data of the K 4s valence band show an exponential decrease of the photoemission yield near the Fermi edge (He I, UHV, ≤ 120 K). This leads, on the one hand, to a decreased reaction rate because of the lack of electrons and on the other hand, to the enhancement of non-adiabatic effects. The later is caused by the reduced interaction between the metal and the adsorbate, which results into an increased lifetime of a possibly injected transient hole state.

9.1.2. Chemicurrent and Exoemission

Chemicurrents were observed on p-type doped Schottky diodes which show excellent diode characteristics at low temperatures. Hot holes are efficiently excited by the oxidation of alkali metal surfaces which has been demonstrated by large chemicurrent yields. The detection of hot electrons in a chemicurrent was not possible because the alkali

metals form Ohmic contacts on n-doped silicon substrates. An attempt to remedy this by the introduction of a palladium buffer layer was not successful.

The exoemission of electrons was monitored alongside the chemicurrent experiments. A delay between the chemicurrent maximum and the peak exoemission was observed, which could not be explained by a simply proportionality between the reaction rate and the respective excitation probabilities. Instead the change of the respective efficiencies while the surface changes its electronic structure must be considered.

An explanation was presented in the framework of the NNL model taking into account the limited band width of the alkali metals. The chemicurrent was explained by the resonant injection of hot holes into the metallic band whereas the exoemission was explained by Auger transitions. For the clean metal surface the charge transfer to the molecule occurs resonantly near the Fermi level causing little electronic excitations. The increasing oxygen coverage reduces the density of available electrons at the surface which enhances the lifetime of electronic hole excitations located on the molecule in front of the surface. This in turn leads to an increasing non-adiabaticity of the reaction and hence increased exoemission and chemicurrent efficiency. Because the recorded signals are the product of the reaction rate and the efficiencies this leads to a maximum in the chemicurrent and the exoemission. Because the exoemission requires an, in a sense, higher degree of non-adiabaticity than the chemicurrent, the maximum of the chemicurrent precedes the one of the exoemission.

9.1.3. Model Calculations

Density functional calculations showed that the interaction potential between the oxygen molecule and a potassium surface only of the order of a few ten milli electronvolts. This leads to a long lifetime of hole states localized on the molecule which in turn is in favor of non-adiabatic excitations. Electronic friction alone cannot account for the excitation spectra calculated in a Newns-Anderson approach. Instead, resonant charge transfer of hot holes within the metal's conduction band seems responsible for the chemicurrent. A pronounced imbalance between electron like and hole like excitations was found. The results are compatible with classical descriptions of charge transfer according to Hagstrum [Hag54] and so called *chemical hole diving* [Gre97].

To solely explain the descent of the molecular levels in front of the surface by the image potential interaction does not seem to capture the complete physics of the process. From the presented molecular dynamics calculations it seems that the vibrational motion of the molecule plays an active role in the excitation of the hot holes. Further theoretical

insights into the role of vibrational excitations as well as into the role of the spin would be highly desirable. Especially multi surface molecular dynamics combined with electronic excitation calculations may be helpful to further understand the mechanism of electronic excitations through molecular adsorption.

9.2. Outlook

The interpretation of chemicurrent data becomes exceedingly complicated if the exact reactions conditions are of importance. Better knowledge of the kinetics of the gas-surface reactions is therefore mandatory. One way to achieve this aim would be to reduce the system size from square centimeter sized Schottky diodes to nano structured devices. Thereby the homogeneity of the surface is hoped to be enhanced. Additionally one may be able to investigate quantum size effects on the surface chemistry. A second approach would be to proceed to well defined surfaces. In this way surface science methods could be employed to learn more about the interaction between geometric structure, electronic structure and non-adiabaticity.

The model calculations showed a great imbalance between hot holes and electrons. Because the electronic excitations are limited to secondary processes and (probably) the electronic friction mechanism, this imbalance should also show in the chemicurrent when experiments on p-doped substrate are compared to studies conducted on n-doped substrate. Due to its importance as a test of this theoretical prediction further attempts to build n-type alkali Schottky diodes (possibly using other buffer layers) should be considered.

A. Diffusion Limited Growth

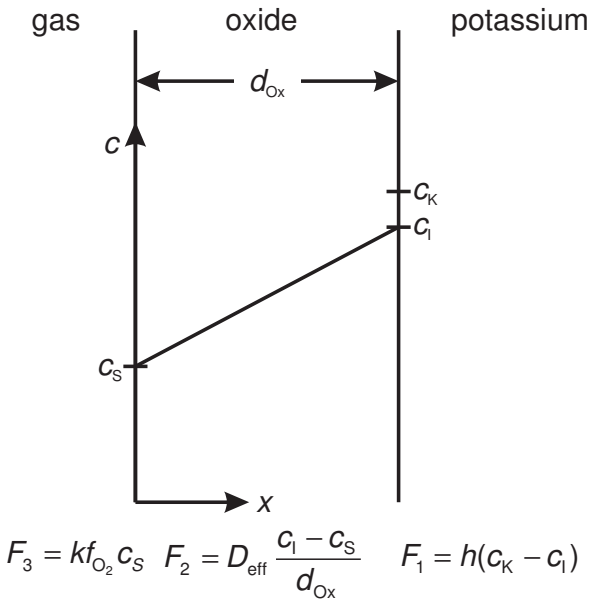

Figure A.1.: Model for the oxidation of potassium (Figure adapted from [DG65]).

The bulk oxidation follows a diffusion controlled process similar to the famous Deal-Grove model used to describe the thermal oxidation of silicon [PK77, DG65]. In the case of silicon oxygen diffuses through the oxide layer and the growth happens at the interface between the oxide and the silicon. For potassium it is the potassium atoms that diffuse through the oxide. The oxide layer is therefore growing from the surface.

Figure A.1 shows the adaptation of Deal and Grove's model for the situation in a potassium film. The flux F_1 of potassium atoms from the metal into the oxide film is given by

$$F_1 = h(c_K - c_I), \tag{A.1}$$

where h is a rate constant coupling the potassium concentration c_{K} in the metal and the concentration of free potassium atoms in the oxide film right at the interface c_{I}. Fick's law states that, assuming steady state conditions, the flux F_2 inside the oxide layer must be constant throughout the thickness of the oxide film d_{ox}. Thus F_2 can be calculated from the difference between the surface concentration c_{S} and the concentration at the interface

$$F_2 = D_{\mathrm{eff}} \frac{c_{\mathrm{I}} - c_{\mathrm{S}}}{d_{\mathrm{Ox}}}, \tag{A.2}$$

where D_{eff} is an effective diffusion constant. The flux out of the surface F_3 is given by the reaction with the oxidant

$$F_3 = k f_{\mathrm{O}_2} c_{\mathrm{S}} \tag{A.3}$$

which is proportional to the potassium concentration at the surface and to the oxygen flux f_{O_2} from the gas phase. Under steady state conditions the flux must be equal

$$F(x) = F_1 = F_2 = F_3 \tag{A.4}$$

at all positions x. Eliminating c_{S} and c_{I} the flux

$$F = \frac{k f_{\mathrm{O}_2} c_{\mathrm{K}}}{1 + \dfrac{k f_{\mathrm{O}_2}}{h} + \dfrac{k f_{\mathrm{O}_2} d_{\mathrm{Ox}}}{D_{\mathrm{eff}}}} \tag{A.5}$$

can be explicitly written as a function of the oxide thickness. The growth of the oxide layer on the other hand is determined by the differential equation

$$\frac{d}{dt} d_{\mathrm{Ox}} = F/\rho = \frac{k f_{\mathrm{O}_2} c_{\mathrm{K}}/\rho}{1 + \dfrac{k f_{\mathrm{O}_2}}{h} + \dfrac{k f_{\mathrm{O}_2} d_{\mathrm{Ox}}}{D_{\mathrm{eff}}}} \tag{A.6}$$

if ρ is the number density of potassium atoms incorporated into a unit volume of the oxide. Equation (A.6) can be easily solved by straightforward integration

$$d_{\mathrm{Ox}} = -\frac{1}{2}\frac{a}{b} + \sqrt{\frac{c}{b}t + \left(\frac{1}{2}\frac{a}{b}\right)^2} \tag{A.7}$$

with

$$a = 1 + \frac{k f_{O_2}}{h} \tag{A.8}$$

$$b = \frac{1}{2}\frac{k f_{O_2}}{D_{\text{eff}}} \tag{A.9}$$

$$c = k f_{O_2}\frac{c_K}{\rho} \tag{A.10}$$

For long reactions times

$$\frac{c}{b}t \gg \left(\frac{1}{2}\frac{a}{b}\right)^2 \tag{A.11}$$

Eqn. (A.7) can be further simplified to the quadratic relation

$$t\left(d_{Ox}\right) = \frac{\rho}{2 c_K D_{\text{eff}}} d_{Ox}^2 \tag{A.12}$$

between the time needed to grow an oxide film and its thickness. Especially, the time needed to thoroughly oxidize the film varies with the square of the initial thickness of the metallic film. Notice also that Eq. (A.12) does not include the oxygen pressure explicitly. The reaction time should therefore be relatively insensitive to pressure changes as long as a sufficient supply of the oxidant is guaranteed. For relatively small reactions times on the other hand, Eqn. (A.7) can be approximated by

$$t\left(d_{Ox}\right) = \frac{\rho\left(1 + \frac{k f_{O_2}}{h}\right)}{k f_{O_2} c_K} d_{Ox} \tag{A.13}$$

a linear relationship which is independent of the diffusion constant but is almost linearly depended on the pressure. In the linear regime the reaction should therefore be insensitive to temperature changes if changes in the chemistry of the reaction can be neglected.

B. Numerical Details

Integration of the Schrödinger equation In a quantum mechanical problem it is often necessary to solve the time dependent Schrödinger equation

$$\hat{H}(t)\Psi(t) = i\frac{\partial}{\partial t}\Psi(t) \tag{B.1}$$

to find the evolution of a wave function $\Psi(t)$. In section 8.2 this procedure was used to calculate electronic excitations in an ensemble of non-interaction electrons that were caused by the adsorption of an adsorbate molecule. A practical approach to a numerical solution of Eqn. (B.1) is to consider the formal solution of the Schrödinger equation

$$\Psi(\Delta t) = \exp\left(-i\hat{H}\Delta t\right)\Psi(0) \tag{B.2}$$

for a time-independent Hamiltonian. Formally, the exponential function can be approximated by

$$\exp(-i\hat{H}\Delta t) = \frac{1 - \frac{i}{2}\hat{H}\Delta t}{1 + \frac{i}{2}\hat{H}\Delta t} \tag{B.3}$$

which is correct to $\mathcal{O}\left(\Delta t^2\right)$. This can be seen by expanding the exponential function in a Taylor series

$$\left(1 + \frac{x}{2}\right)\left(1 - x + \frac{x^2}{2} + \cdots\right) = 1 - x + \frac{x^2}{2} + \frac{x}{2} + \frac{x^2}{2} + \frac{x^3}{4} + \cdots \tag{B.4}$$

$$= 1 - \frac{x}{2} + \frac{x^3}{4} \tag{B.5}$$

$$= 1 - \frac{x}{2} + \mathcal{O}\left(x^3\right) \tag{B.6}$$

and multiplying with $1 + \frac{x}{2}$ from the left. This holds also true for the operator (or matrix) exponential function if

$$\frac{1}{1 + \frac{1}{2}\hat{H}\Delta t} = \left(1 + \frac{1}{2}\hat{H}\Delta t\right)^{-1} \tag{B.7}$$

is considered as the inverse of the denominator. This naturally leads to the well known prescription for the numerical integration of the Schrödinger equation

$$\left(\mathbb{1} + \frac{i}{2}\hat{H}\Delta t\right)\Psi^{n+1} = \left(\mathbb{1} - \frac{i}{2}\hat{H}\Delta t\right)\Psi^{n}. \tag{B.8}$$

If the wave function Ψ is expanded in a finite basis set this equation is a linear equation of the form $AX = B$ which can be solved efficiently using standard methods of numerical mathematics.

Shift of the chemical potential The introduction of an additional state below the chemical potential μ_0 of the unperturbed metall causes a shift of the chemical potential μ. Initially, the metallic states were occupied by a number of electrons N. After the charge transfer to the molecule this number is reduced by one. From this observation the shift of the chemical potential $\mu - \mu_0$ of the equilibirum Fermi distribution $f(\varepsilon, \mu)$ can be calculated by

$$N = \int_{-\infty}^{\infty} \rho_0(\varepsilon) f(\varepsilon, \mu_0)\, d\varepsilon, \text{ and} \tag{B.9}$$

$$N - 1 = \int_{-\infty}^{\infty} \rho(\varepsilon) f(\varepsilon, \mu)\, d\varepsilon. \tag{B.10}$$

Subtracting the second equation provides a way to calculate the shift by solving

$$1 = \int_{-\infty}^{\infty} \rho(\varepsilon)\left(f(\varepsilon, \mu_0) - f(\varepsilon, \mu)\right) d\varepsilon \tag{B.11}$$

Given that the shift of the chemical potential is small, the integral can be approximated by

$$1 = \int_{-\infty}^{\infty} \rho(\varepsilon)\frac{\partial f}{\partial \mu}(\mu_0 - \mu)\, d\varepsilon. \tag{B.12}$$

This equation can be further simplyfied by noticing that because of $f(\varepsilon, \mu) = f(\varepsilon - \mu)$ the partial derivatives satisfy

$$\frac{\partial f}{\partial \varepsilon} = -\frac{\partial f}{\partial \mu} \tag{B.13}$$

and by noticing that $\partial f/\partial\varepsilon$ is only considerably different from zero close to the chemical potential. Finally, the shift of the chemical potential can be calculated from the metallic density of states at the Fermi edge $\rho_0 = \rho_0(\mu_0)$

$$\frac{1}{\rho_0\,(\mu_0 - \mu)} = -\int_{-\infty}^{\infty} \frac{\partial f}{\partial \varepsilon} d\varepsilon \tag{B.14}$$

$$= -(f(\infty) - f(-\infty)) \tag{B.15}$$

$$= 1. \tag{B.16}$$

From the definition of the excitation spectrum n_{ex} given in section 3.6 the non-vanishing thermal part of the spectrum

$$n_{\mathrm{ex}}(\varepsilon) = \rho_0\,(f(\varepsilon, \mu_0) - f(\varepsilon, \mu)) \tag{B.17}$$

$$\approx \rho_0 \frac{1}{\rho_0} \frac{\partial f}{\partial \mu}\,(\varepsilon, \mu_0) \tag{B.18}$$

$$n_{\mathrm{ex}}(\varepsilon) = \frac{\partial f}{\partial \mu}\,(\varepsilon, \mu_0) \tag{B.19}$$

can be calculated which is solely due to the shift of the chemical potential and should not be considered a non-adiabatic excitation.

C. Pulse Counting Electronics

C.1. Circuit Description

During the course of this study it became apparent that the counting electronics, which were available at the time, were not suitable for the counting of electrons for exoemission. Initially, a charge sensitive preamplifier followed by a differentiating amplifier was used. Such a setup is frequently used in nuclear physics because they conserve the initial energy of the impinging particle as the peak height. These preamplifiers have a fast rise time and an extremely long decay time. A short charge pulse at the input therefore leads to a step like output. If the pulse rate is too high, these stairs will add up until the output of the amplifier saturates. This is obviously not desirable. A low cost electronic circuit has therefore been developed.

The circuit comprises three stages: (a) a high voltage decoupling, (b) a fast pulse amplifier and (c) a discriminator circuit for pulse shaping. Parts (a) and (b) are shown in Fig. C.1. A circuit diagram of the discriminator circuit (c) is included in Fig. C.2. The DC high voltage at the channeltron output is decoupled through the three high voltage resistant capacitors. A resistor work fixes the potential and two diodes protect electronics at the output from overvoltages. The amplifier comprises a common base amplifier followed by a common emitter driver stage. The output of the amplifier is fed into a LT1016 comparator circuit which transforms the millivolt output of the amplifier to a $\pm 3\,\mathrm{V}$ output signal, which can be used as the input of any digital counter. The discriminator level can be adjusted by changing the potentiometer at the input of the buffering amplifier. Because of the high frequencies at the output, a terminal resistor of approximately $200\,\Omega$ must be fitted to the far end of the output cable.

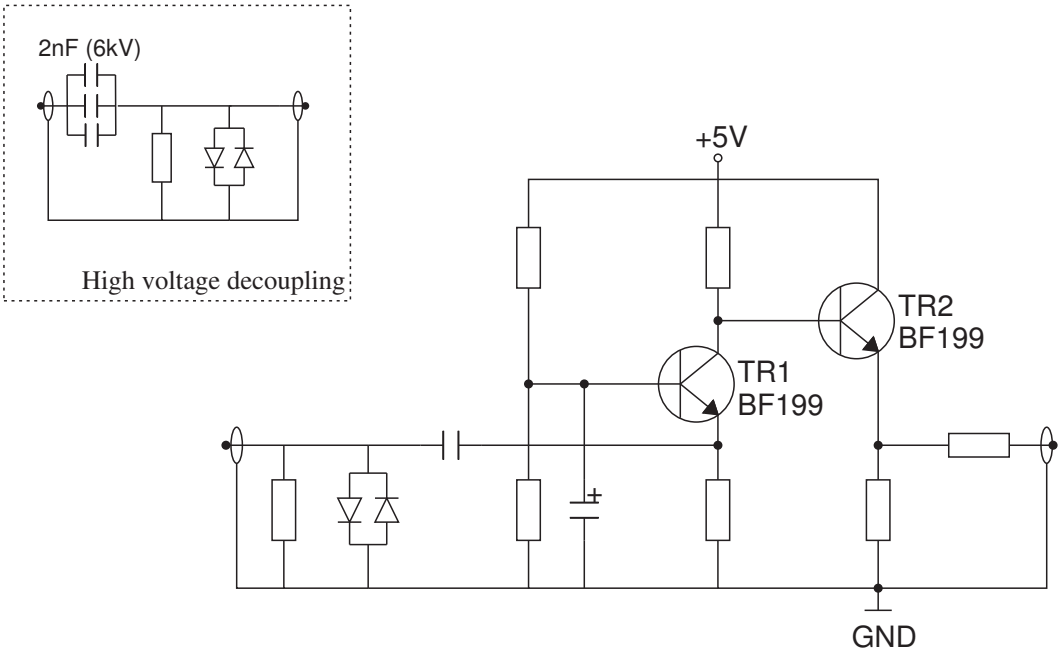

Figure C.1.: Channeltron pulse amplifier for Burle Series 4800 channeltron.

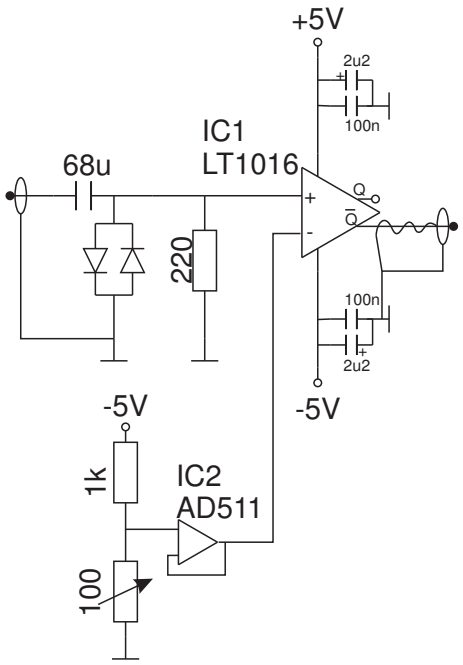

Figure C.2.: Discriminator for pulse amplifier electronics

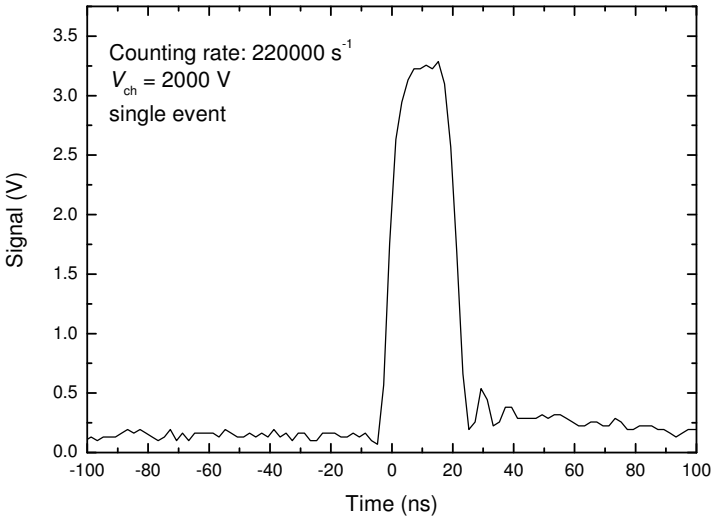

Figure C.3.: Output signal after signal conditioning by the preamplifier and discriminator.

C.2. Signal Characterization

The output signal of a channeltron has a peak width of approximately 4 ns which gets broadened by the electronic circuitry. Figure C.3 shows the output after conditioning by the preampflifier and discriminator recorded with a digitial sampling scope. The rise time of the signal is determined by the LT1016 descriminator. The 20 ns peak width is caused by the capacitances in the circuit. The electronics can be easily used for counting rates of two megahertz and more which is demonstrated in Fig. C.4.

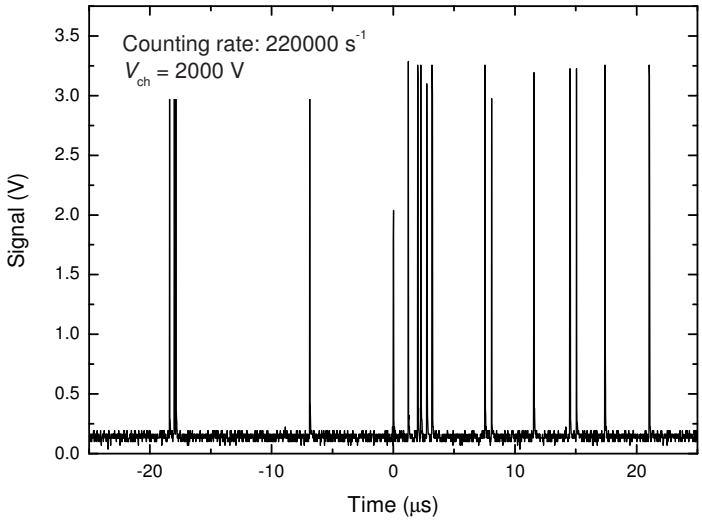

Figure C.4.: Output signal after signal conditioning showing the output at a counting rate of two megahertz.

Bibliography

[Ale71] N. G. Alexandropoulos, *X-Ray Plasmon Scattering of Lithium*, J. Phys. Soc. Jpn. **31** (1971), 1790–1795, DOI 10.1143/JPSJ.31.1790.

[AM76] Neil W. Ashcroft and N. David Mermin, *Solid State Physics*, Sauders College Publishing, 1976.

[Atk98] P. W. Atkins, *Physical Chemistry*, 6th ed., Oxford University Press, Oxford, 1998.

[Aug25] Pierre Auger, *Sur l'effet photoélectrique composé*, J. Phys. Radium **6** (1925), 205–208, DOI 10.1051/jphysrad:0192500606020500.

[Bar47] John Bardeen, *Surface States and Rectification at a Metal Semi-Conductor Contact*, Phys. Rev. **71** (1947), 717–727, DOI 10.1103/PhysRev.71.717.

[Beh04] Jörg Behler, *Dissociation of Oxygen Molecules on the Al(111) Surface*, Ph.D. thesis, Technische Universität Berlin, 2004.

[BGG+93] A. Böttcher, R. Grobecker, T. Greber, A. Morgante, and G. Ertl, *Exoelectron emission during the oxidation of Na films*, Surface Science **280** (1993), 170, DOI 10.1016/0039-6028(93)90365-Q.

[BGI+95] A. Böttcher, R. Grobecker, R. Imbeck, A. Morgante, and G. Ertl, *Exoelectron emission during oxidation of Cs films*, J. Chem. Phys. **95** (1995), 3756, DOI 10.1063/1.460826.

[Blö94] P. E. Blöchl, *Projector augmented-wave method*, Phys. Rev. B **50** (1994), 17953–17979, DOI 10.1103/PhysRevB.50.17953.

[BMLP08] D.M. Bird, M.S. Mizielinski, M. Lindenblatt, and E. Pehlke, *Electronic excitation in atomic adsorption on metals: A comparison of ab initio and model calculations*, Surf. Sci. **602** (2008), 1212 – 1216, DOI 10.1016/j.susc.2008.01.026.

[BN89] R. Brako and D. M. Newns, *Theory of electronic processes in atom scattering from surfaces*, Rep. Prog. Phys. **52** (1989), 655, DOI 10.1088/0034-4885/52/6/001.

[BNRS89] E. Bertel, F. P. Netzer, G. Rosina, and H. Saalfeld, *Alkali-metal oxides. I. Molecular and crystal-field effects in photoemission*, Phys. Rev. B **39** (1989), 6082–6086, DOI 10.1103/PhysRevB.39.6082.

[BO27] M. Born and E. Oppenheimer, *Zur Quantentheorie der Molekeln*, Ann. Phys. **84** (1927), 457.

[BS70] M. J. W. Boness and G. J. Schulz, *Structure of $O2$*, Phys. Rev. A **2** (1970), 2182–2186, DOI 10.1103/PhysRevA.2.2182.

[CCL+95] Kenton D. Childs, Brad A. Carlson, Lori A. LaVanier, John F. Moulder, Dennis F. Paul, William F. Stickle, and David G. Watson, *Handbook of Auger Electron Spectroscopy*, 3rd ed., Physical Electronics, Inc., 6509 Flying Cloud Drive, Eden Prairie, MN 55344, USA, 1995.

[CK96] S. Chand and J. Kumar, *Current transport in Pd2Si/n-Si(100) Schottky barrier diodes at low temperatures*, Appl. Phys. A **63** (1996), 171, DOI 10.1007/s003390050368, Tab. 19.1.

[Con26] Edward Condon, *A Theory of Intensity Distribution in Band Systems*, Phys. Rev. **28** (1926), 1182–1201, DOI 10.1103/PhysRev.28.1182.

[DG65] B. E. Deal and A. S. Grove, *General Relationship for the Thermal Oxidation of Silicon*, J. Appl. Phys. **36** (1965), 3770–3778.

[DH95] G. R. Darling and S. Holloway, *The dissociation of diatomic molecules at surfaces*, Rep. Prog. Phys. **58** (1995), 1595–1672, DOI 10.1088/0034-4885/58/12/001.

[FA94] Hideaki Fujitani and Setsuro Asano, *Schottky-barrier height and electronic structure of the Si interface with metal silicides: $CoSi_2$, $NiSi_2$, and YSi_2*, Phys. Rev. B **50** (1994), 8681–8698, DOI 10.1103/PhysRevB.50.8681.

[FBG+94] G. H. Fecher, J. Bansmann, Ch. Grünewald, A. Oelsner, Ch. Ostertag, and G. Schönhense, *Oxidation of rubidium at platinum (111)*, Surf. Sci. **307-309** (1994), 70–75, DOI 10.1016/0039-6028(94)90372-7.

[FD26] J. Franck and E. G. Dymond, *Elementary processes of photochemical reactions*, Trans. Faraday Soc. **21** (1926), 536, DOI 10.1039/TF9262100536.

[FPDG77] B. Fischer, R. A. Pollak, T. H. DiStefano, and W. D. Grobman, *Electronic structure of* SiO_2*,* $Si_xGe_{1-x}O_2$*, and* GeO_2 *from photoemission spectroscopy*, Phys. Rev. B **15** (1977), 3193–3199, DOI 10.1103/PhysRevB.15.3193.

[GAC70] T.F. Gesell, E.T. Arakawa, and T.A. Callcott, *Exo-electron emission during oxygen and water chemisorption on fresh magnesium surfaces*, Surf. Sci. **20** (1970), 174 – 178, DOI 10.1016/0039-6028(70)90216-5.

[GE03] N. N. Greenwood and A. Earnshaw, *Chemistry of the Elements*, Elsevier Butterworth-Heinemann, Oxford, 2003.

[GFG+94] T. Greber, K. Freihube, R. Grobecker, A. Böttcher, K. Hermann, G. Ertl, and D. Fick, *Nonadiabatic processes during the oxidation of Li layers*, Phys. Rev. B **50** (1994), 8755–8762, DOI 10.1103/PhysRevB.50.8755.

[GGBE94] R. Grobecker, T. Greber, A. Böttcher, and G. Ertl, *Thermally activated emission of exoelectrons accompanying the oxidation of Cs films*, Phys. Status Solidi A **146** (1994), 259–267, DOI 10.1002/pssa.2211460122.

[Gla04] Stefan Glaß, *Detektion von elektronischen Anregungen bei chemischen Reaktionen an Metalloberflächen*, Ph.D. thesis, Universität Duisburg-Essen, 2004.

[GN04] S. Glass and H. Nienhaus, *Continuous Monitoring of Mg Oxidation by Internal Exoemission*, Phys. Rev. Lett. **93** (2004), 168302, DOI 10.1103/PhysRevLett.93.168302.

[GNWM01] B. Gergen, H. Nienhaus, W.H. Weinberg, and E.W. McFarland, *Chemically induced electronic excitations at metal surfaces*, Science **294** (2001), 2521.

[Gre94] T. Greber, *Chemical hole diving*, Chem. Phys. Lett. **222** (1994), 292 – 296, DOI 10.1016/0009-2614(94)00344-0.

[Gre97] T. Greber, *Charge-transfer induced particle emission in gas surface reactions*, Surf. Sci. Rep. **28** (1997), 1, DOI 10.1016/S0167-5729(97)00005-8, and references therein.

[Hag54] Homer D. Hagstrum, *Theory of Auger Ejection of Electrons from Metals by Ions*, Phys. Rev. **96** (1954), 336, DOI 10.1103/PhysRev.96.336.

[HAJ06] Graeme Henkelman, Andri Arnaldsson, and Hannes Jónsson, *A fast and robust algorithm for Bader decomposition of charge density*, Comp. Mat. Sci. **36** (2006), 354–360, DOI 10.1016/j.commatsci.2005.04.010.

[Hei65] Volker Heine, *Theory of Surface States*, Phys. Rev. **138** (1965), A1689–A1696, DOI 10.1103/PhysRev.138.A1689.

[HKMN09] K. Huba, D. Krix, C. Meier, and H. Nienhaus, *Ultrathin K/p-Si(001) Schottky diodes as detectors of chemically generated hot charge carriers*, J. Vac. Sci. Technol. A **27** (2009), 889–894, DOI 10.1116/1.3100218.

[HSSX92] J. Hrbek, T. K. Sham, M. L. Shek, and G. Q. Xu, *Potassium-oxygen interactions on a ruthenium(001) surface*, Langmuir **8** (1992), 2461–2472, DOI 10.1021/la00046a019.

[Hub08] Kornelia Huba, *Reaktivität und Eigenschaften dünner Alkalimetallfilme auf Oberflächen*, Master's thesis, University of Duisburg-Essen, 2008.

[JB51] Herrick L. Johnston and Thomas W. Bauer, *Low Temperature Heat Capacities of Inorganic Solids. VII. Heat Capacity and Thermodynamic Functions of* Li_2O. *Thermodynamics of the* $Li_2O - H_2O$ *System*, J. Am. Chem. Soc. **73** (1951), 1119–1122, DOI 10.1021/ja01147a070.

[JDB92] J. Jupille, P. Dolle, and M. Besancon, *Ionic oxygen species formed in the presence of lithium, potassium and cesium*, Surf. Sci. **260** (1992), 271, DOI 10.1016/0039-6028(92)90042-5.

[KB88] W. J. Kaiser and L. D. Bell, *Direct investigation of subsurface interface electronic structure by ballistic-electron-emission microscopy*, Phys. Rev. Lett. **60** (1988), 1406–1409, DOI 10.1103/PhysRevLett.60.1406.

[KGK+10] D. Kov'acs, A. Golczewski, G. Kowarik, F. Aumayr, and D. Diesing, *Low-energy ion-induced electron emission in metal-insulator-metal sandwich structures,*, Phys. Rev. B **81** (2010), 075411, DOI 10.1103/PhysRevB.81.075411.

[KH93] G. Kresse and J. Hafner, *Ab initio molecular dynamics for liquid metals*, Phys. Rev. B **47** (1993), 558.

[KH94a] G. Kresse and J. Hafner, *Ab initio molecular-dynamics simulation of the liquid-metal-amorphous-semiconductor transition in germanium*, Phys. Rev. B **49** (1994), 14251.

[KH94b] G. Kresse and J. Hafner, *Norm-Conserving and Ultrasoft Pseudopotentials for First-Row and Transition-Elements*, J. Phys.: Condens. Matter **6** (1994), 8245.

[KHN09] D. Krix, K. Huba, and H. Nienhaus, *Chemicurrent measurements using alkali metal covered Pd/p-Si(001) Schottky diodes*, J. Vac. Scie. Technol. A **27** (2009), 918, DOI 10.1116/1.3086643.

[Kit96] Charles Kittel, *Introductino to Solid State Physics*, 7th ed., Wiley, 1996.

[KJ99] G. Kresse and J. Joubert, *From ultrasoft pseudopotentials to the projector augmented wave method*, Phys. Rev. B **59** (1999), 1758, DOI 10.1103/PhysRevB.59.1758.

[Kle32] O. Klein, *Zur Berechnung von Potentialkurven für zweiatomige Moleküle mit Hilfe von Spektraltermen*, Z. Physik **76** (1932), 226–235, DOI 10.1007/BF01341814.

[KLM+73] S. P. Kowalczyk, L. Ley, F. R. McFeely, R. A. Pollak, and D. A. Shirley, *X-Ray Photoemission from Sodium and Lithium*, Phys. Rev. B **8** (1973), 3583–3585, DOI 10.1103/PhysRevB.8.3583.

[KM95] T. U. Kampen and W. Mönch, *Lead contacts on Si(111):H-1×1 surfaces*, Surf. Sci. **331-333** (1995), 490–495, DOI 10.1016/0039-6028(95)00079-8.

[KNN07] David Krix, Ramona Nünthel, and Hermann Nienhaus, *Electrochemical generation of hot charge carriers by hydrogen and deuterium atoms adsorbed on a silver surface*, Phys. Rev. B **75** (2007), 073410.

[KNW+73] M. Krauss, D. Neumann, A. C. Wahl, G. Das, and W. Zemke, *Excited Electronic States of* O_2^-, Phys. Rev. A **7** (1973), 69, DOI 10.1103/PhysRevA.7.69.

[Kra51] J. Kramer, *Untersuchungen mit dem Geiger-Spitzenzähler an bestrahlten Kristallen*, Z. Phys. **129** (1951), 34, DOI 10.1007/BF01333649.

[Kri05] David Krix, *Metall-Halbleiter-Kontakte unter Exposition Reaktiver Gase*, Diplomarbeit, Universität Duisburg-Essen, 2005.

[KTNL79] B. Kasemo, E. Törnqvist, J. K. Nørskov, and B. I. Lundqvist, *Photon and electron emission as indicators of intermediate states in surface reactions*, Surf. Sci. **89** (1979), 554, DOI 10.1016/0039-6028(79)90637-X.

[KW75] B. Kasemo and L. Walldén, *Photon and Electron Emission during Halogen Adsorption on Sodium*, Surf. Sci. **53** (1975), 393, DOI 10.1016/0039-6028(79)90677-0.

[KW78] B. Kasemo and L. Walldén, *Initial oxidation of potassium at 77 and 295 K*, Surf. Sci. **75** (1978), L379, DOI 10.1016/0039-6028(78)90261-3.

[LHPAD04] Florian Ladstädter, Ulrich Hohenester, Peter Puschnig, and Claudia Ambrosch-Draxl, *First-principles calculation of hot-electron scattering in metals*, Phys. Rev. B **70** (2004), 235125, DOI 10.1103/PhysRevB.70.235125.

[Lid95] R.A. Lidin, *Constants of Inoganic Substances: A Handbook*, rev. and augm. ed., Begell House, 1995.

[LM] P. J. Linstrom and W. G. Mallards (eds.), *NIST Chemistry Webbook, NIST Standard Reference Database Number 69*, National Institute of Standards and Technology, Gaithersburg MD, 20899, `http://webbook.nist.gov`, (retrieved November 8, 2009).

[LSR95] B. Lamontagne, F. Semond, and D. Roy, *K overlayer oxidation studied by XPS: the effects of the adsorption and oxidation conditions*, Surf. Sci. **327** (1995), 371, DOI 10.1016/0039-6028(94)00845-0.

[MBPH05] M. S. Mizielinski, D. M. Bird, M. Persson, and S. Holloway, *Electronic nonadiabatic effects in the adsorption of hydrogen atoms on metals*, J. Chem. Phys. **122** (2005), 084710, DOI 10.1063/1.1854623.

[MBPH07] M. S. Mizielinski, D. M. Bird, M. Persson, and S. Holloway, *Spectrum of electronic excitations due to the adsorption of atoms on metal surfaces*, The Journal of Chemical Physics **126** (2007), 034705, DOI 10.1063/1.2431362.

[MBPH08] M.S. Mizielinski, D.M. Bird, M. Persson, and S. Holloway, *Newns-Anderson model of chemicurrents in H/Cu and H/Ag*, Surface Science **602** (2008), 2617 – 2622, DOI 10.1016/j.susc.2008.06.015.

[McA04] Robert McAllister (ed.), *KP6500 Digital Kelvin Probe - User's guide*, McAllister Technical Services, 2004.

[MdCdB80] A. R. Miedema, P. F. de Châtel, and F. R. de Boer, *Cohesion in alloys – fundamentals of a semi-empirical model*, Physica B+C **100** (1980), 1 – 28, DOI 10.1016/0378-4363(80)90054-6.

[MHD06] B. Mildner, E. Hasselbrink, and D. Diesing, *Electronic excitations induced by surface reactions of H and D on gold*, Chem. Phys. Lett. **432** (2006), 133–138, DOI DOI: 10.1016/j.cplett.2006.10.048.

[Mön96] Winfried Mönch, *Electronic properties of ideal and interface-modified metal-semiconductor interfaces*, J. Vac. Sci. Technol. B **14** (1996), 2985–2993, DOI 10.1116/1.588947.

[Mön01] Winfried Mönch, *Semiconductor Surfaces and Interfaces*, 3rd ed., Springer Series in Surface Sciences, Springer-Verlag, 2001.

[MS85] J.M. Mooney and J. Silverman, *The theory of hot-electron photoemission in Schottky-barrier IR detectors*, Electron Devices, IEEE Transactions on **32** (1985), 33–39.

[MSSB95] John F. Moulder, William F. Stickle, Peter E. Sobol, and Kenneth D. Bomben, *Handbook of X-ray Photoelectron Spectroscopy*, Physical Electronics, Inc., 6509 Flying Cloud Drive, Eden Prairie, MN 55344, USA, 1995.

[NBG+99] H. Nienhaus, H. S. Bergh, B. Gergen, A. Majumdar, W. H. Weinberg, and E. W. McFarland, *Electron-Hole Pair Creation at Ag and Cu Surfaces by Adsorption of Atomic Hydrogen and Deuterium*, Phys. Rev. Lett. **82** (1999), 446, DOI 10.1103/PhysRevLett.82.446.

[Nie02] H. Nienhaus, *Electronic excitations by chemical reactions on metal surfaces*, Surf. Sci. Rep. **45** (2002), 3, DOI 10.1016/S0167-5729(01)00019-X.

[NKG07] Hermann Nienhaus, David Krix, and Stefan Glass, *Varying the Schottky barrier of thin film Mg/H:p-Si(111) contacts: properties and applications*, J. Vac. Sci. Technol. A **25** (2007), 950, DOI 10.1116/1.2484574.

[NNL79] J. K. Nørskov, D. M. Newns, and B. I. Lundqvist, *Molecular orbital description of surface chemiluminescence*, Surf. Sci. **80** (1979), 179 – 188, DOI DOI: 10.1016/0039-6028(79)90677-0.

[PBB80] G. Pirug, G. Brodén, and H.P. Bonzel, *Coadsorption of potassium and oxygen on Fe(110)*, Surf. Sci. **94** (1980), 323 – 338, DOI 10.1016/0039-6028(80)90010-2.

[PBE96] John. P. Perdew, Kieron Burke, and Matthias Ernzerhof, *Generalized Gradient Approximation Made Simple*, Phys. Rev. Lett. **77** (1996), 3865–3868, DOI 10.1103/PhysRevLett.77.3865.

[PC73] C.A. Papageorgopoulos and J.M. Chen, *Coadsorption of electropositive and electronegative elements: II. Cs and O2 on W (100)*, Surf. Sci. **39** (1973), 313 – 332, DOI 10.1016/0039-6028(73)90004-6.

[PK77] L.-G. Petersson and S.-E. Karlsson, *Clean and Oxygen Exposed Potassium Studied by Photoelectron Spectroscopy*, Phys. Scr. **16** (1977), 425, DOI 10.1088/0031-8949/16/5-6/041.

[PLF81] R.H. Prince, R.M. Lambert, and J.S. Foord, *Chemisorptive emission and luminescence: I. Chlorine/zirconium*, Surf. Sci. **107** (1981), 605 – 624, DOI 10.1016/0039-6028(81)90548-3.

[PNHH98] J.J Paggel, G Neuhold, H Haak, and K Horn, *Growth morphology and electronic structure of Na films on Si(111)-(7x7) and Si(111)-Na(3x1)*, Surf. Sci. **414** (1998), 221 – 235, DOI DOI: 10.1016/S0039-6028(98)00514-7.

[Red62] P.A. Redhead, *Thermal desorption of gases*, Vacuum **12** (1962), 203 – 211, DOI 10.1016/0042-207X(62)90978-8.

[Ree47] A. L. G. Rees, *The calculation of potential-energy curves from band-spectroscopic data*, Proc. Phys. Soc. **59** (1947), 998, DOI 10.1088/0959-5309/59/6/310.

[RS01] Karsten Reuter and Matthias Scheffler, *Composition, structure, and stability of* $RuO_2(110)$ *as a function of oxygen pressure*, Phys. Rev. B **65** (2001), 035406, DOI 10.1103/PhysRevB.65.035406; Karsten Reuter and Matthias Scheffler, *Erratum: Composition, structure, and stability of* RuO_2*(110) as a function of oxygen pressure (Phys. Rev. B* ***65****, 035406 (2001))*, Phys. Rev. B **75** (2007), 049901, DOI 10.1103/PhysRevB.75.049901.

[RST09] Sharani Roy, Neil Shenvi, and John C. Tully, *Dynamics of Open-Shell Species at Metal Surfaces*, J. Phys. Chem. C **113** (2009), 16311–16320, DOI 10.1021/jp811393w.

[Ryd32] Ragnar Rydberg, *Graphische Darstellung einiger bandenspektroskopischer Ergebnisse*, Z. Phys. **73** (1932), 376–385, DOI 10.1007/BF01341146.

[Sch97] R. F. Schmitsdorf, *Untersuchung zur Barrierenhöhe und deren Inhomogenität an Sn- und Pb/Si-(111)-Schottky-Kontakten*, Dissertation, Gerhard-Mercator-Universität Gesamthochschule, 1997.

[SD79] M. P. Seah and W. A. Dench, *Quantitative electron spectroscopy of surfaces: A standard data base for electron inelastic mean free paths in solids*, Surface and Interface Analysis **1** (1979), 2–11, DOI 10.1002/sia.740010103.

[Ser09] Nicola Seriani, *Ab initio thermodynamics of lithium oxides: from bulk phases to nanoparticles*, Nanotechnology **20** (2009), 445703, DOI 10.1088/0957-4484/20/44/445703.

[SGBF02] T. Schroeder, J. B. Giorgi, M. Bäumer, and H.-J. Freund, *Morphological and electronic properties of ultrathin crystalline silica epilayers on a Mo(112) substrate*, Phys. Rev. B **66** (2002), 165422, DOI 10.1103/PhysRevB.66.165422.

[SKM97] R. F. Schmitsdorf, T. U. Kampen, and W. Mönch, *Explanation of the Linear Correlation between Barrier Heights and Ideality Factors of Real Metal-Semiconductor Contacts by Laterally Nonuniform Schottky Barriers*, J. Vac. Sci. Technol. B **15** (1997), 1221, DOI 10.1116/1.589442.

[SL77] Roberta P. Saxon and B. Liu, *Ab initio configuration interaction study of the valence states of* O_2, J. Chem. Phys. **67** (1977), 5432, DOI 10.1063/1.434764.

[SLC+83] C.Y. Su, I. Lindau, P.W. Chye, S.-J. Oh, and W.E. Spicer, *Photoemission studies of clean and oxidized Cs*, J. Electron Spectrosc. Relat. Phenom. **31** (1983), 221, DOI 10.1016/0368-2048(83)85073-7.

[SRK87] L. Surnev, G. Rangelov, and M. Kiskinova, *Interaction of oxygen with an alkali modified Ru(001) surface*, Surf. Sci. **179** (1987), 283 – 296, DOI 10.1016/0039-6028(87)90059-8.

[Sze81] S.M. Sze, *Physics of Semiconductor Devices*, 2nd ed., John Wiley & Sons, Inc., 1981.

[TCE89] Michael J. Travers, Daniel C. Cowles, and G.Barney Ellison, *Reinvestigation of the electron affinities of O2 and NO*, Chem. Phys. Lett. **164** (1989), 449 – 455, DOI 10.1016/0009-2614(89)85237-6.

[Ter84] J. Tersoff, *Schottky Barrier Heights and the Continuum of Gap States*, Phys. Rev. Lett. **52** (1984), 465–468, DOI 10.1103/PhysRevLett.52.465.

[Ter86] J. Tersoff, *Calculation of Schottky barrier heights from semiconductor band structures*, Surf. Sci. **168** (1986), 275 – 284, DOI 10.1016/0039-6028(86)90857-5.

[TGB+02] J. R. Trail, M. C. Graham, D. M. Bird, M. Persson, and S. Holloway, *Energy Loss of Atoms at Metal Surfaces due to Electron-Hole Pair Excitations: First-Principles Theory of Chemicurrents*, Phys. Rev. Lett. **88** (2002), 166802, DOI 10.1103/PhysRevLett.88.166802.

[TK09] Matthias Timmer and Peter Kratzer, *Electron-hole spectra created by adsorption on metals from density functional theory*, Phys. Rev. B **79** (2009), 165407, DOI 10.1103/PhysRevB.79.165407.

[Tul90] John C. Tully, *Molecular dynamics with electronic transitions*, J. Chem. Phys. **93** (1990), 1061, DOI 10.1063/1.459170.

[Tun91] T. R. Tung, *Electron transport of inhomogeneous Schottky barriers*, Appl. Phys. Lett. **58** (1991), 2821, DOI 10.1063/1.104747.

[UKN10a] U.Hagemann, D. Krix, and H. Nienhaus, *Electronic excitations generated by the deposition of Mg on Mg films*, Phys. Rev. Lett. **104** (2010), 028301, DOI 10.1103/PhysRevLett.104.028301.

[UKN+10b] U.Hagemann, D. Krix, H. Nienhaus, M. Timmer, and P. Kratzer, *Electronic Excitations in Magnesium Epitaxy: Experiment and Theory*, Phys. Rev. B **82** (2010), 155420.

[WCM+05] Jason D. White, Jun Chen, Daniel Matsiev, Daniel J. Auerbach, and Alec M. Wodtke, *Vibrationally promoted emission of electrons from low work function surfaces: Oxygen and Cs surface coverage dependence*, J. Vac. Sci. Technol. A **23** (2005), 1085–1089, DOI 10.1116/1.1861942.

[WOW+05] S. Wendt, E. Ozensoy, T. Wei, M. Frerichs, Y. Cai, M. S. Chen, and D. W. Goodman, *Electronic and vibrational properties of ultrathin SiO2 films grown on Mo(112)*, Phys. Rev. B **72** (2005), 115409, DOI 10.1103/PhysRevB.72.115409.

[WSK+87] B. Woratschek, W. Sesselmann, J. Küppers, G. Ertl, and H. Haberland, *The interaction of cesium with oxygen*, J. Chem. Phys. **86** (1987), 2411–2422, DOI 10.1063/1.452089.

[WTA04] Alec M. Wodtke, John C. Tully, and Daniel J. Auerbach, *Electronically non-adibatic interactions of molecules at metal surfaces*, Int. Rev. Phys. Chem. **23** (2004), 513–539.

Danksagung

An dieser Stelle möchte ich denjenigen Menschen danken, die es mir erst ermöglicht haben diese Arbeit zu erstellen.

Zuvorderst möchte ich meinen Eltern, Brigitte und Udo, danken, die mich über all die Jahre meines Studiums und der anschließenden Dissertation moralisch als auch finanziell unterstütz haben. Danke, ohne euch hätte ich dies alles nicht erreichen können.

Ganz speziell danken möchte ich Ramona Nünthel, die mit viel Geduld an meiner Seite gestanden hat und mich wieder aufgerichtet hat wenn es mal wieder nicht so lief wie es laufen sollte.

Bei Prof. Hermann Nienhaus möchte ich mich bedanken für die Unterstützung durch das Bereitstellen seines Labors für die Messungen und ganz besonders für sein immer offenes Ohr.

An Kornelia Huba und Ulrich Hagemann geht mein Dank für die enge Zusammenarbeit an vielen Projekten. Dank auch für das mühsame Korrekturlesen und für die guten Anregungen für diese Arbeit.

Prof. Rolf Möller und Prof. Axel Lorke danke ich herzlich für die Bereitstellung ihrer Räumlichkeiten.

Den Arbeitsgruppen Möller und Lorke danke ich für die herzliche Aufnahme und die immer gute Arbeitsatmosphäre.